SMALL STRAIN STIFFNESS OF FINE GRAINED SOILS

by

Giulia Viggiani

A Thesis submitted for the Degree of
Doctor of Philosophy

THE CITY UNIVERSITY
Civil Engineering Department

August 1992

CONTENTS

LIST OF TABLES

LIST OF FIGURES

ACKNOWLEDGEMENTS

Three years ago I arrived in London, a little apprehensive about what I might meet. The Geotechnical Engineering Research Centre has been a very interesting and satisfying place to be. This is in no small part due to the efforts of Prof. John H. Atkinson. I am grateful to him for the very many stimulating conversations and for his advice and support as my supervisor.

The research was supported by SERC and carried out in collaboration with the Building Research Establishment, represented by Dr Colin P. Abbiss. Dr Abbiss supervised the field work and shared many hours of hard labour in situ. I am very grateful to him for his constant support and encouragement and also to the other members of the geotechnical division at BRE for providing a very friendly working environment.

All the members of the GERC, both those present and past, have contributed to make the group a very special place to work in. In particular I would like to thank Dr Matthew R. Coop for his friendship and his help with the setting up of the equipment and Dr Sarah E. Stallebrass for her friendly support, for her useful comments on the draft thesis and in general for all her help over the past three years. I would also like to thank all the technicians, but especially Mr Lloyd Martika and Mr Keith Osborne, Miss Heleni Pantelidou who helped with some of the figures and Dr Claudio Mancuso who provided the FFT algorithm.

My family provided love and support and Mrs Maureen Brennan provided the wine and taught me english.

DECLARATION

I grant powers of discretion to the University Librarian to allow this thesis to be copied in whole or in part without further reference to me. This permission covers only single copies made for study purposes, subjected to normal conditions of acknowledgement.

ABSTRACT

Dynamic measurements of very small strain stiffness (ϵ_s = 0.001% and less) were carried out both in the laboratory, using piezoceramic bender elements of the type developed at the Norwegian Geotechnical Institute and at the University College of North Wales, and in situ, using surface wave techniques.

For the purpose of the research described in this dissertation, the piezoceramic bender elements were incorporated in two computer controlled hydraulic stress path cells so that it was possible to measure the very small strain stiffness of the soil at any stage of a triaxial stress path test and compare it directly to shear moduli obtained at larger strain levels. The electronics required to run the bender elements proved to be simple and inexpensive, especially if compared to those required for other dynamic testing techniques. Also the interpretation of the tests was much simpler and more direct than in other dynamic testing techniques. Some preliminary work based on the numerical analysis of the signals at the bender elements was carried out to improve the definition of the arrival of the shear wave.

The dependence of the very small strain stiffness on factors such as stress state and history, as described by mean effective stress, deviatoric stress, voids ratio and overconsolidation ratio, was investigated for fine grained soils of different plasticity (PI = 11–41). The dependence of the very small strain stiffness of fine grained soils on stress state and history could be conveniently expressed as:

$$\frac{G'_{max}}{p_r} = A \left(\frac{p'}{p_r}\right)^n R_o^m$$

where p_r is a reference pressure introduced to render the relationship between shear modulus and mean effective stress non-dimensional and A, n and m are material properties. The values of the parameters A, n and m obtained for the four fine grained soils used in the present work compared well with published data. In particular the multiplier A was found to decrease and the exponents n and m to increase with increasing plasticity. The experimental results also seemed to indicate that the very small strain stiffness of fine grained soils is not significantly affected by an anisotropic state of confinement at least for stress states relatively far from failure. Provided that the stress state and history in situ were taken into account the values of very small strain stiffness obtained from laboratory tests compared well with those obtained from the field dynamic surveys. The laboratory values of very small strain stiffness were found to be about 20% smaller than the in situ values.

At larger strain levels the dependence of stiffness on stress state and history could still be expressed using a power law like the one used for the very small strain stiffness but this time the coefficients A, n and m depended on strain level. In particular coefficient A was found to decrease and the exponent of mean effective stress to increase with increasing strain level. At low strain amplitudes the exponent n approaches values similar to those obtained at very small strains while at larger strains the exponent approaches unity, indicating that the stress strain response is then dominated by frictional behaviour. The dependence of stiffness on overconsolidation ratio was found to be less pronounced at very small strains than at relatively larger strains.

LIST OF SYMBOLS

b	the constant in the equation relating G'_{max} to the $\log R_o$
d	distance between two receivers in surface wave experiment
e	voids ratio
e_λ	voids ratio of isotropically normally consolidated soil when $p' = 1$ kPa
f	wave frequency
g	acceleration due to gravity
k	stress ratio, σ_r'/σ_a'
m	an exponent of R_o, or p'_{max}/p'
n	in general use, an exponent of stress and specifically an exponent of mean effective stress or the pressure exponent
n'	an exponent of mean effective pressure
n_a	an exponent of axial stress
n_r	an exponent of radial stress
n_η	an exponent of stress ratio, η
nc	used to denote normally consolidated states
oc	used to denote overconsolidated states
p'	mean effective stress
p'_a	atmospheric pressure
p_{om}	confining pressure due to membrane restraint
$2p_o'$	mean effective pressure at the intersection of the current swelling line and the normal compression line
p_p'	mean effective pressure used in the calculation of R_o, see figure 1.2.2
p_r	reference pressure of 1 kPa
q'	deviatoric stress
r	distance from vibrating source
s_u	undrained shear strength
t	time
t_{100}	time to complete primary consolidation

t_o, t_1, t_2	travel times corresponding to points 1,2 and 3 on the received signal
t_g	group travel time for a given range of frequencies
u	pore pressure
v	specific volume
v_p	particle velocity
v_κ	specific volume of isotropically overconsolidated soil swelled to p' = 1 kPa
w	water content
x	distance
x_{max}	maximum distance from source of vibration
x, y, z	cartesian coordinate axes
z	depth of soil
z_{max}	maximum depth
A	pressure multiplier
A'	a constant in a power law relationship between G'_{max} and p' for overconsolidated soil
A_c	current area of triaxial sample
A_o	initial area of triaxial sample
B	Skempton's pore pressure parameter
$CC_{yx}(\tau)$	cross correlation function
D_o	initial diameter of sample
D_m	initial diameter of membrane
E	Young's modulus
G, G'	shear modulus
G'_e	elastic shear modulus
G'_{max}	shear modulus for linear elastic behaviour at very small strains
G'_{sec}	secant shear modulus
$G_{yx}(f)$	cross power spectrum of two signals X(t) and Y(t)
J'	modulus coupling shear and volumetric strains
K'	bulk modulus

K_o	coefficient of earth pressure at rest
K'_e	elastic bulk modulus
L	length of travel path for the shear wave
L_R	wavelength of Rayleigh wave
$L_x(f)$, $L_y(f)$	linear spectra of two signals X(t) and Y(t) respectively
L_y^*	complex conjugate of L_y
M	constrained modulus of soil
M	stiffness of the membrane at an average strain of 10%
M_i	initial tangent modulus of the membrane
OCR	overconsolidation ratio defined as the maximum previous vertical effective stress divided by the current vertical effective stress
R_o	overconsolidation ratio defined as p'_p/p'
T	travel time
T_r	time record
V	wave velocity
V_o	wave velocity at ground level
V_p	velocity of compression wave
V_R	velocity of Rayleigh wave
V_s	velocity of shear wave
V_{sp}	shear pulse velocity
V_{pp}	compression pulse velocity
γ, γ_{sat}	engineering shear strain
γ	unit weight of soil
ϵ	strain
ϵ_a	axial strain
ϵ_i	total elastic strain in the diection σ'_i
ϵ^e_{ii}	elastic strain in the direction of the principal effective stress σ'_i due to σ'_i, where i = 1 to 3
ϵ_r	radial strain

ϵ_s	triaxial shear strain
ϵ_v	volumetric strain
ϵ^e_v	elastic volumetric strain
$\dot{\epsilon}$	strain rate
δv^e	elastic change in specific volume
η, η'	stress ratio p'/q'
θ	angle of stress path rotation
$-\kappa$	gradient of a swelling line in v : lnp' space
λ	first Lame's constant, see section 1.4 only
$-\lambda$	gradient of the normal compression line in v : lnp' space
ν, ν', ν_{ij}	Poisson's ratios, where i = 1,2,3 and j = 1,2,3
ρ, ρ_{sat}	mass density
σ	root mean square deviation
σ_1, σ_2, σ_3	principal stresses
σ'	effective stress
σ'_a	axial effective stress – during dynamic loading, stress in plane of shear and in the direction of the shear wave propogation
σ_a	axial total stress
σ_{ac}	axial total stress corrected for the effect of membrane stiffness
σ_{am}	correction to axial stress due to membrane stiffness
σ'_b	during dynamic loading, stress in plane of shear and perpendicular to the direction of shear wave propogation
σ'_c	during dynamic loading, stress orthogonal to the plane of shear
σ'_h	horizontal effective stress
σ'_i	principal effective stresses, where i = 1,2,3
σ'_r	radial effective stress
σ_r	radial total stress
σ_{rc}	radial total stress corrected for the effect of membrane restraint
σ'_v	vertical effective stress

$\sigma_v'_{max}$	maximum vertical effective stress
$\sigma\%$	percentage error
τ	time shift between two traces
τ_{cc}	time shift corresponding to the maximum value of $CC_{yx}(\tau)$
ϕ'	critical state friction angle
Γ	specific volume of soil at critical state when p' = 1 kPa
M	critical state friction coefficient
N	specific volume of isotropically normally consolidated soil when p' =1 kPa
Φ	phase shift between two waves

CHAPTER 1 INTRODUCTION

1.1 Background to the project

Any calculation of ground movements around an engineering structure, be it an excavation or a foundation, requires an evaluation of soil stiffness. It is generally recognized that the stress-strain characteristics of soils are markedly non-linear even at strain levels as low as 0.01% (Simpson et al., 1979, Burland, 1989). This implies that soil stiffness depends on strain level and can change significantly over the range of strains of interest in civil engineering.

Recent research at City University has concentrated on the mechanical behaviour of overconsolidated soils at small strains, when the soil is far from failure. In particular, the dependence of the stiffness of the soil on its recent stress history, defined as either a period of rest at a particular stress state or a rotation of the stress path, has been experimentally investigated for both reconstituted and undisturbed samples (Atkinson et al., 1990, Stallebrass, 1990a). The picture of soil beahviour obtained from triaxial laboratory tests, however, is incomplete, particularly because there are no direct observations of the behaviour at very small strains where the deformations may be truly elastic.

Values of stiffness at very small strains, less than 0.001%, can be obtained using dynamic testing techniques, in which the deformation properties of the soil are related to elastic wave velocities, see section 1.4. In the present project the very small strain stiffness of fine grained soils has been measured using dynamic techniques both in the laboratory and in the field. In the laboratory the measurements have been carried out using piezoceramic bender elements of the type developed at the Norwegian Geotechnical Institute and at the University College of North Wales and in the field using standard surface wave techniques.

In the past, values of stiffness measured in dynamic tests were an order of magnitude higher than those quoted from static tests and were

generally disregarded in the analyses of static problems, such as the calculation of ground movements around engineering structures. Terms like "dynamic stiffness" or "dynamic properties" as opposed to "static stiffness" and "static properties" were also commonly encountered in the literature. However, over the past decade, there have been significant improvements in laboratory testing techniques used for the direct measurements of small strains in static tests so that stiffness data obtained from static and dynamic tests compare better. In recent years, several researchers have also pointed out that the use of the adjectives "static" and "dynamic" when referring to the soil properties is conceptually incorrect and practically misleading and have suggested that the adjectives should only be used to distinguish between loading conditions and not between soil properties. Although dynamic testing of soils is not new, research linking the very small strain stiffness of soils measured in dynamic tests with the non-linear stiffness observed in static tests is relatively recent. The work described in this dissertation falls into this area of research.

The main objectives of the research were as follows:

(i) to modify existing standard hydraulic stress path cells to incorporate piezoceramic bender elements

(ii) to explore the dependence of the very small strain stiffness of fine grained soils on factors such as stress state and history

(iii) to examine the factors affecting the stiffness of fine grained soils over an extended range of strains

(iv) to compare the values of stiffness obtained using dynamic techniques on site with those obtained in the laboratory using the bender elements technique

1.2 Basic framework

1.2.1 A working definition of stiffness

The general form of a constitutive equation for soil is:

$$\{ \delta\sigma' \} = [S] \{ \delta\epsilon \} \qquad (1.2.1)$$

where, in general stress space, [S] is a 6x6 stiffness matrix defining the relationship between increments of strain and increments of effective stress. The 36 components of the stiffness matrix can be expressed as functions of material properties, state and history of the soil. For convenience, in some cases, the constitutive equations are written in terms of invariants of stress and strain, for instance the octahedral invariants or invariants proportional to them such as the mean effective stress, p', and the deviatoric stress, q', defined as:

$$p' = \sigma'_{oct} = (\sigma'_1 + \sigma'_2 + \sigma'_3)/3 \qquad (1.2.2)$$

and:

$$q' = \frac{3}{\sqrt{2}} \tau_{oct} = \frac{1}{\sqrt{2}} \sqrt{(\sigma'_1 - \sigma'_2)^2+(\sigma'_2 - \sigma'_3)^2+(\sigma'_3 - \sigma'_1)^2} \qquad (1.2.3)$$

The appropriate strain invariants associated to these stress invariants are the volumetric strain, ϵ_v, and the shear strain, ϵ_s, defined as:

$$\epsilon_v = 3\epsilon_{oct} = (\epsilon_1 + \epsilon_2 + \epsilon_3) \qquad (1.2.4)$$

and:

$$\epsilon_s = \frac{1}{\sqrt{2}} \gamma_{oct} = \frac{\sqrt{2}}{3} \sqrt{(\epsilon_1 - \epsilon_2)^2+(\epsilon_2 - \epsilon_3)^2+(\epsilon_3 - \epsilon_1)^2} \qquad (1.2.5)$$

Because the stress and strain invariants defined above do not describe the state of stress and strain completely, the stiffness components will depend also on the directions of principal stress and on their rotations. In the work described in this dissertation the stress states applied to the soil will be confined to the triaxial plane. For triaxial conditions the stress and strain invariants defined above reduce to (Schofield and Wroth, 1968):

$$p' = (\sigma'_a + 2\sigma'_r)/3 \qquad q' = (\sigma'_a - \sigma'_r) \tag{1.2.6}$$

and:

$$\epsilon_v = (\epsilon_a + 2\,\epsilon_r) \qquad \epsilon_s = 2(\epsilon_a - \epsilon_r)/3 \tag{1.2.7}$$

where the subscripts a and r refer to axial and radial directions. Using the stress and strain invariants defined above, and following Graham and Houlsby (1983), equations 1.2.1 can be written as:

$$\begin{Bmatrix} \delta p' \\ \delta q' \end{Bmatrix} = \begin{bmatrix} K' & J' \\ J' & 3G' \end{bmatrix} \begin{Bmatrix} \delta \epsilon_v \\ \delta \epsilon_s \end{Bmatrix} \tag{1.2.8}$$

where K' and G' are the bulk modulus and the shear modulus and the moduli J' on the secondary diagonal are introduced to express the cross coupling of shear and volumetric behaviour.

It is often convenient to invert equation 1.2.8 to give the compliance matrix:

$$\begin{Bmatrix} \delta \epsilon_v \\ \delta \epsilon_s \end{Bmatrix} = \frac{1}{Det} \begin{bmatrix} 3G' & -J' \\ -J' & K' \end{bmatrix} \begin{Bmatrix} \delta p' \\ \delta q' \end{Bmatrix} \tag{1.2.9}$$

where Det = $3K'G'-J'^2$ is the determinant of the stiffness matrix.

Most of the tests carried out as part of this research included a stage of drained shear at constant p'. In the interpretation of the data the stress–strain behaviour will be characterised using the tangent to the curves of deviatoric stress versus shear strain obtained from these shearing stages. It must be noted that for undrained loading, for which $\delta\epsilon_v = 0$, from equation 1.2.8 one obtains:

$$\frac{\delta q'}{\delta \epsilon_s} = 3G' \quad or \quad G' = \frac{1}{3} \frac{\delta q'}{\delta \epsilon_s} \tag{1.2.10}$$

so that the tangent to the curve of deviatoric stress versus shear strain obtained from an undrained shearing stage directly defines the shear modulus G'. Conversely, because of the cross coupling of shear and volumetric effects, the gradient of the curve of deviatoric stress versus shear strain obtained from a drained constant p' test, for which $\delta p' = 0$, is not equal to 3G'. From equation 1.2.9 it is:

$$\frac{\delta q'}{\delta \epsilon_s} = \frac{3K'G' - J^2}{K'} \qquad (1.2.11)$$

Only in the special case of an isotropic elastic material, for which J'= 0, equation 1.2.9 reduces to:

$$\begin{Bmatrix} \delta \epsilon_v \\ \delta \epsilon_s \end{Bmatrix} = \begin{bmatrix} 1/K' & 0 \\ 0 & 1/3G' \end{bmatrix} \begin{Bmatrix} \delta p' \\ \delta q' \end{Bmatrix} \qquad (1.2.12)$$

and the shear modulus G' can be directly calculated from the tangent to the stress-strain curve obtained from a constant p' shearing stage.

There are two reasons why constant p' shearing stages were carried out, one of which is "historical" and one related to practical reasons. In soil mechanics it is usual to refer to a formulation like that given in 1.2.5 because most models are elasto-plastic and the terms of the compliance matrix result from the sum of elastic and plastic strains. It is therefore convenient to compare the compliances of the model directly with the compliances obtained experimentally. A constant p' test yields the shear compliance directly, as the reciprocal of the gradient to the stress strain curve . The research described in this dissertation follows on from previous research on deformation characteristics of soils at small strains with which it is consistent. The second reason is that the stiffness of a soil is a function of the strain level and the mean effective stress. In an undrained test p' is not a constant so, as shearing progresses, it is difficult to separate the effects of non-linearity, i.e. the reduction of stiffness with strain amplitude, from the effects of variations in p'.

1.2.2 Basic definitions

The description and analysis of the experimental results presented in this dissertation will be carried out in the framework of critical state soil mechanics. The state of the soil will be defined by the current values of p' and q', as defined above, and by the specific volume v, which is the volume in space occupied by the unit volume of soil grains.

For both isotropic compression and swelling the relationship between the

specific volume and the mean effective stress is assumed to be linear in v:lnp′ space. The equation for the isotropic normal compression line is given by:

$$v = N - \lambda \ln p' \qquad (1.2.13)$$

where N is the value of v when p′ = 1 and λ is the slope of the line in v:lnp′ space, as shown in figure 1.2.1. The same figure also shows a swelling line defined by:

$$v = v_\kappa - \kappa \ln p' \qquad (1.2.14)$$

Additional assumptions are that the possible states for the soil are limited by a state boundary surface and that, on shearing, all soils ultimately reach a critical state, as defined by Schofield and Wroth (1968). The critical state line is defined in v:lnp′ and q′:p′ space, respectively, by the equations:

$$v = \Gamma - \lambda \ln p' \qquad (1.2.15)$$

and:

$$q' = \pm M p' \qquad (1.2.16)$$

In figure 1.2.1a and b the critical state line is shown in v:lnp′ space and q′:p′ space, respectively. Figure 1.2.1b also shows the elliptical yield locus defined by the Modified Cam-clay model (Roscoe and Burland, 1968). The equation of the surface in q′:p′ space is given by:

$$(p' - p'_o)^2 + \frac{q'^2}{M^2} = p'^2_o \qquad (1.2.17)$$

where $2p_o'$ is the mean effective stress at the intersection of the current swelling line and the isotropic normal compression line, see figures 1.2.1a and b. For overconsolidated states the overconsolidation ratio is defined as $R_o = p_p'/p'$. For an isotropically compressed soil p_p' is the mean effective stress at the intersection of the current swelling line and isotropic normal compression line, $p_p' = 2p_o$. For a soil in anisotropic conditions, p_p' is calculated using the modified cam-clay state boundary surface as shown in figure 1.2.2.

1.3 Non-linearity of soil behaviour and relevance of very small strain stiffness

It is generally recognised that the stress strain characteristics of soils are highly non linear even at relatively small strains (Burland, 1989, Atkinson and Sallfors, 1992). However, the results of dynamic laboratory tests demonstrate the existence of a small region at very small strains in which the behaviour of the soil is approximately linear elastic and the shear modulus has a constant value G'_{max}. Data available in the literature (Georgiannou et al., 1991: Lo Presti, 1989) indicate that the threshold strain beyond which the stress strain response becomes apparently non linear, conventionally defined as the strain at which $G'/G'_{max} = 0.95$, lies between 0.001% and 0.01% depending on the plasticity of the soil, higher values being observed for more plastic clays.

There is considerable evidence of linear elastic behaviour below the elastic threshold strain. Stress-strain loops in cyclic loading show little or no hysteresis which means that the behaviour is conservative and little or no energy is dissipated (Papa et al., 1988; Silvestri, 1991); volumetric and shear deformations are fully recoverable (Lo Presti, 1989) and uncoupled so that no pore pressures are generated during undrained shear (Georgiannou et al. 1991, Silvestri et al. 1989).

Beyond the elastic threshold strain the stiffness of the soil decreases significantly with shear strain amplitude and there is evidence of elasto-plastic behaviour (Stallebrass, 1990a). At strains larger than a second threshold strain, generally referred to as the plastic threshold strain, of the order of 0.1% the behaviour of the soil shows all the characteristics of elastoplastic deformations. Large irreversible deformations occur, volumetric and shear strains are coupled so that undrained shearing results in pore pressure generation (Georgiannou et al., 1991), cyclic loading results in hysteresis and accumulated strains. With further straining the stiffness of the soil reduces to very small values and the soil approaches failure.

Figure 1.3.1 shows an idealisation of soil stiffness over the whole range of strains, from very small to large and approximately distinguishes

strain ranges. The work carried out in the present project deals mostly with the stiffness of soils at small and in particular at very small strains. It may be noted that this is the range of strains of interest in most civil engineering problems dealing with the deformations around structures in stiff soils (Burland, 1989).

There are two main approaches to modelling the non-linearity of soil behaviour beyond the range of very small strains.

The first approach is to use non-linear elastic models. These are fundamentally empiric. Specific functions describing the decay of stiffness with shear strain amplitude are fitted to experimental data obtained following particular stress paths. All strains are regarded as elastic. A very large number of non-linear elastic models can be found in the literature. Duncan and Chang (1970) modelled soil behaviour using a hyperbolic relationship, based on only two parameters, namely the maximum shear modulus and the maximum shear stress on a specified plane. To improve the fit to the experimental data in the small strain range, Hardin and Drnevich (1972b) proposed a modified version of the hyperbolic model in which two additional parameters were required. The two additional parameters could be obtained from the experimental data using curve fitting techniques but had no physical meaning. More complex forms of hyperbolic equations have been proposed (Nelson and Baron, 1971) and power terms have been introduced into hyperbolic equations so that failure is reached at finite strains (Prevost and Keane, 1990). Recently, Jardine and Potts (1988) proposed a model based on the results of very high quality laboratory tests in which the stiffness is a periodic logarithmic function of strain.

A common drawback of all these models is that because they assume that the strains are elastic they fail to describe most of the observed characteristics of the soil behaviour such as the coupling of volumetric and shear strains and the irrecoverability of the strains. However, the models have a number of advantages; they are straightforward to understand and relatively easy to implement in finite element calculations. Non-linear elastic models have been used successfully to predict movements around engineering structures (Jardine et al., 1991),

where the introduction of non-linearity alone, considerably improved the quality of the prediction. In most of these models the maximum shear stiffness is one of the required parameters. Hence, for these models, research that relates the very small strain stiffness of soils to state and stress history is very relevant.

An alternative approach is that of using plasticity based formulations. These more fundamental models recognise the elastoplastic nature of the deformation of the soil before the onset of major yielding and can predict the range of behaviour observed at small strains. In addition to non-linearity these models are capable of predicting stress path dependency, shear and volumetric coupling and irrecoverable strains. Most of these models are derived from stress-strain data in the range of small strains rather than very small strains and the influence of the variation of the stiffness at very small strains on the subsequent response of the soil is not fully accounted for. The relevance of research into the very small strain stiffness of soils for this type of models has still to be assessed.

1.4 Relationships between elastic moduli and dynamic wave velocities

The relationships between elastic moduli and dynamic wave velocities are derived by considering the dynamic equilibrium of an isotropic elastic material. Two solutions can be found to the equations of dynamic equilibrium (Timoshenko and Goodier, 1951), both in the form of a wave equation:

$$\rho \frac{\partial^2 \epsilon_v}{\partial t^2} = (\lambda+2G) \nabla^2 \epsilon_v \qquad \left[\nabla^2 = \frac{\partial^2}{\partial x^2}+\frac{\partial^2}{\partial y^2}+\frac{\partial^2}{\partial z^2}\right] \qquad (1.4.1)$$

$$\rho \frac{\partial^2 \gamma_{ij}}{\partial t^2} = G \nabla^2 \gamma_{ij} \qquad (ij = xy, yz, zx) \qquad (1.4.2)$$

where ρ is the mass density of the material and λ (first Lame's constant) is defined as:

$$\lambda = \frac{\nu E}{(1+\nu)(1-2\nu)} \tag{1.4.3}$$

For an infinite continuum equation 1.4.1 corresponds to the propagation of a dilatational wave, also called P-wave or compression wave, see figure 1.4.1a, and equation 1.4.2 to the propagation of a distortional wave, also called S-wave or shear wave, see figure 1.4.1b, travelling at velocities V_p and V_s respectively, where:

$$V_p = \sqrt{(\lambda+2G)/\rho} \tag{1.4.4}$$

and:

$$V_s = \sqrt{G/\rho} \tag{1.4.5}$$

The velocity of the shear wave is directly related to the shear modulus of the material by:

$$G = \rho V_s^2 \tag{1.4.6}$$

while the velocity of the compression wave is related to the constrained modulus, M, by:

$$M = \lambda+2G = \rho V_p^2 \tag{1.4.7}$$

If Poisson's ratio is known, then any other moduli can be calculated for a given V_s. Poisson's ratio can be obtained from the ratio of the compressional wave velocity to shear wave velocity. It is:

$$\nu = \frac{0.5\ (V_p/V_s)^2 - 1}{(V_p/V_s)^2 - 1} \tag{1.4.8}$$

A graphic illustration of equation 1.4.8 is given in figure 1.4.2a.

The two solutions presented above describe elastic waves that propagate within an infinite elastic medium, or body waves. In an elastic half space it is possible to find other solutions to the equations of motion, which correspond to elastic waves whose motion is confined near the boundaries of the half space, or surface waves. Of particular interest in the applications is the Rayleigh wave (Richart et al., 1970), whose characteristic motion is shown in figure 1.4.1c. The motion of the

particles is elliptical and in the plane perpendicular to the surface with an amplitude that decreases quite rapidly with depth, as shown in figure 1.4.3. In a homogeneous half space the velocity of the Rayleigh wave, V_R, is constant and independent of the frequency. The ratio of the Rayleigh wave velocity to the shear wave velocity as a function of Poisson's ratio and as a function of the ratio of compression to shear wave velocity is shown in figures 1.4.2b and 1.4.4, respectively. The ratio of Rayleigh wave velocity to shear wave velocity increases as Poisson's ratio increases. However, the change is small and the ratio can be assumed equal to 0.90 without introducing an error greater than 5%.

The propagation of body waves and surface waves from a circular footing oscillating vertically at the surface of the half space is shown in figure 1.4.5. It can be seen that the distribution of total input energy among the three elastic waves is about 67% Rayleigh wave, 26% shear wave, 7% compression wave. Figure 1.4.5 also shows that while compression and shear waves propagate radially from the source along a hemispherical wave front, surface waves propagate along a cylindrical wave front. Due to this different geometry, at the surface of the half space the amplitude of the body waves decreases as $1/r^2$ while the amplitude of the surface wave only decreases as $1/r^{½}$, if r is the distance from the vibrating source.

The theory outlined above describes the relationships between elastic moduli and dynamic waves propagating in a homogeneous isotropic elastic continuum. To extend the theory to the propagation of dynamic waves into soil deposits, the biphase nature of the medium must be considered. Some insight into the mechanism of the propagation of elastic waves in soils can be obtained considering the behaviour of a porous elastic solid whose pores are filled with a fluid, as presented by Biot (1956). In Biot's theory the solid is assumed to be elastic, homogeneous and isotropic while the fluid is a perfect compressible liquid, free to flow through the pores. In these hypotheses the theory allows the existence of three different waves to be recognized and the expressions for their velocities derived.

The first wave is a distortional wave which involves coupled motion of the elastic structure and the fluid. Because the fluid has no shearing stiffness, the coupling between the elastic structure and the fluid is not "structural" but rather "inertial" and it is due to the relative motions of the solid and the fluid. This inertial coupling results in some additional mass density terms in the expression of the shear wave velocity. For a saturated soil the total mass density, $\rho_{sat} = \gamma_{sat}/g$, where g is the gravity acceleration, can be used as a first approximation and the shear wave velocity related to the shear modulus in the same way as above:

$$G = \rho_{sat} V_s^2 \tag{1.4.9}$$

Biot's theory also shows that in the porous saturated medium two dilatational waves exist, one propagating through the fluid and the other one through the elastic structure. The two waves are coupled both "structurally" because of the bulk stiffnesses of the solid and fluid components of the system as well as "inertially" because of their relative motions. Since water is relatively incompressible if compared to the soil skeleton, it is capable of transmitting the compression wave at a higher velocity than the soil structure. In saturated soils dynamic events which give rise to compression waves are likely to be undrained so that the measurement of the velocity of a compressional wave in a water saturated soil leads to values that are close to the velocity of wave propagation in water.

CHAPTER 2 LITERATURE REVIEW

2.1 Introduction

This literature review examines work carried out in two main areas. Firstly, the development of appropriate experimental techniques for the measurement of the stiffness of soils at small and very small strains and, secondly, current knowledge of the dependence of soil stiffness on stress history and state.

In the section dealing with laboratory experimental techniques the emphasis will be on the development of the triaxial apparatus and on different dynamic techniques both because these are the areas in which most of the recent work has been carried out and because they are directly relevant to the present project. A large number of in situ testing techniques are available for the measurement of the deformation characteristics of soils (Atkinson and Sallfors, 1991). A comprehensive examination of in situ testing techniques is beyond the scope of this review and only dynamic field methods will be covered in the section dealing with in situ techniques.

The basic theories for the dependence of soil stiffness on stress state and history, both at small and very small strains, will be reviewed and discussed in the second part of this literature review. They will represent the framework for the interpretation of the experimental results in chapter 5. In addition to the established theories, some recent experimental work examining different aspects of the stiffness of soils at small and very small strains will be presented in the last part of the literature survey.

2.2 Development of experimental techniques for measuring soil stiffness at small and very small strains

The development of appropriate laboratory techniques and equipment to measure accurately the small strain stiffness of soils was prompted, in the UK, by the need for reliable values of stiffness parameters for prediction of ground movements in stiff overconsolidated soils. In the

early 1970's, accurate field investigations using field loading tests (Marsland, 1973 a,b) and back analyses of observed ground movements around excavations in London clay (Cole and Burland, 1972) found values of stiffness at least 3 to 5 times greater than those obtained in laboratory triaxial tests (see also St. John, 1975). These differences were generally attributed to the inevitable disturbance of laboratory samples (mechanical distortion and stress cycles during sampling, stress relief and opening of fissures) so that laboratory testing was regarded by many as fundamentally inadequate for the correct measurement of the stiffness of overconsolidated soils (Wroth, 1975, Burland, 1979, Marsland, 1973b).

However, in their state-of-the-art report on design parameters for stiff clays Simpson et al.(1979) pointed out that it was because linear elasticity was assumed that laboratory values of moduli compared so badly with field observations. They concluded that if the correct stress paths were followed, the non-linearity of the behaviour taken into account and the strain levels appreciated laboratory tests could be used successfully to measure realistic stiffnesses. This, however, would require high quality sampling, stress path control and accurate measurement of small strains.

The main developments in laboratory testing techniques which led to values of stiffness measured in the laboratory similar to those observed from the back analysis of the behaviour of real engineering structures were, firstly, the development of the hydraulic stress path cell and, secondly, the design and use of a number of devices to measure accurately the strains on the sample inside the cell. Accurate measurements of small strains in static tests also led to values of stiffness which were comparable to the values of stiffness obtained from dynamic tests. Results which demonstrated that the behaviour of the soil was not fundamentally different in dynamic and static conditions, if the non-linearity of the behaviour was taken into account and the strain levels in the different tests appreciated, led to the use of dynamic testing techniques to determine the stiffness of soils at very small strains.

The main developments in the hydraulic stress path triaxial cell and in the techniques used to improve the accuracy of the measurements of small strains in the triaxial apparatus will be outlined in section 2.2.1 and

2.2.2. A brief review of the most common laboratory dynamic testing techniques to measure the very small strain stiffness of soils will be given in section 2.2.3. In addition to this, in section 2.2.4, some of the most commonly used dynamic field methods will be reviewed.

2.2.1 Development of the hydraulic stress path cell

The conventional triaxial test equipment (Bishop and Henkel, 1962) is not suitable for applying different loading paths to the sample. The requirements for the control of stress and strain can be met using a hydraulic stress path triaxial cell similar to that originally developed by Bishop and Wesley (1975). A sketch of the cross section of a typical hydraulic stress path cell is shown in figure 2.2.1. The soil sample sits on an axial ram and is loaded axially through a double bellofram piston acting on the base platen. Strain controlled loading can be achieved by using a motor driven closed ram arrangement, as shown in figure 2.2.2 (Atkinson et al., 1985).

In order to conduct stress path tests, control of three independent pressures is required. A number of options are available for supplying the necessary pressures to the cell. Bishop and Wesley (1975) suggested the use of a system of self-compensating mercury manometers. Menzies et al. (1973) used a system of closed rams with self-contained feedback control. More recently, Atkinson et al. (1983) described a system which used continuous motors automatically controlled by a microcomputer to regulate simple manostat air pressure regulators. Subsequent modifications to this system were described by Atkinson et al.(1985), who substituted the continuously running motors for stepper motors, and by Viggiani (1990), who used analogue pressure converters to regulate the pressures. A common feature of most hydraulic stress path systems is to use microcomputers to control soil tests using feedback from instruments and to log data output.

2.2.2 Measurement of small strains in the triaxial apparatus

In the hydraulic triaxial cell the axial strain is generally measured by means of an external displacement transducer. The principal sources of error in the external measurement of axial strain have been identified, among others, by Baldi et al.(1988) and are shown diagrammatically in

figure 2.2.3. The errors connected to the external measurement of axial strain in the triaxial apparatus may be broadly grouped into two main categories: those connected to the compliance of the loading and load measuring systems and those connected to a variety of sample bedding effects.

Atkinson and Evans (1985) described simple procedures to improve the accuracy of external measurement of axial strains. These included accurate calibration of the system to correct the externally measured values of axial strain to account for the compliance of the system and connection of the sample to the loading system using a rubber suction-cap at early stages in the test so as to reduce bedding effects when shearing is commenced. Atkinson and Evans claimed that the accuracy of the measurements of axial strain that was possible to achieve following these procedures was about ± 0.01%.

Errors in axial strain measurement due to either bedding effects or compliance of the system can be eliminated by measuring axial strains inside the triaxial cell locally to the sample. A large number of methods of measuring locally the strains in the triaxial apparatus have been proposed in the last 15 years. They include displacement transducers (LVDTs) directly attached to the sample (Costa-Filho, 1985, Brown and Snaith, 1974), X-ray and optical methods (Balasubramanian, 1976, Atkinson, 1973, Arthur and Phillips, 1975), proximity transducers (Hird and Yung, 1987), Imperial College strain gauges in both the original electrolevel and the new pendulum inclinometer designs (Burland and Symes, 1982, Jardine et al., 1984, Ackerley et al., 1987), Hall effect transducers (Clayton and Kathrush, 1986, Clayton et al., 1988) and, more recently, thin spring strips of phosphor bronze with strain gauges attached (Goto et al., 1991).

At City University, Hall effect transducers of the type developed by Clayton and Khatrush (1986) are commonly used to measure axial strains locally to the sample. The transducers make use of the Hall effect (i.e. the development of a transverse electric field in a current-carrying conductor placed in a magnetic field) to measure the relative displacement between two points of the sample over a central gauge length. Each transducer is made of two parts: a pendulum which holds two bar magnets suspended to a pad fixed to the specimen and the Hall effect

semiconductor mounted on the specimen by means of another fixing pad. A schematic section of the Hall effect gauge is shown in figure 2.2.4.

In the literature discussions on the accuracy of the measurement of stiffness are invariably linked with the accuracy of the measurement of strain. However, the stiffness is a parameter derived from both strain and stress measurements. If quoted as a tangent its accuracy depends on the accuracy with which it is possible to measure increments of stress and strain and not absolute values and, if quoted as a secant, the required accuracy of measurements diminishes with increasing stress and strain, but, at very small strains depends critically on the correct selection of the origin. The resolution and the accuracy of the different types of transducers listed above vary but, although most of the transducers are capable of resolving strains as small as 0.002%, a realistic lower limit of strains for reliable measurement of stiffness using this kind of technique is about 0.005%.

It is particularly important to measure strains locally to the sample for stiff soils. A controlling factor is the ratio of the stiffness of the sample to the stiffness of the apparatus. For stiff undisturbed clays this ratio can be as large as 1/8 (Rampello, 1989). In similar cases, at low stress levels, the deformations of the soil are of the same order of magnitude of the deformation of the apparatus and even small inaccuracies in the correction of external measurements of axial strains can affect the readings significantly. Also, for very stiff soils, the procedures described by Atkinson and Evans (1985), to reduce bedding errors at the beginning of the shearing stage may be less effective than for relatively softer soils.

At larger stress levels the importance of the local measurements of axial strain reduces both because the relative magnitude of the errors decreases as the strain increases and because, with the increasing non-uniformity of the deformation of the sample, local measurements of strain may become difficult to interpret.

In addition to the errors connected to bedding effects and to the compliance of the system, the effects of end restraint, which causes the sample to deform non-uniformly, will also generate a difference between externally and internally measured values of axial strain.

It is worth noting that, although transducers for the local measurement of radial strain are available (Clayton et al., 1988) it is common practice to derive radial strains from the measurement of axial and volumetric strain by assuming that the sample deforms as a cylinder. The volumetric strain is generally measured outside the cell and refers to the whole sample whereas local axial strain transducers usually only measure the strain over the central portion of the sample. In the calculation of derived quantities, such as the shear strain, consistent sets of measurements should be used, so that in some cases it may be better to use external measurements of axial strain that also refer to the whole of the sample. These issues will be discussed in further detail in section 4.2.4 with reference to the soils tested in the present project.

2.2.3 Laboratory dynamic testing techniques: harmonic vibration methods

Various types of dynamic testing techniques are available to measure the stiffness of soils at small and very small strains. The most common dynamic tests may be broadly divided into harmonic vibration methods and wave propagation methods which differ primarily because of the characteristics of the loads applied to the soil.

The most common test in the first group is the resonant column test in which the response of a cylindrical sample subjected to forced harmonic torsional vibrations is measured. The shear modulus is determined from the resonant frequency of the system. The interpretation is based on the theory of wave propagation in elastic rods (Richart et al., 1970). Starting from the resonance condition the excitation can be switched off and the free vibration of the sample monitored over a period of time (decay test). Once again the elastic properties of the soil are obtained by comparing the observed response of the system to the theoretical response of a simple elastic model. Another type of test that can be performed in the resonant column apparatus, which is not strictly a dynamic test, is the cyclic torsion shear test. In this test the sample is subjected to a given number of low frequency cycles of torsional load (generally $f < 0.1$ Hz). The inertia forces can be neglected and the soil stiffness obtained directly from the torque-twist relationship. A summary of the different loading conditions for the three types of tests is given in fig 2.2.5.

The early designs of the resonant column apparatus (Wilson and Dietrich, 1960, Hardin and Richart, 1963, Hall and Richart, 1963, Hardin and Music, 1965 as described by Richart et al.,1970) differ primarily because of the boundary conditions imposed on the sample. Nowadays the most common design is the fixed-free one in which the base of the sample is fixed while the top end is free to vibrate. Isenhower (1979) modified an original design from the University of Texas so that the same apparatus could operate both as a resonant column and as a cyclic torsion shear apparatus (RCTS). Further modifications were made to the equipment (Allen and Stokoe, 1982) to allow anisotropic confinement of the sample.

The resonant column test can be used to evaluate the stiffness of soils at shearing strains ranging from 0.00001% to 1% . However, as pointed out by Isenhower (1979), the methods of analysis of the resonant column test are based on the assumption of linear elasticity so that the validity of these analyses is dependent on the magnitude of the shear strain at which the measurements are made. For most soils the validity of the analyses decreases at strain levels higher than 0.001% as the soil behaviour becomes increasingly non-linear. Recently new interpretation procedures have been examined for the higher strain levels that take into account the non-linearity of the behaviour (Papa et al., 1989; Silvestri, 1991).

2.2.4 Laboratory dynamic testing techniques: wave propagation methods

Wave propagation methods include all those tests in which the frequency of the applied load is much higher than the natural frequency of vibration of the volume of soil under examination. In these tests it is generally possible to measure directly the velocity of propagation of either shear or compression waves and relate these velocities to the elastic properties of the soil using the relationships presented in section 1.4. The principle is similar to that used in dynamic field investigations which will be described in the following section, with the difference that the state of a laboratory sample can be controlled and the dependence of the stiffness of the soil on factors such as stress state or history investigated.

The sources of elastic waves are generally small if compared to the dimensions of the sample and independent of the system used to control

the state of stress in the sample. Mechanical sources of vibration were used by Knox et al. (1982) to generate elastic waves in large cubic samples of sand with 2 metres sides. The tests were conducted in a large scale triaxial device in which the velocities of both compression and shear waves could be investigated under a wide range of states of stress. More recently small electromechanical transducers have been developed which are suitable to transmit and receive elastic waves in laboratory samples.

The earliest work involving electromechanical transducers to generate and receive shear waves through samples of soil made use of shear plates of either quartz or piezoelectric ceramic (Lawrence, 1963, 1965, as reported by Brignoli and Gotti, 1992). Figure 2.2.6 shows a schematic representation of a shear plate. As an electric voltage is applied to the transducer, the plate deforms in the manner indicated by the dotted lines in the figure. If one of the faces of the element which experiences transverse motion is in contact with a sample of soil a shear wave will be propagated in a direction perpendicular to the face. Because piezoelectric transducers exhibit reciprocity they can be used both to generate and receive shear waves.

The main problem with the shear plate is the mismatch between the characteristic impedance of the transducer and that of most soils, the transducer being much stiffer than the soil. This problem is largely overcome using piezoceramic bender elements. The bender element was originally developed with the aim of producing a transducer that would be suitable for site testing on very soft marine sediments (Shirley and Hampton, 1977, Shirley, 1978). Figure 2.2.7 shows a schematic representation of a bender element transducer. Under the application of an electrical voltage the element bends to one side generating a shear wave which propagates parallel to the length of the element. Because the bender element is a thin plate it exhibits a much lower stiffness than an equivalent sized shear plate, thus providing a better coupling with the soil.

Despite the popularity of the bender element, the use of shear plates is still recommended when testing very stiff soils (Brignoli and Gotti, 1992). Unlike the bender element the shear plate is a contact transducer, i.e. it lies against the surface of the sample so that there

is no need to cut slots into the soil to insert it. Also, for very stiff soils, the coupling between the shear plate and the soil may be better than the coupling between the bender element and the soil.

Small electromechanical transducers can be easily incorporated into a variety of soil testing apparatus. Schulteiss (1982) described the use of the bender elements in various types of laboratory apparatus, including the oedometer. He also suggested an original technique for the self monitoring of the transmitter element. More recently, the use of the piezoceramic transducers was reported by Bates (1989) who used both shear wave and compression wave transducers in a standard Wykeham Farrance triaxial cell, for tests on soft marine sediments. The most comprehensive description of the techniques for wiring, casing and mounting the piezoelectric transducers into conventional soil testing apparatus was given by Dyvick and Madshus (1985).

The interpretation of the bender element test is relatively straightforward if compared to the interpretation of other dynamic tests, such as the resonant column test or the decay test, where the stiffness of the soil can only be obtained by solving the dynamic equilibrium of the system consisting of the sample and the apparatus. However, there are still some problems of interpretation related to the definition of the length of the path of the shear wave in the soil sample and to the identification of the first arrival of the shear wave at the receiver.

Because the bender elements protrude into the soil, the problem arises whether the correct length to use in the calculation of the shear wave velocity is the full length of the sample or this same length minus the protrusions of the bender elements into the soil. The problem of the definition of the correct length of travel for the shear wave has been addressed in a number of different ways. Brignoli and Gotti (1992) tested different samples under the same conditions but varying the penetration of the bender elements from 3% to 14% of the total length of the sample. They then compared the results from the bender element tests with the results of shear plate tests and resonant column tests on identical samples of soil. Based on the data reproduced in figure 2.2.8 they concluded that the results from the different tests were consistent only if it was assumed that the shear wave travelled from the tip of the transmitter element to the tip of the receiver element.

A similar approach was also followed by Dyvick and Madshus (1985) who mounted a set of bender elements into a resonant column apparatus and performed simultaneous measurements of small strain stiffness by both techniques. The results from this set of experiments are shown in figure 2.2.9. Once again, the data demonstrate that the two sets of results were in excellent agreement if it was assumed that the shear wave was propagated from the tip of the transmitter to the tip of the receiver element.

With regard to the identification of the first arrival of the shear wave, it is common practice to refer to the point of first deflection of the signal at the receiver. However, numerical studies by Mancuso and Vinale (1988) simulating the propagation of elastic waves in an elastic medium, have shown that, depending on the distance between source and receiver, the first deflection of the signal may not correspond to the arrival of the shear wave but to the arrival of the so called "near field" components which travel with the velocity of the compression wave. The inversion of the polarity of the received signal on reversal of the source does not help in the identification of the first arrival of the shear wave because it produces the inversion of all the components of the signal, including the near field terms.

Brignoli and Gotti (1992) provided experimental evidence that the first deflection of the signal at the receiver is associated with the arrival of the near field terms, travelling at the velocity of the compression wave. In their experiments they took simultaneous readings of shear wave velocity and compression wave velocity and compared the traces obtained at the receivers. Their data are shown in figure 2.2.10. It is clear that the first deflection of the signal corresponds to a wave that travels with the velocity of the compression wave.

The problem of the correct identification of the first arrival of the shear wave is a general drawback of the wave propagation methods. A close study has been made, as part of the present project, to improve the identification of the first arrival of the shear wave in the bender element test, see section 4.6.4. It is, however, the opinion of the writer that further research is required before the uncertainty connected with the choice of the arrival time can be taken down to acceptable values with simple routine interpretation procedures.

2.2.5 Field dynamic techniques

The main field dynamic techniques for the measurement of soil stiffness were reviewed, among others, by Yoshimi et al.(1977) and, more recently, by Atkinson and Sallfors (1991). General seismic investigation methods are also described in many textbooks (Griffith and King, 1981, Dobrin, 1960). The general principle of all in situ dynamic testing methods is that of generating an elastic wave at some point in the soil and measuring the travel time for the vibration to reach one or more other points in the soil. Elastic moduli are then derived from shear wave velocity and density measurements, using the relationships discussed in section 1.4. Seismic tests develop strains in the field of the order of 0.0001% and less, well below the elastic threshold strain for most soils, see section 1.3, so that the assumption of linear elasticity, implicit in the interpretation of the results is generally justified.

Dynamic field testing techniques can be broadly divided into surface techniques, including seismic refraction, steady state vibration or Rayleigh wave technique, spectral analysis of surface waves and analysis of seismic noise, and bore hole techniques, including down-hole, up-hole, cross-hole and seismic cone.

From the surface the deformation characteristics of large zones of the soil can be investigated by means of shear wave refraction surveys or steady-state (Rayleigh wave) techniques. Both techniques were used as part of the present work and details of the experimental procedures are given in chapter 3. A variation of the Rayleigh wave technique, better known as the spectral analysis of surface waves or SASW, has been described by Nazarian and Stokoe (1986 a,b). The vertical steady state vibration at fixed frequency that is used as the source of surface waves in the traditional method is substituted in the SASW by a transient vertical impact. The Rayleigh wave velocities corresponding to different frequencies are then obtained from the phase information of the cross power spectrum of the signals from two receivers, located at a certain distance from the source. Abbis and Ashby (1983) described an original technique which allows the variation of shear wave velocity with depth to be determined, and hence the variation of shear modulus with depth found, based on the measurement of the velocity of naturally occurring seismic noise. The technique does not require the generation of elastic

waves at any point in the soil.

Bore-hole techniques are used mostly to obtain detailed information on the variation of the small strain stiffness with depth at given locations. In the cross-hole technique (Stokoe and Woods, 1972) at least two holes are required but generally a larger number of holes are used. The source of vibration is installed in one hole and receivers are placed at the same depth in the other hole(s). Inclinometer measurements are recommended to determine the spacing of the receivers with depth (Anderson and Woods, 1975). In the up-hole and down-hole techniques only one hole is required. The two techniques differ only in the location of the source and the receivers, as shown in figure 2.2.11. A variation of the down-hole method is the seismic cone (Campanella et al., 1986), where a standard CPT is equipped with a velocity transducer so it can act as a receiver of seismic waves, see figure 2.2.12. The penetration of the cone is stopped at regular intervals and a dynamic test is carried out.

The conventional analyses of the bore-hole techniques are based on the identification of the first arrival times for the wave at points spaced at known distances from the source. Mancuso et al. (1989) reported developments in the interpretation of the cross-hole technique based on the numerical analysis of recorded data. They concluded that the most significant analyses for determining the soil s-wave velocity are the cross correlation and group velocity methods.

2.3 Basic theories for the dependence of stiffness on state

One of the central ideas of the models derived in the framework of critical state soil mechanics is that the mechanical behaviour of a soil is essentially frictional so that the main properties depend linearly on the stress level. A further feature of soil behaviour is that the properties normalised with respect to some measure of stress depend solely on the overconsolidation ratio. If the soil is idealised as an assembly of rigid frictional particles, one would expect the stiffness to depend linearly on the pressure. However, if the soil is idealised as an assembly of elastic spheres in contact, theoretical considerations (Hertz, 1881 as reported by Richart et al., 1970) lead to the conclusion that the shear modulus should depend on the stress raised to a one third

power.

The observed behaviour lies somewhere in between these two limits. If the dependence of the modulus on the mean effective stress is expressed as a power law, the exponent to which the pressure is raised changes significantly with the strain amplitude with values of n close to 0.5 at very small shear strain amplitudes and close to 1 at higher amplitudes (Wroth et al., 1979).

Some insight into the mechanisms of deformation of a particulate material such as soil can be gained by considering the mechanical behaviour of the simple system shown in figures 2.3.1(a) and (b), consisting of two perfectly elastic frictional spheres (Hardin, 1978). With the assumption that only normal forces are applied to the contact surface between the spheres, as in figure 2.3.1(a), the relationship between load and displacement is elastic, i.e. the deformations are fully recoverable, even if non-linear and strain hardening. When a tangential force is applied to the system, no matter how small, slippage of the two spheres occurs along an annular surface, as shown in figure 2.3.1(b). The relationship between tangential load and displacement is once again non-linear but this time the displacements are not fully recoverable and the behaviour is strain softening. For both loading and unloading slippage occurs and energy is dissipated by friction. This point is further illustrated in figure 2.3.2 where the elastic bending of thin plate-like particles is accompanied by slippage at the contacts between the particles. Recently, large random systems of elastic spheres of different size have been studied to simulate the behaviour of real soils with some success (Dobry et al., 1989). The analysis of such systems shows that the overall deformation always results from both elastic deformations of the particles and slippage and rearrangement of the particles. It would be expected that a smooth transition between elastic and plastic behaviour would be observed as one of the two mechanisms of deformation gradually becomes more important than the other.

In the present section some of the most common ways of expressing the dependence of stiffness on state both at small and very small strains will be presented. These will represent a framework against which the experimental results can be evaluated.

2.3.1 Dependence of stiffness on state at very small strains

Based on the Hertz equation Rowe (1971) suggested that it was possible to express the elastic component of the strain in the direction of the principal effective stress σ'_i, due to σ'_i, as:

$$\epsilon^{\bullet}_{ii} = C_i \left[\frac{\sigma'_i}{E}\right]^{1-n} \qquad (2.3.1)$$

where E is the Young's modulus of the particle material, C_i is a dimensionless coefficient and n an exponent which can take values between 0 and 1. Note that for an elastic continuum $C_i = 1$ and $n = 0$. Rowe (1971) also suggested that the total elastic strain increment $d\epsilon_i^{\bullet}$ in the direction of σ'_i is given by:

$$d\epsilon^{\bullet}_i = d\epsilon^{\bullet}_{ii} - \nu_{ij} d\epsilon^{\bullet}_{ij} - \nu_{ik} d\epsilon^{\bullet}_{ik} \qquad (2.3.2)$$

where the ν_{ij} are elastic Poisson's ratios. For an isotropic material $\nu_{ij} = \nu$.

Equations 2.3.1 and 2.3.2 allow theoretical expressions linking the elastic moduli to the state of effective stress in the soil to be derived. In particular, for isotropic conditions of stress ($\sigma'_i = \sigma'$) and for an isotropic material ($C_i = C$), the elastic shear modulus can be expressed as:

$$G'_{max} = \frac{1}{(1-n)\,C} E^{1-n} \sigma'^{n} \qquad (2.3.3)$$

The main drawback of the formulation above is that the dependence of the stiffness of the soil on the state does not contain any of the parameters that are commonly used in soil mechanics to characterise the state of the soil and its stress history, such as for instance e or v to express the volumetric state of the soil and OCR or any equivalent parameter to characterise the overall stress history.

Based on the results of wave propagation tests and small amplitude cyclic simple shear tests, Hardin and Black (1968) suggested the following empirical equation:

$$G'_{max} = 1230\, OCR^{k}\, \frac{(2.973-e)^2}{1+e}\, \sigma'^{0.5} \qquad (2.3.4)$$

where e is the void ratio of the soil, OCR is the overconsolidation

ratio, σ' is the mean effective stress and k is an exponent related to the plasticity index of the soil. Test results seemed to indicate that k takes values between 0 and 0.5 when the plasticity index of the soil varies from 0 to 100% (Hardin and Drnevich, 1972b). Equation 2.3.4 is not non-dimensional and both G'_{max} and σ' are expressed in psi.

From a comparison of equations 2.3.3 and 2.3.4, Hardin (1978) suggested that it was possible to write:

$$\frac{1}{(1-n)\,C}\,E^{1-n} = S\,f(e)\,OCR^{k}\,p_a^{1-n} \qquad (2.3.5)$$

where S is a dimensionless coefficient which accounts for the nature of the soil, f(e) is a decreasing function of the voids ratio which accounts for the volumetric state of the soil, p_a is the atmospheric pressure and n is an elastic parameter defining the power to which the stress is raised, and he proposed a revision of equation 2.3.4, as:

$$G'_{max} = S\,f(e)\,OCR^{k}\,p_a^{1-n}\,\sigma'^{n} \qquad (2.3.6)$$

Both equations 2.3.3 and 2.3.6 consist of three similar parts. Each contain a dimensionless stiffness coefficient, $1/(1-n)C$ in equation 2.3.3 and $S\cdot f(e)\cdot OCR^k$ in equation 2.3.6. In both equations the stress is raised to a power $n \neq 1$ and, because $n \neq 1$, both equations contain a term that satisfies the dimensions, E^{1-n} in equation 2.3.3 and p_a^{1-n} in equation 2.3.6. If the differences in Young's modulus for the different minerals are reflected in the stiffness of the system of particles, then the use of E rather than the atmospheric pressure or any other reference pressure to render the equation non dimensional would probably result in a smaller variability of the stiffness coefficients. In practice the Young's modulus of the particle materials is very seldom used.

Semi-empirical equations of the type of equation 2.3.6 have been proposed by a number of research workers, most of them deduced from the results of low-amplitude resonant column tests in isotropic conditions of confinement. Among others, Lo Presti (1989) proposed the following expression:

$$G'_{max} = S\,f(e)\,OCR^{k}\,p_a^{1-n}\,\sigma'^{n} = M_G\,p_a^{1-n}\,\sigma'^{n} \qquad (2.3.7)$$

where the non dimensional quantity M_G takes the place of the product $S\cdot f(e)\cdot OCR^k$ and represents the value of G'_{max} corresponding to the unit mean effective stress. Experimental values of M_G for a large variety of

soils are plotted against the voids ratio in figure 2.3.3.

Equation 2.3.7 is similar to the equation proposed by Janbu (1963) for the initial tangent Young's modulus measured in triaxial compression starting from isotropic states of confinement:

$$E_{max} = K_E \, p_a^{1-n} \, \sigma'^n \qquad (2.3.8)$$

where K_E is a non dimensional stiffness coefficient.

2.3.2 Dependence of stiffness on state at larger strains

The behaviour of many soils beyond the range of very small strains and before major plastic deformations occur is described as elastic by models derived in the framework of critical state soil mechanics. In the original version of the Cam-clay model (Schofield and Wroth, 1968) the soil could experience volumetric elastic strains but not shear elastic strains inside the state boundary surface. The elastic volumetric strains were defined by the relationship:

$$\delta\epsilon_v^e = -\frac{\delta v^e}{v} = \kappa \, \frac{\delta p'}{vp'} \qquad (2.3.9)$$

where κ is the constant slope of the elastic swelling lines as defined in section 1.2.2. It follows that the elastic bulk modulus K'_e is equal to vp'/κ and the elastic shear modulus is infinite. A minor modification to this model was proposed by Butterfield (1979) who suggested that the logarithm of the specific volume should be linked to the logarithm of the mean effective stress. This results in a bulk modulus which is directly proportional to the mean effective stress:

$$\delta\epsilon_v = \frac{\kappa}{p'} \, \delta p' \quad or \quad K'_e = \frac{p'}{\kappa} \qquad (2.3.10)$$

Atkinson and Bransby (1978) suggested that the elastic shear modulus G_e' was not infinite as in the original formulation of Cam-clay but would vary with mean effective stress in the same manner as the elastic bulk modulus K_e'. By assuming a constant elastic Poisson's ratio, ν', they expressed G_e' as:

$$G'_e = K'_e \frac{3(1-2\nu')}{2(1+\nu')} = const \frac{vp'}{\kappa} \qquad (2.3.11)$$

Experimental evidence of the dependence of the elastic shear modulus on the mean effective stress and of ν' being a constant was given by Wroth (1971) who re-analysed data by Webb (1967) on undisturbed samples of London clay from the Ashford Common shaft. As part of this study Wroth (1971) concluded that, when normalised by the current value of the mean effective stress, the elastic moduli G_e' and K_e' varied linearly with the logarithm of the overconsolidation ratio. In the original study the overconsolidation ratio was represented using the parameter $e_\lambda = e + \lambda \ln p'$ which is related to the overconsolidation ratio, R_o, by:

$$\delta e_\lambda = -\lambda \, \delta(\ln R_o) \qquad (2.3.12)$$

The approximately linear relationship between G'/p' and e_λ is reproduced in figure 2.3.4.

The stress paths for a set of three undrained triaxial tests on reconstituted samples of a glacial till soil are shown in figure 2.3.5 with superimposed contours of equal axial strain, for strains in the range $0.02\% < \epsilon_a < 0.6\%$ (Little and Atkinson, 1988). The information contained in the equal axial strain contours is evidence of the variation of the stiffness with mean effective stress. In particular, the contours of equal axial strain are approximately radial through the origin, which indicates that the stiffness increases linearly with p'. The results of undrained triaxial tests on overconsolidated samples of the same glacial till soil as in figure 2.3.5 are reproduced in figure 2.3.6 (Little and Atkinson, 1988). In this figure the normalised shear stiffness G'/p' at two different values of axial strain is plotted against the logarithm of the overconsolidation ratio, R_o. The data indicate that the stiffness at a particular stress and strain increases linearly with the logarithm of the overconsolidation ratio, which is consistent with that observed by Wroth (1971).

Recently Houlsby and Wroth (1991) proposed expressing the variation of stiffness with overconsolidation ratio using a power function of the type:

$$\frac{G'}{p'} = \left(\frac{G'}{p'}\right)_{nc} R_o^m \qquad (2.3.13)$$

where m is a constant taking values between 0 and 1. The main advantage of a formulation of this type is that, since the dependence of the undrained shear strength, s_u, on overconsolidation ratio is often expressed in a similar way, the rigidity index, G'/s_u, can also be expressed as power function of the overconsolidation ratio. Houlsby and Wroth (1991) noted that critical state models imply a variation of s_u with overconsolidation ratio of the type:

$$\frac{s_u}{p'_o} = \left(\frac{s_u}{p'_o}\right)_{nc} R_o^\Lambda \qquad (2.3.14)$$

where p_o' is the initial mean effective stress and $\Lambda = (\lambda - \kappa)/\lambda$. Assuming that isotropic elasticity applies at least for the initial stages of shearing so $p' = p_o'$ and, combining equations 2.3.13 and 2.3.14, the rigidity index is given by:

$$\frac{G'}{s_u} = \left(\frac{G'}{s_u}\right)_{nc} R_o^{m-\Lambda} \qquad (2.3.15)$$

They also compared this expression with data from Ladd and Edgers (1972) on the variation of G'/s_u with overconsolidation ratio for Boston Blue clay, see figure 2.3.7, to obtain a value of m of about 0.15.

At small strains the stiffness of soils is affected not only by the stress state and overall stress history, but also by the recent stress history, defined by the angle θ of rotation between the previous and current stress path directions, see figure 2.3.8 (Atkinson et al.,1990). Figure 2.3.9 shows the stiffnesses obtained from a series of tests with different stress path rotations. With particular reference to figure 2.3.9 (a), which shows the shear stiffnesses measured in constant p' tests, it can be noted that the soil has its highest stiffness for $\theta = 180°$, which corresponds to a full reversal of the stress path direction, and is least stiff for $\theta = 0°$, when the loading direction is constant. The curves for $\theta = \pm 90°$ lie between these two extremes. The effect also seems to reduce as the soil is loaded and to run out when the strains have reached approximately 0.1%.

2.4 Recent experimental investigations on the stiffness of soils at small and very small strains

2.4.1 Comparison between values of stiffness obtained from laboratory static and dynamic tests

Several researchers have assumed or implicitly shown that the stiffness of soils at small and very small strains is independent of the loading rate. Hardin and Drnevich (1972a) examined the effects of strain rate on the very small strain stiffness ($\epsilon_s < 0.001\%$) of sands and clays using the results of cyclic and dynamic torsion shear tests. They concluded that for a range of frequencies from 0.1 to 260 Hz the effect of frequency of loading on the very small strain stiffness was negligible and treated the data from the cyclic and dynamic tests without distinguishing between them.

Plenty of recent laboratory test data are available comparing the stiffness of sands under dynamic and static loading conditions. Among these, Bolton and Wilson (1988) compared the stress–strain behaviour of dry Leighton Buzzard sand observed from resonant column tests and from very low frequency cyclic tests on identical specimens of sand. Their results, in terms of torque versus strain curves are given in figure 2.4.1. The comparison between dynamic and static tests indicates that for strains from 0.0015% and 0.07% and loading frequencies between 0.001 Hz (quasi static) and 120 Hz (resonant column) the behaviour of the soil is independent of the frequency of the loading.

A direct comparison between the shear moduli obtained from resonant column tests and static torsional shear tests for dry Toyoura sand was carried out by Iwasaki et al. (1978). The curve of stiffness versus shear strain shown in figure 2.4.2 consists of the results of two series of tests on isotropically consolidated specimens. The first portion of the curve, at strains less than about 0.04%, was obtained from resonant column tests while the second portion of the same curve, at strains larger than about 0.004%, was obtained from static cyclic tests. The coincidence of the values of stiffness in the range of strains from 0.004% and 0.04%, where the two curves overlap demonstrates the independence of the stiffness of Toyoura sand from the frequency of loading. Similar results were obtained by Ni (1987) on a dry uniform

mortar washed sand. Typical curves of variation of shear modulus with shear strain amplitude obtained from both resonant column and torsion shear tests are shown in figure 2.4.3. Once again the values of stiffness obtained with the two different tests are the same, at least in the strain range under examination (0.0001 to 0.1%).

Less experimental data are available for saturated clays, probably because of the difficulties connected with the correct definition of the drainage conditions and the measurements of pore pressures generated during fast dynamic loading (Silvestri, 1991). Pane and Burghignoli (1988) investigated the dependence of the stiffness of a soft Italian silt with clay (Fucino clay) on strain amplitude and frequency of loading. The stiffness of the soil was investigated using both resonant column tests and cyclic torsional shear tests. The resonant frequency in the resonant column tests was about 20 to 25 Hz while in the torsional shear tests the frequency varied between $7x10^{-3}$ and $7x10^{-1}$ Hz. Typical curves of shear modulus versus shear strain amplitude and shear modulus versus frequency are shown in figure 2.4.4. In figure 2.4.5 the results from 25 tests are summarised as curves of shear modulus versus frequency. The data indicate that the variation of G with frequency is independent of strain amplitude at least for strains in the range 0.0006% to 0.1% and also of mean effective stress. The increase of shear modulus over the whole range of frequencies is about 20% of the value of stiffness from resonant column tests, and Pane and Burghignoli (1988) conclude that the small variation of G may be due to some effect of pore pressure build up during torsional shear. Similar values of increase of shear modulus with frequency, about 4% per logarithmic increase in frequency, were reported by Isenohwer (1979) for the San Francisco Bay Mud.

Rampello and Pane (1988) found good agreement between the results of resonant column tests and triaxial tests on a stiff Italian clay, Todi clay. In figure 2.4.6 the values of stiffness obtained from the resonant column test are compared with the values of stiffness obtained from undrained triaxial tests with internal measurement of axial strain. Despite the different modes of shearing and the very different rates of loading in the two types of tests the results are in excellent agreement over the strain range in which the data overlap.

Similarly, Georgiannou et al. (1991) performed a comparison of the stiffnesses of four natural clays measured in undrained triaxial tests, cyclic torsional shear tests and resonant column tests. In the torsional shear tests the rate of loading was controlled so that the average strain rate was the same as in the triaxial tests. In the resonant column tests the strain rate at resonance was one to four orders of magnitude higher than the strain rate in the triaxial or torsion shear tests. Typical results from Vallericca clay are shown in figure 2.4.7. At strains less than 0.01% the values of stiffness obtained from torsion shear tests are about 10% less than the values obtained from the resonant column tests. Within the range of strain from 0.01 to 0.1% the results from the different tests plot in a very narrow band. It is interesting to notice that the results from the triaxial tests compare better with the results from the resonant column tests even if the rates of loading in the triaxial tests were much closer to the rates of loading in the torsion shear test. This may indicate that the agreement between the results from dynamic torsional shear tests and triaxial compression tests, which are two very different modes of shearing at very different rates, may be due to the effect of a number of errors of opposite sign which are cancelling out.

2.4.2 Effects of stress anisotropy and time on stiffness

The first comprehensive review of the effect of different parameters on the shear modulus of both cohesive soils and clean sands as deduced from the results of cyclic torsional shear and resonant column tests was carried out by Hardin and Drnevich (1972 a). Their conclusions on the relative importance of a number of factors on the stiffness of soils are summarised in table 2.4.1. At a given strain amplitude the most important factors affecting the stiffness of cohesive soils were indicated to be the mean effective stress, the voids ratio and the degree of saturation. The overconsolidation ratio, which in this context must be intended as mechanical overconsolidation, was listed as a less important factor.

It must be noted that, at least for reconstituted samples in isotropic conditions, the state of the soil is fully defined by any two out of mean effective stress, voids ratio and overconsolidation ratio, in this case intended as a measure of the distance of the state of the soil from the

normal compression line, see section 1.2.2. The choice of the voids ratio or the overconsolidation ratio as the parameter to locate the position of the state of the soil relative to the normal compression line is merely a matter of convenience. It is hardly surprising that, once the data have been normalised to take into account the effect of voids ratio, the overconsolidation ratio would only have a minor effect, because the two parameters are not independent. Most of the data available from dynamic tests at the time when Hardin and Drnevich (1972a) were evaluating the influence of the different factors on the very small strain stiffness of soils referred to sands. In this context the choice of the voids ratio as the parameter defining the state of the soil seems quite a logical one. However, when analysing results from tests on clays it may be more convenient to use a measure of overconsolidation rather than a measure of volume to reduce data and the position of the two parameters in table 2.4.1 should be considered interchangeable. The degree of saturation was considered a very important factor for fine grained soils because of the difficulty in determining the effective stress in such soils when partly saturated.

The effects of anisotropic initial states of stress on the values of very small stiffness for sands were found to be very small. This is clearly indicated in figure 2.4.8, where the values of stiffness obtained at the same value of mean effective stress but with different values of octahedral shear stress for a dry clean sand are plotted against the shear strain (Hardin and Drnevich, 1972a).

In order to consider the effect of anisotropic conditions of confinement on the very small stiffness of soils, Ni (1987) proposed the following equation which is a more general form of equation 2.3.6:

$$G'_{max} = S\, f(e)\, OCR^{k}\, p_a^{1-n}\, \sigma'^{n_a}_{a}\, \sigma'^{n_b}_{b}\, \sigma'^{n_c}_{c} \qquad (2.4.1)$$

where $n = n_a + n_b + n_c$, σ_a' and σ_b' are the normal effective stresses in the plane of shear and σ_c' is the normal effective stress orthogonal to the plane of shear, see figure 2.4.9. Based on the results of a large number of resonant column tests on hollow cylindrical samples of dry washed mortar sand, both in biaxial loading conditions ($\sigma_b' = \sigma_c'$) and in true triaxial conditions, Ni (1987) concluded that G'_{max} is affected in about the same way by σ_a' and σ_b' ($n_a \simeq n_b$) while the influence of σ_c' is practically negligible. However, the loading process in all the tests

was such that the effective stress in the direction of shear wave propagation, σ_a', was always greater than or equal to the other two stresses, σ_b' and σ_c', and this may have an effect on the observed values of the exponents of the individual stresses, see section 5.3.

Another set of data which explores the dependence of the stiffness of Toyoura sand on an initial anisotropic state of confinement is shown in figure 2.4.10 (Tatsuoka et al., 1979).. In this figure the ratio of the shear modulus obtained in anisotropic conditions of confinement (both triaxial extension and compression) to the shear modulus obtained in isotropic conditions at the same mean effective stress obtained from cyclic torsional shear tests at different strain amplitudes is plotted against the stress ratio. The data indicate that at a constant value of p' in triaxial compression the shear modulus is almost independent of the shear stress level, when the principal stress ratio σ_1'/σ_3' is less than about 3. In extension there seems to be a larger effect of the stress ratio on the modulus, but when the initial conditions are not close to those at failure, the stiffness seems to be rather insensitive to the shear stress level at constant p'. This is further confirmed by the data shown in figure 2.4.11, which shows the initial portion of the shear stress–shear strain curves obtained from monotonic torsion shear tests on loose Toyoura sand (Teachavorasinskun et al., 1991). The data clearly show that the initial value of stiffness, G'_{max} is rather insensitive to the initial shear stress.

Little recent data are available to define the effect of an initially anisotropic state of confinement for fine grained soils. Experimental evidence of the very small effect of anisotropic states of confinement on the values of the very small strain stiffness of a kaolinite clay was given by Hardin and Black (1968). In their study, five specimens of clay were subjected to the ambient states of stress shown in figure 2.4.12 and values of G'_{max} were obtained at each point from low amplitude resonant column tests. The results three groups of points (zones 1,2 and 3) in which the isotropic component of stress was nearly constant are shown in figure 2.4.13. Once again, the results indicate that the very small strain stiffness is essentially independent of the deviatoric component of ambient stress.

The effect of time other than frequency or rate of loading effects on

small strain stiffness of cohesive soils has also been investigated by a number of research workers. The very small strain stiffness of soils is shown to increase with the duration of confinement. In most of the dynamic work, loads are applied to the soil as discrete increments rather than varied smoothly. The increase of very small strain stiffness after application of a load is characterised by two phases. The first one corresponds to primary consolidation. As the excess pore pressures generated by the application of the load dissipate the soil experiences major changes of effective stress and specific volume so that major variation of the very small strain stiffness of the soil are expected. Following primary consolidation long term time effects are reported to occur for all soils, see figure 2.4.14 (Anderson and Stokoe, 1978). The increase of shear modulus with time in this second phase seems to be larger than that accounted for by changes in voids ratio and it is approximately linear with the logarithm of time. For fine grained soils time effects are reported to increase as the mean grain diameter of the soil decreases and the confining pressure increases. Similar conclusions on the dependence of the very small strain stiffness of a kaolinite clay were reached by Hardin and Black (1968), who also observed that the long term increase in stiffness could be partly destroyed by abrupt changes in effective stress.

The implications of this work are mostly connected to the possibility of estimating field values of G'_{max} from laboratory tests. Anderson and Stokoe (1978) recommend that corrections to take into account the increase in stiffness due to the geological age of the deposit should always be made to laboratory values of G'_{max} before trying to relate these values with field values.

2.4.3 Comparisons between laboratory and field measured values of stiffness

Several methods are available to obtain the in situ stiffness of soil deposits for ground movement calculations. Some of these methods are based on the results of relevant laboratory tests on high quality laboratory samples (Jardine et al., 1984). It has already been discussed how, until recently, the value of stiffness of overconsolidated clays measured in the laboratory were invariably lower than the those obtained from the back analysis of real life engineering structures, see section

2.2, so that the engineers tended to rely more on the results of relevant in situ tests, such as plate loading tests, than on the results of laboratory tests. Recently improved laboratory testing techniques have led to a better agreement between laboratory and field stiffnesses. A recent example of the comparison between the stiffness of a glacial clay obtained from large diameter plate loading tests and triaxial tests is given by Hird et al. (1991). In both the plate loading tests and the triaxial tests special instrumentation was used to measure the strains in the soil which was critical to the interpretation of the data. In figure 2.5.1 the plate test data are compared with the triaxial data, showing a good agreement over a significant strain range.

Another class of methods for the evaluation of the in situ stiffness of soil deposits is based on field measurements of the shear wave velocity which is related to the shear stiffness of the soil at very small strains (ϵ_s = 0.001% and less). In order for these methods to give values of stiffness relevant to most engineering calculations, a function must be assumed describing the dependence of stiffness on strain level. This is generally evaluated from laboratory tests. A recent example of this approach can be found in Powell and Butcher (1991). In their study Powell and Butcher (1991) compared the values of stiffness obtained using a number of in situ loading tests, including pressuremeter tests and plate loading tests, and in situ geophysical measurements (Rayleigh wave) at a number of clayey sites. The geophysical measurements give values of stiffness at very small strains and were corrected to account for the strain level using the modified hyperbolic model by Hardin and Drnevich (1972 b). The results obtained for a site at Cowden, on a glacial clay, shown in figure 2.5.2, indicate a good agreement between the different tests with the only exception of the pressuremeter moduli which are higher than the other values.

The underlying assumption of all the methods just described is that the decay of stiffness with strain amplitude observed in the laboratory is similar to that in situ, whereas the value of stiffness at very small strains measured in the laboratory may not be equal to the in situ value, so that it is necessary to measure it directly on site. This may not necessarily be so. Burland (1989) reported successful comparisons between the shear moduli obtained from field seismic surveys (Abbiss, 1981) and the initial values of stiffness obtained from undrained

triaxial tests on undisturbed samples of London clay.

Cunny and Fry (1973) compared the values of G obtained using the steady-state vibration technique at 14 different sites with the values obtained in the laboratory using the resonant column apparatus. They found that the laboratory shear moduli ranged within 50% of the in situ moduli and that the agreement of the two sets of results could be improved for cohesive soils by taking into account secondary time effects.

More recently Silvestri (1991) compared the values of stiffness obtained from resonant column tests with the results of cross-hole tests carried out on the core of a dam composed of silt. In figure 2.5.3 the data are plotted as very small shear stiffness versus mean effective stress. An evaluation of the in situ stress state was made in order to convert the stiffness profiles obtained from the cross-hole technique into shear modulus versus mean effective stress data. The overall agreement of the results is satisfactory even if the laboratory values are slightly smaller than the in situ values. This was attributed partly to sample disturbance.

A comparison of the stiffnesses obtained from Rayleigh wave surveys and bender element tests was carried out for a site at Brent on London clay by Powell and Butcher (1991), see figure 2.5.4. The average values of G'_{max}/p_o' from the Rayleigh wave method were found to be much lower (about 60%) of the average values of G'_{max}/p_o' from the bender element tests. This unusual finding was partly explained by Powell and Butcher (1991) as an effect of frequency of loading, which is much higher in the bender element tests than in the Rayleigh wave survey.

2.5 Summary

The first section of this literature survey shows that there are a number of techniques available to measure the stiffness of soils at small and very small strains. In particular dynamic techniques can be used to measure the stiffness of soils at very small strains (ϵ_s = 0.001% and less) both in the field and in the laboratory.

A number of expressions describing the dependence of soil stiffness on

stress state and history have been reviewed both for the very small and for the small strain range. Some of these expressions, such as those based on the Hertz contact theory or those derived in the framework of critical state soil mechanics, have a theoretical basis while others are just empirical or semi empirical.

The review of the recent experimental work, carried out in the last section of this survey, indicates conclusively that the stiffness of sands does not depend on the frequency of the applied loading, dynamic and static tests giving the same results in terms of stiffness. For clays, small differences are observed between the values of stiffness under dynamic or static loading conditions but these differences could be attributed to small excess pore pressures building up during fast dynamic loading, rather than to a truly viscous material behaviour.

The effect of stress anisotropy on the initial stiffness of soils is not well established. For sands the effect seems to be small, at least for initial stress conditions that are far from failure. Indications that the very small strain stiffness of sands depends about equally on the two normal stresses in the plane of shear and is relatively independent of the stress in the out-of-plane direction can also be found in the literature. Less work on the subject of anisotropic states of stress has been carried out on fine grained soils, but once again there are indications that this may not be very relevant. An increase of very small strain stiffness with time of confinement, that cannot be accounted for by changes in voids ratio due to secondary consolidation, is observed in all soils.

CHAPTER 3 SITE WORK

3.1 Introduction

The bulk of the field work undertaken as part of the present project was carried out during summer 1989, under the supervision of Dr C.P. Abbiss from the Building Research Establishment. This work consisted mainly of field measurements of shear and compression wave velocities using surface wave techniques and shear and compression pulse refraction surveys. Both the techniques that were used in the field can be classified as surface techniques, see section 2.2.5. They were preferred to borehole techniques such as cross-hole, down-hole or up-hole because of the obvious advantage that profiles of stiffness with depth can be obtained from the surface without forming any boreholes in the ground.

Seismic tests generally develop strains in the field of the order of 10^{-3} to 10^{-4}% and less. The strains involved in the refraction survey are not constant, decreasing from a maximum close to the hammer source. Also in the surface wave experiment, the wave changes in amplitude with depth and the shear strain amplitude is maximum near the surface. It has been shown (Harrison, 1989) that the shear strain amplitude can be obtained from the ratio of the particle velocity to the wave velocity, $\varepsilon = v_p/V$, so that estimates of the strain amplitude can be made in individual experiments by using calibrated geophones.

Three sites were examined, all in the London area, and a total of 17 surface wave surveys and 7 seismic refraction surveys were carried out, as summarised in table 3.1.1(a) and (b). On each site profiles of seismic wave velocities with depth were obtained following the procedures that will be described in sections 3.2 and 3.3. The theoretical relationships between seismic wave velocities and elastic moduli have been discussed in some detail in section 1.4. Based on these relationships, the profiles of seismic wave velocities were converted into profiles of stiffness with depth.

On all sites the velocity of the shear pulse obtained from the refraction surveys was significantly higher than the velocity of the continuous shear wave obtained from the surface wave surveys. In the refraction

survey the arrival of the leading edge of the refracted pulse is timed at various distances from the source. As discussed by Abbiss (1981), due to an effect of pulse broadening, the leading edge of the pulse could be travelling at a velocity higher than the continuous shear wave velocity, at which the centre of the pulse travels. Therefore, in the present work, the stiffness profiles were obtained from the continuous shear wave data rather than from the shear pulse data.

The techniques used in the field were substantially the same as those used in standard practice which have been comprehensively described elsewhere (Abbiss, 1981). This is because the main objective of the field work was the collection of field data to be compared, at a later stage of the project, with the results of the laboratory testing, rather than the development of experimental techniques and interpretation procedures. Any development in the experimental techniques, that resulted from experience of the techniques themselves, is described in the relevant sections.

As part of the field work, boreholes were formed to compare the stiffness profiles obtained from the dynamic techniques with the actual stratigraphy at the sites. The boreholes were also used to retrieve samples to be tested in the laboratory. In this chapter the profiles of stiffness obtained at the different sites will be presented and discussed. Comparison of the data with laboratory results is left until the full discussion of data in chapter 5.

3.2 Surface wave experiment

In the surface wave experiment, sometimes referred to as the steady state vibration experiment, seismic waves are generated in a continuous form using a vibrator that oscillates vertically at the surface of the ground. As discussed in section 1.4, in these conditions, about two thirds of the total input energy are transmitted away from the source in the form of Rayleigh waves. Also, the geometrical damping for this kind of wave is less severe than for the body waves. As a result, it would be expected that a vertical receiver located on the surface at a certain distance from the source of vibration would sense the vertical component of the Rayleigh wave as it travels past it. In the most common experimental

arrangement the propagation of the Rayleigh wave at the surface is detected using two receivers placed at a known distance apart, in line with the vibrator, as shown in figure 3.2.1.

3.2.1 Dispersive characteristic of surface waves.

The theoretical attenuation of the displacement components of the Rayleigh wave was shown in figure 1.4.3. Based on the shape of the attenuation curves it seems reasonable to assume that the majority of the Rayleigh wave travels in a layer that is about one wavelength deep. If the frequency of vibration is decreased, the wavelength increases and the wave samples a greater depth; if the frequency is increased both the wavelength and the sampled depth decrease.

For a homogeneous half space the material properties are independent of depth and the Rayleigh wave velocity, V_R, is independent of frequency. Each frequency, f, has a corresponding wavelength, L_R according to:

$$L_R = \frac{V_R}{f} \tag{3.2.1}$$

For a half space in which material properties change with depth the velocity of Rayleigh waves varies with the frequency of the input excitation because different wavelengths sample material with different average properties. The variation of Rayleigh wave velocity with frequency or with wavelength is called dispersion and the plot of surface wave velocity against wavelength is called a dispersion curve.

The surface wave velocity can be obtained by measuring the phase shift, Φ, between the signals from the two receivers. A phase shift of 2π would be equivalent to a travel time equal to the period of the wave, $T = 1/f$; therefore, for each frequency, the travel time between receivers can be calculated as:

$$t(f) = \frac{\Phi(f)}{2\pi}\frac{1}{f} \tag{3.2.2}$$

and the Rayleigh wave velocity that corresponds to the frequency f simply obtained as:

$$V_R(f) = \frac{d}{t(f)} \tag{3.2.3}$$

where d is the known distance between the receivers. The corresponding wavelength is equal to:

$$L_R(f) = \frac{V_R(f)}{f} \qquad (3.2.4)$$

By repeating the procedure outlined in equations 3.2.2 to 3.2.4 for a range of frequencies, the Rayleigh wave velocity corresponding to each wavelength and the dispersion curve can be obtained.

3.2.2 Inversion of the dispersion curve

The velocities determined with this method may be thought as representative of an average of the properties of the ground in a characteristic layer. The problem arises of determining the shear wave velocity distribution with depth from the apparent Rayleigh wave velocity versus wavelength information. The procedure of determining the shear wave velocity profile from the dispersion curve is generally called inversion of the dispersion curve, or, in short, inversion.

The simplest way to approach the problem of inversion is to postulate that, since the bulk of the Rayleigh wave travels through a zone of the half space which is about one wave length deep, the apparent velocity of the wave corresponds to that of the material at a depth of about one half wave length ($z = L_R/2$). Both Richart et al. (1970) and Abbiss (1981) reported several examples in which transitions between materials with different properties were located successfully using the depth of $L_R/2$.

Nazarian and Stokoe (1986a,b), working on the development of a method for *in situ* determination of elastic moduli of pavement systems proposed an inversion method based upon a modified version of the Haskell-Thomson's matrix solution for surface waves propagating in a horizontally stratified medium. The proposed method is an iterative process in which a shear wave velocity profile is assumed and, based on it, a theoretical dispersion curve generated. The assumed profile is modified until the experimental and theoretical dispersion curves match within a specified approximation.

A more fundamental approach was adopted by Gazetas (1982) in an analytical study of the dynamic behaviour of heterogeneous deposits. The dispersion and attenuation characteristics of Rayleigh waves were

examined for four heterogeneous deposits in which shear wave velocity increased continuously with depth according to:

$$V = V_0 (1 + bz)^m \qquad (3.2.5)$$

where V_0 is the velocity at zero depth and b and m are constants. Different types (m = 1, 2/3, 1/2, 1/4, 0) and rates (b = 3, 1) of heterogeneity were considered. The solution of the governing plane wave equation could be obtained analytically only for m = 1 that is the case in which velocity increases linearly with depth. For all other cases numerical-analytical methods were adopted. In figure 3.2.2 the variation with frequency of the depth to wavelength ratio, z/L_R, for four heterogeneous deposits having b = 3 is shown. The ratio is a slightly decreasing function of frequency with an average value of 0.25, essentially independent of the exact type of heterogeneity. Milder rates of heterogeneity (b < 3) would yield larger values of the ratio, closer to the commonly used value of 0.5. As a result of this study, Gazetas (1982) concluded that, if shear wave velocity increases with depth, a shallower value than $z = L_R/2$ should be adopted for the correct inversion of dispersion curves. In particular, for a realistic range of rates of heterogeneity ($1 < b < 3$), $z = L_R/3$ was the recommended value.

These findings were confirmed by Vrettos (1990) who carried out an analytical study of the propagation characteristics of surface waves in a linear elastic, isotropic half space with constant mass density and Poisson's ratio and shear modulus varying with depth according to a continuous bounded function, as shown in fig 3.2.3. This type of variation of stiffness with depth can realistically describe a wide range of real soil profiles. The asymptotic behaviour of the shear modulus at large depths can be interpreted as a base layer with only slightly varying stiffness. Dispersion relations were evaluated for a wide range of the parameters involved. An equivalent depth of about a third of the wave length was again recommended for use in connection with surface wave techniques for soil exploration.

In the present project, the inversion of the dispersion curves was carried out following the recommendations of Gazetas and Vrettos using an equivalent depth equal to a third of the wavelength.

3.2.3 Field equipment and procedures

The general configuration of the source, receivers and recording equipment used for the surface wave experiment is shown in figure 3.2.4.

The surface waves were generated using a Ling Dynamics electromagnetic vibrator type 400 connected to a plate, about 0.20 m diameter, resting on the ground . The vibrator was powered by a Ling oscillator and power amplifier model TPO 100 and was used over the frequency range 8–200 Hz. The surface waves were generally detected using two geophones, model Sensor SM6, placed at known distances from the source in line with the centre of the vibrator. In one case, in conjunction with the phasemeter technique described below, the receivers were seismometers model Willmore MKIII A. Both geophones and seismometers are vertically polarised velocity transducers whose response to an imposed motion is a function of frequency. Typical response curves for the model Sensor SM6 are shown in figure 3.2.5.

A set of preliminary experiments was carried out at the North Field site to assess the influence of the spacing of the geophones on the observed values of Rayleigh wave velocities, see section 3.5. In this set of experiments the distance between the source and the first receiver was varied from 1.0 to 5.0 m while the spacing between the two receivers was varied from 1.0 to 3.0 m. The results, shown in figure 3.2.6, indicate that the effect of spacing is practically negligible, at least for the range of spacings examined. However, for the largest spacings the data tended to become quite scattered, probably because the signal to noise ratio tends to decrease as the distance from the source of vibration increases. Most of the surface wave velocity data presented in this chapter were therefore obtained using a spacing of 1.5 to 2.0 m between the source and the first geophone and between the two geophones.

Several options are available to measure the phase shift between the signals from the two receivers. The simplest technique used in the present work was that of connecting the receivers, in this case seismometers, to a digital phasemeter and recording the phase shift between the two signals for each value of frequency used. There were several drawbacks to this technique. Firstly, no direct measurement of the frequency of the signals was carried out so that, in the calculation

of the Rayleigh wave velocity and wavelength, it was necessary to assume that the frequency of excitation corresponded to the frequency selected on the vibrator controller, which is not very accurate. Moreover, it was not possible to check directly the quality and the shape of the generated vibrations. Most of all, at low frequencies, the readings at the phasemeter became extremely unstable making the measurement of phase shift virtually impossible. Because the low frequencies correspond to greater depths it was only possible to examine relatively shallow depths using this technique.

Two alternative techniques were used in this project. The first used the experimental arrangement shown in figure 3.2.4(a) where the phase shift between the signals was measured using a Hewlett Packard dual channel spectrum analyser model 3582A. The spectrum analyser is a digital oscilloscope linked to a 16 bit microcomputer that can perform a finite Fourier transform of the signals using a fast Fourier transform algorithm. The phase spectrum between the signals from the two geophones can be computed and the information displayed on the screen as a graph of phase shift versus frequency. The technique is a variation of the method described by Nazarian and Stokoe (1986 a,b), only they used single blows for the excitation instead of a sinusoidal vibration at a fixed frequency.

The main reason for using the spectrum analyser was that it allowed very accurate measurements of the phase shift of the main Fourier component of the signal to be made, even when the quality of the signal deteriorated, thus overcoming the problems encountered using the phasemeter technique. The spectrum analyser clearly revealed how, at low frequencies ($f < 30$ Hz), the waves produced by the vibrator were often far from being sinusoidal, probably due to imperfect coupling between the base of the vibrator and the surface of the ground.

The spectrum analyser also had an averaging facility that enabled averages of sets of data to be considered. This was very convenient because background noise is random in nature, so its sum in the signal tends to zero as the averaging process is carried on. Another advantage of averaging was that the coherence function between the outputs from the two channels could be calculated. Coherence is a measure of the causality between the two signals and can be used to assess the

importance of the noise relative to the signal for each component of the spectrum. A value of coherence equal to 100% would indicate that the signal in the second channel is completely derived from that in the first channel; a zero value would show no connection. For the measurements to be meaningful a common requirement is that the coherence function at the frequency under examination should be above 80% (Abbiss, 1992). In the present work all data with a coherence value less than 95% were disregarded.

In a second experimental set up, shown in figure 3.2.4(b), the measurement of the phase shift was carried out using a Hewlett Packard digital correlator model 3721A. The correlator can calculate the cross correlation function of the two signals which is a measure of their degree of correlation as a function of the time shift imposed to the signals. If the waveforms are two sinusoidal functions with the same frequency and Φ is the phase shift between them, their cross correlation will be a cosinusoidal function with the same frequency and a phase shift equal to Φ. Once more, because noise is random in nature and cross correlation detects similarities between signals, it can be effectively used to separate a signal from noise when a reference signal is available for comparison and to reveal phase shifts between the two signals.

The output from the geophone closer to the vibrator was first amplified and then filtered at a frequency corresponding to the excited one. This was done in order to obtain a good quality reference signal against which the output from the other geophone could be compared. The cross correlation function was calculated twice for each frequency used; the first time with the two geophones side by side (no phase shift, reference reading) and the second time at a distance d apart (phase shift equal to Φ). To allow a visual inspection of the quality and shape of the generated vibrations a simple two channel oscilloscope was added to the instrumentation, as shown in figure 3.2.4(b).

The main reason why the correlator technique was introduced was that it used electronics which was always available at BRE and therefore did not incur hire charges. In addition, the capital cost of the equipment is much less than that of the spectrum analyser. However, a longer time was required to carry out the surface wave survey using the correlator technique because of the need for a reference reading for each value of

frequency used. Moreover, the lowest value of frequency at which measurements could be made satisfactorily using the correlator was about 12 Hz while with the spectrum analyser the limit was about 8 Hz.

The correlator technique was extensively tested in the North Field, see section 3.5. Several surveys were carried out to assess the influence of various parameters on the observed values of Rayleigh wave velocities. In addition to the effect of spacing, tests were carried out to define the optimum of number of averages to be taken with the instrument to compromise between the stability of the readings and the speed of the survey. The results obtained from these preliminary tests are shown in figure 3.2.7 and again the effect of spacing was found negligible. In addition, increasing the number averages from N = 32x1024 to N = 64x1024 did not make much difference to the results. Therefore tests were typically carried out with a spacing of 1.5 to 2.0 m and using a number of averages N = 32x1024.

3.3 Seismic refraction experiment

In the seismic refraction experiment a pulse of either shear or compression waves, is generated at the surface of the ground and the first arrival of the refracted pulse timed at various distances from the source, as shown in figure 3.3.1. From the curve of travel time versus distance the distribution of velocity with depth can be obtained. The properties of the ground control the maximum depth of investigation that it is possible to obtain with this technique. The method is well suited to the exploration of soil and rock deposits whose stiffness increases markedly with depth.

3.3.1 Basic theory

The theory on which the seismic refraction technique is based is well established and described at length in a number of text books on soil dynamics and geophysical prospecting (see, for instance, Richart et al., 1970 or Griffiths and King, 1981). A common method of interpretation is based on the assumption that the ground consists of horizontal homogeneous layers of increasing velocity. In these conditions, the wave rays consist of segments of straight lines and the first arriving signals

travel either directly from the source to the receiver or after refraction at a particular layer interface, as shown in figure 3.3.2. In the same figure, the plot of travel time versus distance is also reported. For horizontal homogeneous layers this plot consists of segments of straight lines. Each line corresponds to a particular layer and the velocity of the layer can be calculated as the inverse of the slope of the relevant segment of straight line.

In a medium with velocity varying gradually with depth, Snell's law of refraction requires that the wave rays are no longer straight lines but have a curvature that depends on the gradient of velocity in the medium. For a linear variation of velocity with depth given by:

$$V = V_o + kz \tag{3.3.1}$$

where V_o is the velocity at zero depth and k is a constant, the refraction paths are segments of circles with centres at a distance V_o/k above the surface, as schematically shown in figure 3.3.3. The expression of the travel time, T, as a function of distance, x, can be obtained in a closed form (Dobrin, 1960) as:

$$T(x) = \frac{2}{k} \sinh^{-1} \frac{kx}{2V_o} \tag{3.3.2}$$

The depth of greatest penetration for the circular ray emerging at a distance x is given by:

$$z = \frac{V_o}{k} \left\{ \left[1 + \left(\frac{kx}{2V_o} \right)^2 \right]^{1/2} - 1 \right\} \tag{3.3.3}$$

3.3.2 Field equipment and procedures

At each of the three sites investigated, parallel shear wave (s-wave) pulse and compressional wave (p-wave) pulse refraction surveys were carried out.

Two types of source were used to produce the shear wave pulse. The simplest consisted of a steel pipe hammered into the ground. By striking the pipe on one side with a hammer, perpendicularly to the line of survey, a horizontally polarised shear pulse was produced. The direction of the pulse could be reversed simply by striking the pipe on the

opposite side. Alternatively, the source consisted of a 1.5 m long section of aluminium channel in contact with the surface of the ground and weighed down by the back wheels of a van. The shear pulses were produced by striking the aluminium channel alternatively at either end by pendulums weighing about 20 kg. The source used to produce the compressional wave pulse was a hammer vertically striking a square aluminium plate of 0.20 m side resting on the ground.

The pulses were detected using horizontally polarised (s-wave) or vertically polarised (p-wave) geophones placed at various distances from the source, as shown in figure 3.3.1. The signals from the geophones were recorded using a Nimbus enhancement seismograph, triggered by an inertia switch on the hammer. The instrument was capable of storing the traces digitally and adding or stacking the traces resulting from successive blows. As the signals from each blow were fairly repeatable, the stacking process could be used effectively to average out the background noise, as discussed in section 3.2.3. Theoretically, the higher the number of signals averaged, the closer to the true signal the final result. Practically the number of blows had to be optimised. For the larger spacings, where the signal to noise ratio tended to be smaller, up to five blows were used.

The resultant summation trace was displayed on a cathode ray tube and the arrival time measured directly off the screen using an electronic marker with a digital read out. The possibility of reversing the pulse was also important as this reversal, as observed on the screen, helped in the identification of the arrival of the shear wave, often in the wake of the compression wave.

For both p-waves and s-waves the arrival of the leading edge of the pulse was plotted as a function of the distance from the source. The time distance experimental data were fitted using equation 3.3.2 and the maximum depth of survey calculated using equation 3.3.3.

3.4 The sites and the results

The techniques described above were applied on three clayey sites in the London area. The location of the sites is shown on the map in figure

3.4.1. The first site, extensively used because of its convenient location, was the North Field test site at the Building Research Station, Garston, on boulder clay. The other two sites were the BRE test site at Canons Park and the BRE test site at Chattenden, both on London Clay. At all sites boreholes were formed in the immediate vicinity of the areas used for the dynamic surveys in order to compare directly the stiffness profiles obtained using these techniques with the stratigraphy and the geology of the sites. At the North Field and at the Chattenden sites the boreholes were also used to retrieve samples to be tested in the laboratory.

3.4.1 North Field (BRS)

The North Field test site lies within the boundaries of the Building Research Station in Garston, Hertfordshire. The site is located at the southwest corner of the Vale of St. Albans whose geology has been extensively investigated because of its importance in the study of the Quaternary in southeast England (Gibbard, 1977; Little, 1984). The Geological Survey revised 1:50000 (Drift), sheet 239, Hertford, reproduced in figure 3.4.2, shows that the area is covered by extensive deposits of glacial gravel and associated chalky till or boulder clay underlain by chalk. The soil profile at the site, as obtained from a borehole very close to the area were the dynamic surveys took place, is shown in figure 3.4.3. The depth of the chalk on the site, however, is very variable and, at another site on the station, the chalk was found to be at a depth of about 19 m (Abbiss,1981).

Because of its convenient location the North Field site was used as a pilot site for all the preliminary experiments to assess the influence of various parameters on the observed values of Rayleigh wave velocities and to try out and compare different experimental techniques. A total of 13 surface wave surveys were carried out on the site, following the procedures outlined in the previous sections.

The first measurements on the North Field were carried out using the phasemeter technique. The results of these measurements are shown in figure 3.4.4 in terms of Rayleigh wave velocity versus depth. The Rayleigh wave velocity data obtained can be fitted very closely using a straight line of equation:

$$V_R(z) = 105.1 + 24.3z \qquad (3.4.1)$$

with a root mean square deviation, $\sigma = \pm 11.4$ ms^{-1}, which corresponds to an error $\sigma\% = 6.9\%$ at an average depth of 2.5 m. However, as discussed in section 3.2.2, using the phasemeter technique it was not possible to achieve depths much larger than 5 or 6 m because of the instability of the signals at low frequencies.

A second set of results from the same site was obtained using the spectrum analyser. In figure 3.4.5 the same data shown in figure 3.2.6 have been fitted using a straight line:

$$V_R(z) = 121.1 + 26.3z \qquad (3.4.2)$$

This time the maximum depth of survey was about 20 m, with a root mean square deviation of ± 13 ms^{-1}, corresponding to an error of only 3.6% at an average depth of 10 m.

The data obtained using the correlator are generally more dispersed, and tend to give lower values of velocity near the surface and higher values at depth, if compared to the values obtained using the spectrum analyser. The data are shown in figure 3.4.6, together with the best fit line:

$$V_R(z) = 87.3 + 36.9z \qquad (3.4.3)$$

The maximum depth of penetration with the correlator technique was about 15 m. The root mean square deviation for this set of data is $\sigma = \pm 15.6$ ms^{-1}, corresponding to an error of $\sigma\% = 4.3\%$ at an average depth of 7.5 m.

The whole of the experimental results for the North Field site are plotted together in figure 3.4.7; the overall agreement between the different results was considered satisfactory and a single straight line fitted to the data, of equation:

$$V_R(z) = 104.9 + 30.3z \qquad (3.4.4)$$

The root mean square deviation is $\sigma = \pm 25.2$ ms^{-1}, corresponding to an error of 6.2% at an average depth of 10 m.

Pulse refraction surveys were also carried out on the North Field site using the techniques outlined in section 3.3.2. The arrival time versus

distance plots for both shear and compression surveys are shown in figure 3.4.8. The experimental data were fitted using equation 3.3.2 and the variation of shear pulse and compression pulse velocities with depth deduced. The shear pulse velocity, V_{sp}, and the compression pulse velocity, V_{pp}, were found to vary with depth according to:

$$V_{sp}(z) = 118 + 47z \tag{3.4.5}$$

$$V_{pp}(z) = 450 + 80z \tag{3.4.6}$$

For the shear pulse survey the maximum distance from the source was x_{max} = 20.0 m, which corresponded to a depth of maximum penetration z_{max} = 7.8 m, as from equation 3.3.3. A larger survey range was used for the compression pulse survey with x_{max} = 30.0 m, corresponding to a maximum depth z_{max} = 10.4 m.

From the ratio of the shear pulse velocity to that of the compressional pulse the Rayleigh wave velocities were corrected into shear wave velocities, see section 1.4. This corresponded to an increase in velocity of some 5% so that for the continuous shear wave:

$$V_s(z) = 108.8 + 32.7z \tag{3.4.7}$$

This is shown in figure 3.4.9, where all the velocity profiles obtained for the North Field are reported together. It may be noted how the shear pulse velocity, V_{sp}, is higher than the continuous shear wave velocity, V_s. The ratio of the two varies from about 1.1 at the surface to about 1.4 at a depth of 20.0 m. In addition to the effects of pulse broadening discussed in section 3.1 this may also be due to some effects of anisotropy. The particle motion for the Rayleigh wave is in the vertical plane containing the direction of propagation of the wave, while, for the shear pulse, the particle motion is in a plane which is in the direction of refraction and can be approximated by a horizontal plane.

At the North Field site a direct determination of unit weight was carried out. This gave a value of ρ = 1.85 kg/m^3 at a depth of about 0.50 m. It was assumed that the unit weight was constant with depth and this value was used to convert the shear wave velocity profile into a shear modulus profile using equation 1.4.6. In figure 3.4.10 the continuous line is the profile of shear modulus that is obtained assuming that the shear wave velocity varies linearly with depth according to equation 3.4.7.

The data points represent the values of shear modulus derived directly from the shear wave velocity data.

3.4.2 Canons Park

The Canons Park site is located in Middlesex, some 16 km northwest of central London. The subsoil of this BRE test site had already been subjected to extensive investigations by a number of research workers. The soil profile obtained from a borehole very close to the area where the dynamic surveys took place compared well with a profile from the same site taken from work by Jardine (1985) and shown in figure 3.4.11. The site consists essentially of London Clay with a top layer of gravel to a depth of about 1.0 to 2.0 m. The ground water conditions and the water content and bulk density profiles as determined by Powell (1989) are shown in figure 3.4.12.

Two Rayleigh wave surveys were carried out on the site along two perpendicular directions. After an initial decrease the Rayleigh wave velocity was found to be almost constant from a depth of about 2.0 m downwards, with a value $V_R \approx 140$ ms^{-1}, as shown in figure 3.4.13.

Compression and shear pulse refraction surveys were also carried out at the Canons Park site. The arrival time versus distance plots are shown in figure 3.4.14. Due to the characteristics of the site (shear wave velocity almost constant with depth), the shear pulse refraction was not very successful. The arrival time versus distance data for the shear wave survey show a large scatter about the best fit line. This indicates a variation of shear pulse velocity with depth given by:

$$V_{sp}(z) = 284 + 25z \qquad (3.4.8)$$

with a maximum depth of survey $z_{max} = 3.8$ m obtained for the maximum survey range $x_{max} = 20.0$ m.

The arrival time versus distance data for the compression pulse survey show that after low initial values, the velocity of the compression pulse is practically constant and corresponds quite closely to the speed of sound in water, or about 1500 ms^{-1}. The data were interpreted using a bilinear diagram, as shown in figure 3.4.13. This is the arrival time versus distance plot which corresponds to the case in which the subsoil

consists of two layers with increasing stiffness. The depth to the interface between the two layers can be calculated from the intercept at which the second segment of straight line meets the time axis and, in the present case, represents the depth at which the ground water level is located. From the data shown in figure 3.4.14, this was calculated to be at a depth of about 1.6 m below the surface which is consistent with the data shown in figure 3.4.12.

At the surface Poisson's ratio was calculated from the ratio of the compression pulse to the shear pulse velocity to be $\nu = 0.30$. At larger depths Poisson's ratio was found to increase tending to values closer to $\nu = 0.5$ characteristic of saturated clays. A profile of Poisson's ratio with depth is shown in figure 3.4.15. Based on this profile, the Rayleigh wave velocity data were corrected into shear wave velocities. Using the values of bulk density reported in figure 3.4.12, the shear modulus profile was finally obtained. As shown in figure 3.4.16, the shear modulus was found to be almost constant or perhaps slightly increasing below a depth of about 2 m, in the London clay. An average value for the shear modulus is $G'_{max} \simeq 40$ MPa. Higher values of modulus were obtained in the upper layer of gravel. No attempt was made to fit the shear wave velocity data with any known function and the data points in figure 3.4.16 correspond directly to the shear wave velocity data.

3.4.3 Chattenden

The third site investigated was on London Clay at Chattenden, Kent, about 45 km east of central London. From one borehole close to the area where the seismic surveys took place the London Clay was found to extend from the surface to depths greater than 30 m. As shown in figure 3.4.17, the upper part of the London Clay consists of brown weathered material whilst at depths greater than about 12 m the clay is grey.

Two surface wave surveys were carried out on the Chattenden site close to an area extensively used by research workers from Surrey University for different types of geophysical testing. The results of these surveys, in terms of Rayleigh wave velocity versus depth are shown in figure 3.4.18. One set of results was obtained in the summer of 1989 and another one was obtained in the summer of 1990, using the spectrum analyser technique. In both cases the Rayleigh wave velocity was found

to be almost constant from a depth of about 1.0 m downwards, with some higher values near the surface. However the results of the two surveys are not very consistent with each other, the average value of Rayleigh wave velocity being $V_R \simeq 115$ ms^{-1} in one case and $V_R \simeq 80$ ms^{-1} in the other.

One shear pulse and two compression pulse refraction surveys were carried out at Chattenden. The arrival time versus distance data are shown in figure 3.4.19. From these data the shear pulse velocity was found to vary with depth as:

$$V_R(z) = 118 + 15z \qquad (3.4.9)$$

with a maximum depth of survey $z_{max} = 9.1$ m, corresponding to the maximum range of survey $x_{max} = 30$ m.

Once more, the data from the both the compression pulse surveys show that below a certain depth the compression pulse velocity is constant and equal to the speed of sound in water. From the arrival time versus distance data the ground water table was calculated to be at a depth of about 1.3 m.

A survey of water contents was carried out at Chattenden (Crilly, 1990). Based on this the unit weight profile shown in figure 3.4.20 was obtained and the velocity data converted into a profile of shear modulus with depth following the usual procedure. As shown in figure 3.4.21, the shear modulus was found to be almost constant with depth below about 1.0 m. The values of the shear modulus range between about 15 and 30 MPa. Higher values of modulus were obtained near the surface. Once more, no attempt was made to fit the data with any known function.

3.4.4 Discussion

On the site on boulder clay (North Field) the shear wave velocity was found to increase linearly with depth. This leads to a profile of shear modulus which increases quadratically with depth from a value of about 25 MPa at the surface up to 500 MPa at a depth of 15 m. The error in the shear modulus can be calculated from the error in shear wave velocity ΔV and the error in density. From equation 1.4.6:

$$\Delta G = \Delta\rho + 2\Delta V \qquad (3.4.10)$$

For the North Field the error in the shear wave velocity was $\Delta V = \sigma\% = 6.2\%$ at an average depth of 10.0 m. A full survey of densities was not carried out so the $\Delta\rho$ is not known. Therefore a minimum estimate for the error in shear modulus is $\Delta G = 12.4\%$.

At the North Field site no discontinuities in the velocity profiles and therefore in the modulus profile are observed at the depths corresponding to the transitions between the different layers. With hindsight it is possible to detect a greater scatter of the data points at critical depths for some of the sets of data, see for instance test NFA10COR reported in figure 3.4.22. However, the test results have clearly not provided enough evidence to locate the change of strata. This may be because in a situation where softer layers are underlain by stiffer layers the Rayleigh wave averages out the properties.

On the two sites on London clay the shear wave velocity was found to be almost constant with depth after an initial decrease from higher values. The transition between shallow stiffer layers and deeper softer layers is clearly indicated. At Canons Park this transition seems to correspond to that between the superficial layer of gravel and the top of the London clay, as indicated in the soil profile in figure 3.4.11. At Chattenden the London clay is at the surface and there is no obvious reason why the stiffness values near the surface should be higher than at depth, other than some effect of desiccation, that may create a stiffer layer in the clay near the surface. However, the values of stiffness near the surface are higher than expected. The two surface wave surveys carried out at Chattenden indicated consistent trends of variation of G'_{max} with depth but gave values of moduli that differed by about 50%. During the survey in summer 1990 some problems arose with the specrum analyser, such that it did not always give a zero reading for the phase shift when the two geophones were side by side. Only data where the problem did not occur were included in figure 3.4.21. The data from the survey in summer 1989 were considered to be more reliable and it is this profile of stiffness that will be referred to when comparing laboratory data and in situ data.

The pulse refraction technique is only suitable for situations where the stiffness of the subsoil increases markedly with depth. As a result, the

pulse refraction surveys at both Canons Park and Chattenden, where the shear wave velocity was almost constant with depth, were not very satisfactory and the arrival time versus distance data show a certain scatter around the best fit lines. Because the water table constitutes an interface for the compression wave its position was clearly indicated by the results of the compression pulse refraction surveys at both the Chattenden and Canons Park sites. As expected, the shear pulse was not influenced by the water table because the pore water cannot transmit shear, see section 1.4.

The order of magnitude of the values of stiffness obtained with the techniques outlined above are generally consistent with data from triaxial tests at comparable stress and strain levels (Stallebrass, 1990a; Rampello, 1991). A detailed comparison of the values of stiffness as measured in the field with the results from the laboratory tests carried out as part of the present project will be carried out in chapter 5.

CHAPTER 4 LABORATORY EQUIPMENT AND TESTING PROCEDURES

4.1 Introduction

The laboratory experimental work carried out as part of this research project consisted mostly of triaxial tests on reconstituted samples of fine grained soils of different plasticity. The tests were performed using three hydraulic computer controlled triaxial cells, two of which were modified to incorporate piezoceramic bender elements of the type developed at the Norwegian Geotechnical Institute and at the University College of North Wales, Bangor.

Development of apparatus included both modifications to the triaxial system related to details of the computer control, the analogue to digital conversion and the control of pressures, and, more specifically, the development of the experimental set up for operating the piezoceramic bender elements. The modifications to the triaxial system followed on from work carried out at City University over the last decade on the development of computer aided control systems for triaxial stress path testing. Most of the characteristics of the system were the same as those described elsewhere (Atkinson et al., 1985; Richardson, 1988; Ho, 1988; Pickles, 1989). The sections describing the triaxial apparatus will concentrate on the changes made to the existing system and on some aspects that are particularly relevant to the present project, such as the accuracy of the measurement of axial and volumetric strain.

For the research described in this dissertation, piezoceramic bender elements were incorporated in two triaxial stress path cells so that it was possible to measure the very small strain stiffness of the soil at any stage of a stress path test and compare it directly to shear moduli obtained at higher strain levels.

The bender elements are piezoelectric transducers that can be located at each end of a triaxial specimen which transmit and receive shear wave pulses through the specimen. The test result consists essentially of the time that the shear wave needs to propagate along the length of the triaxial specimen. From this travel time the shear wave velocity, V_s, can be calculated and in turn the shear modulus obtained using the

relationships discussed in section 1.4. The shear wave amplitude is not constant along the sample due to both geometrical and material damping. The maximum shear strain near the transmitter is estimated to be about 0.001% (Dyvick and Madshus, 1985).

In this chapter the experimental techniques used for the dynamic measurement of very small strain stiffness will be described in detail together with the method of interpretation of the test results. In addition to the standard interpretation procedure which is based on the visual inspection of the traces at the transmitter and at the receiver, two alternative techniques, based on the numerical analysis of the traces, will be described.

4.2 The triaxial system

4.2.1 Triaxial cells and instrumentation

All the triaxial tests carried out as part of the research described in this dissertation were conducted using standard hydraulic triaxial cells similar to those described by Bishop and Wesley (1975). The cells were designed to test 38 mm diameter samples. Conventional instrumentation was attached to the cells, as shown in figures 4.2.1 and 4.2.2.

Axial load was measured using a 5 kN load cell manufactured by Wykeham Farrance based on an original design by Surrey University. The load cell was mounted inside the triaxial cell to eliminate inaccuracies in the measurement of axial load due to friction on the shaft and was attached to the top of the sample using a rubber suction cap. Cell water pressure and pore pressure at the base of the sample were measured using two Druck pressure transducers with a measuring range of 0–1000 kPa.

Axial strain was measured externally by means of an LVDT transducer attached to the top of the cell, against a cross head on the ram. In a number of tests the axial strain was also measured internally using Hall effect transducers directly attached to the sample (Clayton et al, 1988). Volumetric strain was measured using a standard 50 cc Imperial College volume gauge fitted with an LVDT of the same type as the one used for the measurement of axial strain.

All transducers were recalibrated every three to four months following standard procedures in use at City University (Lau, 1988; Stallebrass, 1990b). Typical calibration curves for all transducers are given in figures 4.2.3 to 4.2.7. Ideally the calibration curve of a transducer should be linear; in practice the transducers were linear only within certain ranges of the output voltages. Single calibration constants were obtained by optimising the readings within the linear range and these were incorporated into the computer control program. The main characteristics of the transducers used during the experimental work are listed in table 4.2.1.

4.2.2 Control and logging system

Two systems were used to operate the triaxial cells which differed mainly in the type of computer used, in the way in which the analogue to digital conversion was operated and in the system for the control of pressures.

The "BBC" system, shown in figure 4.2.1, has been described in detail before (Pickles, 1989). The system consisted of a BBC microcomputer and a Spectra Micro-ms analogue to digital (A/D) converter which logged and controlled a hydraulic triaxial cell. The Micro-ms carried out the analogue to digital conversion on a 12 bit basis and had up to 32 channels available. In this system the computer controlled a set of relays which operated incremental stepper motors driving electromanostats to regulate cell pressure, back pressure and axial ram pressure. A simple variable time relay (clicker box) was used to operate a stepper motor driving a screw control cylinder or Bishop ram (Bishop and Henkel, 1962) in strain controlled loading.

The "IBM" system was developed as part of the present project, based on previous experience at City University (Taylor and Coop, 1989). The system is shown in figure 4.2.2; it consisted of an IBM-XT compatible personal computer and an Alpha Super Plug-in Multifunction Interface Card manufactured by CIL Electronics Ltd to provide analogue to digital conversion. The card provided A/D and D/A conversion through 8 analogue inputs and 4 analogue outputs. In addition it had 4 relays and 16 logic input-output lines. Conversion of the analogue signal into a digital one was carried out on a 16 bit basis, which resulted in a resolution of about 1 to 32,000 of full scale. The pressures were regulated using

analogue pressure controllers directly operated by the computer through the analogue output channels of the interface card, as described in Viggiani (1990). The stepper motor driving the Bishop ram for strain controlled shearing could be operated either independently of the computer control program, as in the BBC system, or through the relays of the card.

Changing from a BBC microcomputer to an IBM personal computer gave several advantages. The IBM computers represented more up to date technology making them easier to maintain, more reliable and more versatile, particularly with respect to the availability of programming languages. They were also compatible with the other computers used for the analysis of the data.

From the point of view of the A/D conversion the main difference between the two systems was that in the BBC system the Spectra unit would automatically select the gain of its channels to match the signals from the transducers as closely as possible while in the IBM system the channels of the interface card only had one fixed gain selected from three possible values that corresponded to full scale input voltages of ± 10 V, ± 1 V and ± 100 mV. However, in the IBM system, the A/D conversion was performed using a significantly larger number of bits than in the BBC system, so that the resulting resolution of the conversion was in most cases better than the resolution that it was possible to achieve with the BBC system (see tables 4.2.2a and 4.2.2b). Moreover, if maximum resolution was required, it was possible to operate a form of autoranging of the channels through the software as described in Viggiani (1990).

From the point of view of the control of pressures there were several advantages of the IBM over the BBC system, mostly in the quickness and accuracy of the control. The response of the analogue pressure converters to the required changes of pressure was virtually immediate, the only time lag between the signal from the computer and the actual change in pressure being due to the compressibility of the air in the interfaces. In the BBC system any significant change in pressure required some time for the stepper motors to turn the electromanostats to the desired position, thus rendering the operation of the cell much slower. With the analogue pressure converters the control of pressure was potentially as accurate as the resolution of the D/A conversion; the

actual control was limited only by the accuracy with which it was possible to measure the pressures. In the BBC system the accuracy of the control of pressures was limited to the change in pressure that corresponded to 1 step of the stepper motor, about ± 0.4 kPa.

4.2.3 Accuracy and resolution of transducers

The resolution and the accuracy of the transducers that were used during the experimental work is given in tables 4.2.2a and 4.2.2b. The resolution of each channel results from the combination of the gain of that particular channel and the number of bits on which the A/D conversion is operated. For each transducer the accuracy is quoted as an absolute value below which the measurements are not reliable plus a percentage value representing the worst expected error as a percentage of the current reading of the transducer, following the approach adopted by Stallebrass (1990a). The absolute error results from the noise in the output of the transducer while the percentage error represents the sum of drift, hysteresis and non linearity as evaluated during calibration of the transducers. As shown in table 4.2.2b, for the IBM system the resolution of the A/D conversion was always better than the overall accuracy of the transducer so that it was not necessary to carry out the autoranging of the channels, as mentioned in section 4.2.2.

In the IBM system the magnitude of the transducer output did not affect the resolution of the readings as the gain of each channel was fixed, irrespective of the transducer output. On the contrary, the BBC system resolved strains to less than 0.001% when the transducer output was close to zero, but this would drop to as low as 0.01% at higher voltage outputs which corresponded to less sensitive ranges of the A/D converter. Hence, at the beginning of the shearing stages the position of the axial strain and volumetric strain transducers was always adjusted to give a voltage output as close as possible to zero.

4.2.4 Accuracy of the measurement of axial and volumetric strain

Compliance of the triaxial cell and of the load measuring device may cause significant errors in the external measurement of axial strain, as discussed in section 2.2.2. In the arrangement adopted in the present work the expansion of the cell itself did not affect the external

measurement of axial strain because the displacement transducer was attached to the top of the cell and the majority of the axial compliance was due to the deflections of the internal load cell.

External measurements of axial strain were always corrected to allow for system compliance by placing a dummy steel sample in the cell and monitoring the axial strain that occurred under application of a given stress path. Two typical load deflection curves obtained by increasing the axial load at constant cell pressure are shown in figures 4.2.8(a) and (b). The data show that the Surrey University load cell exhibits a relatively stiff behaviour, a typical compliance value being of the order of 2.2×10^{-4} mm/N. Moreover, no sudden jump in the axial deflection measurement is observed around zero axial load and the compliance curve is linear through the origin, as the strain gauged element of the load cell is manufactured in a solid block. The only discontinuity in measured deflection with changing axial load is recorded at higher tensile axial load and is due to slackness in the threads of the load cell mounting. The value of the axial load at which the discontinuity takes place can be calculated from the equilibrium of the load cell shaft and depends on the value of the cell pressure (Viggiani, 1990). The discontinuity is of the order of 0.15 mm and represents the largest part of the axial compliance; it can be eliminated using the simple locking device shown in figure 4.2.9.

The compliance curves are affected by the value of the cell pressure and by the direction of loading. Because all the shearing stages carried out during the present project were conducted at constant values of mean effective stress, sets of compliance data were obtained for each cell with different values of mean effective stress. An example of such a set of data is shown in figure 4.2.10. The data indicate that the system is more compliant at smaller values of mean effective stress, the compliance ranging from about 2.0×10^{-3} mm/N at $p' = 50$ kPa to 1.8×10^{-4} mm/N at $p' = 400$ kPa. It may be useful to recall that, for a 38 mm diameter and 76 mm height sample, 1 mm deflection corresponds to an axial strain of about 1.3% and 1 kN deviatoric load to an axial stress of about 880 kPa. The relation between the compliance of the system and the value of mean effective stress seems to be approximately linear, as shown in figure 4.2.11.

Another common source of systematic error in the external measurements of axial strain, that cannot be eliminated by calibration of the system, is represented by bedding effects due to irregularities and lack of parallelism of the two ends of the sample, see section 2.2.2. In the present work all samples were connected to the load cell at an early stage in the test, prior to the consolidation stages. For soft reconstituted samples, even very small values of axial load were usually sufficient to bed the platens into the sample so that, by the time the test reached the start of the shearing stage additional effects of seating, bedding and tilting were negligible.

A certain number of tests were carried out with Hall effect local axial strain transducers directly attached to the sample. As shown in table 4.2.2b, these transducers were more susceptible to noise and drift than the ordinary axial strain transducers. Figure 4.2.12 shows a comparison between local axial strain measurements and external measurements corrected for compliance, taken from the shearing stage of test RLCD2 on reconstituted London clay. The sample was isotropically compressed to p'= 400 kPa, swelled to p'= 200 kPa and then sheared at constant p'= 200 kPa. Details of the test can be found in section 4.5.3. The data in figure 4.2.12 show that the corrected external and the internal measurements of axial strain are practically the same up to an axial strain ϵ_a = 0.06%, corresponding to a deviatoric load q'= 10 kPa. At strains larger than 0.06% the external measurements were smaller than the average internal strains. It is worth pointing out that the readings of one of the two internal gauges were practically the same as the external corrected readings while the other gauge was measuring rather larger strains, which may indicate some bending of the sample. The difference between the strains measured using the two internal gauges was larger than the difference between external readings and average internal readings. At strains larger than 0.5% the internal gauges run out of their linear range so that the corrected external strains had to be considered in the analysis of the data.

A quite dramatic example of a case in which bedding effects at the beginning of the shearing stage were not negligible is provided by the shearing stage of test ULCD on undisturbed London clay. The sample was sheared to failure at a constant p'= 225 kPa. Details of the test are given in section 4.5.4. The data in figure 4.2.13 show that up to a

deviatoric stress q'≃ 50 kPa the external transducer was reading very large displacements while the internal gauges were registering very small strains on the sample. At deviatoric stresses larger than 50 kPa the stress strain curve defined by the internal gauges and that defined by the external transducer are parallel, indicating that the sample was bedded into the end platens. The reason for such a dramatic bedding effect lies in the procedure adopted to insert the bender elements into the sample. The procedure, which is described in detail in section 4.4.1, resulted in the bender elements not having penetrated into the sample sufficiently for the sample to be fully resting on the end platens. Therefore, when the deviatoric load was raised, the two bender elements cut their way further into the sample, which caused the large external strain measurements.

In general, the corrected external axial strains can be larger or smaller than the internal axial strains according to the relative magnitude of the deflections due to bedding errors and the disparity between the strains in the middle third and the overall strains in the sample. Data by Stallebrass (1990b) also indicate that, whenever reliable compliance measurements can be made, corrected external strain measurements may be more accurate than internal strain measurements carried out using Hall effect transducers. External axial strain measurements for the whole sample also relate better to volume strain measurements made over the whole of the sample, so that, in the calculation of the shear strains it seems more consistent to refer to the corrected external measurements rather than to the internally measured strains.

To obtain reliable volumetric strain measurements it was necessary to maintain a constant back pressure during drained tests, as the calibration of the volume gauge was affected by the value of the back pressure, and to carry out frequent leakage tests. The leakage tests were particularly critical to the present project as, especially at the early stages of equipment development, it proved quite difficult to find a satisfactory method of sealing the holes for the electrical leads to the bender elements and several tests were lost because of water leaking from the cell through the sample into the volume gauge.

4.3 Dynamic equipment

4.3.1 Piezoelectric transducers

Piezoelectricity is the ability of a material to generate a voltage when a mechanical force is applied, or to generate a mechanical force when a voltage is applied. Piezoelectric properties occur naturally in some crystals, such as quartz or tourmaline, and can be induced in some polycristalline ceramics, such as lead zirconate and lead titanate, under application of an intense electric field. Piezoceramic elements can be used very effectively as electromechanical transducers as they can be manufactured in a wide range of shapes and sizes and their electrical and mechanical axes precisely oriented in relation to their shape.

The piezoelectric ceramic used for the present application is a PZT Bimorph manufactured by Vernitron. The piezoceramic element consists of two thin transverse-expander plates bonded together, with conducting surfaces in between them and on the outside. The direction of polarisation is such that, when a driving voltage is applied to the element the two plates deform in opposite directions, i.e. one expands and the other contracts. The resultant force causes the element to bend. Conversely, mechanical bending of the element results in a voltage across the electrodes. Figure 4.3.1 shows the mechanism of deformation of a ceramic bender element. In the bender element test the transducers are located at the two ends of a triaxial specimen. When a driving voltage is applied to one of the elements it bends to one side generating a shear wave that propagates along the sample. The other element, which acts as a receiver, converts the deflection due to the particle motion into an electrical signal, thus detecting the arrival of the shear wave at the other end of the sample.

Two types of Bimorph ceramic are available, which differ in the orientation of the piezoelectric ceramic in the plates. The usual arrangement of the electrical connections for each type is shown in figure 4.3.2. The parallel connected element provides twice the displacement as the series one for the same applied voltage and is therefore preferred as a transmitter, especially when a limited driving voltage is available. On the other hand, a series connected element, which provides twice the voltage as a parallel connected one for the same

applied displacement, is generally preferred as a receiver.

In addition to the standard receiver and standard transmitter a third type of transducer was produced at City University from piezoelectric ceramic of the series type. This was a self monitoring transmitter element, after an idea originally proposed by Schulteiss (1982). The self monitoring transmitter is shown in figure 4.3.3. On one of the external electrodes a groove was formed to isolate a central strip of the conducting surface. The element was excited by applying a voltage across the external electrodes and monitored by reading the voltage generated across the strip and the central electrode, which is electrically independent of the driving voltage.

The first pair of bender elements used during the experimental work were bought from Geonor. The bender elements were already cut to the appropriate size, wired and cased in a waterproof epoxy as described by Dyvick and Madshus (1985). Further elements, including the self monitoring transmitter were produced at City University from relatively large sheets of ceramic obtained by Vernitron. The dimensions of the elements and their shape were kept the same as in the Geonor elements for convenience and are shown in figure 4.3.4.

The sheets of Birmorph ceramic were cut to the size of 10.0 x 13.0 mm using an emery wheel and the electrical leads soldered to the electrodes as required for the different types. The casing was moulded around the elements. Because the bender elements are high impedance devices, contact with water would short the transducers. A good waterproof casing was obtained using a two component araldyte produced by Ciba-Geigy.

The epoxy cased bender elements were mounted in the two triaxial cells that were controlled by the IBM system. This required some modifications to the base pedestal and the top cap, as shown in figure 4.3.5. The bottom of the slots in the base pedestal and top cap were filled with araldyte and the electrical wires passed through the holes. The elements were held in position till the araldyte had cured. The gap between the bender elements and the sides of the holes in the base pedestal and top cap was filled with silicon rubber. The elements were mounted so that a length of about 3.0 mm protruded into the soil as a cantilever. On the base pedestal a porous stone with a slot that corresponded to the bender

element was used. All the wires from the transducers ran into nylon tubes and came out of the cell through pressure proof plugs into its base.

4.3.2 The electronics

The electronics required to operate the bender elements are shown schematically in figure 4.3.6. A Farnell FG1 function generator was used to supply the transmitter with the driving voltage. The signal used to drive the transmitter and the output signal from the receiver were displayed on a Tektronix 2211 50 MHz digital storage oscilloscope. Because the time it takes the shear wave to propagate from one end of the sample to other is very short, typically in the range 0.2 - 0.7 ms, an oscilloscope of high resolution and accuracy was required.

The TEK 2211 is a two channel oscilloscope that can operate either in digital or analogue mode, with a maximum sampling rate of 20×10^6 samples per second per channel. The oscilloscope has digital cursors so that measurements of time delay between characteristic points of the signals can be taken directly off the screen. For better accuracy the traces can be amplified up to 50 times. The traces displayed on the screen can be digitally recorded using 4000 records per channel and stored for further reference. The data recorded by the oscilloscope were transferred to an IBM-AT compatible personal computer via an RS232C serial interface. An external plotter was added to the instrumentation to provide a hard copy of all recorded data.

4.3.3 Calibrations and preliminary checks

The system was calibrated to determine any time delay between the excitation of the transmitter and its response that may be induced by the electronics or by the epoxy casing. For this purpose the receiver was placed directly in contact with the transmitter and the trace from the receiver displayed on the oscilloscope together with the signal used to drive the transmitter. As shown in figure 4.3.7, in these conditions, a time lag of less that 3 μs was found between the two signals. This was considered very satisfactory and, in the standard testing procedure, the signal used to drive the transmitter was also used to trigger the oscilloscope and provide a zero reference time. The response of the

transmitter could be observed directly, once the self-monitoring element was built. Using the self-monitoring transmitter, no time lag was observed between the excitation and the response, and probably the 3 μs time lag recorded in the previous experiment was due more to an imperfect contact between transmitter and receiver than to an actual delay in the response of the transmitter itself.

The possibility of travel paths other than through the soil sample was checked by testing the equipment with no sample on the base pedestal and the cell full of water. In these conditions no arrivals were recorded at the receiver when shear pulses were sent from the transmitter.

Because the bender elements protrude into the soil sample the question arises whether the correct length to use in the calculation of the shear wave velocity is the full length of the sample or this same length minus the protrusion of the bender elements into the specimen, see section 2.2.4.

The potential error in the shear modulus can be calculated from equation 1.4.6. It is:

$$G_{max} = \rho V_s^2 = \rho \frac{L^2}{T^2} \qquad (4.3.1)$$

where L is the length of the travel path and T is the travel time. Hence:

$$\Delta G\% = 2\Delta L\% + 2\Delta T\% \qquad (4.3.2)$$

where ΔL% is the percentage error in the effective length and ΔT% is the percentage error in the arrival time. The typical length of a 38 mm diameter triaxial sample is L = 76 mm. The bender elements protrude 3 mm on each side into the soil sample, so that the maximum uncertainty connected to the choice of the effective length is 6 mm, which corresponds to 7.9% of the length of the sample. Leaving aside the uncertainty connected to the arrival time, which will be discussed in further detail in section 4.6.4, the maximum error in shear modulus deriving only form an incorrect estimate of the effective length is about 15.8%.

As discussed in section 2.2.4, some authors have solved the problem of the definition of the effective length by calibrating the bender element

technique against the results of some other dynamic technique (Divick and Madshus, 1985; Brignoli and Gotti, 1992). In this case a direct calibration was performed in order to define the correct length of travel. A set of reconstituted samples of Speswhite kaolin of different lengths was tested under the same conditions. The length of the sample was plotted against the arrival time, as shown in figure 4.3.8. Each line refers to a different stress state. The data fall on straight lines with an intercept of about 6 mm on the y-axis. This confirms that the shear wave is effectively travelling from the tip of the transmitter to the tip of the receiver element rather than through the full length of the sample. If that had been the case, the data would have fallen on a straight line through the origin. By performing this calibration it was possible to eliminate the uncertainties about the effective length.

4.4 Experimental procedures

4.4.1 Sample preparation

(i) Reconstituted samples

Reconstituted samples were prepared following the procedures commonly used at City University (Richardson, 1988; Ho, 1988) with minor modifications, as outlined below.

In all cases the soil was mixed with de-aired distilled water to form a slurry that was then one dimensionally consolidated in a 38 mm diameter consolidation press. Speswhite kaolin and slate dust were mixed into a slurry starting from dry soil in the form of a powder while London Clay and North Field clay were mixed starting from their natural water content. The water contents of the slurries used for the different soils are given in table 4.4.1. It may be noted that, with the only exception of Speswhite kaolin, the water contents at which the slurries were prepared lie between 1 and 1.5 the liquid limit of the soil following the reccomendations by Burland (1991).

Once the slurry was formed it was put under vacuum for a time long enough to release the air trapped during mixing and then poured into the consolidation press. This was a thick-walled perspex cylinder with top

and bottom pistons with porous stones set into the end faces, as shown in figure 4.4.1. The inner walls of the tube were lightly greased with silicon oil to reduce friction between the pistons and the press and slightly oversized filter papers used on the porous stones to prevent soil from squeezing between the tube and the piston, thus causing jamming of the loading system. All samples were loaded with discrete increments up to a maximum nominal load of 8 kg, which on a 38 mm diameter sample corresponds to about 70 kPa vertical stress. Consolidation was allowed after each load step. The base perspex ring of the press was removed during loading to allow uniform consolidation.

At the end of consolidation the sample was weighed in the perspex cylinder and extruded directly on the base pedestal of the triaxial cell. In most cases no trimming of the ends was required as a measured quantity of slurry, sufficient to produce a sample approximately 76 mm long at the end of consolidation had been poured into the press. The dimensions of the sample were measured once the sample had been extruded on the base pedestal. Because the soil was placed into the cell in a relatively soft state there was no need to create special slots for the bender elements as they easily penetrated into the sample when this was assembled in the triaxial cell.

(ii) undisturbed sample

To obtain the only undisturbed sample of London clay used in the experimental work, the soil was extruded from the U100 sampling tube into a 38 mm diameter brass tube of wall thickness 0.8 mm which corresponds to an area ratio of about 4.25%. The brass tube was clamped rigidly above the centre of the U100 tube and, as the U100 tube was extruded using a hydraulic jack, excess soil was removed with a knife from around the base of the brass tube. Once a sufficient quantity of soil was obtained, the brass tube was removed and the sample extruded in a cradle where it was trimmed to a length of about 76 mm using a wire saw. Care was taken to ensure that the ends of the sample were plane, parallel and perpendicular to the axis of the sample. At this stage slots for the bender elements were formed in both ends of the sample. Because the soil was stiff and slightly fissured, care was taken to prevent the soil from splitting by accident while the slots were formed. In order to ensure good contact between the soil and the bender elements, the slots were cut

slightly undersize and the bender elements forced into the slots when the sample was assembled into the cell. All the operations described above were carried out in a humidity controlled room with a relative humidity of about 80%. The dimensions of the sample were measured when the sample was assembled on the base pedestal.

4.4.2 Setting up the sample and saturation stages

Samples were assembled in the cell following standard procedures in use at City University (Lau, 1988; Ho, 1988), as shown in figure 4.4.2. The samples were provided with filter papers at both ends and standard type (Bishop and Henkel, 1962) side drains to allow all round drainage. The side drains were modified, following Pickles (1989) with a pattern of cuts to make their stiffness negligible either in compression or extension. Both top and bottom filter papers and side drains were dampened before use.

The samples were enclosed in a single membrane sealed against the base pedestal and the top cap using a film of silicon grease and two pairs of 'O'-rings. The membrane was first passed over the sample, then the top cap was inserted and finally the membrane was released on the top cap. Care was taken to ensure that the top bender element was in line with the bottom one. The flexibility of the silicon rubber used to seal the hole for the electrical wires to the top bender element ensured that it was possible to pass the 'O'-rings over the top cap while assembling the sample and then fold the wires sideways to obtain a flat-to-flat contact when the suction cap was screwed to the top platen. The load cell was not connected until after the saturation stages.

At this stage two Hall effect transducers were mounted on opposite sides of the sample as shown in figure 4.4.3, if required. Each transducer consisted of two parts: a pendulum which held two bar magnets suspended to a pad fixed to the sample and the Hall effect semiconductor chip which was inserted in another pad mounted on the sample. The two fixing pads were first glued to the sample, then pinned to the sample through the membrane and finally the membrane was re-sealed using a vulcanising solution. Once the vulcanising solution had set the chip was inserted in the bottom pad and its position adjusted until the required output voltage was obtained.

All reconstituted samples were initially loaded under isotropic conditions by raising the cell pressure to a given value with the drainage valve shut and waiting until the pore pressure in the sample had reached equilibrium. The cell pressure was adjusted undrained until the equilibrium value of the pore pressure in the sample was equal to the pre-set back pressure, generally 100 kPa. The main source of poor saturation of the system was air trapped in the gap between the slot in the porous stone and the bender element, which is necessary for the bender element to be able to move. The drainage lines and the porous stone were therefore completely flushed through to remove the air trapped during setting up. In some cases, to achieve saturation it was necessary to increase the value of the cell pressure until the equilibrium pore pressure in the sample reached 200 kPa and saturate the sample, drained, against a corresponding back-pressure in the volume gauge. It was assumed that the small negative volumetric strains that were observed during the saturation stage were due to air dissolving in the system.

System saturation was checked by observing the pore pressure response to given increments of cell pressure in undrained conditions. The minimum value accepted for Skempton's pore pressure parameter B was 0.98. Once the saturation stages were completed the top of the sample was attached to the internal load cell using a rubber suction cap, following the procedures described by Lau (1988).

4.4.3 Isotropic compression and swelling stages

The majority of the samples were initially isotropically compressed and swelled to different values of mean effective stress and overconsolidation ratio. Because the load cell was always connected to the top of the sample immediately after the saturation stages, the isotropic compression stages were always carried out with simultaneous control of radial and axial stress. Except for a very limited number of stages in which one-step consolidation or swelling occurred, the stress was always varied smoothly. The one-step consolidation or swelling stages were generally carried out to determine values for t_{100}, the time required to complete primary consolidation, for the different soils used in the experimental work. The rates of loading were chosen using the methods described by Cherrill (1990) to minimise excess pore pressures generated in the sample. The loading rates used for the different soils

are given in tables 4.5.3 to 4.5.9.

At the end of each compression or swelling stage, the sample was held at a constant stress state for a time sufficient to complete primary consolidation before starting the following stage. The volumetric strains observed during consolidation indicated that the excess pore pressures generated in the sample were always less than about 9 kPa.

4.4.4 Shearing stages

After the compression stages were completed most samples were sheared to failure, in drained conditions, at a constant value of mean effective stress. The shearing stages were always initially carried out at a constant rate of change of stress and then changed to constant rate of strain, by closing the valve to exclude the air water interface and operating the Bishop ram at a constant speed. Once more, the rates of loading in the stress controlled part of the shearing stages were selected following the methods devised by Cherrill (1990) and are given in tables 4.5.2 to 4.5.5. The change from stress to strain controlled conditions was generally made at a stress ratio $q'/p' \simeq M/2$, where M is the critical state value of the stress ratio. The constant rate of strain was selected to match the rate of strain that the soil had achieved at this point of the test, generally $\dot{\epsilon} \simeq 0.3\%/hr$. At the end of the shearing stages the samples were removed from the cells with the drainage lines shut and a determination of the final water content carried out.

4.4.5 Bender element tests

Each time the soil sample had reached a state at which a reading of very small strain stiffness was required, the current stage of the test was interrupted and the sample allowed to reach equilibrium. The transmitter element was then excited using either a square wave with a frequency of 50 Hz and an amplitude of $\pm$ 10 V, or a single sinusoidal pulse of given frequency, generally in the range 1 to 10 kHz, and an amplitude of $\pm$ 10 V, as will be discussed in further detail in section 4.6.4.

The signal used to drive the transmitter and the signal from the receiver were displayed on the oscilloscope. The signal used to drive the

transmitter was also used to trigger the oscilloscope and provide a zero reference time. A reversal of the input signal corresponded to a reversal of the whole waveform. The repeatability of the received waveform was checked by storing a reference trace and comparing it with subsequent traces. The times corresponding to all the characteristic points of the received signal such as peaks and troughs were measured using the cursors of the oscilloscope and then the traces were transferred to the hard disk of an IBM XT compatible computer for future reference. The oscilloscope was typically set with a record time of 2.0 ms which was long enough to observe the main characteristics of the received pulse. With this setting, the cursors could read the arrival time to an accuracy of about ± 0.5 μs. However, because of noise in the signal, it was only possible to locate the cursors on the characteristic points of the received wave to an accuracy of ± 1.0 μs. For travel times of the order of 0.2 to 0.5 ms this corresponds to an accuracy of the shear modulus of 0.4 to 1.0%.

The time needed to make one measurement of very small strain stiffness using the bender elements was less than a minute, which allowed very closely spaced readings to be taken if required, for instance at the beginning of a consolidation stage. The time required to transfer the traces to the computer was about 5 to 6 minutes, during which the oscilloscope had to be continuously in operation.

4.5 Testing programme

4.5.1 Tested soils

Four types of fine grained soils were used in the experimental work: Speswhite kaolin, London clay from the site in Chattenden, a glacial till from the site in North Field and a powdered slate dust. The index properties and the critical state parameters of the four soils are summarised in table 4.5.1 and 4.5.2, respectively.

The largest number of tests were carried out on reconstituted samples of Speswhite kaolin. This is a commercially available china clay whose mechanical behaviour has been extensively investigated before (among others, see for instance Atkinson et al., 1986). Speswhite kaolin has

a considerably higher value of permeability than most natural clays which allows relatively fast rates of loading to be used without generating high excess pore pressures (Atkinson, 1984). This makes the soil particularly suitable for carrying out a large number of preliminary tests used to assess experimental procedures and to determine the major characteristics of the behaviour.

The London clay was obtained from the site in Chattenden from a borehole close to the area were the dynamic surveys took place (see section 3.4.3). The soil profile at this site has been shown in figure 3.4.17. From the results of the dynamic surveys the water table was estimated to be at about 1.3 m below the surface. Several samples were retrieved from different depths using U100 sampling tubes of wall thickness 4 mm. All the tests on London clay were conducted on reconstituted samples with the exception of test ULCD1 that was tested undisturbed. The sample was taken in the brown London clay at a depth of 6.0 to 6.5 m below the surface.

The third soil that was tested was a clay from the North Field site and, from now onwards, will be referred to as North Field clay. The soil profile at the North Field site has been shown in figure 3.4.3. The soil used for laboratory testing was taken at a depth of 4.5 to 5.0 m below the surface and was a clay with some coarser particles. All tests on North Field clay were conducted on reconstituted samples.

The last soil used in the experimental programme was a powdered slate dust which was obtained by sieving, through a 52 size sieve, material taken from the rolled fill of the Llyn Brianne Reservoir Dam in Wales (Lewin, 1978). This is a Silurian cleaved, blue-grey, cemented silty mudstone. The soil was included in the experimental programme as an example of a fine grained soil of very low plasticity (PI = 11).

4.5.2 Tests on Speswhite kaolin

Three groups of tests were carried out on reconstituted samples of Speswhite kaolin: groups KAOD (5 tests), LSK (10 tests) and KAOS (2 tests). The details of these groups of tests are given in tables 4.5.3 to 4.5.5 and a brief description of the tests is given below.

(i) KAOD (KAOlin Dynamic readings)

All the tests in this group were carried out in the triaxial cells controlled by the 'IBM' system, modified to incorporate bender elements. The basic form of the test consisted of a number of stages of isotropic compression and swelling so that the state of the soil described a regular grid of mean effective stresses and overconsolidation ratios, as shown by the data in figure 5.2.1, extracted from the compression stages of test KAOD2. The maximum confining pressure and the maximum overconsolidation ratio were $p' = 400$ kPa and $R_o \simeq 8$, respectively. Each time the soil reached a state corresponding to an intersection on the grid in figure 5.2.1 the current stage was interrupted and a dynamic reading of very small strain stiffness taken, following the procedures outlined in section 4.4. Each test consisted of up to 15 isotropic compression and swelling stages and needed 4 to 6 weeks to be completed. At the end of the isotropic compression and swelling stages some of the samples were sheared to failure at constant p'. Typically this was carried out with a mean effective stress $p' = 200$ kPa and an overconsolidation ratio $R_o \simeq 2$. The back pressure was kept constant during shearing, typically $u = 100$ kPa. The tests were carried out using samples of significantly different initial heights, to establish the effective length of travel, as described in section 4.3.3.

(ii) LSK (Larger Strains Kaolin)

This group of tests was carried out in the triaxial cell controlled by the BBC system. No dynamic readings of very small strain stiffness were taken. Each sample was isotropically compressed and swelled till its state reached one of the points of the same grid used for the dynamic readings in tests KAOD, see figure 5.2.1, and then sheared to failure at a constant value of p'. Four samples (tests LSK1 to LSK4) were sheared with $R_o = 1$, at increasing values of mean effective stress ($p' = 50$, 100, 200 and 400 kPa). The remaining samples were sheared in overconsolidated conditions ($R_o \simeq 2$, 4 and 8) at the same values of confining pressures ($p' = 50$, 100 and 200 kPa). Details of the tests are given in table 4.5.4.

(iii) KAOS (KAOlin aniSotropic confinement)

The samples in this group of tests were initially isotropically compressed to a p'= 50 kPa and then loaded either by increasing the axial stress smoothly while the radial stress was kept constant, or by increasing the radial stress while keeping the axial stress constant. Successive stages of increasing axial stress and increasing radial stress were alternated to produce the stress paths shown in figures 5.3.2 and 5.3.3. Dynamic readings of very small strain stiffness were taken at characteristic values of stress ratio, σ'_r/σ'_a = 0.50, 0.67, 0.75, 1.00, 1.33, 1.50, 2.

4.5.3 Tests on London clay, North Field clay and slate dust

These tests included three groups: RLC (Reconstituted London Clay, 3 tests), RNF (Reconstituted North Field clay, 2 tests) and SLD (SLate Dust, 2 tests). All tests followed the same stress paths as the tests included in group KAOD and were carried out in the cells controlled by the IBM system, modified to incorporate bender elements. Details of these tests are given in tables 4.5.6 to 4.5.8.

4.5.4 Special tests

The details of the last two tests that comprised the experimental work, tests ULCD (undisturbed London Clay Dynamic) and KAOL (KAOlin Last), are given in table 4.5.9

Test ULCD was the only test in the experimental programme on undisturbed soil. The soil was London clay from the site in Chattenden. In the test the soil was taken to a number of stress states that were considered to be representative of the conditions on site, and dynamic readings of very small strain stiffness taken, as shown schematically in figure 5.5.1. At the end of the compression stages the soil was sheared drained to failure at a constant value of p'= 225 kPa.

Test KAOL, on a reconstituted sample of Speswhite kaolin, consisted of two stages of isotropic compression followed by a stage of shearing to failure at a constant value of p'= 100 kPa. The compression stages were carried out as one step loading followed by consolidation and the value

of very small strain stiffness was monitored during consolidation. Also the very small strain stiffness of the soil was monitored as shearing progressed, as schematically shown in figure 5.3.14.

4.6 Interpretation procedures

4.6.1 Calculation of specific volume, λ and N

The calculation of the specific volume of the soil was based on the volume changes measured during the test and the final specific volume of the sample, measured at the end of the test. The final specific volume was calculated as:

$$v = 1 + w G_s \qquad (4.6.1)$$

where w is the water content of the soil and G_s is the specific gravity of the soil particles. Data from the isotropic compression stages of all the tests on reconstituted samples of Speswhite kaolin are shown in figure 4.6.1. If the measurements in the calculation above are accurate the specific volumes of all the samples should fall on a unique normal compression line. Assuming that the errors in volume strain measurements due to leakage or changing back pressure have been eliminated as described in section 4.2.4, the scatter in the data is caused by inaccuracies in the measurement of sample dimensions and changes in water content of the filter papers or of the sample itself during the final stages of the test. In particular, because the samples were always removed from the cell with the drainage lines shut, any variation in water content at this stage of the test was not recorded by the volume gauge. This may cause inconsistency between the final water content of the sample and the volumetric strains measured during the test.

Average values of λ and N were obtained by fitting a straight line through all the points corresponding to the end of primary consolidation, as shown in figure 4.6.1. In all cases the specific volumes were adjusted so that the calculated specific volume at the end of the compression stage in the test fell on the average isotropic compression line. The adjustment made to the specific volumes ensured that the definition of quantities such as R_o, see section 1.2.2, were consistent between different tests.

4.6.2 Calculation of axial and radial stress and membrane corrections

Axial stress was calculated taking into account the variation of the cross sectional area of the sample, based on the assumption that the specimen deforms as a cylinder with a constant diameter through its height. The current area of the sample is given by:

$$A_c = A_o \frac{1 - \epsilon_v}{1 - \epsilon_a} \qquad (4.6.2)$$

where A_o is the initial area of the sample and ϵ_v and ϵ_a are the current volumetric and axial strain respectively.

The stresses on the sample were corrected to take into account the effect of membrane restraint following the approach used by La Rochelle et al. (1988). A first correcting term derives from the lateral confining pressure that the membrane applies to the sample. This term is a function of the initial stiffness of the membrane and of the initial diameter of the membrane and of the sample. The confining pressure due to the membrane restraint can be calculated as:

$$P_{cm} = 2M_i \frac{D_o - D_m}{D_o D_m} \qquad (4.6.3)$$

where D_o is the initial diameter of the sample, D_m is the initial diameter of the membrane and M_i is the initial tangent modulus of the membrane. With the appropriate values for D_m and M_i, this term is of the order of 0.03 to 1.7 kPa depending on the value of the initial diameter of the sample at the beginning of the shearing stage and it only becomes significant at low cell pressures for very soft soils. The second correcting term is applied to the axial stress. It depends on the stiffness of the membrane and is independent of cell pressure. In the assumption that the cell pressure is high enough to hold the membrane against the sample and no buckling of the membrane occurs, this term can be calculated as:

$$\sigma_{am} = \frac{\pi D_o M \epsilon_a}{A_c} \qquad (4.6.4)$$

where M is the stiffness of the membrane at an average strain of 10%. With the appropriate value for M and typical values of D_o this term, which increases with axial strain, is of the order of 10 kPa at strain levels of about 20%. Once more the correction is more significant for

soft soils tested at low values of confining pressure. The radial and axial stresses were always corrected as follows:

$$\sigma_{rc} = \sigma_r + p_{om} \qquad (4.6.5)$$

$$\sigma_{ac} = \sigma_a - \sigma_{am} \qquad (4.6.6)$$

4.6.3 Calculation of the tangents to the stress-strain curve

As discussed in section 1.2.1, the stress-strain behaviour for all the shearing stages was characterised using the tangent to the deviatoric stress versus shear strain curve at particular shear strain levels. The procedures used to calculate the tangent to the stress-strain curve were different depending on which triaxial system had been used.

Figure 4.6.2a shows the initial part of the stress-strain curve obtained from the shearing stage of test LSK1 on a reconstituted sample of Speswhite kaolin. The sample was isotropically consolidated at p'= 400 kPa and then sheared at constant p'. The test was carried out in the cell controlled by the BBC system. Because of the poor resolution of the load cell the curve shows a typical "stepped" shape, each step corresponding to a $\Delta q' \simeq 1.5$ kPa. Prior to the calculation of the tangent to the stress-strain curve the data from the BBC system were always edited in the manner outlined below. Each set of data points for a given value of deviatoric stress was substituted by a single point with the same deviatoric stress and a shear strain corresponding to the average shear strain of the step, as shown in figure 4.6.2b. A straight line was fitted to overlapping sets of five points and the tangent calculated as the slope of the line. The tangent at each point was taken as the mean slope of three calculated best fit lines. In this way seven points contributed to the definition of the tangent at each point, which corresponds to a stress change $\Delta q' \simeq 7.5$ kPa.

Figure 4.6.3a shows the initial portion of the deviatoric stress versus shear strain curve obtained from tests KAOL, on a reconstituted sample of Speswhite kaolin, carried out in one of the cells controlled by the IBM system. The sample was isotropically compressed to p'= 100 kPa and then sheared at constant p'. This time the stress-strain curve was much smoother and better defined than that obtained by the BBC system and a

very large number of data points were acquired. However, because of scatter in the data, a procedure based on the linear regression of successive sets of five points produced erratic results. Therefore, for the data obtained in the IBM system, the first part of the curve was substituted by multipiece polynomials whose order and extent varied from test to test. In figure 4.6.3b the same data as in figure 4.6.3a are shown together with the best fit fifth order polynomial. At strains larger than about 0.01% the scatter in the data reduced and a linear regression on successive sets of five raw data points could be used again. The combined stiffness versus shear strain curve obtained for the data in figure 4.6.3 is shown in figure 4.6.4. The polynomial fit can be obviously used to obtain stiffnesses down to the origin of loading. However, a reliable limit for the measurement of stiffness is probably about 0.005%.

4.6.4. Operation of the bender elements and definition of the arrival time

The standard procedure used to operate the bender elements was derived from Dyvick and Madshus (1985). The transmitter was excited using a driving square wave with an amplitude of ± 10 V (20 V peak to peak) and a frequency of 50 Hz. The amplitude of the excitation was limited by the necessity of avoiding depolarisation of the ceramic plates. The frequency of the square wave was always sufficiently large that the subsequent step of the wave did not interfere with the decaying received wave generated by the previous step.

The interpretation of the bender element test is based on the identification of the point on the received signal which corresponds to the first arrival of the shear wave. An example of the time record obtained for a reconstituted sample of clay form the North field site is shown in figure 4.6.5. The first deflection of the signal, with a positive polarity, occurs at point 0, where the dotted cursor is located. The signal intensity gradually increases up to point 1, where a sharp reversal of polarity is recorded. After a number of peaks and troughs (points 1, 2, 3, 4 and 5) the signal fades.

It is common practice to locate the first arrival of the shear wave at the point of first deflection of the received signal. However, theoretical studies (Salinero et al., 1986) show that the propagation of

a shear signal is always accompanied by the propagation of another signal of opposite polarity that travels with the velocity of the compressional waves and whose amplitude decays rapidly with the number of wavelengths from the source. This is the first signal to reach the receiver, and depending on the distance between source and receiver it can mask the arrival of the shear wave. Inverting of the polarity of the source does not help in the identification of the shear wave because it produces the reversal of all the components of the signal.

Parametric studies by Mancuso and Vinale (1988) show that, for a distance between source and receiver of 1/4 to 4 wavelengths the near field components carry enough energy to mask the arrival of the shear wave. An estimate of the wavelength of the shear wave generated by the square pulse can be obtained from the ratio of the shear wave velocity and the average frequency of the received signal, $\lambda = V_s/f$. In the example in figure 4.6.5, the distance between transmitter and receiver was calculated to be only 2 or 3 wavelengths and a near field effect may be expected.

Without further analysis it is reasonable to assume that the arrival of the shear wave may correspond to any of points 0 to 3. For the example given in figure 4.6.5, this corresponds to an uncertainty in the arrival time of ± 0.2 ms on an average time of about 0.5 ms. This is an error of ± 40% on the arrival time corresponding to an error of ± 80% on the shear modulus according to equation 4.3.2. This is clearly an unacceptably high value of the error if absolute values of shear modulus are required. However, if the choice of the arrival time is consistent throughout the analysis of the data, this error does not apply to comparisons between shear moduli.

In the present work, despite the fact that a reversal of polarity of the driving signal corresponded to a reversal of polarity of the whole of the received signal, it was assumed that the first arrival of the shear wave corresponded to point 1 rather than to the point of first deflection. The orientation and the polarity of the transducers were always checked prior to testing so as to have an idea about the expected polarity of the received signal. It is believed that the first part of the signal, from point 0 to point 1, may be due to some near-field effect.

In attempt to improve the accuracy of the absolute measurement of shear modulus a different procedure was devised to operate the bender elements. This time, the transmitter was driven using a single sinusoidal pulse of given frequency, rather than a continuous square wave. The amplitude of the pulse was again ± 10 V (20 V peak to peak) while its frequency ranged between 1 and 10 kHz. Different values of frequency were used each time a reading was taken in order to select the optimum value at which the received signal had maximum amplitude. The first interesting observation was that, as the frequency of the pulse used to drive the transmitter was increased, i.e. the number of wavelengths between the source and receiver was increased, the initial deflection of the signal tended to attenuate. This phenomenon had already been observed by Brignoli and Gotti (1992), see figure 4.6.6.

A visual inspection of the traces allows a number of characteristic points of the signal to be recognised and hence it is possible to evaluate the wave travel times. Figure 4.6.7 shows results from a test on the same soil as in figure 4.6.5, this time using a single sinusoidal pulse with a frequency of 5 kHz to drive the transmitter (note that the polarity of the received signal on the screen of the oscilloscope was inverted for convenience, so that a first arrival of the same polarity as the source should be expected). The comparison of the driving signal with the record at the receiver allows a number of characteristic wave points to be recognised, as peaks and troughs, that correspond to each other (points 0 and 0', 1 and 1', 2 and 2'). A certain spreading effect can also be noticed: during propagation the wave has changed its shape increasing the time distances between peaks and troughs. Increasing travel times were obtained for each of the recognisable features of the driving signal to propagate along the length of the sample: t_o = 0.489, t_1 = 0.520 and t_2 = 0.533 ms. It is worth noting that all these travel times are much larger than the arrival time that corresponded to the point of first deflection in figure 4.3.12, t_o = 0.280 ms, and seem to compare better with the travel time corresponding to point 1, t_1 = 0.485 ms.

In addition to the visual analysis of the traces two alternative interpretation procedures were used, based on numerical analysis techniques similar to those described by Mancuso et al. (1989) and originally used for the interpretation of cross-hole tests. The

techniques described below were only developed at an advanced stage of the project. Because at this stage a large number of tests had already been carried out, the new techniques were mainly used to assess the assumptions about the initial part of the received signal, which had been made in the interpretation of the majority of the tests.

Most numerical techniques operate in the frequency domain rather than in the time domain. Their use requires the time domain record to be decomposed into a group of harmonic waves of known frequency and amplitude. A convenient algorithm that can be used for this purpose is the fast Fourier transform (FFT). A computer program was written in FORTRAN77 that would convert the traces acquired at the oscilloscope into a format suited to the FFT algorithm and calculate a number of functions as defined below.

The cross correlation function $CC_{yx}(\tau)$ is a measure of the correlation degree of two signals, X(t) and Y(t), versus the time shift τ imposed to the traces. The analytical expression of the cross correlation function is:

$$CC_{yx} = \lim_{T_r \to \infty} \frac{1}{T_r} \int_{T_r} X(t) \cdot Y(t+\tau)\, dt \qquad (4.6.1)$$

where T_r is the time record.

The linear spectrum $L_x(f)$ of a signal X(t) is a function of frequency and can be calculated as:

$$L_x(f) = FFT\,[X(t)] \qquad (4.6.2)$$

For each frequency the linear spectrum L_x is a vector in the complex field; its magnitude and phase are respectively the amplitude and the phase shift of each of the harmonic components of the signal X(t). The linear spectra of the signals at the transmitter and at the receiver that were shown in the example of figure 4.6.5 are given in figure 4.6.8. The spreading effect observed above can also be recognised in the receiver linear spectrum by the secondary peak in amplitude at lower frequencies. The peaks at higher frequencies represent the noise in the received signal.

The cross power spectrum $G_{yx}(f)$ of two signals X(t) and Y(t) is calculated as the product of the linear spectrum L_x of X(t) versus the complex

conjugate L_y^* of the linear spectrum of Y(t):

$$G_{yx}(f) = L_x(f) \cdot L_y^*(f) \qquad (4.6.3)$$

For each frequency the magnitude and phase of the cross power spectrum are respectively the product of the amplitudes and the phase difference of the components of the two signals at that frequency. From the magnitude of the cross power spectrum it is possible to identify the range of frequencies that are common to both signals. The cross correlation can also be calculated from the cross power spectrum as:

$$CC_{yx}(\tau) = IFFT\ [G_{yx}(f)] \qquad (4.6.4)$$

where IFFT is the inverse fast Fourier transform and $G_{yx}(f)$ is the cross power spectrum of the two signals, as defined above.

A first procedure of analysis was based on the assumption that the time required for the shear wave to propagate from the transmitter element to the receiver was equal to the time shift, τ_{cc}, corresponding to the maximum of equation (4.6.1), where X(t) is the signal at the receiver and Y(t) the driving signal. From a physical point of view τ_{cc} represents the time the whole waveform needs to propagate from one end of the sample to the other. Figure 4.6.9 shows the cross correlation of the signals presented in figure 4.6.7, normalised with respect to its maximum absolute value, $CC_{xy\ max}$. The time shift corresponding to the maximum of the cross correlation function was found to be τ_{cc} = 0.524 ms.

Another interpretation procedure that was used was based on the analysis of the cross power spectrum of the signals at the receiver and at the transmitter. From the cross power spectrum phase, $\Phi(f)$, it is possible to determine the apparent velocity, or phase velocity, for each frequency component:

$$V(f) = \frac{\lambda}{T_r} = \lambda f = 2\pi f \frac{L}{\Phi(f)} \qquad (4.6.5)$$

where λ is the wavelength and L is the distance between transmitter and receiver. A group travel time for a given range of frequencies, t_g, can be defined by linearly interpolating the absolute cross power spectrum phase diagram in that range of frequencies (Bodare and Massarsch, 1984). The cross power spectrum relative to the time records shown in figure 4.6.7 is shown in figure 4.6.10. From the magnitude of the cross power spectrum it is possible to recognise that the range of frequencies that

are common to both received and transmitted signal is between 2 and 7 kHz. The absolute cross power spectrum phase diagram is shown in figure 4.6.11, with the best fit line for the range of frequencies of interest. The group travel time, t_g, is defined as:

$$t_g = \frac{\alpha}{2\pi} \tag{4.6.7}$$

where α is the slope of the line. The group travel time was calculated to be $t_g = 0.530$ ms.

The interpretation procedures outlined in the section above were extensively used since the time of their development. For the North Field clay, the cross correlation time, τ_{cc}, and the group travel time, t_g, were always larger than the arrival time corresponding to point 1 in figure 4.6.5 and always lower than the arrival time corresponding to point 2 in the same figure. The shape of the received signals varied slightly from soil to soil. However, for all the soils used in the experimental work both τ_{cc} and t_g were much larger than the time corresponding to the point of first deflection. This seemed to provide sufficient evidence to support the choice made on the arrival time and to reduce substantially the errors in the absolute values of shear modulus.

CHAPTER 5 TEST RESULTS AND ANALYSIS

5.1 Introduction

The bulk of the experimental work carried out as part of this research project consisted of triaxial tests on reconstituted samples of fine grained soils of different plasticity. The main objectives of the laboratory experimental programme were as follows:

(i) to obtain relationships between the very small strain stiffness of fine grained soils and factors such as state (as described by mean effective stress, deviatoric stress and specific volume) and overall stress history (as described by overconsolidation ratio)

(ii) to assess the influence of the plasticity of the soil on the parameters describing these relationships

(iii) to compare and contrast the major characteristics of the behaviour at very small strains with those observed at larger strains in order to obtain a unifying picture of the stiffness of fine grained soils over an extended range of strains

(iv) to compare the values of stiffness obtained using dynamic techniques on site with those obtained in the laboratory using the bender elements technique.

In order to fulfil the objectives above multi-stage tests on a total of 25 reconstituted samples of fine grained soils of different plasticity and one undisturbed sample of London clay were carried out as summarised in section 4.5.

The programme of tests on reconstituted samples was designed to provide data to understand the basic behaviour of the soil at small and very small strains and was carried out mostly on samples of Speswhite kaolin. At the same time the tests on reconstituted samples of Speswhite kaolin were used to assess the experimental procedures used for the bender elements test and to define the effective length and the travel time, as outlined in sections 4.3.3 and 4.6.4.

The tests on reconstituted samples of soils from the sites where the dynamic surveys were carried out were added to the testing programme both to assess the influence of plasticity on the observed behaviour and to compare directly the laboratory results with the results from site. The powdered slate dust was introduced in the testing programme as an extreme example of a fine grained soil of very low plasticity.

5.2 Dependence of very small strain stiffness on state in isotropic conditions

As discussed in section 2.3.1, several expressions can be found in the literature relating the very small strain stiffness to the state of the soil. This are all of the general form:

$$G'_{max} = f(p', v, R_o) \qquad (5.2.1)$$

where p' may be replaced by some other measure of stress, v represents the volumetric state of the soil and R_o is some measure of the overconsolidation ratio. For reconstituted soils in isotropic conditions the state of the soil is fully defined once any two out of the three parameters p', v and R_o are fixed and one of the three parameters in equation 5.2.1 is therefore redundant. The current stress p' is usually easily determined and the dependence of the very small strain stiffness on state may be put in either of the forms:

$$G'_{max} = f(p', v) \quad \text{or} \quad G'_{max} = f(p', R_o) \qquad (5.2.2)$$

The choice of one or the other parameter, v or R_o, to locate the position of the state of the soil relative to the normal compression line is merely a matter of convenience. It is likely that, for reasons similar to those for which results from tests on sand tend to be normalised with reference to an equivalent specific volume and results from tests on clay tend to be normalised with reference to an equivalent stress (Atkinson and Bransby, 1978) the first representation will be preferred for sands and the second will be preferred for clays. In the analysis that follows the state of the soil in isotropic conditions will be described using the current values of mean effective stress, p', and overconsolidation ratio, Ro, as defined in section 1.2.2.

In order to separate the effects of p' and R_o on the very small strain

stiffness, a basic form of test was devised. As shown in figure 5.2.1, the soil was subjected to a number of cycles of isotropic compression and swelling so that the state of the soil described a regular grid of mean effective stress and overconsolidation ratios. Details of this type of test (KAOD, RLC, RNF and SLD) were given in section 4.5. Every time the soil reached a state corresponding to an intersection on the grid in figure 5.2.1 a dynamic measurement of very small strain stiffness was carried out. Along each line parallel to the normal compression line, R_o is a constant and the variation of very small strain stiffness with mean effective stress can be examined. Also, along a constant p' line, the effect of different overconsolidation ratios can be examined.

A typical set of data, from test KAOD4, is plotted in figure 5.2.2 as G'_{max} versus p'. The data clearly indicate that the very small strain stiffness increases with increasing mean effective stress, although not in a linear fashion, and that the very small strain stiffness increases with overconsolidation ratio, the values of G'_{max} on an unloading reloading loop being larger than the values of G'_{max} on first loading, at the same value of mean effective stress.

In the following two sections the variation of the very small strain stiffness with mean effective stress and overconsolidation ratio will be explored in more detail with reference to typical data from four independent tests on reconstituted samples of Speswhite kaolin (tests KAOD3, KAOD4, KAOD6 and KAOD7). Tests KAOD1 and KAOD5 were lost because of leakages through the holes for the wires to the bender elements, as discussed in section 4.2.4. The results from test KAOD2 which was one of the first tests carried out with new equipment were disregarded because of the poor quality of the trace at the receiver which made it difficult to locate the shear wave arrival times with confidence.

5.2.1 Dependence of G'_{max} on p'

The variation of very small strain stiffness with mean effective stress for Speswhite kaolin is examined in figure 5.2.3, using data from test KAOD7. In this figure all the values of G'_{max} corresponding to normally consolidated states (R_o = 1) are plotted as the logarithm of G'_{max}/p_r versus the logarithm of p'/p_r. In order to make the relationship between shear modulus and mean effective stress dimensionless, see section 2.3.1,

both the shear modulus and the mean effective stress were normalised with respect to a reference pressure p_r = 1 kPa. As shown in the figure, all the data fall very close to a single straight line given by:

$$\log\left[\frac{G'_{max}}{p_r}\right] = a + n \log\left[\frac{p'}{p_r}\right] \qquad (5.2.3)$$

where a = 3.32 and n = 0.65.

Equation 5.2.3 is equivalent to the power law:

$$\left[\frac{G'_{max}}{p_r}\right] = A\left[\frac{p'}{p_r}\right]^n \qquad (5.2.4)$$

where $A = 10^a = 2088$. Coefficients A and n in equation 5.2.4 are both dimensionless and will be referred to as the pressure multiplier and the pressure exponent, respectively.

Values for the constants A and n in equation 5.2.4 were determined for each test using a linear regression curve fitting method. The results obtained for the four tests are summarised in table 5.2.1. The values of n determined for each of the tests are practically the same and the small differences between the values of A between one test and another can be attributed to experimental scatter. The overall values for the coefficients A and n for Speswhite kaolin, obtained by fitting a single straight line through all the available data were A = 1964 and n = 0.65.

The values of G'_{max} corresponding to overconsolidated states (nominal R_o = 2, 4 and 8) are plotted together with the values of G'_{max} corresponding to normally consolidated states in figure 5.2.4, once again using data from test KAOD7. The readings corresponding to overconsolidated states lie somewhat above the line defined by the readings corresponding to R_o = 1, but, for each value of R_o, they seem to fall on a straight line parallel to the one for normally consolidated states.

In figures 5.2.5 and 5.2.6 the logarithm of G'_{max}/p_r is plotted against the logarithm of p'/p_r for a nominal overconsolidation ratio R_o = 2 and R_o = 4, respectively. Each set of data falls on a straight line whose slope represents the exponent of pressure at that particular overconsolidation ratio. The values of n obtained by fitting straight lines through all the available data at constant values of R_o are plotted

against R_o in figure 5.2.7. Despite some experimental scatter, the data in figure 5.2.7 indicate that, at least for a nominal $R_o \leq 4$, the exponent of pressure does not depend on R_o. Based on the data presented so far it is not possible to make any statements on the independence of n on R_o at values of R_o larger than 4, because only one value of G'_{max} was obtained at $R_o = 8$ in each test and always at the same value of mean effective stress, $p' = 50$ kPa. However, data from test ULCD on undisturbed London clay from Chattenden, confirm the independence of the exponent of pressure on R_o at overconsolidation ratios as large as about 40, see section 5.5.1.

5.2.2 Dependence of G'_{max} on R_o

As discussed in section 2.3.2, data available in the literature indicate that, at relatively large strains, the normalised stiffness, G'/p', at a particular strain level increases linearly with the logarithm of the overconsolidation ratio (Little and Atkinson, 1988). Wroth et al. (1979), reinterpreting data by Webb (1967), expressed the dependence of shear modulus on overconsolidation ratio in the form:

$$\left(\frac{G'}{p'}\right) = \left(\frac{G'}{p'}\right)_{nc} [\, 1 + c \ln R_o \,] \qquad (5.2.5)$$

where $(G'/p')_{nc}$ is the normalised shear modulus in a normally consolidated state, assumed to be constant for a given clay and c is another constant.

The dependence of G'_{max} on overconsolidation ratio was explored by assuming that, in analogy with that which holds at larger strains, it is possible to express the very small strain stiffness in an overconsolidated state as:

$$\left(\frac{G'_{max}}{p'^n}\right) = \left(\frac{G'_{max}}{p'^n}\right)_{nc} [\, 1 + b \log R_o \,] \qquad (5.2.6)$$

or:

$$G'_{max} = (G'_{max})_{nc} [\, 1 + b \log R_o \,] \qquad (5.2.7)$$

where b is a constant. An alternative way of expressing the dependence of very small strain stiffness on overconsolidation ratiowhich is very common in the literature of soil dynamics (Hardin and Drnevich, 1972b) is by using a power law of the type:

$$\left[\frac{G'_{max}}{p_r}\right] = A \left[\frac{p'}{p_r}\right]^n R_o^m \qquad (5.2.8)$$

This type of expression has been proposed recently by Wroth and Houlsby (1991). This is taken to apply also at strains larger than those associated with dynamic tests, mainly because of the convenience of dealing with simple power functions, when trying to relate the stiffness of the soil to other properties, such as the undrained shear strength, see section 2.3.2.

Figure 5.2.8 shows the variation of R_o^m with $\log R_o$, for different values of m. For values of m between 0.2 and 0.4 and for R_o less than 10 the relation between R_o^m and the logarithm of R_o is approximately linear so that, as pointed out by Wroth and Houlsby (1991), it is reasonable to expect that the same data that supported equation 5.2.6 or 5.2.7 would be consistent with equation 5.2.8.

The variation of very small strain stiffness with overconsolidation ratio is examined in figure 5.2.9. In this figure the values of G'_{max} normalised by the values of $(G'_{max})_{nc}$ predicted by equation 5.2.4 are plotted against the logarithm of R_o. Despite some experimental scatter, the data define a single straight line whose slope, determined using a linear regression curve fitting method, represents coefficient b in equation 5.2.7. The overall value determined for Speswhite kaolin was $b = 0.51$.

In figure 5.2.10 the same data as in figure 5.2.9 are plotted as the logarithm of G'_{max} normalised with respect to $(G'_{max})_{nc}$ versus the logarithm of R_o. Once again the data fall quite close to a single straight line, whose slope represents the exponent of overconsolidation ratio in equation 5.2.8. The overall value of the exponent of R_o for Speswhite kaolin was found to be $m = 0.20$.

5.3. Effect of stress anisotropy on very small strain stiffness

It is generally assumed (Bishop and Henkel, 1962) that in the triaxial apparatus the axial direction and the radial direction are directions of

principal stress. When the sample is loaded in compression the axial stress is larger than the radial stress, $\sigma_a > \sigma_r$, and consequently $\sigma_a = \sigma_1$ and $\sigma_r = \sigma_2 = \sigma_3$. When the sample is loaded in extension the radial stress is larger than the axial stress, $\sigma_r > \sigma_a$, so that $\sigma_r = \sigma_1 = \sigma_2$ and $\sigma_a = \sigma_3$.

During the bender element test the transmitter piezoceramic element bends to one side, generating a shear wave that propagates vertically along the sample, as illustrated in the diagram in figure 5.3.1. Therefore, the axial effective stress is always the stress in the direction of wave propagation. Two more characteristic directions can be identified. The first one, orthogonal to the bender element, is the direction of particle motion and the second, parallel to the bender element, is the direction out of the plane of vibration. In the triaxial apparatus only axial stress and radial stress can be varied independently. This implies that the stress in the direction of particle motion is always equal to the stress in the out-of-plane direction and it is not possible to separate the effects of these two stresses on the very small strain stiffness of the soil.

Two alternative ways of expressing the dependence of the very small strain stiffness on an anisotropic state of confinement can be envisaged. A first possibility, which emphasizes the role played by the individual stresses, is that of writing:

$$\left(\frac{G'_{max}}{p_r}\right) = A \left(\frac{\sigma'_a}{p_r}\right)^{n_a} \left(\frac{\sigma'_r}{p_r}\right)^{n_r} \qquad (5.3.1)$$

where A, n_a and n_r are three dimensionless constants. Alternatively the effect of the stress ratio may be included in an equation similar to equation 5.2.4 and the very small strain stiffness in anisotropic conditions written as:

$$\left(\frac{G'_{max}}{p_r}\right) = A \left(\frac{p'}{p_r}\right)^{n} \eta^{n_\eta} \qquad (5.3.2)$$

where $\eta = q'/p'$ and n_η is a constant. It may be worth pointing out that, in the special case of isotropic conditions, $\sigma_a' = \sigma_r' = p'$ and, consequently, $n = n_a + n_r$ but this is not necessarily so for the general case, where $\sigma_a' \neq \sigma_r'$.

In this section the effects of an anisotropic state of confinement on the very small strain stiffness will be examined with reference to the results from two tests on reconstituted samples of Speswhite kaolin (tests KAOS1 and KAOS2). Details of the tests were given in section 4.5.2. The stress paths followed by the soil in the two tests are shown in figures 5.3.2 and 5.3.3, which show the stress paths followed by the two tests with different axes. During the first stages of isotropic compression and shear (in compression for tests KAOS1 and in extension for test KAOS2) the stress paths followed by the soil continuously expanded the state boundary surface, so that R_o was always equal to 1. During some subsequent stages of shear and recompression, the stress paths may have been directed just inside the state boundary surface so that, strictly, R_o was slightly greater than 1. However, because the mean effective stress was always increasing during the tests, the state of the soil was never very far from the state boundary surface, and for all practical purposes the soil can be considered to be normally consolidated throughout all stages of each test.

5.3.1 Influence of σ_a' and σ_r' on G'_{max}

The dependence of the very small strain stiffness on axial stress and radial stress will be examined first with reference to the data from test KAOS1, in which $\sigma_a' > \sigma_r'$ (compression).

In figure 5.3.4 the logarithm of G'_{max}/p_r is plotted against the logarithm of σ_a'/p_r for all the stages in which the radial stress was kept constant. Consistent with equation 5.3.1, in order to make the relationship between shear modulus and axial stress dimensionless, both G'_{max} and σ_a' were normalised with respect to a reference pressure p_r = 1 kPa. Under the stress ratios applied ($k = \sigma_r'/\sigma_a'$ = 1/2, 2/3 and 1) the very small strain stiffness increased with increasing axial stress for all the values of constant radial stress (σ_r = 50, 100 and 200 kPa). For each value of constant radial stress a linear relationship was found to exist between the logarithm of G'_{max} and the logarithm of σ_a'. The exponent of axial stress in equation 5.3.1, n_a, can be obtained as the slope of the log G'_{max} vs log σ_a' plot. From the data in figure 5.3.4, values of n_a were found to be n_a = 0.39, 0.35 and 0.33 for σ_r' = 50, 100 and 200 kPa respectively.

To examine whether the value of σ_r' affected the exponent of axial stress the values of n_a obtained at different values of radial stress were plotted against the radial stress, as shown in figure 5.3.5. The data indicate that the exponent of axial stress, n_a, is essentially independent of the radial stress (if anything it slightly decreases with increasing radial stress). The average value of the exponent of axial stress was found to be $n_a = 0.36$.

In figure 5.3.6 the dependence of the very small strain stiffness on radial stress is examined, again using data from test KAOS1. In this figure the logarithm of G'_{max}/p_r is plotted against the logarithm of σ_r'/p_r, for all the stages in which the axial stress was kept constant. Both G'_{max} and σ_r' were normalised with respect to the reference pressure $p_r = 1$ kPa. The data show that, under all the stress ratios applied ($k = \sigma_r'/\sigma_a' = 1/2$, 3/4 and 1) G'_{max} increased with increasing radial stress for all the values of constant axial stress ($\sigma_a' = 100$, 200 and 400 kPa). A linear relationship was found to exist between the logarithm of G'_{max} and the logarithm of σ_r' for each value of constant axial stress, so that the exponent of radial stress, n_r, to be used in equation 5.3.1, could be obtained from the slope of the log G'_{max} vs log σ_r' plot.

The values of n_r obtained at different values of axial stress were plotted against the axial stress, as shown in figure 5.3.7. The data indicate that the exponent of radial stress is essentially independent of the axial stress applied to the soil, at least for the range of stress ratios under examination ($1/2 < k < 1$). This is the same conclusion as for the exponent of axial stress, n_a. An average value of n_r for Speswhite kaolin was found to be $n_r = 0.28$.

It is interesting to notice that, for test KAOS1, the exponent of the axial stress and the exponent of radial stress were found to be similar to each other, with the exponent n_a being only slightly larger than the exponent n_r. This indicates that, in triaxial compression, the very small strain stiffness depends about equally on the stress in the direction of wave propagation and on the lateral stress, which is consistent with the data by Ni (1987), presented in section 2.4.2. However, the data from test KAOS2, in which the stress state was always $\sigma_r' > \sigma_a'$ (extension), do not support this finding.

The results obtained from test KAOS2 are shown in figure 5.3.8 and 5.3.9. Once more, for all the stress ratios examined ($k = \sigma_r'/\sigma_a' = 1$, 4/3, 3/2 and 2) the very small strain stiffness was found to increase with axial stress for all the values of constant radial stress ($\sigma_r' = 100$, 200 and 400 kPa) and to increase with radial stress for all the values of constant axial stress ($\sigma_a' = 50$, 100 and 200 kPa). A linear relationship was found to exist between the logarithm of G'_{max} and the logarithm of σ_a' and between the logarithm of G'_{max} and the logarithm of σ_r'. The values of n_a and n_r obtained from the data in figures 5.3.8 and 5.3.9, however, are very different from the values of n_a and n_r obtained from the data from test KAOS1. In particular $n_a = 0.17$, 0.17 and 0.25 for $\sigma_r' = 100$, 200 and 400 kPa, respectively and $n_r = 0.41$, 0.52 and 0.43, for $\sigma_a' = 50$, 100 and 200 kPa, respectively. Average values for n_a and n_r from the data from test KAOS2 are $n_a = 0.20$ and $n_r = 0.45$.

5.3.2 Dependence of G'_{max} on p' and η

In figure 5.3.10 and 5.3.11 all the data from tests KAOS1 and KAOS2, respectively, are replotted as the logarithm of G'_{max} versus the logarithm of p', both normalised by the reference pressure $p_r = 1$ kPa. Under all the stress ratios applied ($\eta = q'/p' = -0.60$, -0.38, -0.27, 0, 0.3, 0.43 and 0.75) the very small strain shear modulus was found to increase with the mean effective stress. Irrespective of the value of η all the data from each test consistently locate a single straight line in the log G'_{max} vs log p' plane, whose slope represents the coefficient n in equation 5.3.2. Values of n for both tests KAOS1 and KAOS2 were found to be $n = 0.66$. It is interesting to notice that the exponent of mean effective stress obtained from the tests in anisotropic conditions of confinement is practically the same as the exponent of mean effective stress that was found in isotropic conditions, $n = 0.65$.

In figure 5.3.12 the logarithm of G'_{max} normalised with respect to the value of G'_{max} in isotropic conditions at the same mean effective stress is plotted against the logarithm of η. The data fall very close to a horizontal line, which demonstrates that the exponent of η is $n_\eta = 0$, or, in other words, that the stress ratio has a negligible effect on the very small strain stiffness. It is interesting to note that, both for test KAOS1 and test KAOS2 the values of n_a and n_r given in section 5.3.1 give $n_a + n_r \simeq n$.

The data obtained in the present research project seem to indicate that under anisotropic conditions of confinement the very small strain stiffness depends on the mean effective stress p' rather than on the individual stresses σ_a' and σ_r'. In all the stages of test KAOS2 which were run at constant radial stress the logarithm of p' was not changing as much as in the corresponding stages of test KAOS1, see figures 5.3.10 and 5.3.11 which is why the modulus was not changing as much. Also the data presented in the previous section seem to indicate that the exponents n_a and n_r are not constant but vary significantly with the particular stress path that is followed so that, strictly, equation 5.3.1 does not hold unless a stress path is specified.

The linear relationships between the logarithm of G'_{max} and the logarithm of p' defined by the data from tests KAOS1 and KAOS2 are compared with the linear relationship between the logarithm of G'_{max} and the logarithm of p' defined by the data from the group of tests KAOD in isotropic conditions in figure 5.3.13. Despite a certain experimental scatter between different tests the data from tests KAOS1 and KAOS2 cannot be distinguished from the data from the group of tests KAOD both in terms of pressure exponent, n, and of pressure multiplier A.

5.3.3 Monitoring G'_{max} during shear

Another set of data which seem to confirm the independence of the very small strain stiffness from the stress ratio was obtained from the shearing stage of test KAOL, on a reconstituted sample of Speswhite kaolin. The sample was isotropically compressed to p'= 100 kPa and then sheared to failure at constant p'= 100 kPa. Details of the test were given in section 4.5.3.

As shearing progressed the very small strain stiffness of the soil was monitored up to a maximum stress ratio $\eta = q'/p' = 0.45$, as shown in figure 5.3.14. In figure 5.3.15, the tangent to the deviatoric stress shear strain curve obtained from the constant p' shearing stage is plotted versus the logarithm of the shear strain. The data describe the usual s-shaped curve of decay of stiffness with shear strain amplitude indicating that the behaviour of the soil is highly non-linear in the strain range $0.001\% < \epsilon_s < 0.1\%$.

In the same figure the values of G'_{max} obtained from the bender elements as shearing progressed are plotted for comparison. The data indicate that the very small strain shear modulus reduces from a maximum of about 42 MPa at the beginning of shearing to a minimum of about 40 MPa when the overall shear strain has reached 0.1%. This is a variation of only 5% and may well be due to small excess pore pressures during shear which would slightly reduce the value of p' below that calculated from the pore pressures measured at the base of the sample.

5.4 Behaviour of soils other than Speswhite kaolin at very small strains

In this section the dependence on state of the very small strain stiffness of three fine grained soils of different plasticity will be examined. The data used will be from tests RLC, RNF and SLD on reconstituted samples of London clay, North Field clay and slate dust, respectively. Details of the tests were given in section 4.5.3. All the tests included in this group were of the same type as the tests included in group KAOD and were devised to isolate the effects of mean effective stress and overconsolidation ratio on the very small strain stiffness of the soil in isotropic conditions. No tests in anisotropic conditions of confinement were conducted on soils other than Speswhite kaolin.

5.4.1 Dependence of G'_{max} on state

The dependence of the very small strain stiffness on mean effective stress is examined in figures 5.4.1 to 5.4.3, for London clay, North Field clay and slate dust, respectively. In these figures the values of G'_{max} are plotted against the logarithm of p'. (Consistent with equation 5.2.4, both the shear modulus and the mean effective stress were normalised with respect to a reference pressure p_r = 1 kPa).

In all cases, the readings corresponding to normally consolidated states (R_o = 1) fall very close to a straight line of equation:

$$\left[\frac{G'_{max}}{p_r}\right] = A \left[\frac{p'}{p_r}\right]^n \qquad (5.4.1)$$

where A and n are two dimensionless constants. Values for the parameters A and n obtained for the different soils are summarised in table 5.4.1, where in all cases $n < 1$.

The points corresponding to overconsolidated states lie somewhat above the lines for normally consolidated states, but, as already observed for Speswhite kaolin, for each value of R_o, they fall on a line parallel to the line corresponding to normally consolidated states. This confirms that, in all cases, the exponent of mean effective stress does not depend on overconsolidation ratio.

The values of G'_{max}, normalised with respect to $(G'_{max})_{nc}$ as predicted by equation 5.4.1, are plotted against the logarithm of R_o in figures 5.4.4 to 5.4.6 for London clay, North Field clay and slate dust, respectively. In all cases the data fall on a straight line of equation:

$$\frac{G'_{max}}{(G'_{max})_{nc}} = [\, 1 + b \log R_o \,] \qquad (5.4.2)$$

where b is a dimensionless constant. The logarithm of G'_{max}, normalised on $(G'_{max})_{nc}$ is plotted against the logarithm of R_o in figures 5.4.7 to 5.4.9. In all cases the data locate a straight line through the origin of equation:

$$G'_{max} = G'_{max_{nc}} R_o^m \qquad (5.4.3)$$

where m is a dimensionless constant. The values of b and m obtained for the different soils are listed in table 5.4.1.

5.4.2 Dependence of the parameters A, n, b and m on the plasticity of the soil

The values of the pressure multiplier, A, and the pressure exponent, n, obtained for the different soils are plotted against the plasticity index of the soil in figures 5.4.10 and 5.4.11, respectively. The data are compared with other data available in the literature.

The general trend indicated by the data available in the literature is that of a decrease of A and an increase of n with increasing plasticity. Both the trends appear reasonable. A less plastic clay would be expected to be stiffer than a more plastic clay at the same mean effective stress

and overconsolidation ratio, and so would have a higher stiffness multiplier. Also, the plasticity of a soil is a measure of the slope of its normal compression line, so the specific volume of a more plastic clay would decrease more than that of a less plastic clay for the same increase in applied mean effective stress. Hence, one would expect that the shear modulus increase would be greater, i.e. the pressure exponent would be greater.

As shown in figures 5.4.10 and 5.4.11, the data produced in the present research project, fall more or less within the general trends indicated in the literature. However the results are scattered and the data do not confirm conclusively that the factor on which the parameters A and n depend is the plasticity index of the soil alone. Work reviewed in section 2.3.1 indicated that the Young's modulus of the soil particles may have an influence on the overall stiffness of the aggregate of particles and it was suggested that the use of this parameter to render non-dimensional the relationship between stiffness and mean effective stress may have the effect of reducing the variability of the multiplier of the mean effective stress. It is likely that other factors such as the mineralogy or the shape of the particles may have a comparable effect on the values taken by n and A and that the plasticity index on its own is not sufficient to characterise the soil fully. Further work is needed in this area to establish more clearly the relationship between the nature of the soil and the values taken by parameters A and n.

Very few data are available in the literature about the exponent of overconsolidation ratio m or coefficient b in equations 5.2.7 and 5.2.8. The values obtained in the present work are plotted against plasticity index in figure 5.4.12 and 5.4.13, respectively. The values of the overconsolidation exponent, m, were found to be in the range $0.2 < m < 0.3$ and the values of b were found to be in the range $0.5 < b < 0.8$. Both parameters increase slightly with the plasticity index of the soil.

5.5 Behaviour of undisturbed London clay

In this section the results from test ULCD on an undisturbed sample of London clay will be presented and compared with those obtained from the tests on reconstituted samples of the same soil. The London clay was

taken from the site at Chattenden at a depth of 6.0 to 6.5 m below ground level. In the test the soil was taken to a number of stress states that were considered representative of the stress conditions on site and dynamic readings of very small strain stiffness taken, as shown in figure 5.5.1. Details of the test were given in section 4.5.4.

The state of the soil in the v:lnp' plane is shown in figure 5.5.2. In the same figure the normal compression line obtained from the tests on reconstituted samples is also shown. The states of the soil lie well inside the normal compression line demonstrating that the soil is heavily overconsolidated. The overconsolidation ratio of the soil, R_o, was calculated consistently with the definition given in section 1.2.1, with reference to the normal compression line defined by the reconstituted samples. It must be noted that for overconsolidated soils and stress states below the preconsolidation pressure, p'_{max}, a change of mean effective stress corresponds to a simultaneous change of R_o, and therefore the effects of p' and R_o cannot be conveniently isolated as for the tests on reconstituted samples.

5.5.1 Dependence of G'_{max} on p'

The dependence of G'_{max} on mean effective stress for the sample of undisturbed London clay is examined in figure 5.5.3, where the logarithm of G'_{max} normalised by the reference pressure p_r = 1 kPa is plotted versus the logarithm of p'/p_r. The data fall on a straight line of equation:

$$\frac{G'_{max}}{p_r} = A' \left(\frac{p'}{p_r}\right)^{n'} \qquad (5.5.1)$$

The value of the exponent of pressure obtained with a linear regression curve fitting method is n' = 0.50 which is much smaller than the value of the exponent of pressure n = 0.76 obtained from the reconstituted samples of London clay. This is hardly surprising if one considers that the soil under test is overconsolidated and that an increase of mean effective stress corresponds to a decrease of R_o. As a first approximation one may express the overconsolidation ratio as p'_{max}/p'. If the dependence of G'_{max} on mean effective stress and overconsolidation ratio can still be expressed using a relationship of the type of equation 5.2.8, then:

$$\frac{G'_{max}}{p_r} = A\left(\frac{p'}{p_r}\right)^n \left(\frac{p'_{max}}{p'}\right)^m = A\left(\frac{p'_{max}}{p_r}\right)^m \left(\frac{p'}{p_r}\right)^{n-m} \qquad (5.5.2)$$

From the comparison of equations 5.5.1 and 5.5.2 it is obvious that $A' = A(p'_{max}/p_r)^m$ and $n' = n - m$. The values of n and m that were obtained from the results of the tests on reconstituted samples were $n = 0.76$ and $m = 0.25$, which gives a value of $n - m = 0.51$, which is in fact very close to the value of n' obtained from the data. It may be noted that the value of $n - m$ for London clay also compares quite well with the values indicated by Weiler (1988) and Silvestri (1991) for other natural clays of medium to high plasticity.

In figure 5.5.4 the logarithm of $G'_{max}/(p_r R_o^m)$ is plotted against the logarithm of p'/p_r. When plotted in this fashion all the readings fall on a single straight line of equation:

$$\frac{G'_{max}}{p_r R_o^m} = A\left(\frac{p'}{p_r}\right)^n \qquad (5.5.3)$$

where the values of A and n obtained with a linear regression curve fitting method are $A = 400$ and $n = 0.80$. In the same figure the line which describes the dependence of G'_{max} on mean effective stress for normal consolidated samples in isotropic conditions of confinement, as obtained from the tests on reconstituted samples, is shown for comparison. The two lines are practically the same which demonstrates that the same relationships which applies for reconstituted samples holds also for undisturbed samples and that, as already observed for Speswhite kaolin, see section 5.3, an anisotropic state of confinement does not affect significantly the values of G'_{max} at the same mean effective stress. The data also indirectly confirm the independence of the exponent of pressure, n, at overconsolidation ratios of about 40.

5.5.2 Dependence of G'_{max} on Ro

In figure 5.5.5 the logarithm of G'_{max} normalised by the values of $(G'_{max})_{nc}$ as predicted by equation 5.4.1 with the values of A and n appropriate to London clay, is plotted against the logarithm of the overconsolidation ratio, R_o. In the same figure all the data obtained from the reconstituted samples of London clay are reported for comparison. The data fall very close to a single straight line of

equation:

$$\frac{G'_{max}}{G'_{max_{nc}}} = R_o^m \qquad (5.5.4)$$

whose slope represents coefficient m, or the exponent of R_o. Once again the data from the undisturbed sample are practically indistinguishable from the data obtained from the reconstituted samples which further confirms the independence of the exponent of pressure on the overconsolidation ratio.

In figure 5.5.6 the values of G'_{max} normalised with respect to the values of $(G'_{max})_{nc}$ as predicted by equation 5.4.1 are plotted against the logarithm of the overconsolidation ratio. The data from the tests on reconstituted samples are reported for comparison. Up to an R_o of about 18 the data from the test on undisturbed London clay fall on the same straight line as the data from the tests on reconstituted London clay:

$$\frac{G'_{max}}{G'_{max_{nc}}} = 1 + b\log R_o \qquad (5.5.5)$$

However, at larger values of R_o the data from the test on undisturbed London clay deviate from the straight line. This indicates that the dependence of small strain stiffness on overconsolidation ratio is better expressed by a power law of the type 5.2.8, which seems to hold even at relatively large values of R_o.

5.6 Comparison between laboratory and field results

In this section the comparison between field data and laboratory data will be carried out with reference to the site at Chattenden, on London clay. Only two profiles of very small strain stiffness with depth were obtained at the site in Chattenden using the surface wave technique, as described in section 3.4. The main reason for selecting this particular site rather than the North field site, where a larger number of dynamic surveys were carried out is that the geology of the ground at Chattenden is much more uniform than the geology of the ground at North field which makes an estimate of the stress conditions in the field more straightforward.

Based on the results of the laboratory tests the relationship found to describe the dependence of the very small strain stiffness of the soil on state in isotropic conditions is given by:

$$\left[\frac{G'_{max}}{p_r}\right] = A\left[\frac{p'}{p_r}\right]^n R_o^m \qquad (5.6.1)$$

where, for London clay, A = 407, n = 0.76 and m = 0.25. In the previous section this relationship was shown to hold also for undisturbed London clay.

No tests with anisotropic conditions of confinement were carried out on reconstituted samples of London clay. However, based on the results of tests KAOS1 and KAOS2, on reconstituted samples of Speswhite Kaolin, see section 5.3, and on the results from the test on undisturbed London clay, the assumption was made that the very small strain stiffness of the soil is essentially independent of stress ratio.

5.6.1 Stress state in situ

In order to compare the values of G'_{max} predicted by equation 5.6.1 with those obtained from the field dynamic surveys a knowledge of the stress state and the stress history in situ are required. In general, the vertical and horizontal effective stresses at a depth z below the ground surface can be written as:

$$\sigma'_v = \gamma z - u \qquad (5.6.2)$$

$$\sigma'_h = K_o \sigma'_v \qquad (5.6.3)$$

where γ is the average unit weight of the overlying material, u is the pore pressure at the depth under examination and, by definition, K_o is the coefficient of earth pressure at rest.

At Chattenden the vertical effective stress, σ_v', can be readily determined from the density measurements reported in figure 3.4.20 and a knowledge of the position of the ground water table at a depth of about 1.3 m below the surface, see section 3.4. The assumption is made that at least in the few first meters below the ground water table the distribution of porewater pressure is hydrostatic. No specific data on the depth of overburden removed by erosion or on the values of K_o at

Chattenden was found in previous work nor produced as part of the present work. It is obvious that, without a knowledge of the overconsolidation ratio and of the values of K_o the stress state of the soil cannot be completely defined, nor can a profile of very small strain stiffness be defined on the basis of equation 5.6.1.

An estimate of the reduction of vertical effective stress due to erosion was obtained from Skempton (1961). The site examined by Skempton was a site at Bradwell, Essex, about 50 km northeast of central London, whose geology resembles very closely the geology at Chattenden. Based on geological data and oedometer tests, Skempton estimated a reduction of the vertical effective stress due to erosion of about 1500 kPa.

There are two possible ways in which the stress state in situ may be evaluated. The simplest option is that of assuming that K_o is constant with depth. This is no more than a very rough estimate of the stress state of the ground but can be used very quickly to assess whether the values of G'_{max} obtained in situ compare with those obtained in the laboratory. Also, by considering different values of K_o (K_o = 1, 1.5, 2 and 2.5) the sensitivity of the prediction of the shear modulus profile to a variation of K_o and hence the importance a correct evaluation of K_o can be assessed. However, because of the non realistic assumption on the variation of K_o with depth (K_o = constant) it can be hardly expected that the shape of the variation of G'_{max} with depth predicted by equation 5.6.1 would match very closely that obtained in situ.

A slightly more complex option is that of trying to obtain the most realistic prediction of the variation of K_o with depth, starting from the few available data. Once an estimate of the maximum overburden is made, it is possible to derive the profile of OCR = $\sigma_v'_{max}/\sigma_v'$ with depth for the site, as shown in figure 5.6.1. Values of K_o at different values of OCR can be determined following the method proposed by Wroth (1975).

The method is based on the results of oedometer tests carried out in a modified oedometer with an instrumented confining ring. Figure 5.6.2a shows diagrammatically the results of a cycle of one-dimensional loading and unloading in the β:lnA plane. (Parameters β and A are defined in the same figure). The calculation of the coefficient of earth pressure at rest at a particular OCR $(K_o)_{oc}$ is carried out by solving by trial and

error the following equation, which represents the unload path 2–3 in figure 5.6.2a:

$$\beta_{oc} = \beta_{nc} + \frac{1}{m} \ln A \qquad (5.6.4)$$

where $\beta_{oc} = 3[1-(K_o)_{oc}]/[1+2(K_o)_{oc}]$, $\beta_{nc} = 3[1-(K_o)_{nc}]/[1+2(K_o)_{nc}]$, $A = [1+2(K_o)oc]/\{OCR[1+2(K_o)nc]\}$ and a value for m can be obtained from the data in figure 5.6.2b.

An approximate value of the coefficient of earth pressure at rest in normally consolidated conditions can be obtained from the semi-empirical expression given by Jaky (1944):

$$(k_o)_{nc} = 1 - \sin \phi' \qquad (5.6.5)$$

The value of ϕ' for the London clay at Chattenden was obtained from the constant p' shearing stages of tests RLC2, RLC3 and ULCD. The stress paths in the q':p' plane and the plots of stress ratio versus shear strain for these three tests are shown in figures 5.6.3 and 5.6.4, respectively. From the data in the figures a value of M = 0.90 was calculated which corresponds to $\phi' = 23°$ and $K_o = 0.62$.

The profile of K_o which was obtained with this method is shown in figure 5.6.5. It may be noticed that the values of K_o calculated following the method outlined above are not less than 1.7. The profile of K_o obtained with this method compares quite well with other profiles of K_o obtained for London clay using different methods (Stallebrass, 1990a).

5.6.2 Profiles of very small strain stiffness with depth

The profiles of very small strain stiffness predicted by equation 5.6.1 with the assumption that K_o is constant with depth are shown in figure 5.6.6 for different values of K_o. The discontinutity in the curve corresponds to the position of the ground water table. In the same figure, the profiles of G'_{max} obtained from the site dynamic surveys are shown for comparison. It is worth noting that the values of very small strain stiffness predicted on the basis of the laboratory results are not dramatically influenced by the value of K_o. However, the predicted increase in shear modulus with depth is more marked than that observed in situ. This is probably due to the assumption that K_o is constant with depth and the variation of G'_{max} with depth would be less marked if K_o was

allowed to reduce with depth.

In figure 5.6.7 the values of G'_{max} predicted by equation 5.6.1 with the assumption that K_o varies with depth as in figure 5.6.5 are compared with the results of the site dynamic survey. The calculations were carried out using a reduction of vertical effective stress due to erosion $\Delta\sigma_v'$ = 1000, 1500 and 2000 kPa. Once again the value of the maximum overburden did not affect the prediction significantly. The increase of very small strain stiffness with depth is less marked than in the previous case where K_o was assumed to be constant with depth.

The absolute values of very small strain stiffness obtained from laboratory tests are about 20% less than the values obtained in situ in summer 1989. This may be explained by effects of ageing, see sections 2.4.2 and 2.4.3. However, it must be noted that there is a significant uncertainty both in the values predicted from the laboratory results, because of the uncertainties in the in situ stress state and history, and in the in situ values,as the two surveys were not consistent with each other.

5.7 Stiffness of Speswhite kaolin at small strains

In this section the dependence of stiffness on state at relatively larger strains will be examined based on the results of 10 triaxial tests on reconstituted samples of Speswhite kaolin (group of tests LSK).

Almost all of the tests on reconstituted samples of Speswhite kaolin that were carried out in the two cells modified to incorporate piezoceramic bender elements included a stage in which the soil was sheared to failure at a constant value of mean effective stress. However, partly because of the low rate of success of the tests at the early stages of equipment development and partly because the tests were designed primarily to investigate the behaviour of the soil at very small strains, the data obtained from these tests did not provide enough information to compare the main features of the behaviour at relatively larger strains with those observed at very small strains. For this reason, parallel to further dynamic testing on reconstituted samples of soils of different plasticity, a programme of tests was started on reconstituted samples of

Speswhite kaolin in an ordinary stress path triaxial cell. Details of this group of tests can be found in section 4.5.2.

The programme of tests was designed to explore the dependence of the stiffness of the soil at small strains on the same factors that had proved relevant to the behaviour at very small strains. In particular, the dependence of the exponent of pressure on shear strain amplitude and the dependence of the stiffness of the soil on overconsolidation ratio at strains larger than those associated with the bender elements test were examined.

5.7.1 Dependence of G' on p'

Figure 5.7.1 shows the stress paths for a set of three undrained triaxial compression tests on reconstituted samples of a glacial till (Little and Atkinson, 1988). The contours of equal axial strain are approximately radial through the origin which indicates that, at least for the strain level at which the measurements were taken, the stiffness increases linearly with the mean effective stress, p'. As discussed in section 2.3, this idea is a common feature of many models derived in the framework of critical state soil mechanics. However, at very small strains, equations have been proposed (Hardin, 1978, Wroth and Houlsby, 1985) in which the stiffness depends on the stress raised to a power n ≠ 1. As discussed in section 2.3.1, these equations are based on a combination of elements from the theoretical elastic stress strain relations by Rowe (1971) with the empirical equations for the initial tangent modulus by Janbu (1963) and Hardin and Black (1968). Test results indicate that values of n are typically in the range 0.5 to 0.9. The data presented so far also show that, for all the fine grained soils that were examined in the present research, the very small strain stiffness depends on the stress raised to an exponent $n < 1$.

The dependence of stiffness on mean effective stress throughout the whole range of strain from the start of loading to close to failure for normally consolidated states ($R_o = 1$) will be examined by assuming that, in analogy with that which holds at very small strains, it is possible to write:

$$\frac{G'}{p_r} = A \left[\frac{p'}{p_r}\right]^n \qquad (5.7.1)$$

where coefficients A and n depend on shear strain amplitude.

The tangent stiffnesses obtained from four tests on reconstituted samples of Speswhite kaolin (tests LSK1 through LSK4) are plotted against the logarithm of the shear strain in figure 5.7.2. Values of stiffness were extracted from these data at different shear strain levels and plotted as the logarithm of G' against the logarithm of p', as shown in figure 5.7.3. (Consistent with equation 5.7.1 both the shear modulus and the mean effective stress were normalised with respect to a reference pressure p_r = 1 kPa). Each set of data falls on a straight line whose inclination and whose intercept with the log G' axis (at p'= 1 kPa) represent respectively the exponent of pressure, n, and the logarithm of the pressure multiplier, A, at that particular strain level. The line obtained from the dynamic readings for Speswhite kaolin is also shown in the figure for comparison. As the shear strain amplitude increases the stiffness of the soil decreases and the slope of the constant shear strain line increases.

In figure 5.7.4 the values of A obtained at different shear strain levels are plotted against the logarithm of the shear strain amplitude. The values of the pressure multiplier decay very rapidly from about 500 at a strain amplitude ϵ_s = 0.005% to about 100 at a strain amplitude ϵ_s = 0.05%, demonstrating the highly non-linear behaviour of the soil over this range of strains. The value of A obtained from the dynamic reading is also reported in figure 5.7.4 and associated to shear strain amplitudes $\epsilon_s < 0.001\%$. The value of A at very small strains seems not to link in with the data obtained at larger strain levels but to be slightly large. On this point, it must be noted that, particularly for the values of A, which is a measure of the magnitude of the shear modulus at a given mean effecive stress and overconsolidation ratio, some effect of stress path rotation may be hidden in the data. Dynamic tests correspond to a complete reversal of the stress path, i.e. to a rotation of the stress path θ = 180°. The experimental data produced at larger strain levels correspond to stress path rotations θ = -90°, for all the normally consolidated samples and θ = 90° for all the overconsolidated samples. Data available in the literature, presented in section 2.3.2, indicate that the values of stiffness corresponding to a 180° rotation

are higher than the values of stiffness for ±90° rotations, which are generally comparable with each other.

The variation of the exponent of pressure n with shear strain amplitude is examined in figure 5.7.5 where the values of n are plotted against the logarithm of the shear strain. At a shear strain ϵ_s = 0.005%, which corresponds to the lower limit at which reliable measurements of stiffness could be made in the triaxial apparatus, the exponent of pressure is n = 0.72, just above the value observed in the dynamic tests. As the shear strain increases the exponent gradually increases. At a strain level ϵ_s = 0.05% the exponent of pressure is n ≃ 0.95; a value of n = 1 would indicate that the stress strain response is dominated by frictional behaviour.

5.7.2 Contours of equal shear strain

Figure 5.7.6 shows a detail of the initial portion of the stress paths for the four shearing stages of tests LSK1 through LSK4 in the q':p' plane. Note that the scales used for the deviatoric stress and the mean effective stress are very different in order to magnify the start of shearing. In the same figure contours of equal shear strain are reported from a shear strain ϵ_s = 0.005% to a shear strain ϵ_s = 0.1%. The information contained in the contours of equal shear strain is indirect evidence of the variation of the shear modulus with the mean effective stress. It is evident that, at least at the small strains considered in the figure, the contours of equal shear strain are not radial through the origin.

In figure 5.7.7 the secant stiffnesses obtained from tests LSK1 through LSK4 are plotted against the logarithm of the shear strain. In the same way as for the tangent stiffnesses in section 5.7.1, values of secant stiffness were extracted from the data in figure 5.7.7 at different shear strain amplitudes and plotted as the logarithm of G'_{sec} versus the logarithm of p', as shown in figure 5.7.8. Once again, each set of data falls on a straight line of equation:

$$\frac{G'_{sec}}{p_r} = A \left[\frac{p'}{p_r}\right]^n \qquad (5.7.2)$$

where coefficients A and n depend on shear strain amplitude. The variation of A and n with shear strain amplitude are shown in figures

5.7.9 and 5.7.10, respectively.

The shape of the equal shear strain contours may be deduced as follows:

$$\frac{q'}{p_r} = 3\,\frac{G'_{sec}}{p_r}\,\epsilon_s = 3\,A\left[\frac{p'}{p_r}\right]^n \epsilon_s \qquad (5.7.3)$$

In this way, for ϵ_s equal to a constant, the deviatoric stress q' is proportional to the mean effective stress raised to a power $n \neq 1$.

In figure 5.7.11 the equal shear strain contours predicted by equation 5.7.3 are compared with the experimental data that were already shown in figure 5.7.6. The quantitative agreement between the experimental data and the predicted contours is hardly surprising since the values of the parameters A and n were obtained from the same data that are shown in the figure. However, the shape of the predicted shear strain contours is of some relevance. Consistent with the pattern shown by the experimental data, the contours of equal shear strain predicted by equation 5.7.3 are not straight lines through the origin but are curved. As the shear strain amplitude increases the exponent of pressure, n, tends to 1 and the shear strain contours become straighter and closer to straight lines through the origin, which is the pattern indicated by the experimental data.

5.7.3 Dependence of G' on R_o

As discussed in section 2.3.2, data available in the literature indicate that the normalised stiffness G'/p' at a particular strain level increases linearly with the logarithm of the overconsolidation ratio (Little and Atkinson, 1988; Wroth et al., 1979). In figure 5.7.12 the tangent stiffnesses obtained from a set of six tests on overconsolidated samples of Speswhite kaolin (tests LSK5 through LSK10) are plotted against the logarithm of the shear strain.

Values of stiffness at given shear strain amplitudes were extracted from the data in figure 5.7.12. For each strain level the stiffness was normalised with respect to the mean effective stress raised to the appropriate exponent and plotted against the logarithm of R_o, as shown in figure 5.7.13. Each set of data fall on a straight line of equation:

$$\frac{G'}{p'^n} = A\,[1 + b\,\log R_o] \qquad (5.7.3)$$

As the shear strain amplitude increases the coefficient A decreases while the coefficient b increases with increasing shear strain, as shown in figure 5.7.16, where the values of b obtained at the different shear strain amplitudes are plotted against the logarithm of the shear strain. The value of b varies from about 0.86 at a shear strain $\epsilon_s = 0.05\%$ to about 1.42 at a shear strain $\epsilon_s = 0.5\%$. Both values are higher than the value of b obtained from dynamic tests.

For a direct comparison with the behaviour observed at very small strains using dynamic techniques, all data are plotted as G'/Ap'^n against the logarithm of R_o in figure 5.7.14. When plotted in this fashion all the data fall on lines which have intercept 1 at $R_o = 1$. The data from the dynamic tests lie somewhat below those obtained from the triaxial tests, indicating that the dependence of stiffness on overconsolidation ratio is less marked at very small strains than it is for larger strain levels.

Finally, the stiffnesses obtained at different shear strain amplitudes in overconsolidated states, normalised by the stiffness predicted by equation 5.7.1 at the appropriate strain level, are plotted against R_o on a double logarithmic scale, in figure 5.7.15. For each strain level all the data fall on straight lines through the origin whose slope represents the coefficient m in:

$$\frac{G'}{A\,p'^n} = R_o^m \qquad (5.7.4)$$

The values of m vary from about 0.30 at a shear strain $\epsilon_s = 0.05\%$ to about 0.44 at a shear strain $\epsilon_s = 0.5\%$, as shown in figure 5.7.17. The data obtained from the dynamic tests are also included in the figure for comparison. Once again, the data from the dynamic tests lie below the data obtained from the constant p' shearing stages demonstrating that the dependence of stiffness on overconsolidation ratio is less marked at very small strains than at relatively larger strains.

CHAPTER 6 SUMMARY AND CONCLUSIONS

6.1 Experimental techniques

The stiffness of soils at very small strains (ϵ_s = 0.001% and less) can be obtained from the measurement of the velocity of propagation of elastic waves, see section 1.4. As part of the present project dynamic measurements of the very small strain stiffness of fine grained soils were carried out both in the laboratory, using piezoceramic bender elements of the type developed at the Norwegian Geotechnical Institute and at the University College of North Wales, and in situ, using surface wave techniques.

6.1.1 Laboratory experimental techniques

For the research described in this dissertation piezoceramic bender elements were incorporated in two computer controlled stress path triaxial cells so that it was possible to measure the very small strain stiffness of the soil at any stage of a triaxial stress path test and compare it directly to shear moduli obtained at higher strain levels. In other words, the combined use of dynamic and static techniques made it possible to measure directly the stiffness of soils over the whole range of strains, from very small to large, on the same specimen of soil.

The electronics required to run the test proved to be simple and inexpensive, especially when compared to those required by other dynamic testing techniques, see section 4.3.2. Also the interpretation of the test is much simpler and more direct than in other dynamic testing techniques and requires only the length of travel and the travel time for the shear wave to be determined, see section 4.4.5. A direct calibration of the system was carried out to determine the correct length of travel to be used in the calculation of the shear wave velocity, see section 4.3.3.

Some preliminary work, based on numerical analysis of the signal used to drive the transmitter and the signal from the receiver element, was carried out to improve the definition of the arrival time of the shear wave. It was shown that the cross correlation and the group velocity

analyses can be used to reduce substantially the error in the shear modulus caused by the uncertainty in the identification of the arrival of the shear wave, see section 4.6.4. A major drawback of these analyses was that the received signal was correlated to the input driving signal, which may or may not represent correctly the actual vibration of the transmitter element. Further work in this area may involve the combined use of the self-monitoring transmitter element and the numerical analysis techniques outlined in section 4.6.4..

6.1.2 Field experimental techniques

Dynamic measurements of very small strain stiffness were carried out in situ using the Rayleigh wave technique. Provided that an inversion procedure is established to convert curves of shear wave velocity versus frequency into curves of shear wave velocity versus depth, see section 3.2, the Rayleigh wave technique can be used to obtain profiles of very small strain stiffness with depth from the surface, without having to form any holes in the ground.

Different experimental configurations were used to measure the time delay on passage of the Rayleigh waves between a pair of geophones, including the use of a spectrum analyser and of a filter and a correlator. The results from the various experimental techniques compared well with each other.

6.2 Stiffness of fine grained soils at very small strains

The stress-strain characteristics of soils are highly non-linear even at relatively small strains. However, there is a region at very small strains where the behaviour of the soil is approximately linear elastic and the shear modulus takes a constant maximum value, G'_{max}. For most soils the threshold strain beyond which the stress-strain response of the soil becomes apparently non-linear lies between 0.001% and 0.01% depending on plasticity, higher values being observed for more plastic clays, see section 1.3.

The values of the very small strain stiffness of soils depend on stress state and history. Several semi-empirical expressions can be found in

the literature relating the very small strain stiffness to the state of the soil, see section 2.3. Most of them are of the general form:

$$G'_{max} = f(p', v, R_o) \qquad (6.2.1)$$

However, only two parameters out of p', v and R_o are required to describe fully the state of a reconstituted clay in isotropic conditions of confinement. In these conditions the dependence of the very small strain stiffness on stress state and history can be conveniently expressed in the form:

$$\frac{G'_{max}}{p_r} = A \left[\frac{p'}{p_r}\right]^n R_o^m \qquad (6.2.2)$$

where p_r is a reference pressure introduced to render the relationship between shear modulus and mean effective stress non-dimensional and A, n and m are material properties, see section 5.4.1. The values of A, n and m seem to be related to the plasticity of the soil. In particular, A was found to decrease and n and m were found to increase with increasing plasticity, see section 5.4.2. Although these trends are confirmed by data available in the literature it does not seem that the plasticity index alone can fully account for the variation of the coefficients in equation 6.2.2. Other factors that may affect the values taken by A,n and m are the mineralogy of the soil and the shape of its particles.

Experimental results from tests on Speswhite kaolin indicate that the very small strain stiffness of fine grained soils is not significantly affected by an initial anisotropic state of confinement, at least for stress ratios in the range $\eta' = -0.60$ to $\eta' = 0.75$, that is for stress states relatively far from failure, see section 5.3. Hence, equation 6.2.2 also adequately describes the dependence of the very small strain stiffness of soils on state for anisotropic conditions of confinement.

Conversely, an expression that relates the very small strain stiffness of normally consolidated soils in anisotropic conditions of confinement to the individual stresses:

$$\frac{G'_{max}}{p_r} = A \left[\frac{\sigma'_a}{p_r}\right]^{n_a} \left[\frac{\sigma'_r}{p_r}\right]^{n_r} \qquad (6.2.3)$$

was shown not to describe the experimental results adequately because the

exponent n_a and n_r in equation 6.2.3 varied with the imposed stress path. However, both for triaxial compression ($\sigma_a' > \sigma_r'$) and triaxial extension ($\sigma_a' < \sigma_r'$) the sum of the two exponents was the same and equal to the exponent of mean effective stress in equation 6.2.2, $n_a + n_r \simeq n$.

The same expression as given in equation 6.2.2 derived for reconstituted samples with a maximum $R_o \simeq 8$, was shown to hold for undisturbed samples even at R_o as large as about 40. For overconsolidated soils and stress states below the preconsolidation pressure, p'_{max}, a change of mean effective stress corresponds to a simultaneous change of R_o. In particular, an increase of mean effective stress results in a decrease of R_o. If this is not explicitly taken into account the dependence of very small strain stiffness on mean effective stress for heavily overconsolidated soils is apparently less marked than for normally consolidated soils. In other words the data from overconsolidated soils can still be interpreted using a power law of the type:

$$\frac{G'_{max}}{p_r} = A' \left[\frac{p'}{p_r}\right]^{n'} \qquad (6.2.4)$$

but the pressure multiplier A' is larger than the pressure multiplier A in equation 6.2.2 and the pressure exponent n' is smaller than the pressure exponent. Simple algebra can be used to show that $n' = n - m$ and $A' = A\ p'_{max}{}^{m}\ p_r{}^{2n-m}$, see section 5.5.

6.3 Stiffness of fine grained soils at small strains

At strains larger than about 0.001% the stress strain behaviour of soils becomes increasingly non-linear and the shear stiffness decreases markedly with shear strain amplitude, reducing by a factor of ten over about the first 1% strain. At a given strain amplitude the stiffness of soils depends on stress state and history, see sections 1.3 and 2.3.2.

The results from tests on reconstituted samples of Speswhite kaolin indicate that the dependence of the stiffness of fine grained soils on state and history can still be conveniently expressed in the form:

$$\frac{G'}{p_r} = A \left[\frac{p'}{p_r}\right]^{n} R_o^{m} \qquad (6.3.1)$$

where p_r is once again a reference pressure introduced to render the

relationship between shear modulus and mean effective stress non-dimensional but, this time, A, n and m depend on shear strain amplitude, see section 5.7.

The pressure multiplier A was found to reduce by a factor of about 3 over the strain range ϵ_s = 0.005% to ϵ_s = 0.05% which indicates that the behaviour of the soil is highly non-linear. Over the same range of strains the pressure exponent n was found to increase from about 0.70, which is just above the value obtained in the dynamic tests n = 0.65, to about 1, indicating that the stress-strain response is then dominated by frictional behaviour, see section 2.3. The coefficient m was found to increase from about 0.30 at a shear strain amplitude ϵ_s = 0.05% to about 0.44 at a shear strain amplitude ϵ_s = 0.5%. Both values are higher than the value obtained from dynamic tests m = 0.20 which indicates that the dependence of the stiffness of soils on overconsolidation ratio increases as the shear strain amplitude increases.

6.4 Comparison between values of stiffness obtained from laboratory and in situ tests

Profiles of very small strain stiffness with depth were obtained on three clayey sites in and around London using surface wave techniques, see chapter 3. For the site at Chattenden, on London clay, a detailed comparison was carried out between the values of very small strain stiffness obtained in the laboratory and in situ.

Based on the results of laboratory tests on both reconstituted and undisturbed samples of London clay the relationship found to describe the dependence of the very small strain stiffness of the soil on state is given by:

$$\left(\frac{G'_{max}}{p_r}\right) = A \left(\frac{p'}{p_r}\right)^n R_o^m \qquad (6.4.1)$$

where A = 407, n = 0.76 and m = 0.25.

Using reasonable assumptions about the stress state and history in situ the trend of variation of G'_{max} with depth predicted by equation 6.4.1 compares well with that obtained from the field seismic surveys, see

section 5.6.2. The values of G'_{max} predicted on the basis of the laboratory results were found to be about 20% less than the in situ values. But it is not easy to compare the results quantitatively because of the unceratinties in both the sets of data, see section 5.6.2.

6.5 Implications of the research

At strains less than the elastic threshold strain ($\epsilon_s \simeq 0.001\%$) the shear modulus of fine grained soils has been shown to depend on the current value of mean effective stress and on the overconsolidation ratio as:

$$\frac{G'_{max}}{p_r} = A \left(\frac{p'}{p_r}\right)^n R_o^m \qquad (6.5.1)$$

where A, n and m are material properties.

Expressions similar to equation 6.5.1 may be used in conjunction with elasto-plastic kinematic hardening models to provide a more realistic description of the variation of the elastic moduli with stress state and history, often neglected in these models, see sections 1.3 and 2.3.2. However, the observed dependence of the elastic shear modulus on the current value of the mean effective stress gives rise to a conceptual problem. It has been noted that the assumption of a pressure dependent elastic shear modulus is not thermodynamically correct unless the elastic bulk modulus is allowed to depend to a certain extent on the current value of the deviatoric stress (Zytinski et al., 1978). No data were produced as part of the present project to examine the dependence of the elastic bulk modulus on stress state and history, but the available experimental evidence seems to indicate that there is little or no dependence of the bulk modulus on the shear stress.

At strains larger than the elastic threshold strain ($\epsilon_s \simeq 0.001\%$) the dependence of soil stiffness on stress state and history can still be put in the form:

$$\frac{G'_{max}}{p_r} = A \left(\frac{p'}{p_r}\right)^n R_o^m \qquad (6.5.2)$$

but this time A, n and m depend on shear strain amplitude.

For equation 6.5.2 to have any practical use in numerical modelling

specific functions must be fitted to the experimental data describing the variation of A, n and m with the shear strain amplitude. These function could be used to describe the non-linearity of soil behaviour inside the state boundary surface with the advantage of implicitly containing the dependence of stiffness on stress state and history. The behaviour on the state boundary surface could still be represented by classical elasto-plastic models such as, for instance, Modified Cam-clay.

An approach similar to the one outlined above to describe the non-linearity of soil behaviour inside the state boundary surface is essentially empirical and has all the drawbacks of non-linear elastic models, see section 1.3. In particular it requires test data to be produced by following appropriate stress paths. It must be noted that the experimental data produced as part of the present project were obtained following consistent stress paths. The stress path rotation at the beginning of the shearing stage was $\theta = -90°$ for all the normally consolidated samples and $\theta = 90°$ for all the overconsolidated samples, see section 5.7.1. Different stress path rotations will affect the values taken by the coefficients in equation 6.5.2 and particularly the values taken by coefficient A, which is a measure of the magnitude of the shear modulus at a given mean effective stress and overconsolidation ratio.

6.6 Limitations of the work

The main limitations of the laboratory work undertaken as part of the research described in this dissertation were as follows:

(i) The experimental work included only tests on reconstituted samples with the sole exception of test ULCD on an undisturbed sample of London clay from the site at Chattenden.

(ii) Because of the limitations of the apparatus only a relatively small range of confining pressures were applied to the soil ($p' = 50 - 600$kPa). For reconstituted samples this resulted in a maximum R_o of about 8, while for the undisturbed sample this meant that it was not possible to reach the range of normal consolidation.

(iii) A limited number of fine grained soils were examined with a limited range of plasticities (PI = 11 - 41%). In particular no fine grained soils of very high plasticity were included in the experimental programme.

(iv) The investigation of the effect of an anisotropic state of confinement on the very small strain stiffness of fine grained soils was limited both quantitatively and qualitatively. Only two tests on reconstituted samples of Speswhite kaolin were carried out in anisotropic conditions of confinement and, because of limitations inherent to the apparatus only stress states in the triaxial plane were examined.

(i) No investigations of the effect of the duration of confinement on the very small strain stiffness of fine grained soils were undertaken.

Although the results from the test on the undisturbed sample of London clay seemed to fit in the general picture obtained from the tests on reconstituted samples, more tests should be carried out to confirm that the general pattern of behaviour is consistent for reconstituted and undisturbed samples. In particular, for soils in which structure affects the mechanical behaviour, careful definitions should be devised to express the overconsolidation ratio.

To extend the range of mean effective stresses and overconsolidation ratios under examination, which may prove critical if a systematic programme of tests on undisturbed stiff soils had to be undertaken, the bender elements should be incorporated into a high-pressure triaxial system. A more exhaustive study of the effects of anisotropic states of confinement would include the examination of stress states outside the triaxial plane and could be achieved by mounting the bender elements in a true triaxial device. Both high-pressure stress path cells and a true triaxial testing device are currently available at City University.

The range of soils examined should be extended, particularly to include fine grained soils of very high plasticity. A systematic investigation of the effects of soil mineralogy, grading and shape of particles on the values taken by the pressure multiplier, A, the pressure exponent, n, and

the exponent of R_o, m, in the very small strain range, should also be carried out.

It is already possible to investigate the effects of the duration of confinement on the very small strain stiffness of soils using the experimental set up described in this dissertation. It would be interesting to clarify, by monitoring G'_{max} during secondary consolidation, whether the increase of stiffness with time can be accounted for by the increase in R_o as the soil creeps or whether it should be attributed to a true effect of ageing.

6.7 Summary

(i) Dynamic testing techniques can be used effectively to measure the stiffness of soils at very small strains (ϵ_s = 0.001% and less) both in the laboratory and in situ. In the laboratory, using a combination of dynamic testing techniques and static testing techniques it is possible to measure the stiffness of soils over the whole range of strains, from very small to large, on the same specimen.

(ii) At very small strains (ϵ_s < 0.001%) the behaviour of the soil is very nearly linear elastic. For fine grained soils the dependence of the very small strain stiffness on stress state and history can be conveniently expressed as:

$$\frac{G'_{max}}{p_r} = A \left[\frac{p'}{p_r}\right]^n R_o^m$$

where p_r is a reference pressure used to satisfy dimensions and A, n and m are material properties. The anisotropy of the stress state appears to have little effect on the very small strain stiffness of fine grained soils.

(iii) Provided that the in situ stress state and history are taken into account, values of G'_{max} from laboratory tests compare reasonably with those obtained from seismic surveys. The laboratory values of G'_{max} are about 20% smaller than those in situ.

(iv) At strains larger than about 0.001% the behaviour of the soil becomes highly non-linear and the stiffness depends on strain

amplitude. The dependence of stiffness on stress state and history can be still put in the form:

$$\frac{G'}{p_r} = A \left[\frac{p'}{p_r}\right]^n R_o^m$$

but, this time, coefficients A, n and m depend on shear strain amplitude.

(v) the experimental investigation should be extended as indicated above to include different soils, undisturbed samples, a wider range of stress states and the influence of time.

REFERENCES

Abbiss, C.P., (1981). Shear wave measurements of the elasticity of the ground. Geotechnique Vol 31, No 1, 94–104.

Abbiss, C.P. (1989). Settlements prediction from surface wave measurements with a spectrum analyser in clay. (Submitted for publication in Geotechnique).

Abbiss, C.P., Ashby, K.D., (1983). Determination of ground moduli by a seismic noise technique on land and on the sea bed. Geotechnique Vol 33, No 4, 445–451.

Ackerly, S.K., Helling, J.E., Jardine, R.J., (1987). Discussion on: Clayton,C.R.I. and Khatrush,S.A., (1986). A new device for measuring local axial strains on triaxial specimens. Geotechnique Vol 37, No 3, 414–417.

Afifi, S.S., Richart, F.E., (1973). Stress history effects of shear modulus of soils. Soils and Foundations, vol.13, No 1.

Allen, J.C., Stokoe, K.H.,II, (1982). Development of resonant column apparatus with anisotropic loading. Geotechnical Engineering Report GR82–28, Geotechnical Engineering Research Centre, The University of Texas at Austin.

Anderson, D.G., Stokoe, K.H., (1978). Shear modulus: a time dependent materisl properties. Dynamic Geotechnical Testing, ASTM STP 654.

Anderson, D.G., Woods, R.D., (1975). Comparison of field and laboratory shear moduli. ASCE, Vol I.

Arthur, J.R.F., Phillips, A.B., (1975). Homogeneous and layered sand in triaxial compression. Geotechnique Vol 25, No 4, 799–815.

Atkinson, J.H., (1973). The deformation of undisturbed London Clay. Ph.D. Thesis. University of London.

Atkinson, J.H., (1984). Rates of loading in drained and undrained stress path and triaxial tests. Geotechnical Engineering Research Centre Research Report GE/84/01. The City University.

Atkinson, J.H., Bransby, P.L., (1978). The Mechanics of Soils. McGraw-Hill, London.

Atkinson, J.H., Evans, J.S., (1985). Discussion on: Jardine, R.J., Symes, M.J.R.P., and Burland, J.B., (1984). The measurement of soil stiffness in the triaxial apparatus. Geotechnique Vol 35, No 3, 378-382.

Atkinson, J.H., Evans, J.S., Scott, C.R., (1983). Development of a new microcomputer based controller for stress path testing. Geotechnical Engineering Research Centre Research Report GE/83/02. The City University.

Atkinson, J.H., Evans, J.S., Scott, C.R., (1985). Developments in stress path testing equipment for measurements of soil parameters. Ground Engineering, vol. 18, No 1, 15-22.

Atkinson, J.H., Richardson, D., Robinson, P.J., (1986). Compression and exrension of Ko NC kaolin clay. Geotechnical Engineering Research Centre Research Report GE/86/05.

Atkinson, J.H., Richardson, D., Stallebrass, S.E., (1990). Effect of recent stress history on the stiffness of overconsolidated soil. Geotechnique Vol. 40, No 4, 351-541.

Atkinson, J.H., Sallfors, G., (1991). Experimental determination of stress-strain-time characteristics in laboratory and in-situ tests. Proc. X ECSMFE, Florence. Vol III, 915-956.

Balasubramanian, A.S., (1976). Local strains and displacement patterns in triaxial specimens of a saturated clay. Soils and Foundations, vol. 16, No 1, 101-114.

Baldi, G., Hight, D.W., Thomas, G.E., (1988). A reevaluation of conventional triaxial test methods. Advanced Triaxial Testing of Soil and Rock (eds. R.T. Donaghe, R.C. Chaney, M.L. Silver). ASTM, STP 977, 219-263.

Bates, C.R., (1989). Dynamic soil property measurements during triaxial testing. Geotechnique Vol 39, No 4, 721-726.

Biot, M.A., (1956). Theory of propagation of elastic waves in a fluid saturated porous solid. I and II. Journal of the Acoustical Soc. of America, Vo. 28, No. 2.

Bishop, A.W., Henkel, D.J., (1962). The measurement of soil properties in the triaxial test. Edward Arnold.

Bishop, A.W., Wesley, L.D., (1975). A hydraulic triaxial apparatus for controlled stress path testing. Geotechnique Vol 25, No 4, 657-670.

Bodare, A., Massarsch, K.R., (1984). Determination of shear wave velocity by different cross-hole methods. Proc. VIII WCEE, S. Francisco, Vol III, 39-45.

Bolton, M.D., Wilson, J.M.R., (1989). An experimental and theoretical comparison between static and dynamic torsional soil tests. Geotechnique Vol 39, No 4, 585-599.

Brignoli, E., Gotti, M., (1992). Misure della velocita di onde elastichedi taglio in laboratorio con l'impiego di trasduttori piezoelettrici. Rivista Italiana di Geotecnica. Vol 26, No 1, 5-16.

Brown, S.F., Snaith, M.S., (1974). The measurement of recoverable and irrecoverable deformation in the repeated load triaxial test. Geotechnique Vol 24, No 2, 255-259.

Burland, J.B., (1979). Contribution to discussion - Session 4. Proc. VII ECSMFE, Brighton, vol. 4, 137.

Burland, J.B., (1989). The Ninth Laurits Bjerrum Memorial Lecture. 'Small is beautiful': the stiffness of soils at small strains. Canadian Geotechnical Journal.

Burland, J.B., (1990). On the compressibility and shear strength of natural clays. The XXX Rankine Lecture. Geotechnique Vol 40, No 3, 329-378.

Burland, J.B., Symes, H.J.R.P., (1982). A simple displacement gauge for use in the triaxial apparatus. Geotechnique Vol 32, No 1, 62-64.

Butterfield, R., (1979). A natural compression law for soils. Geotechnique Vol 29, No 4, 469-480.

Campanella, R.G., Robertson, P.K., Gillespie, D., (1986). Seismic cone penetration test. Proc. In-situ 86 Specialty Conference on Use of In-situ Tests in Geotechnical Engineering. Blacksburg, Virginia. ASCE, 116-130.

Cherrill, H.E., (1990). Rates of loading in the triaxial test. Ph.D. Thesis. The City University.

Clayton, C.R.I., Kathrush, S.A., (1986). A new device for measuring local axial strains on triaxial specimens. Geotechnique Vol 36, No 4, 593-597.

Clayton, C.R.I., Kathrush, S.A., Bica, A.V.D., Siddique, A., (1988). The use of Hall effect semiconductors in geotechnical instrumentation. Geotechnical Testing Journal, GTJODJ, vol. 12, No 1, Mar, 69-76.

Cole, K.W., Burland, J.B., (1972). Observation of retaining wall movements associated with a large excavation. Proc. V ECSMFE, Madrid.

Costa-Filho, L.M., (1985). Measurement of axial strains in triaxial tests on London Clay. ASTM, Geotechnical Testing Journal, vol. 8, No 1, 3-13.

Crilly, M.S., (1990). Personal communication.

Cunny, R.W., Fry, Z.B., (1973). Vibratory in situ and laboratory soil moduli compared. Proc. ASCE 99, No SM12, 1055–76.

Dobrin, M.B., (1960). Introduction to geophysical prospecting. McGraw-Hill. London.

Dobry, R., Ng, T-T., Petrakis, E., (1989). Deformation characteristics of granular soils in the light of particulate mechanics. Atti delle Conferenze Geotecniche di Torino. XIV Ciclo: Comportamento dei Terreni e delle Fondazioni in Campo Dinamico.

Duncan, J.M., Chang, C.Y., (1970). Non liner analysis of stress and strain in soils. JSMFD, ASCE 96, 1629–1653.

Dyvick, R., Madshus, C., (1985). Laboratory measurements of Gmax using bender elements. ASCE Convention, Detroit, Michigan.

Gazetas, G., (1982). Vibrational characteristics of soil deposits with variable wave velocity. Int. Journal for Numerical and Analytical Methods in Geomechanics, 6, 1–20.

Georgiannou, V.N., Rampello, S., Silvestri, F., (1991). Static and dynamic measurement of undrained stiffness of natural overconsolidated clays. Proc. X ECSMFE, Florence. Vol. I, 91–96.

Gibbard, P.L., (1977). Pleistocene history of the Vale of St. Albans. Philosophical Transactions of the Royal Society of London. Vol 280 (B957), 445–483.

Goto, S., Tatsuoka, F., Shibuya, S., Kim, Y-S., Sato, T., (1991). A simple gauge for local small strain measurements in the laboratory. Soils and Foundations Vol. 31, No 1, 169–180.

Graham, J., Houlsby, G.T., (1983). Anisotropic elasticity of a natural clay. Geotechnique Vol 33, No 2, 165–180.

Griffiths, D.H., King, R.F., (1981). Applied geophysics for geologists and engineers. Pergamon. Oxford.

Hall, J.R., Richart, F.E., Jr, (1963). Dissipation of elastic wave energy in granular soils. Journal of the Soil Mechanics and Foundation Division, ASCE, vol. 89, No SM6, Nov, 27-56.

Hardin, B.O., (1978). The nature of stress-strain behaviour for soils. State of the Art Report. Proc. Geotechnical Engineering Division Specialty Conference on Earthquake Engineering and Soil Dynamics, Pasadena, California, ASCE.

Hardin, B.O., Black, W.L., (1968). Vibration modulus of normally consolidated clay. Journal of the Soil Mechanics and Foundation Division. ASCE, vol. 95, No SM6, Nov, 1531-1537.

Hardin, B.O., Drnevich, V.P., (1972,a). Shear modulus and damping in soils. I. Measurement and parameter effects. Journal, Geotechnical Engineering Division. ASCE, vol. 102, No GT9, Sep, 975-987.

Hardin, B.O., Drnevich, V.P., (1972,b). Shear modulus and damping in soils. II. Design equation and curves. Journal, Geotechnical Engineering Division. ASCE, vol. 98, No SM7, Jul, 667-692.

Hardin, B.O., Music, J., (1965). Apparatus for vibration during the triaxial test. Symp. on Instrumentation and Apparatus for Soils and Rocks. ASTM, STP, No 392.

Hardin, B.O., Richart, F.E., Jr, (1963). Elastic wave velocities in granular soils. Journal of the Soil Mechanics and Foundation Division, ASCE, vol. 89, No SM1, Feb, 33-65.

Harrison, R., (1989). Personal communication.

Hird, C.C., Yung, P., (1987). Discussion on: Clayton, C.R.I., Khatrush, S.A., (1986). A new device for measuring local axial strains on triaxial specimens. Geotechnique Vol 37, No 3, 413-414.

Hird, C.C., Powell, J.J.M., Yung, P.C.Y., (1991) Investigations of the stiffness of a glacial clay till. Proc. X ECSMFE, Florence, Vol I, 107-110.

Ho, E.W.L., (1988). Geotechnical properties of deep ocean sediments: a critical state approach. Ph.D. Thesis. The City University.

Houlsby, G.T., Wroth, C.P., (1991). The variation of shear modulus of a clay with pressure and overconsolidation ratio. Soils and Foundations Vol 31, No 3, 138-143.

Isenhower, W.M., (1979). Torsional simple shear/Resonant column properties of S. Francisco Bay Mud. M.S. Thesis. The University of Texas at Austin.

Iwasaki, T., Tatsuoka, F., Takagi, Y., (1978). Shear moduli of sands under cyclic torsional shear loading. Soils and Foundations Vol 18, No 1, 39-56.

Janbu, N., (1963). Soil compressibility as determined by oedometer and triaxial tests. Proc. ? ECSMFE, Wiesbaden.

Jardine, R.J., (1985). Investigation of pile-soil behaviour with special reference to the foundations of offshore structures. Ph.D. Thesis. University of London.

Jardine, R.J., Potts, D.M., (1988). Hutton tension leg platform foundation: an approach to the prediction of pile behaviour. Geotechnique Vol 38, No 2, 231-252

Jardine, R.J., Potts, D.M., St.John, H.D., Hight, D.W., (1991). Some practical applications of a non-linear ground model. Proc X ECSMFE, Florence, Vol I, 223-228.

Jardine, R.J., Symes, M.J.R.P., Burland, J.B., (1984). The measurement ofsoil stiffness in the triaxial apparatus. Geotechnique Vol 34, No 3, 323-340.

Knox, D.P. Stokoe, K.H., Kopperman, S.E., (1982). Effect of state of stress on velocity of low amplitude shear wave propagating along principal stress directions in dry sand. Geotechnical Engineering Research Report GR 82-23. University of Texas at Austin.

Ladd, C., Edgers, L., (1972). Consolidated-undrained direct simple shear tests on saturated clays. MIT Research Report R 72-82.

LaRochelle, P., Leroueil, S., Trak, B., Blais-Leroux, L., Tavenas, F., (1988). Observational approach to membrane and area corrections in triaxial testing. Advanced Triaxial Testing of Soil and Rock (eds. R.T. Donaghe, R.C. Chaney, M.L. Silver). ASTM, STP 977, 715-731.

Lau, W.H.W., (1988). The behaviour of clay in simple shear and triaxial tests. Ph.D. Thesis. The City University.

Lawrence, F.V., (1963). Propagation of ultrasonic waves through sand. MIT Research Report R 63-08.

Lawrence, F.V., (1965). Ultrasonic shear wave velocity in sand and clay. MIT Research Report R 65-05.

Lewin, P.I., (1978). The deformation of soft clay under generalised stress conditions. Ph.D. Thesis. University of London.

Little, J.A., (1984). Engineering properties of glacial tills in the Vale of St. Albans. Ph.D. Thesis. The City University.

Little, J.A., Atkinson, J.H., (1988). One-dimensional consolidation characteristics of a glacial till. Quarterly Journal of Engin. Geology Vol 21, No 1, 183-199

Lo Presti, D.C.F., (1989). Proprieta dinamiche dei terreni. Atti delle Conferenze di Geotecnica di Torino, XIV Ciclo. "Comportamento dei Terreni e delle Fondazioni in Campo Dinamico".

Mancuso, C., Vinale, F., (1988). Propagazione delle onde sismiche: teoria e misura in sito. Atti del Convegno del Gruppo Nazionale di Coordinamento per gli Studi di Ingegneria Geotecnica, Monselice, 115-138.

Mancuso, C., Simonelli, A.L., Vinale, F., (1989). Numerical analysis of in situ S-wave measurements. Proc. XII ICSMFE, Rio de Janeiro.

Marsland, A., (1973,a). Large in situ tests to measure the properties of stiff fissured clays. Garston. BRE Current Paper 1/73.

Marsland, A., (1973,b). Laboratory and in situ measurements of the deformation moduli of London clay. Garston. BRE Current Paper 24/73.

Menzies, B.K., Sutton, H., Davies, R.E., (1977). A new system for automatically simulating K_o consolidation and K_o swelling in the conventional triaxial cell. Geotechnique Vol 27, No 4, 593-596.

Nazarian, S., Stokoe, K.H., (1986,a). In situ determination of elastic moduli of pavement systems by spectral analysis of surface waves method. Practical aspects. Research Report 368-IF, Centre for Transportation Research, The University of Texas at Austin.

Nazarian, S., Stokoe, K.H., (1986,b). In situ determination of elastic moduli of pavement systems by spectral anlysis of surface wave method. Theoretical aspects. Research Report 437-2, Centre for Transportation Research, The university of Texas at Austin.

Nelson, I., Baron, M.L., (1971). Application of variable moduli models to soil behaviour. Int. Journ. Solids Structures, 7, 399-417.

Ni, S-H, (1987). Dynamic properties of sand under true triaxial stress states from resonant column/torsion shear tests. Ph.D. Thesis. The University of Texas at Austin.

Pane, V., Burghignoli, A., (1988). Determinazione in laboratorio delle caratteristiche dinamiche dell'argilla del Fucino. Atti del Convegno del Gruppo Nazionale di Coordinamento per gli Studi di Ingegneria Geotecnica, Monselice, 115-140.

Papa, V., Silvestri, F., Vinale, F., (1988). Analisi delle proprieta di un tipico terreno piroclastico mediante prove di taglio semplice. Atti del Convegno del Gruppo Nazionale di Coordinamento per gli Studi di Ingegneria Geotecnica, Monselice, 265-286

Papa, V., Silvestri, F., Vinale, F., (1989). Cyclic/dynamic simple shear tests: recent developments. Proc. XII ICSMFE, Rio de Janeiro.

Pickles, A.R., (1989). The application of critical state soil mechanics to predict ground deformations below an embankment constructed on soft alluvium. Ph.D. Thesis, The City University.

Powell, J.J.M., (1989). Personal Communication.

Powell, J.J.M., Butcher, A.P., (1991). Assessment of ground stiffness from field and laboratory tests. Proc. X ECSMFE, Florence, Vol I, 153-156.

Prevost, J.H., Keane, C.M., (1990). Shear stress strain curve generation from simple material parameters. JGED, ASCE 116, 1255-1263.

Rampello, S., (1989). Effetti del rigonfiamento sul comportamento meccanico di argille fortemente sovraconsolidate. Ph.D. Thesis. University of Roma "La Sapienza".

Rampello, S., Pane, V. (1988). Deformabilita non drenata statica e dinamica di un'argilla fortemente sovraconsolidata. Atti del Convegno del Gruppo Nazionale di Coordinamento per gli Studi di di Ingegneria Geotecnica, Monselice, 141-160.

Richardson, D., (1988). Investigation of threshold effects in soil deformation. Ph.D. Thesis. The City University.

Richart F.E., Hall, J.R., Woods, R.D., (1970). Vibration of soils and foundations. Prentice-Hall Inc., Englewood Cliffs, NJ, 414 pp.

Roscoe, K.H., Burland, J.B., (1968). On the generalised stress strain behaviour of wet clay. Engineering Plasticity. Cambridge University Press.

Rowe, P.W., (1971). Theoretical meaning and observed values of deformation parameters for soils. Proc. Roscoe Memorial Symposium on Stress-Strain Behaviour of Soils.

Salinero, I.S., Roesset, J.M., Stokoe, K.H., (1986). Analytical studies of body wave propagation and attenuation. Report GR 86-15, University of Texas at Austin.

Schofield, A.N., Wroth, C.P., (1968). Critical State Soil Mechanics. McGraw-Hill, London.

Schulteiss, P.J., (1982). Influence of packing structure on seismic wave velocities in sediments. Ph.D. Thesis. University College of North Wales.

Shirley, D.J., (1978). An improved shear wave transducer. Journal of the Acoustical Society of America, vol. 63, No 5, May, 1643-1645.

Shirley, D.J., Hampton, L.D., (1977). Shear-wave measurements in laboratory sediments. Journal of the Acoustical Society of America, vol. 63, No 2, Feb, 607-613.

Silvestri, F., (1991). Analisi del comportamento dei terreni naturali in prove cicliche e dinamiche di taglio torsionale. Ph.D. Thesis. University of Napoli "Federico II".

Silvestri, F., Viggiani, C., Vinale, F., (1989). Analisi del comportamento dei terreni da prove cicliche e dinamiche di laboratorio. Atti delle Conferenze di Geotecnica di Torino, XIV Ciclo. "Comportamento dei Terreni e delle Fondazioni in Campo Dinamico".

Simpson, B., Calabresi, G., Sommer, H., Wallays, M. (1979). Design parameters for stiff clays. General Report. Proc. VII ECSMFE, Brighton, vol. 1, 91-125.

Skempton, A.W., (1961). Horizontal stresses in an overconsolidated Eocene clay. Proc. X ICSMFE Paris, Vol I, 351-357.

Stallebrass, S.E., (1990a). Modelling the effect of recent stress history on the deformation of overconsoliadted soils. Ph.D. Thesis. The City University.

Stallebrass, S.E., (1990b). Stress path tests on undisturbed London clay using local axial strain gauges. Geotechnical Engineering Research Centre Research Report GE/90/22, The City University.

St.John, H.D., (1975). Field and theoretical studies of the behaviour of ground around deep excavations in London Clay. Ph.D. Thesis. University of Cambridge.

Stokoe, K.H.,II, Woods, R.D., (1972). In situ shear wave velocity by cross-hole method. Journal of the Soil Mechanics and Foundation Division. ASCE, vol. 98, No SM5, May, 443-460.

Tatsuoka, F., Iwasaki, T., Fukushima, S., Sudo, H., (1979). Stress conditions and stress history affecting shear modulus and damping of sand under cyclic loading. Soils and Foundations Vol 19, No 2, 29-43.

Taylor, R.N., Coop, M.R., (1991). Stress path testing of Boom clay from Mol, Belgium. Proc. 25th Annual Conf. Eng. Group Geol. Soc. In the press.

Teachavorasinskun, S., Shibuya, S., Tatsuka, F., Kato, H., Horii, N., (1991). Stiffness and damping of sands in torsion shear. Proc. II Int. Conference on Recent Advances in Geotechnical Earthquake Engineering and Soil Dynamics, St.Louis, Vol I, 103-110.

Timoshenko, S.P., Goodier, J.N., (1951). Theory of elasticity. McGraw-Hill. New York.

Viggiani, G., (1990). Measurement of soil stiffness in dynamic field and laboratory tests. Geotechnical Engineering Research Centre Research Report GE/90/26. The City University.

Vrettos, C.H., (1990). In-plane vibrations of soil deposits with variable shear modulus: I surface waves. Int. Journ. for Numerical and Analytical Methods in Geomechanics, Vol 14, 209-222.

Webb, D.L., (1967). The mechanical properties of undisturbed samples of London clay Pierre shale. Ph.D. Thesis. University of London.

Weiler, W.A., (1988). Small strain shear modulus of clay. Proc. Geot. Eng. Division Specialty Conf on Earthquake Engineering and Soil Dynamics, II. ASCE. Park City, Utah.

Wilson, S.D., Dietrich, R.J., (1960). Effects of consolidation pressure on elastic and strength properties of clay. Proc. Research Conference on Shear Strength of Cohesive Soils, ASCE, Boulder, Colorado.

Wroth, C.P., (1971). Some aspects of the elastic behaviour of overconsolidated clay. Proc. Roscoe Memorial Symposium. Foulis, 347-361.

Wroth, C.P., (1975). In situ measurement of initial stresses and deformation characteristics. State-of-the-art report. Proc. Geotechnical Engineering Division Specialty Conference on In Situ Measurement of Soil Properties, Raleigh, North Carolina, ASCE, vol. II, 181-230.

Wroth, C.P., Randolph, M.F., Houlsby, G.T., Farhey, M., (1979). A review of the engineering properties of soils with particular reference to the shear modulus. OUEL Report No 1523/84. University of Oxford.

Wroth, C.P., Houlsby, G.T., (1985). Soil Mechanics- Property characterisation and analysis procedures. Proc. XI ICSMFE, S.Francisco, Vol I, 1-55.

Yoshimi, Y., Richart, F.E., Jr, Prakash, S., Barkan, D.D., Ilyichev, V.A., (1977). Soil dynamics and its application to foundation engineering. State of the Art Report. IX ICSMFE, Tokio, vol. 2, 605-650.

Zytinski, M., Randolph, M.F., Nova, R., Wroth, C.P., (1978). On modelling the unloading-reloading behaviour of soils. Int. Journal for Numerical and Analytical Methods in Geomechanics, vol. 2, 87-94.

importance to		PARAMETER	importance to	
modulus	damping		sands	clays
<u>very important</u>				
X	X	strain amplitude	X	X
X	X	mean effective stress	X	X
X	X	voids ratio	X	X
	X	number of cycles of loading	X	X
X	U	degree of saturation		X
<u>less important</u>				
X	X	octahedral shear stress	X	X
X	X	overconsolidation ratio		X
X	X	effective strength envelope	X	X
	X	frequency of loading (>0.1 Hz)		X
X	X	other time effects		X
<u>relatively unimportant</u> (except as they affect the above parameters)				
X	X	grain characteristics, size, shape, gradation, mineralogy	X	X
X	X	soil structure		X
X	X	dilation	U	X

Note: "X" stands for Yes, " " stands for No, "U" stands for unknown.

Table 2.4.1 Factors affecting shear modulus and damping of soils (after Hardin and Drnevich, 1972a)

site	date	test	technique	spacing (m)	number of averages
North Field	12.06.89	NFA01ANA	spectrum analyser	1.0+1.0	-
	12.06 89	NFA02ANA		2.0+2.0	-
	13.06.89	NFA03ANA		2.0+2.0	-
	13.06.89	NFA04ANA		3.0+3.0	-
	13.06.89	NFA05ANA		5.0+3.0	-
	26.06.89	NFA06PHA	phasemeter	1.0+1.0	-
	29.06.89	NFA07COR	correlator	1.0+1.0	32x1024
	30.06.89	NFA08COR		2.0+2.0	32x1024
	10.07.89	NFA09COR		2.0+2.0	64x1024
	20.07.89	NFA10COR		1.5+1.5	32x1024
	24.07.89	NFA11COR		1.5+1.5	32x1024
	24.07.89	NFA12COR		1.0+1.0	32x1024
	24.07.89	NFA13COR		2.0+2.0	32x1024
Canons Park	04.08.89	CAN01COR	correlator	1.5+1.5	32x1024
	04.08.89	CAN02COR		1.5+1.5	32x1024
Chattenden	19.09.89	CHA01ANA	spectrum analyser	1.5+1.5	-
	30.07.90	CHA02ANA		1.0+1.0	-

a)

site	date	type	spacing (m)	z_{max} (m)	d_{max} (m)
North Field	03.07.89	p-wave	3.0	10.4	30.0
	03.07.89	s-wave	2.0	7.8	20.0
Canons Park	03.08.89	p-wave	2.0	-	20.0
	03.08.89	s-wave	2.0	3.8	20.0
Chattenden	20.09.89	p-wave	2.0	-	20.0
	30.07.90	p-wave	2.0	-	30.0
	30.07.90	s-wave	2.0	9.1	30.0

b)

Table 3.1.1 a) surface wave and b) seismic refraction surveys

function	instrument	working range	signal range	typical output
axial stress	Surrey University Wykeham Farrance load cell 4958	± 5 kN *± 4400 kPa*	± 2.5 mV	≃ 3 mV/kN *≃ 3.5x10⁻³ mV/kPa*
pore pressure cell pressure	Druck pressure transducer WF17060	0–1000 kPa	± 100 mV	≃ 9.4×10^{-2} V/kN
axial strain	LVDt displacement transducer 500A RDP ElectronicsLtd	L.R. ≃ 25 mm *≃ 33 %*	± 10 V	≃ 1.8×10^{-1} V/mm *≃ 1.3x10⁻¹ V/%*
volume strain	50cc Imperial Coll volume gauge + LVDT 500A RDP Elec	L.R. ≃ 35 cc *≃ 40 %*	± 10 V	≃ 9.7×10^{-2} V/cc *≃ 8.4X10⁻² V/%*
local axial strain	Surrey University Hall effect transducer	L.R. ≃ 5 mm *≃ 6.5 %*	± 10 V	≃ 2.4×10^{-1} V/mm *≃ 1.8x10⁻¹ V/%*

Note: values in italic are calculated for a 38mm diameter 76mm long sample

Table 4.2.1 Characteristics of the transducers used in the experimental work

transducer	resolution	sources of error				overall accuracy[2]
		noise	histeresys	drift[1]	non-linearity	
Surrey University load cell	±1.5kPa	±1.5kPa	±0.4%	±0.2%	±0.1%	±1.5 kPa ±0.7%
pore or cell pressure transducer	0.4kPa	±0.2kPa	±0.2%	—	±0.4%	±0.2kPa ±0.2%
external LVDT for axial strain	0.0005%[3]	±0.002%	—	±0.03%	±0.4%	±0.002% ±0.43%
volume gauge + LVDT	0.001%[3]	±0.005%	—	±0.1%	± 0.2%	±0.005% ±0.3%

a)

transducer	resolution	sources of error				overall accuracy[2]
		noise	histeresys	drift[1]	non-linearity	
Surrey University load cell	0.03kPa[4]	±1.0kPa	±0.4%	±0.2%	±0.1%	±1.0kPa ±0.7%
pore or cell pressure transducer	0.03kPa	±0.2kPa	±0.2%	—	±0.4%	±0.2kPa ±0.6%
external LVDT for axial strain	0.0023%	±0.002%	—	±0.03%	±0.4%	±0.002% ±0.43%
volume gauge + LVDT	0.0037%	±0.005%	—	±0.1%	±0.2%	±0.005% ±0.3%
Hall effect transducer	0.0017%	±0.004%	—	±0.7%	±0.4%	±0.004 ±1.1%

b)

Notes:
1. calculated for a 24 hr long stage; $\Delta\sigma_3$ = 100kPa; $\Delta\epsilon$ = 1%
2. overall accuracy consists of the absolute error due to noise plus the percentage error due to hysteresis, drift and non-linearity
3. close to zero output voltage
4. with 300 times amplification

Table 4.2.2 Resolution and accuracy of transducers for a) BBC and b) IBM systems

SOIL	WATER CONTENT
Speswhite kaolin	150%
London clay	100%
North field clay	80%
slate dust	40%

Table 4.4.1 Initial water contents of slurries

SOIL	PL	LL	PI
Speswhite kaolin	34	58	24
London clay	28	69	41
North Field clay	27	56	29
slate dust	18	29	11

Table 4.5.1 Index properties of the soils used in the experimental work

SOIL	N	λ^1	κ^2	M
Speswhite kaolin	2.964	0.151	0.034	0.80
London clay	3.306	0.219	0.07	0.90
North field clay	2.889	0.173	0.038	—
slate dust	2.168	0.077	0.016	—

Notes: 1. calculated as discussed in section 4.6.1
2. average on the stress range p'= 50 kPa to p'= 400 kPa

Table 4.5.2 Critical state parameters of soils used in the experimental work

TEST	drainage conditions	compression and swelling			shear to failure		
		p'_{max} (kPa)	$(R_o)_{max}$	rate (kPa/h)	p' (kPa)	R_o	rate[1] (kPa/h)
KAOD2	ends only	400	8	6	200	2	6
KAOD3	ends only	400	4	6	—	—	—
KAOD4	ends only	400	8	6	—	—	—
KAOD6	ends only	400	8	10	—	—	—
KAOD7	ends only	400	8	6	200	2	6

Note: 1. rate of loading refers to start of shear

Table 4.5.3 Details of group of tests KAOD

TEST	drainage conditions	compression and swelling			shear to failure		
		p'_{max} (kPa)	$(R_o)_{max}$	rate (kPa/h)	p' (kPa)	(R_o)	rate[1] (kPa/hr)
LSK1	all round	400	1	9	400	1	9
LSK2	all round	200	1	9	200	1	9
LSK3	all round	100	1	9	100	1	9
LSK4	all round	50	1	9	50	1	9
LSK5	all round	400	8	one step	50	8	9
LSK6	all round	400	4	9	100	4	9
LSK7	all round	400	2	9	200	2	9
LSK8	all round	200	4	9	50	4	9
LSK9	all round	200	2	9	100	2	9
LSK0	all round	100	2	9	50	2	9

Note: 1. rate of loading refers to start of shear

Table 4.5.4 Details of group of tests LSK

TEST	drainage conditions	stress state	rates (KPa/h)
KAOS1	all round	compression	5
KAOS2	all round	extension	5

Table 4.5.5 Details of group of tests KAOS

TEST	drainage conditions	compression and swelling			shear to failure		
		p'_{max} (kPa)	$(R_o)_{max}$	rate (kPa/h)	p' (kPa)	R_o	rate[1] (kPa/h)
RLC1	all round	400	4	4	—	—	—
RLC2	all round	400	8	one step	200	2	6
RLC3	all round	400	8	4	100	4	3

Note: 1. rate of loading refers to start of shear

Table 4.5.6 Details of group of tests RLC

TEST	drainage conditions	compression and swelling		
		p'_{max} (kPa)	$(R_o)_{max}$	rate (kPa/h)
RNF1	all round	600	8	4[1]
RNF2	all round	400	2	4

Note: 1. isotropic compression stage to p'= 100 kPa was one-step loading

Table 4.5.7 Details of group of tests RNF

TEST	drainage conditions	compression and swelling			shear to failure		
		p'_{max} (kPa)	$(R_o)_{max}$	rate (kPa/h)	p' (kPa)	R_o	rate[1] (kPa/h)
SLD1	all round	400	4	4	—	—	—
SLD2	all round	400	8	one step	200	2	6

Note: 1. rate of loading refers to start of shear

Table 4.5.8 Details of group of tests SLD

TEST	drainage conditions	compression stages		shearing stages	
		p'_{max} (kPa)	rate (kPa/hr)	p' (kPa)	rate[1] (kPa)
ULCD	all round	225	5	225	3
KAOL	all round	100	one step[2]	100	9[3]

Note: 1. rate of loading refers to start of shear
2. G'_{max} monitored during consolidation
3. G'_{max} monitored during shear

Table 4.5.9 Details of tests ULCD and KAOL

TEST	A	n
KAOD3	1910	0.653
KAOD4	1922	0.653
KAOD6	1827	0.650
KAOD7	2088	0.654

Table 5.2.1 Values of A and n from different tests on kaolin

SOIL	A	n	m	b
Speswhite kaolin	1964	0.65	0.20	0.51
London clay	407	0.76	0.25	0.76
North Field clay	660	0.81	0.24	0.66
slate dust	2474	0.72	0.21	0.54

Table 5.2.2 Values of A, n, m and b for the different soils used in the experimental work

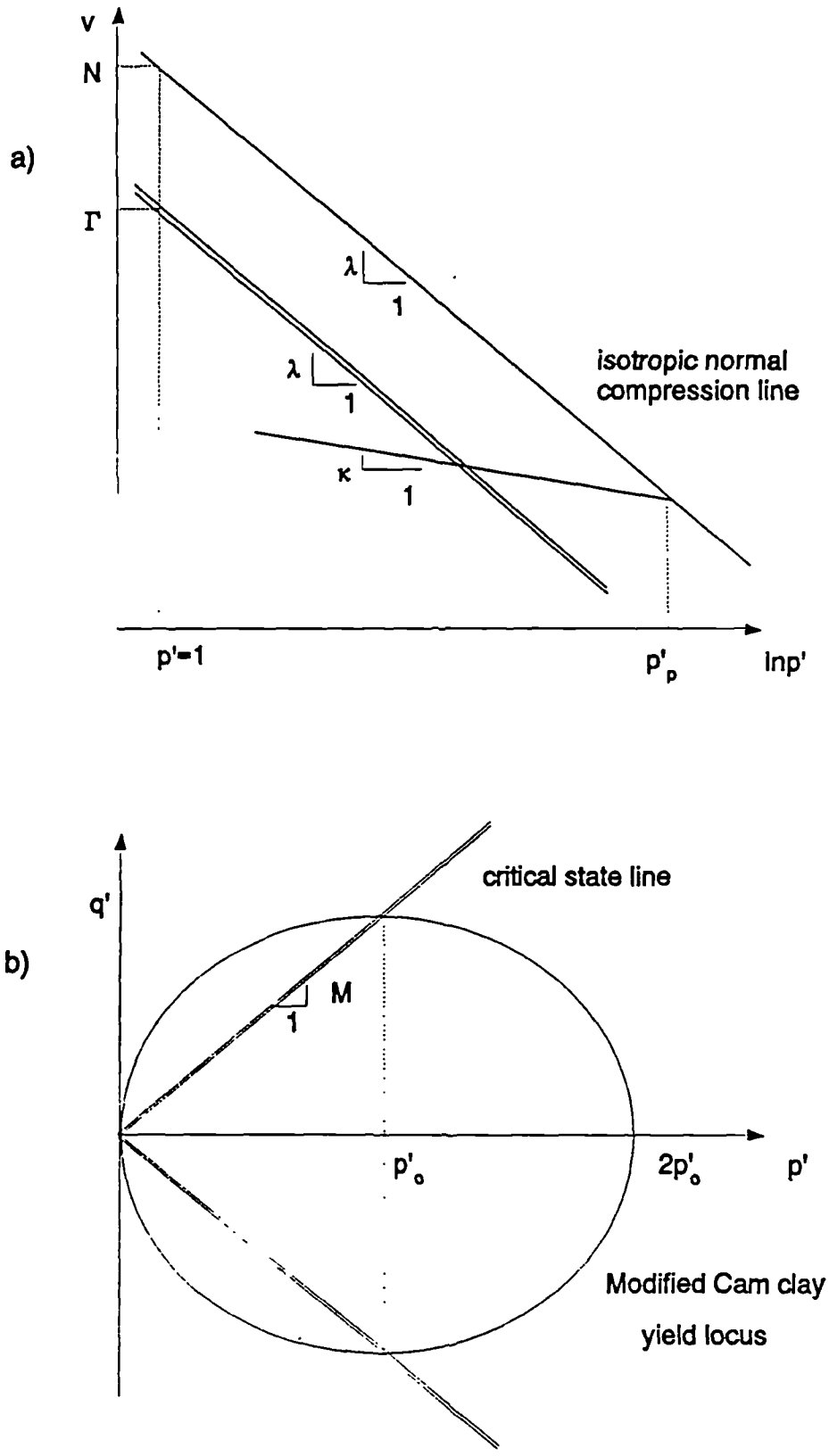

Figure 1.2.1 Diagram defining the main parameters of Modified Cam-clay a) in v:lnp' space b) in q':p' space

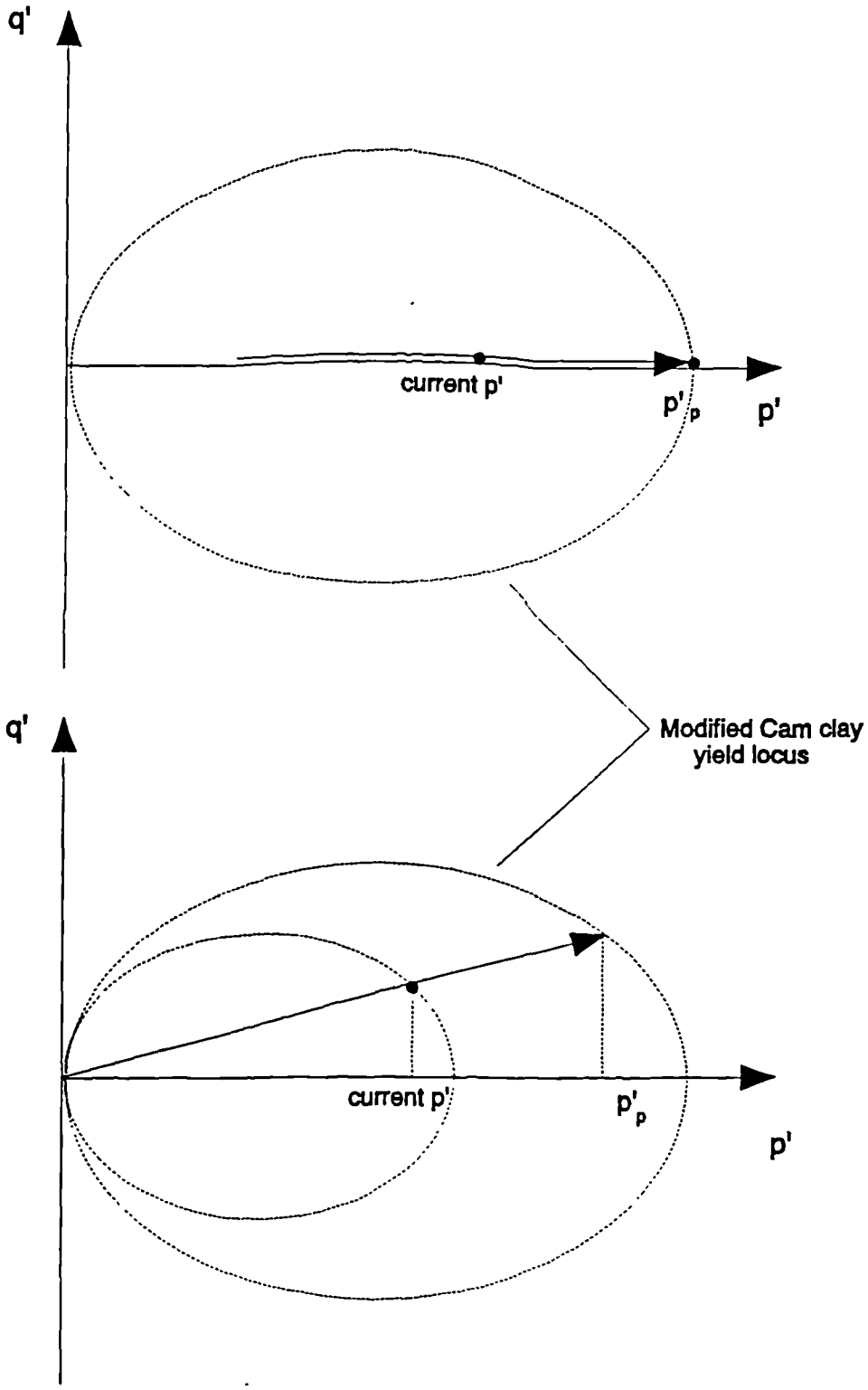

Figure 1.2.2 Definition of p_p' for isotropic and anisotropic loading

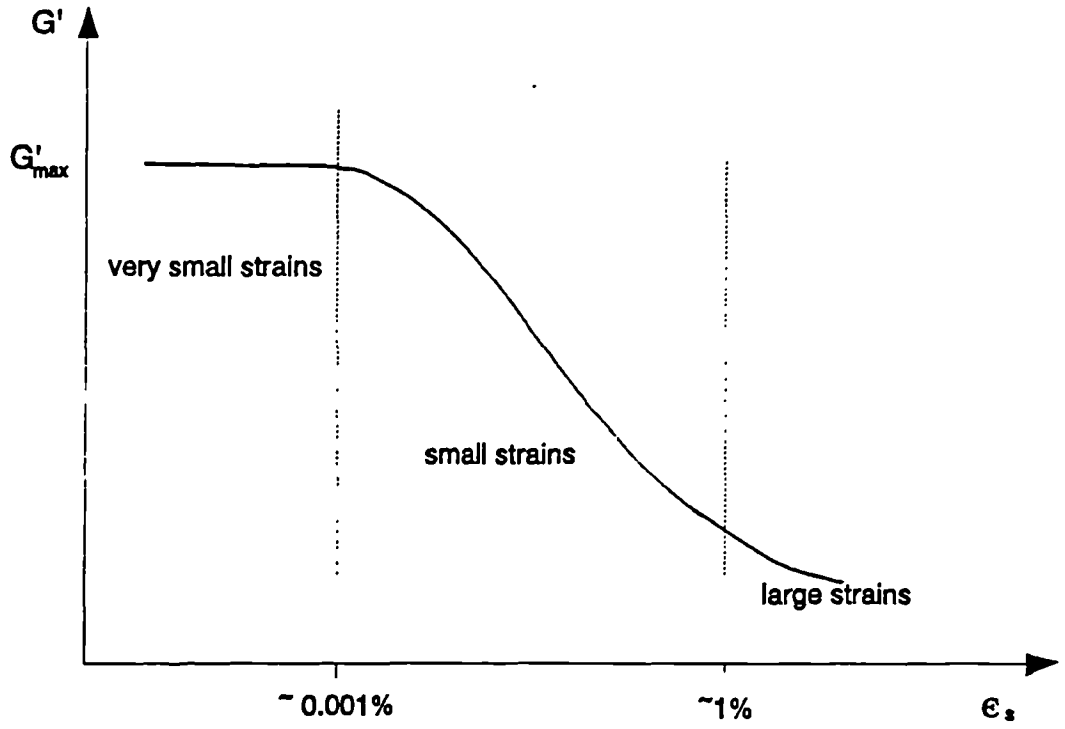

Figure 1.3.1 Diagram showing the typical decay of shear stiffness with shear strain amplitude

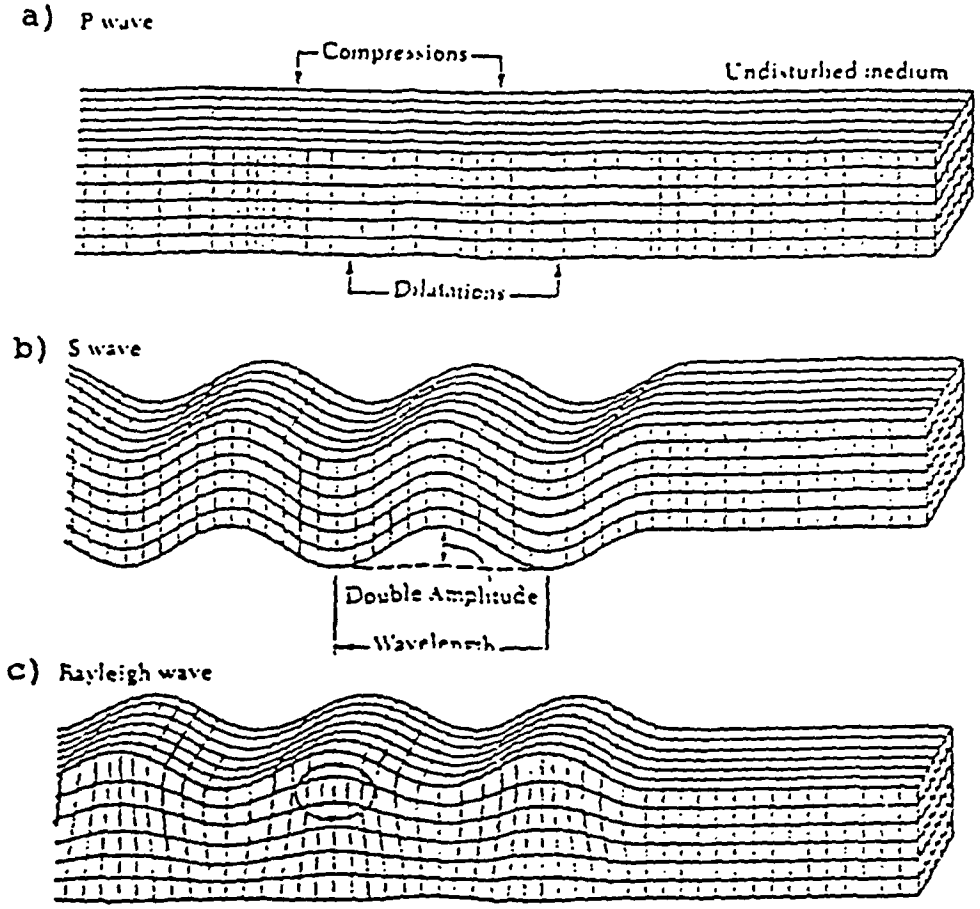

Figure 1.4.1 Characteristic motion of a) compression b) shear and c) Rayleigh waves (after Nazarian and Stokoe, 1986)

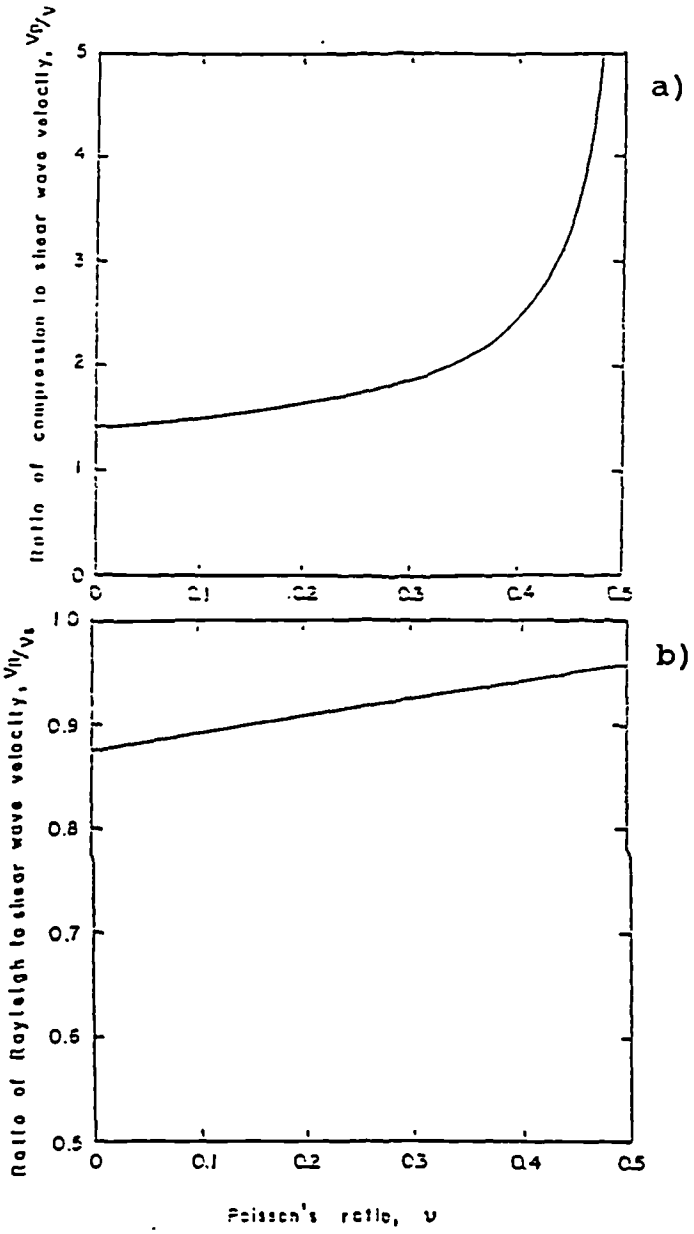

Figure 1.4.2 a) V_p/V_s versus Poisson's ratio and b) V_R/V_s versus Poisson's ratio (after Nazarian and Stokoe, 1986)

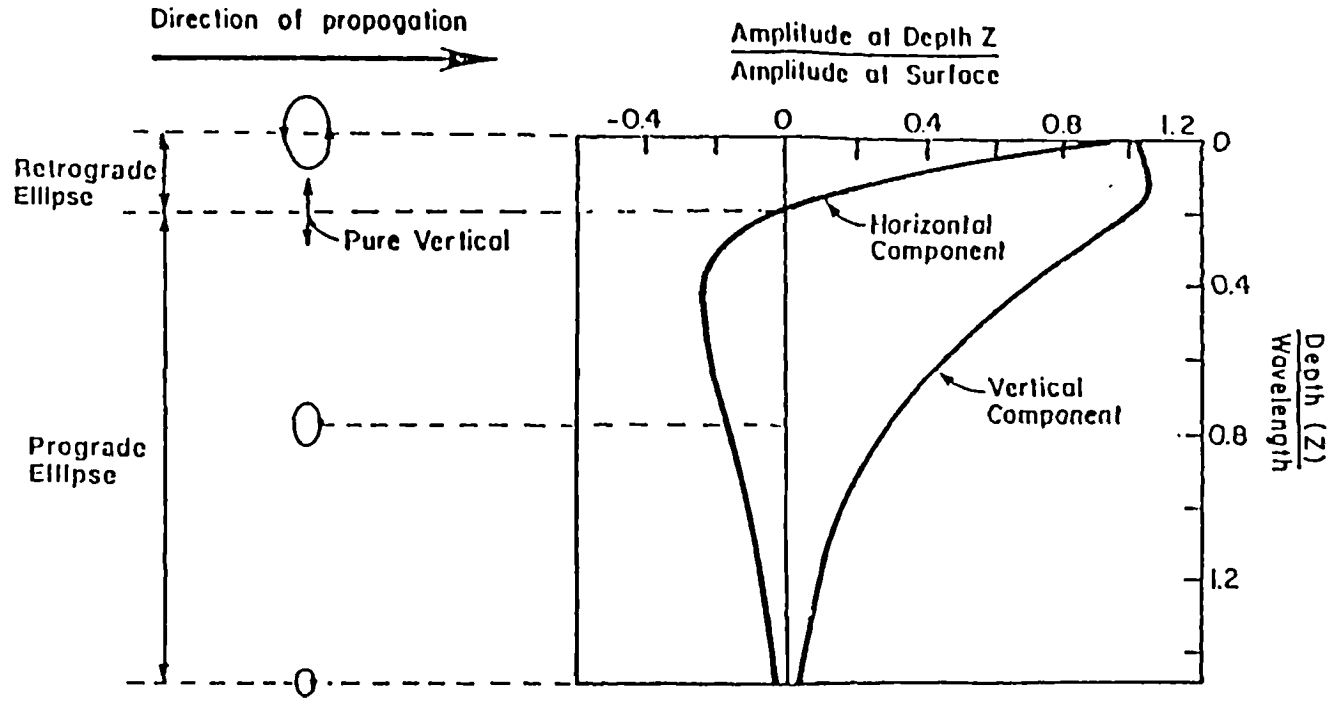

Figure 1.4.3 Amplitude and particle motion distribution with depth for Rayleigh wave (after Nazarian and Stokoe, 1986)

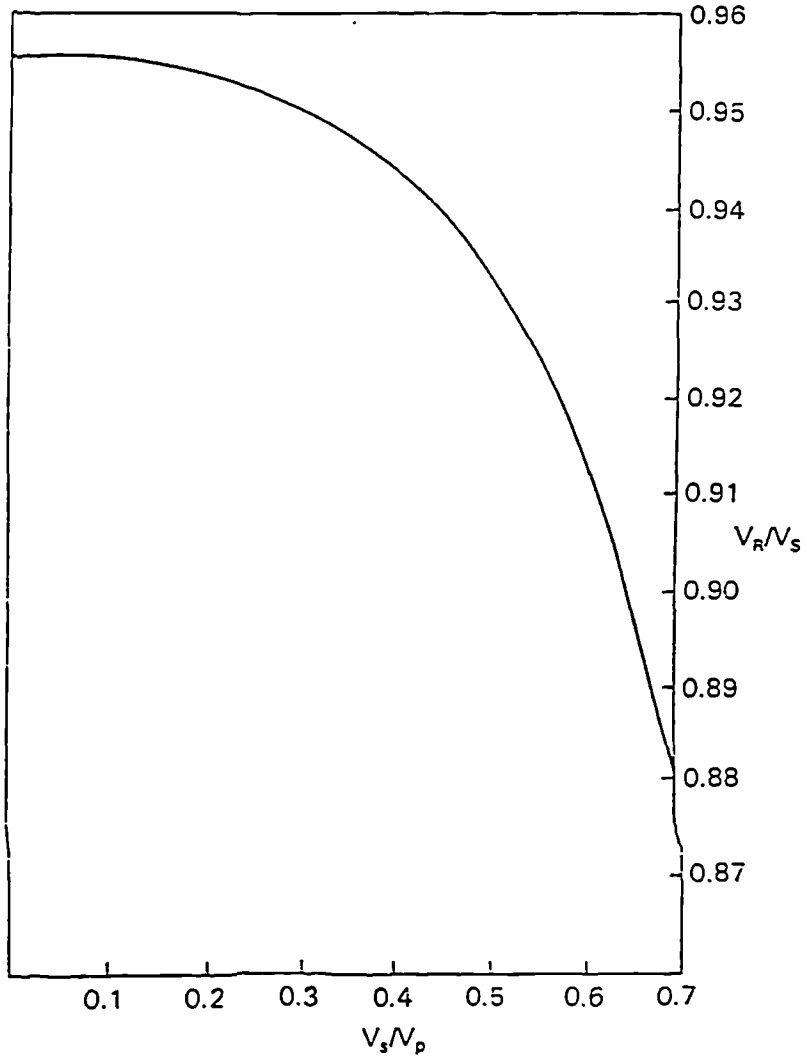

Figure 1.4.4 V_R/V_s versus V_s/V_p (after Abbiss, 1989)

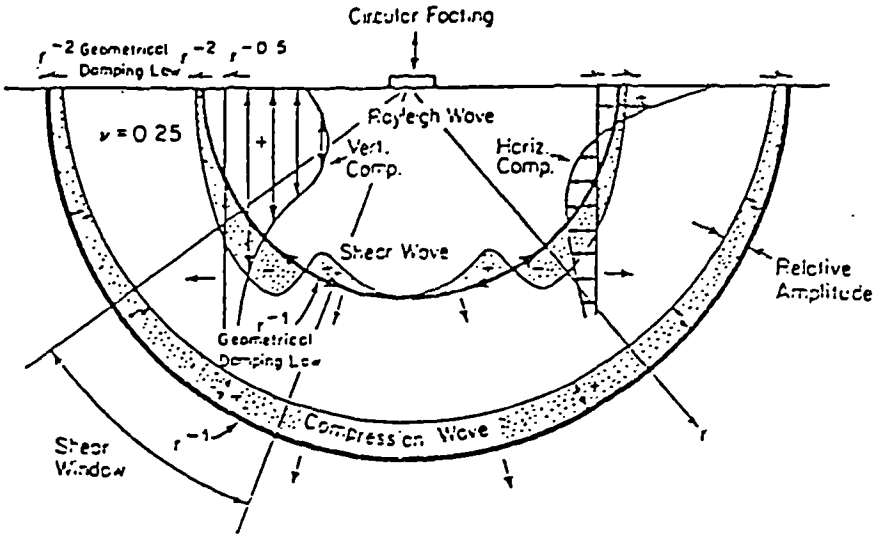

Wave Type	Per Cent of Total Energy
Rayleigh	67
Shear	26
Compression	7

Figure 1.4.5 Distribution of displacement waves from a circular footing oscillating on a homogeneous isotropic elastic half space (after Richart et al., 1970)

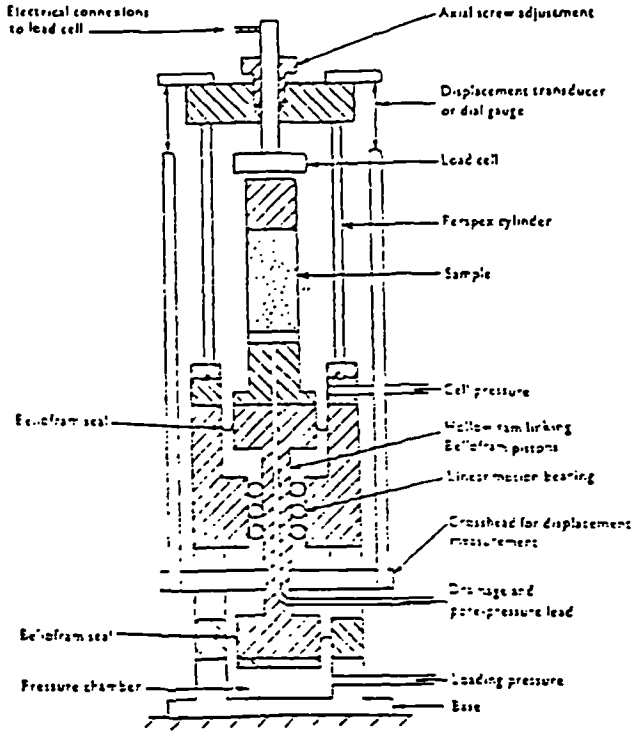

Figure 2.2.1 Cross section of typical hydraulic stress path cell (after Bishop and Wesley, 1975)

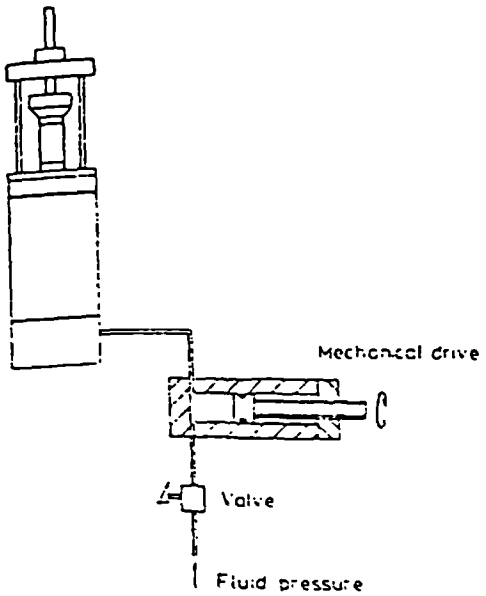

Figure 2.2.2 Provision of stress control or strain control for a hydraulic cell (after Atkinson et al., 1985)

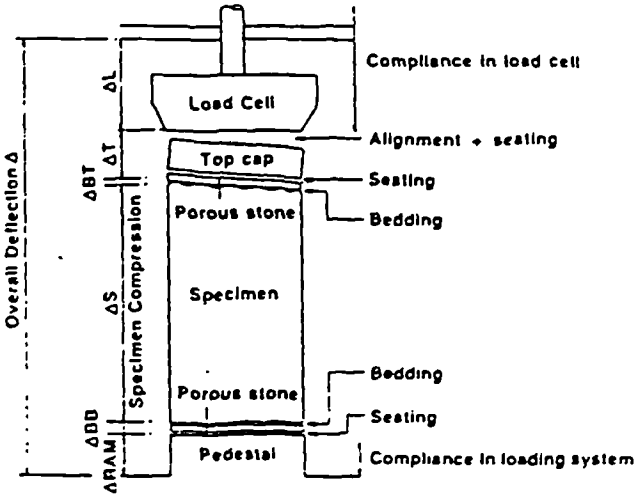

Figure 2.2.3 Sources of error in conventional measurement of axial strain in triaxial testing (after Baldi et al., 1988)

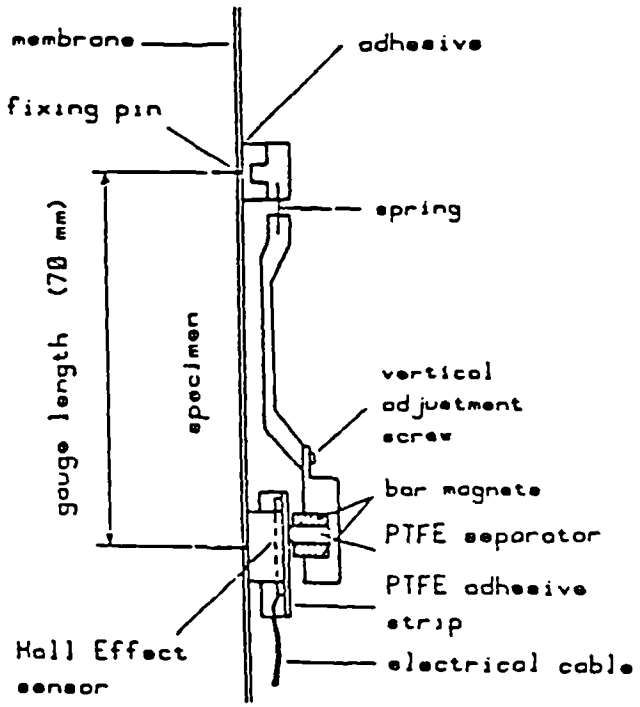

Figure 2.2.4 Schematic section of Hall-effect gauge (after Clayton et al., 1989)

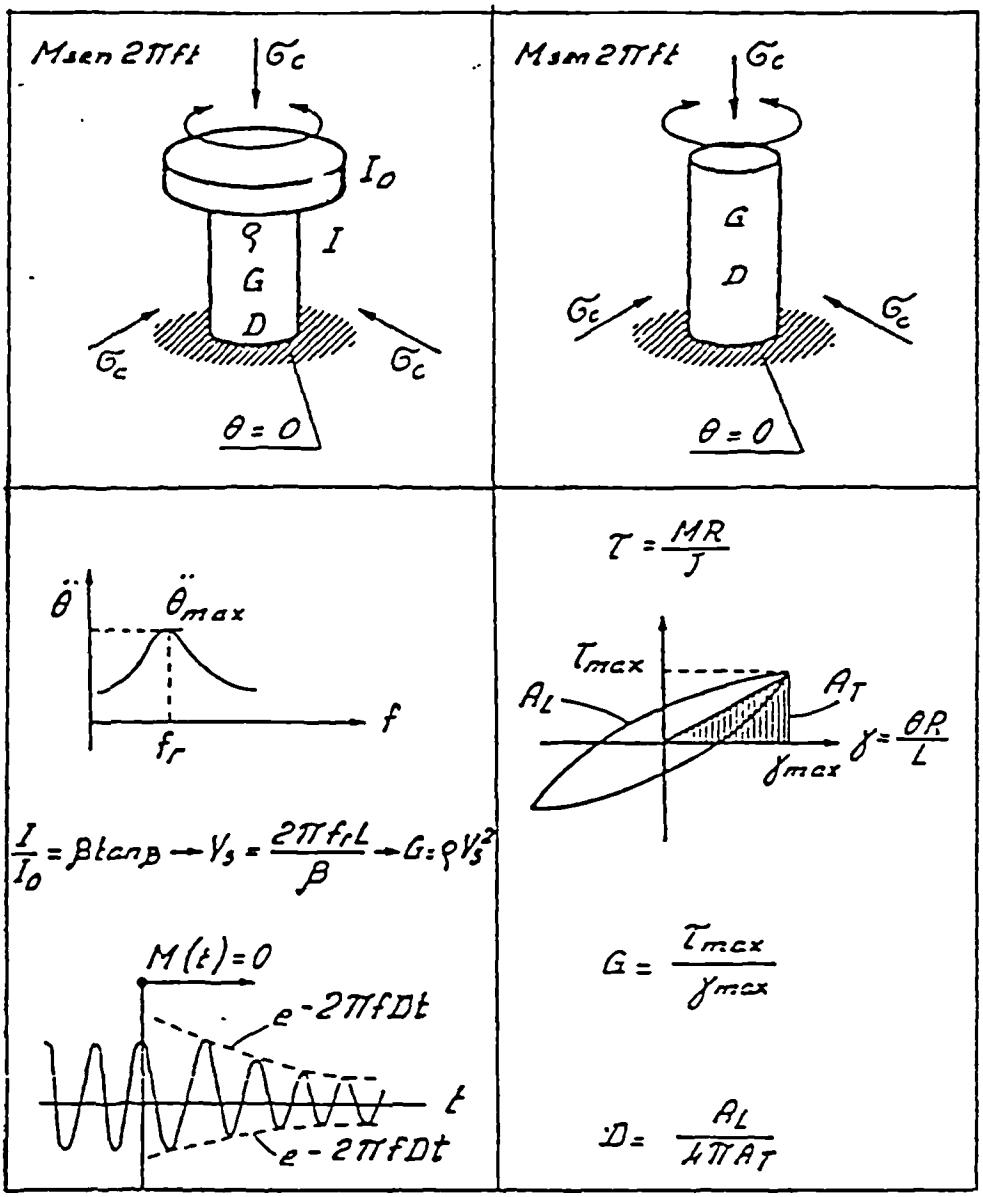

Figure 2.2.5 Loading conditions for resonant column, decay and cyclic torsion shear tests

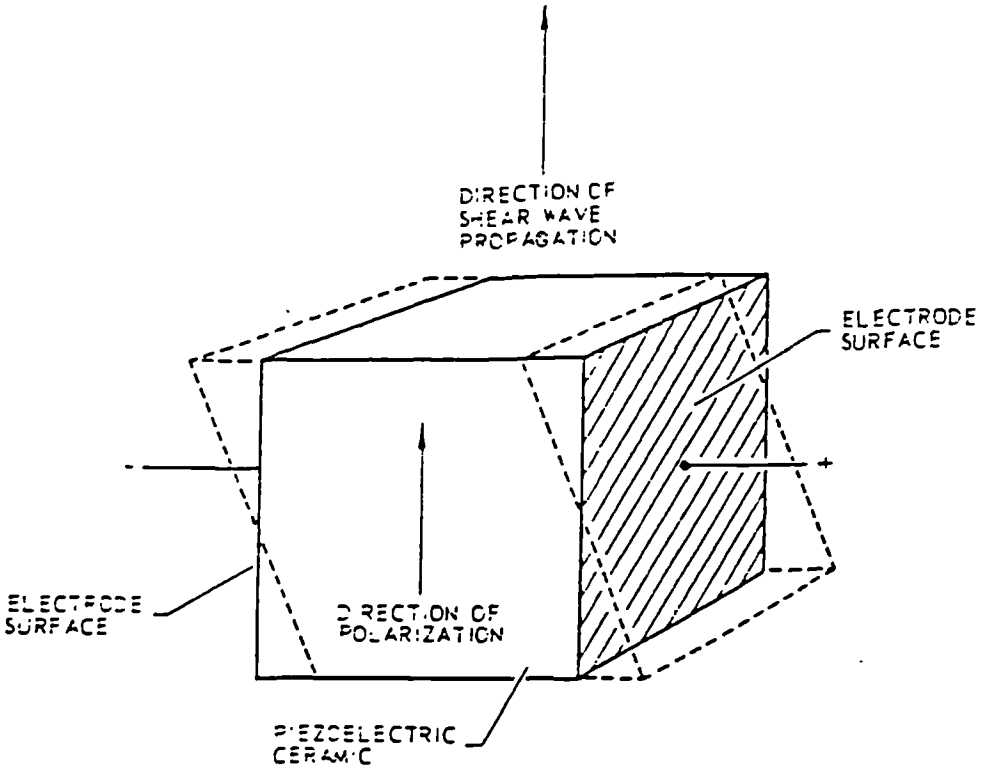

Figure 2.2.6 Shear plate transducer (after Shirley and Hampton, 1977)

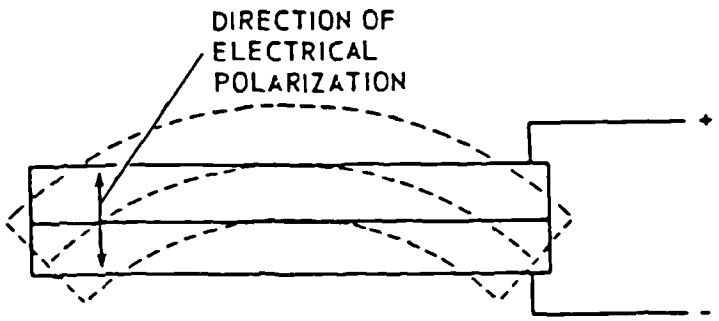

Figure 2.2.7 Bender element transducer (after Shirley, 1978)

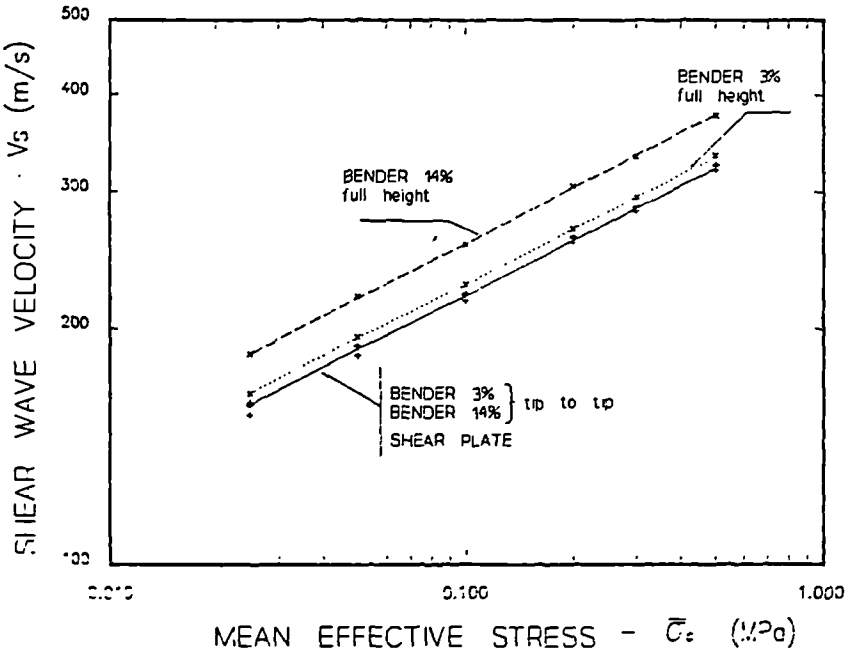

Figure 2.2.8 Calibration for effective length (after Brignoli and Gotti, 1992)

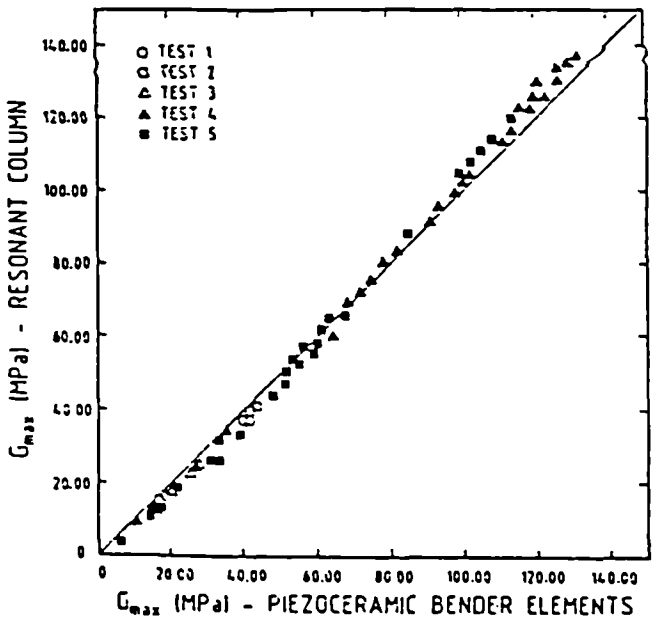

Figure 2.2.9 Comparison of very small strain stiffness as obtained from resonant column and bender element tests (after Dyvick and Madshus, 1985)

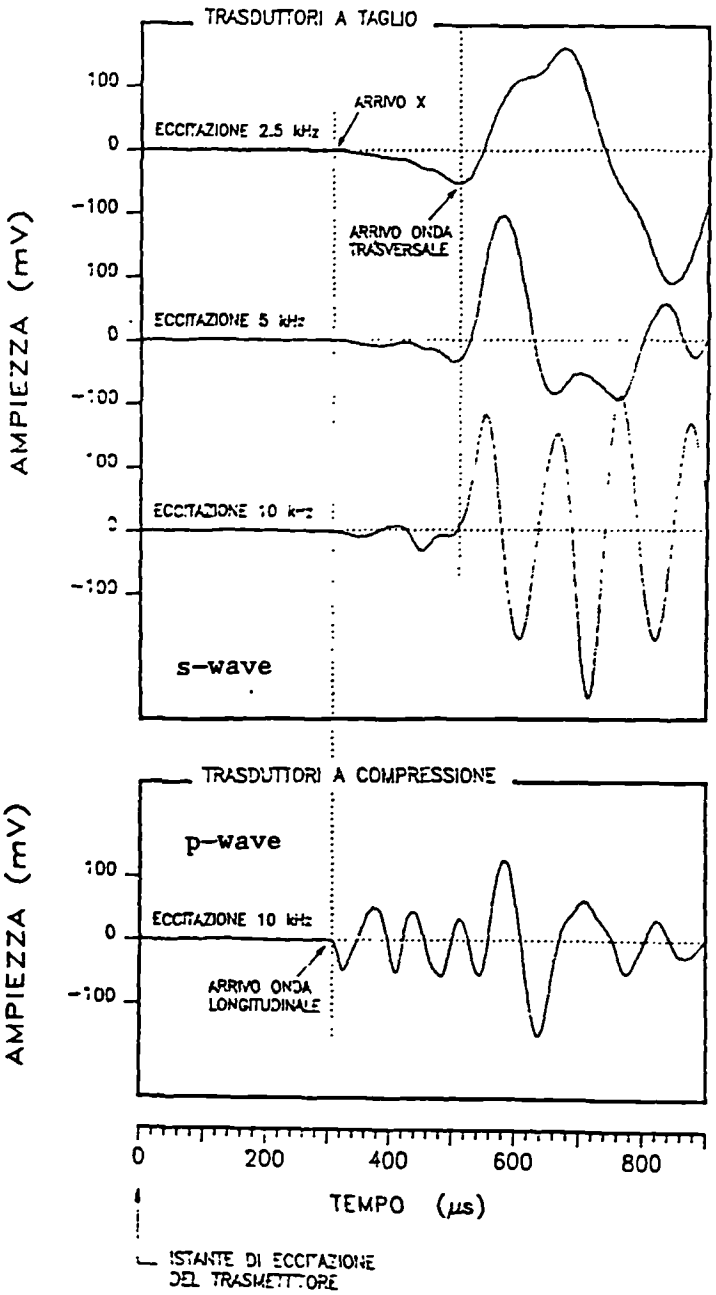

Figure 2.2.10 Measurement of wave velocities with piezoelectric transducers: example of the received signals. (after Brignoli and Gotti, 1992)

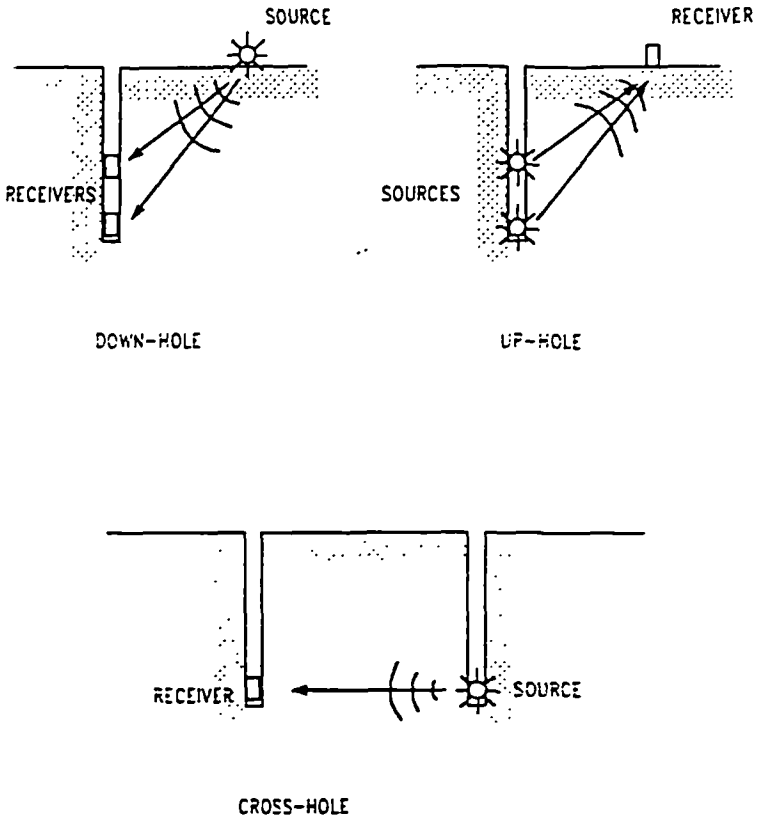

Figure 2.2.11 Location of source and receivers in cross-hole, down-hole and up-hole techniques

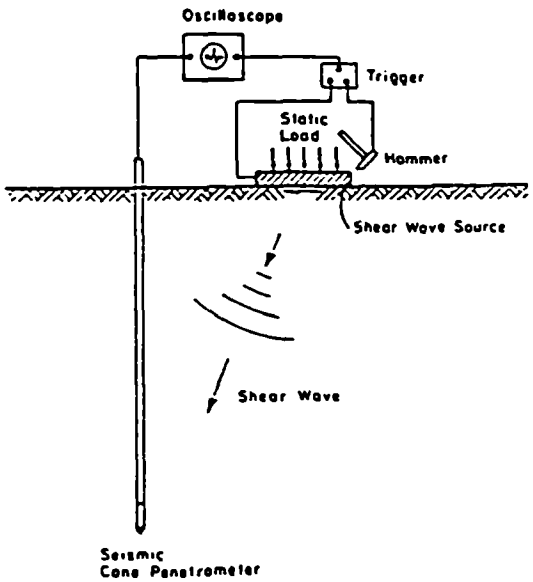

Figure 2.2.12 Schematic layout of seismic cone technique (after Campanella, 1986)

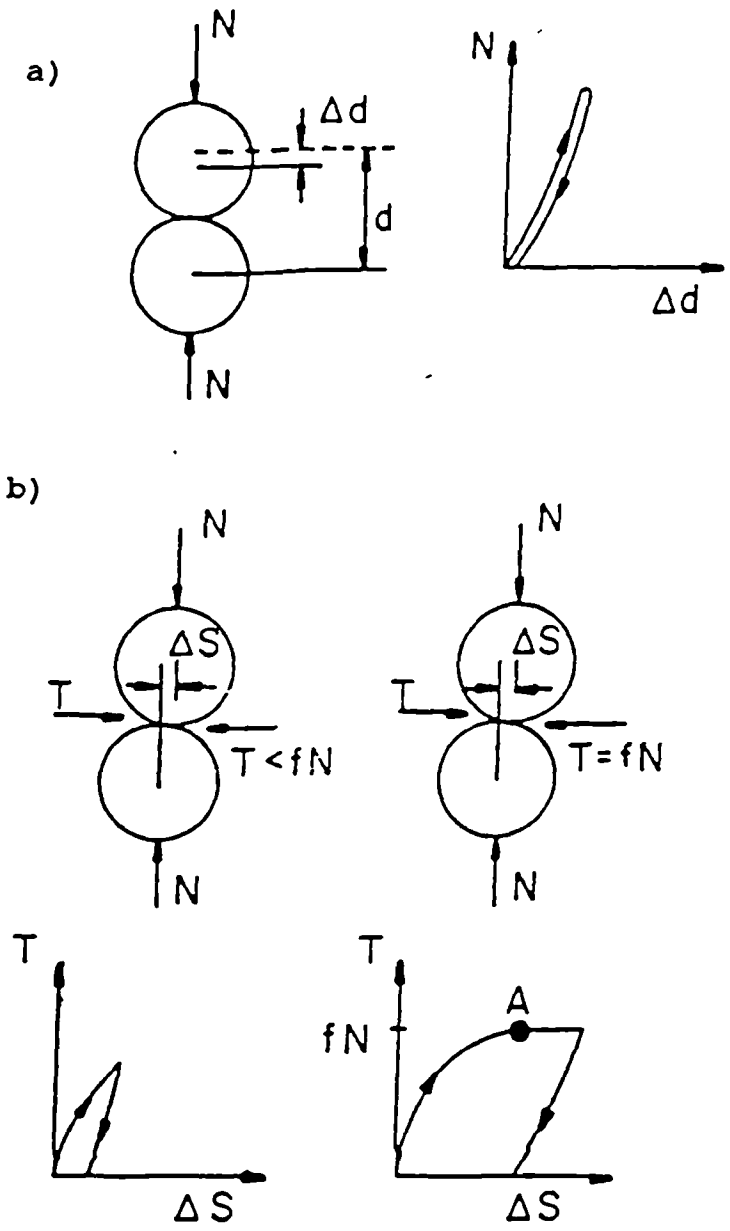

Figure 2.3.1 Deformation of two elastic spheres in contact. (a) under normal loads only (b) under normal and tangential forces (after Hardin, 1978)

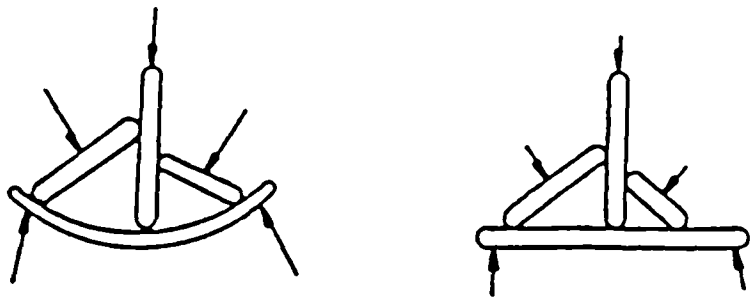

Figure 2.3.2 Deformation of thin plate-like particles (after Hardin, 1978)

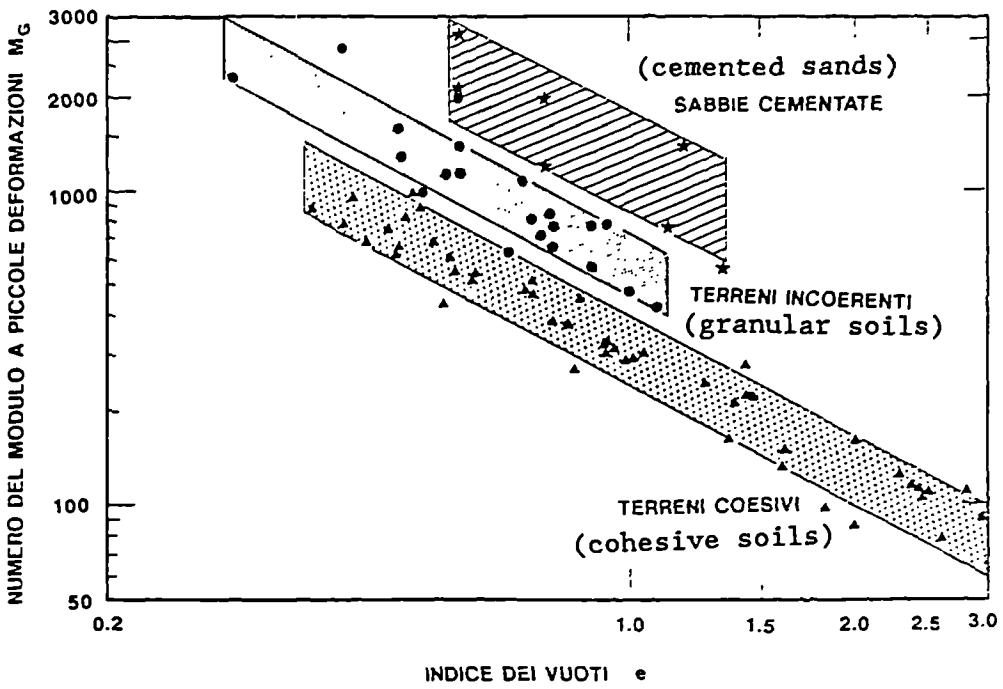

Figure 2.3.3 Experimental values of M_G for different soils plotted against voids ratio (after Lo Presti, 1989)

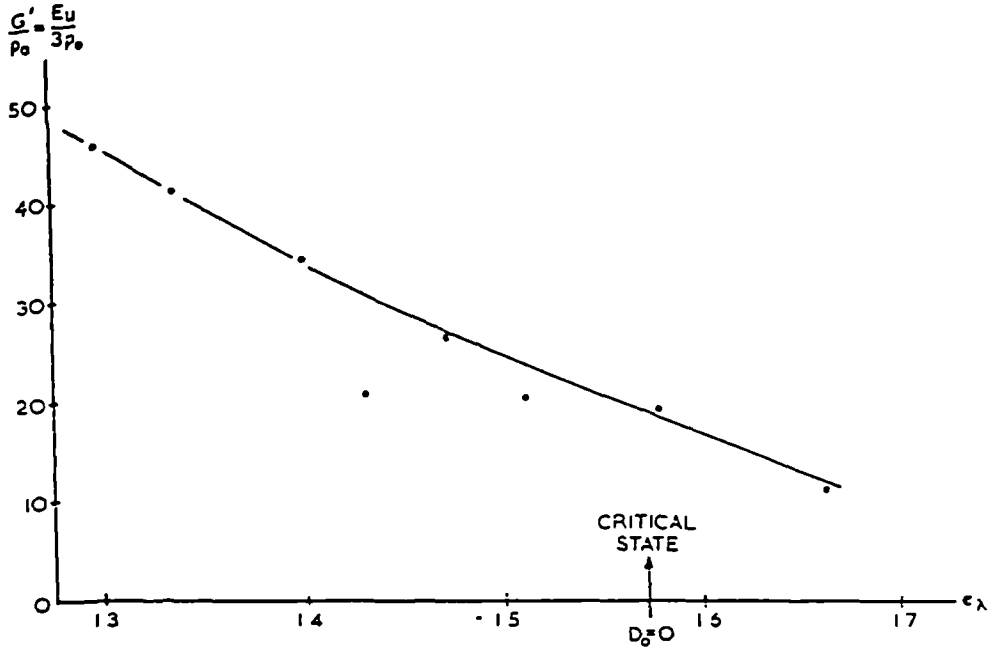

Figure 2.3.4 Variation of normalised stiffness with e_λ for undisturbed London clay (after Wroth, 1971)

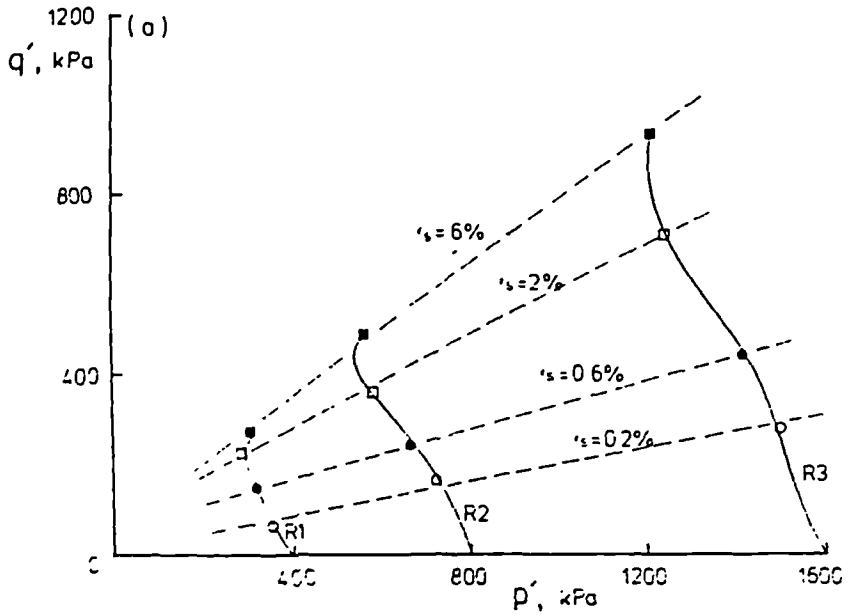

Figure 2.3.5 Stress paths and equal axial strain contours for a set of three undrained triaxial tests on a glacial till soil (after Little and Atkinson, 1988)

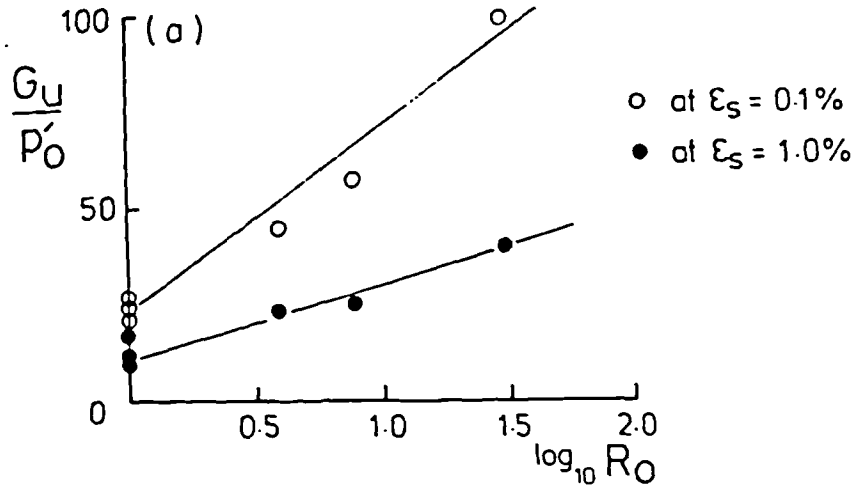

Figure 2.3.6 Variation of normalised stiffness with overconsolidation ratio at different strain levels for a glacial till soil (after Little and Atkinson, 1988)

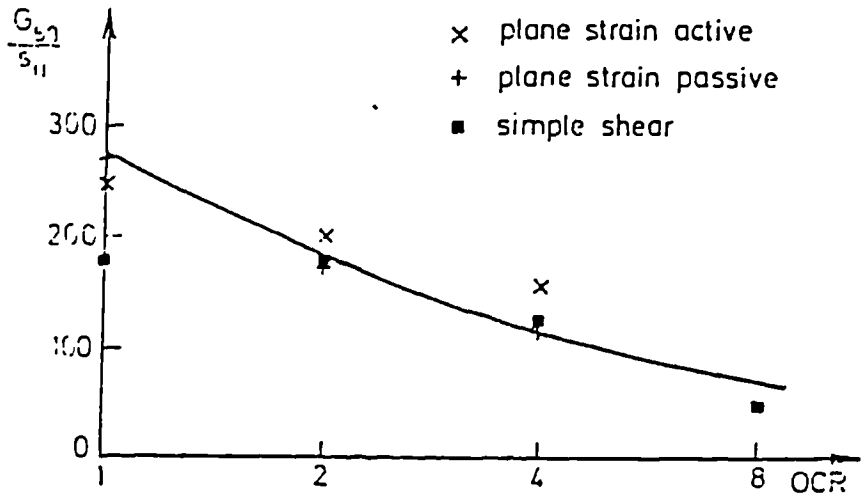

Figure 2.3.7 Variation of rigidity index with overconsolidation for Boston Blue clay (after Houlsby and Wroth, 1991)

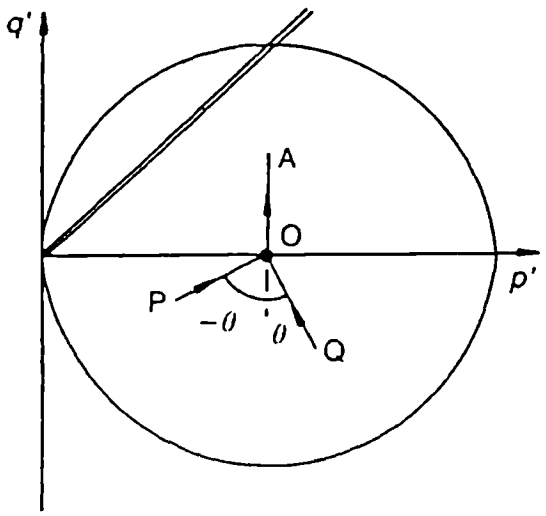

Figure 2.3.8 Definition of the angle θ of rotation between previous and current stress paths (after Atkinson et al., 1990).

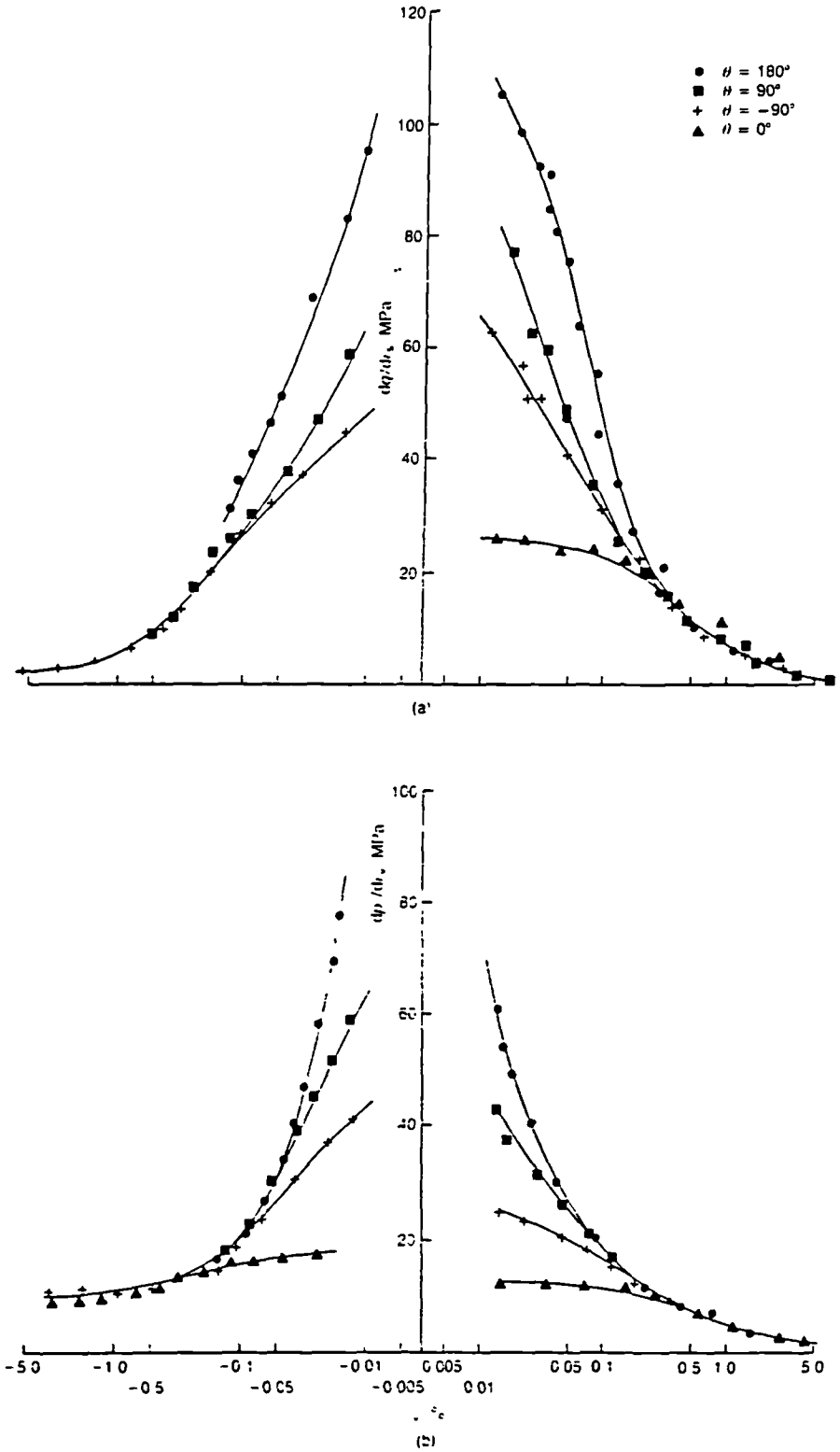

Figure 2.3.9 Stiffness of reconstituted London clay measured in a) constant p′ tests and b) constant q′ tests.

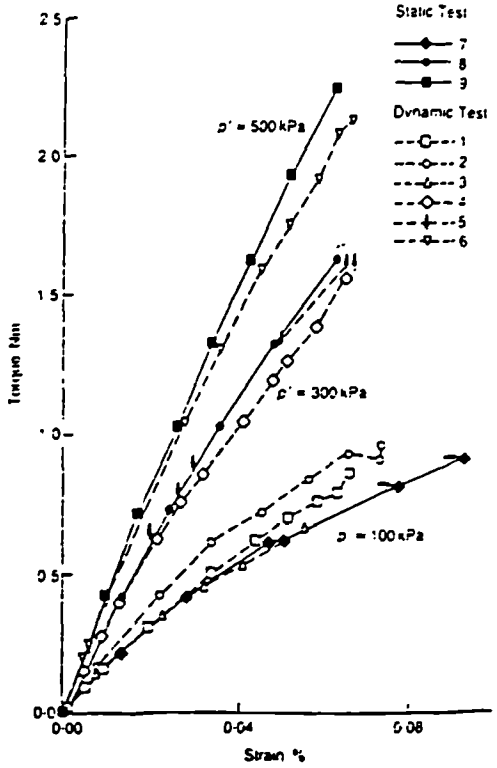

Figure 2.4.1 Torque–strain curves at different frequencies for Leighton Buzzard sand (after Bolton and Wilson, 1988)

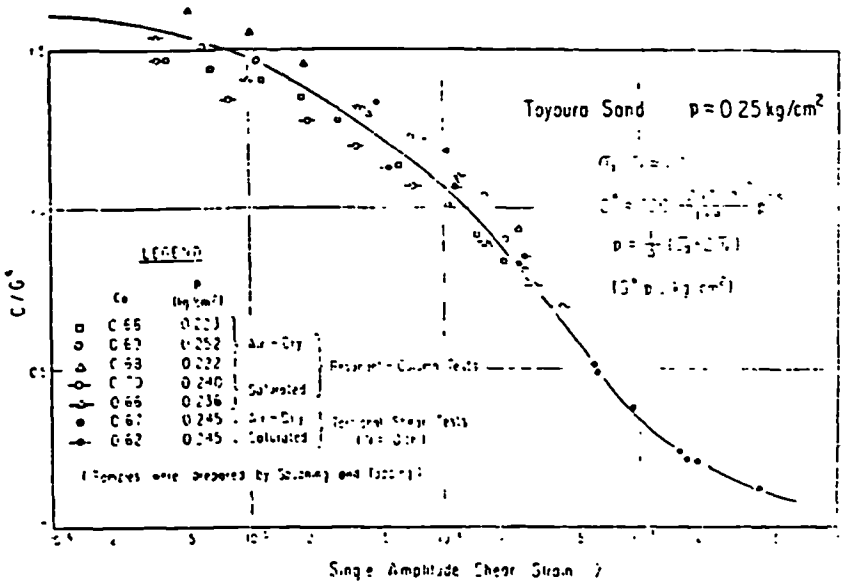

Figure 2.4.2 Decay of stiffness with shear strain amplitude for Toyoura sand from resonant column and cyclic torsion shear tests (after Iwasaki et al., 1978)

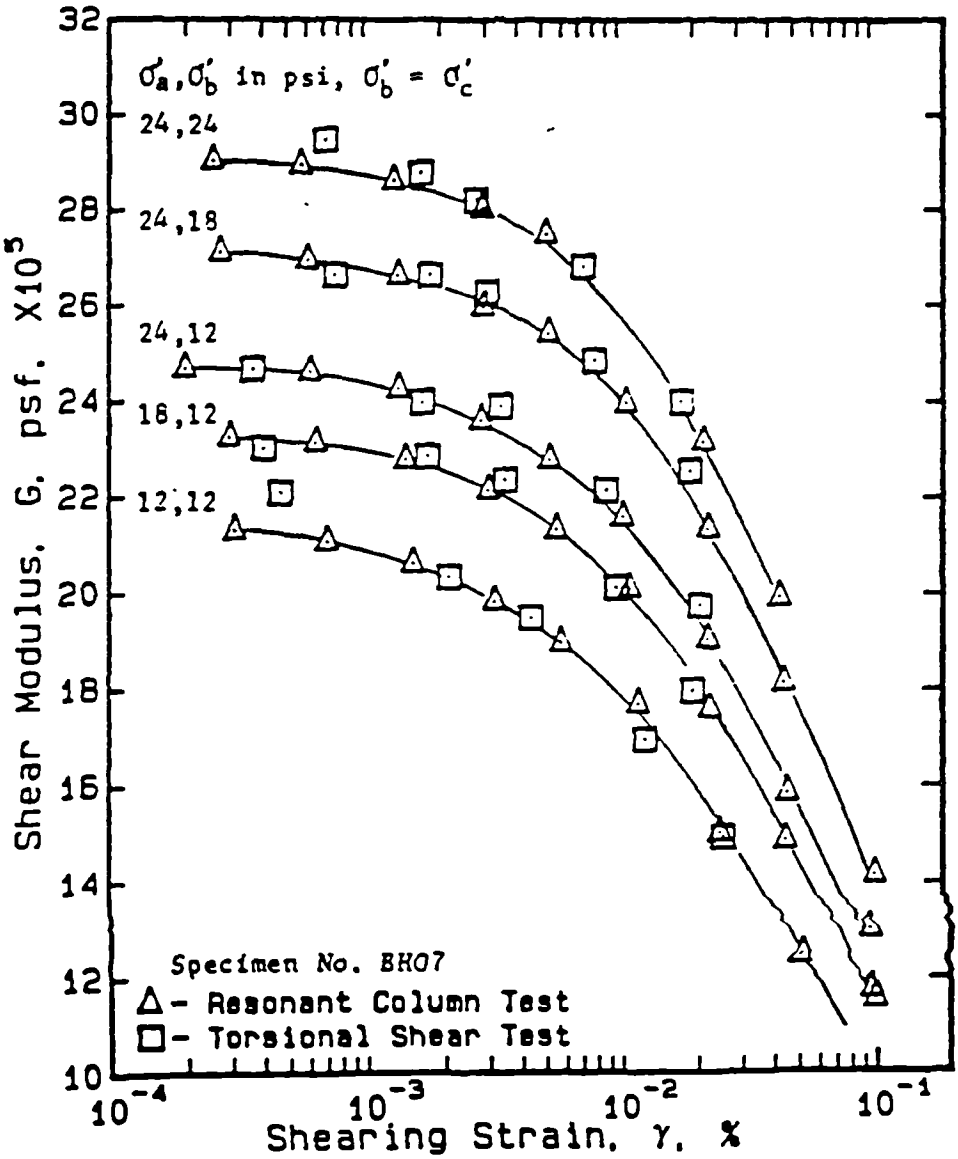

Figure 2.4.3 Decay of stiffness with shear strain amplitude for dry uniform washed mortar sand from resonant column and cyclic torsion shear tests (after Ni, 1987)

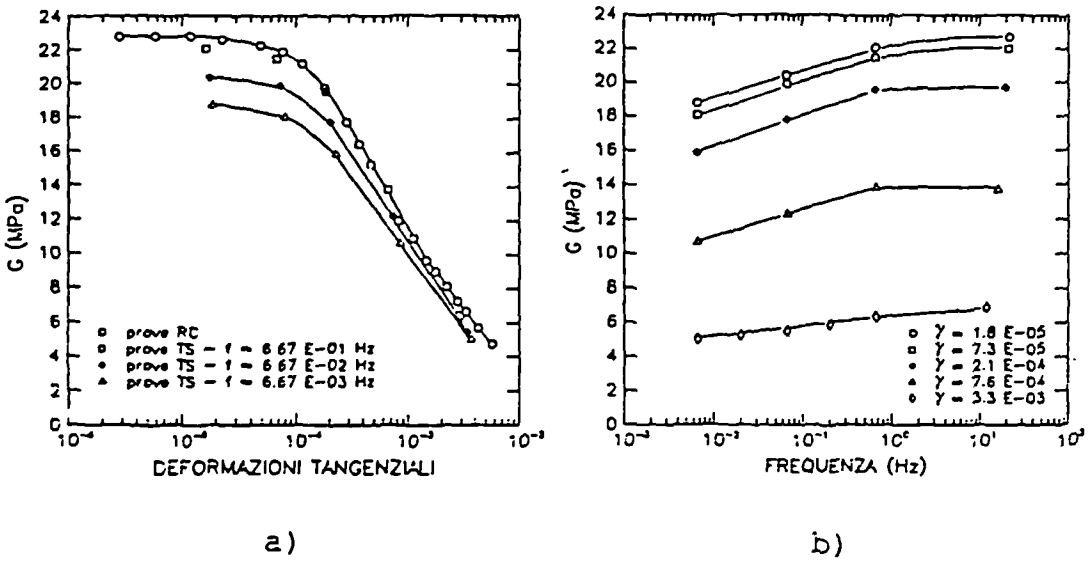

Figure 2.4.4 Typical curves of variation of shear modulus with (a) shear strain amplitude and (b) frequency of loading for Fucino clay (after Pane and Burghignoli, 1988)

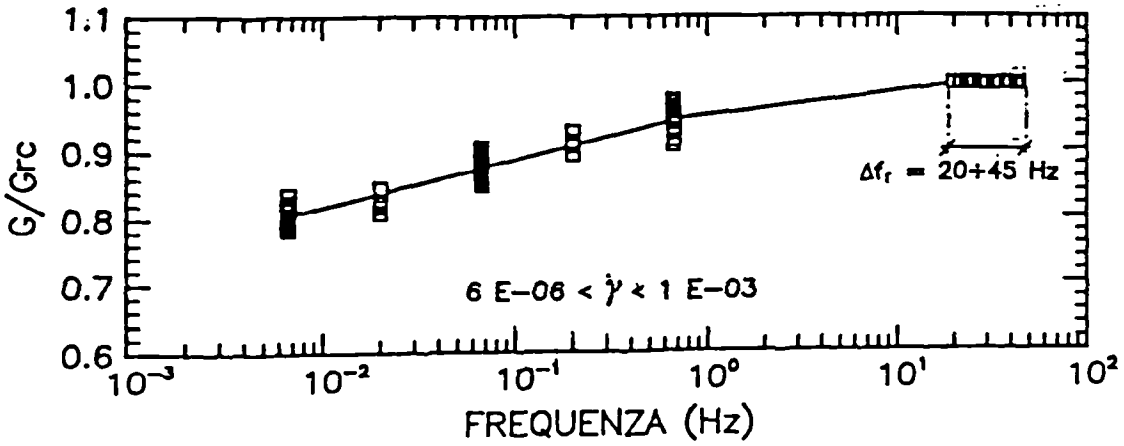

Figure 2.4.5 Variation of normalised shear modulus with frequency for Fucino clay (after Pane and Burghignoli, 1988)

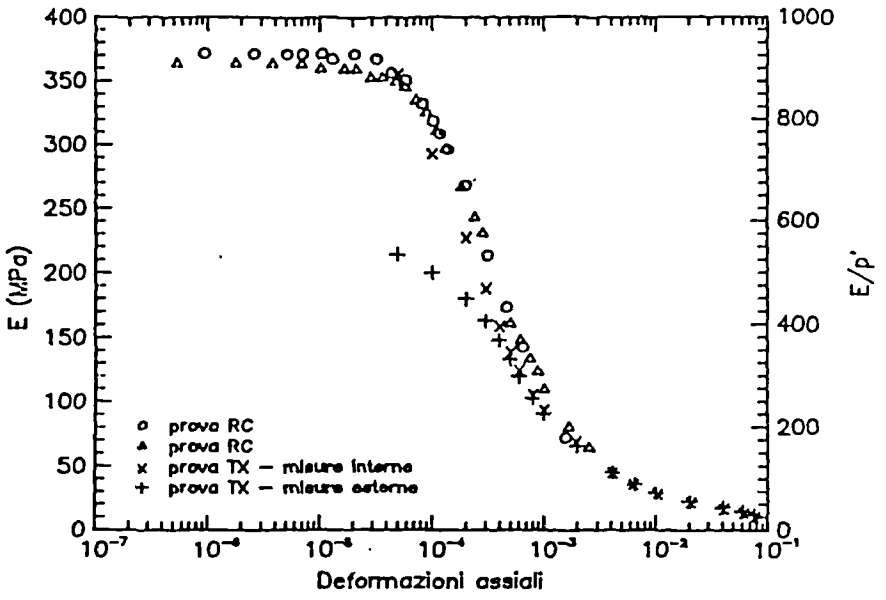

Figure 2.4.6 Comparison of shear stiffness as obtained from resonant column tests and undrained triaxial tests for Todi clay (after Rampello and Pane, 1988)

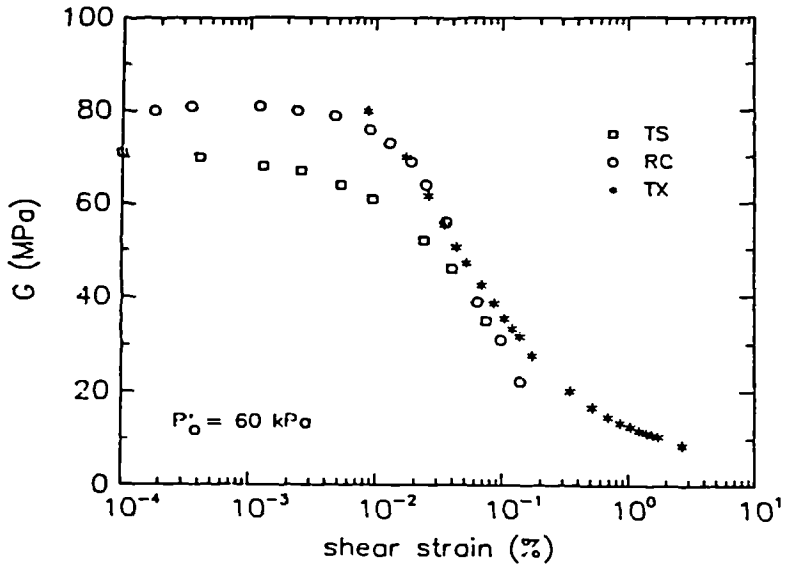

Figure 2.4.7 Comparison of shear stiffness as obtained from resonant column tests, cyclic torsion shear tests and undrained triaxial tests for Vallericca clay (after Georgiannou et al., 1991)

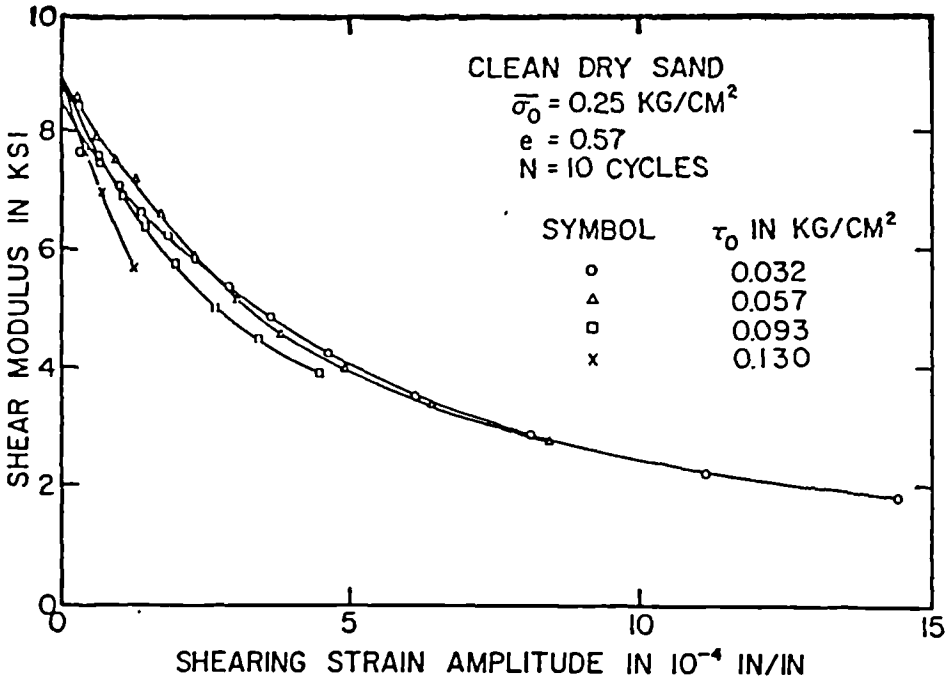

Figure 2.4.8 Decay of stiffness with shear strain amplitude under different initial stress states for a dry clean sand (after Hardin and Drnevich, 1972 a)

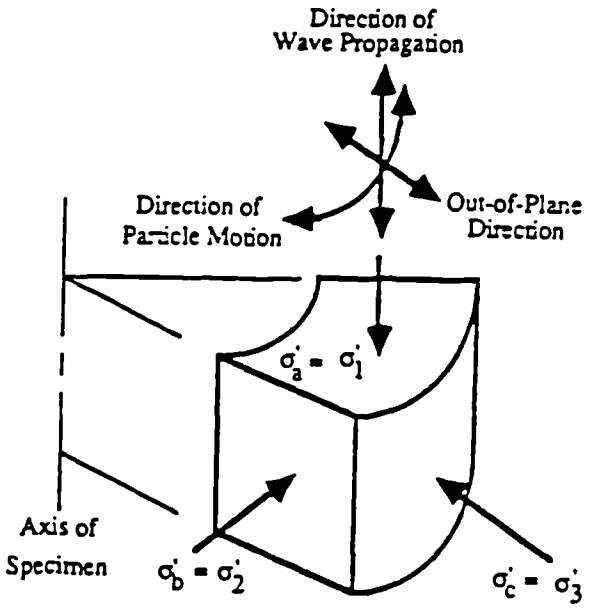

Figure 2.4.9 Stress state in torsion shear tests on hollow cylindrical samples (after Ni, 1987)

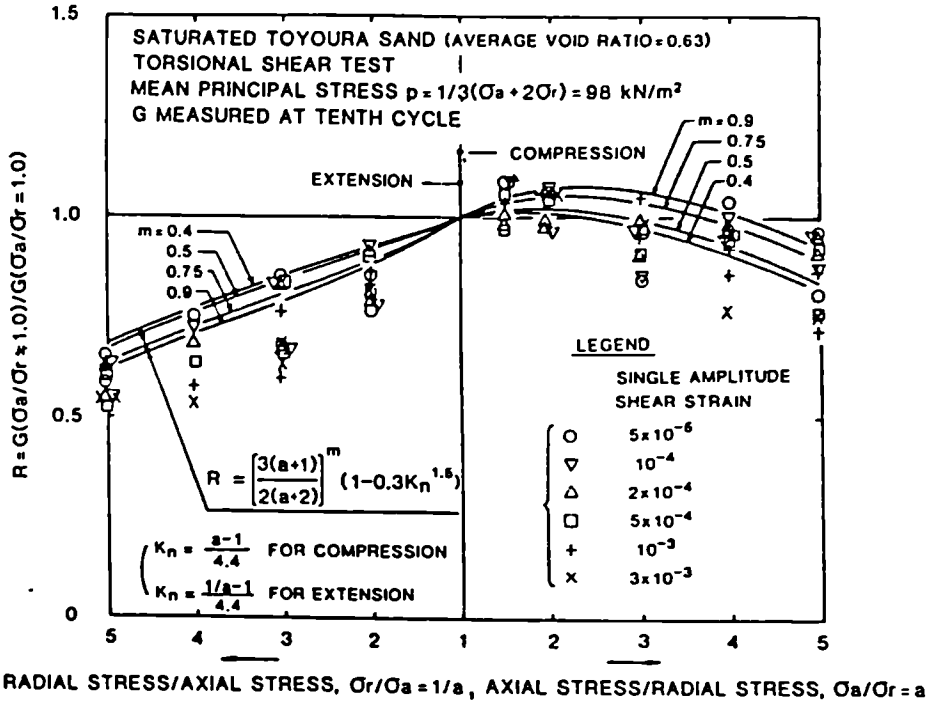

Figure 2.4.10 Dependence of very small strain stiffness on stress ratio (after Tatsuoka et al., 1978)

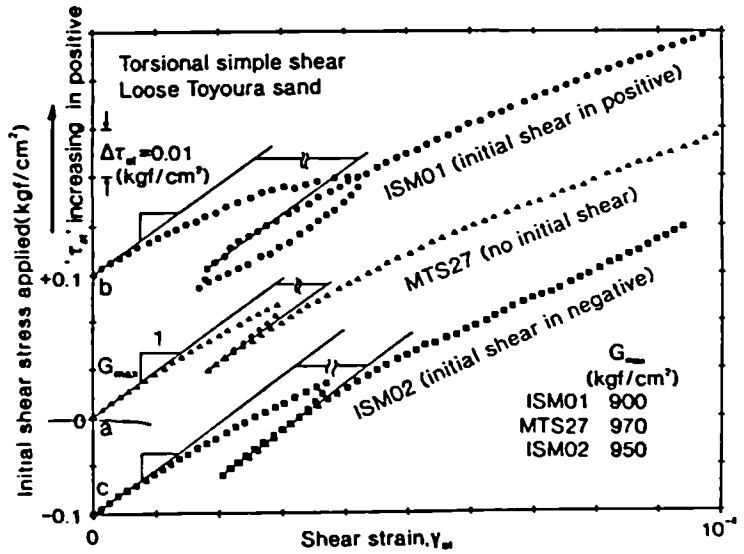

Figure 2.4.11 Detail of the initial part of the stress-strain curve obtained from monotonic torsion shear tests on loose Toyoura sand (after Teachavorasinskun et al., 1991)

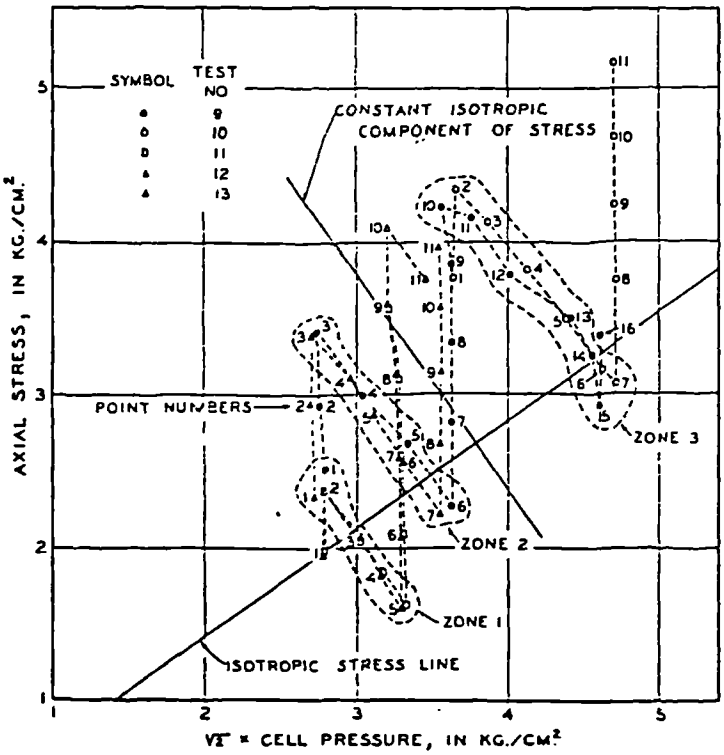

Figure 2.4.12 Stress paths and states of stress for vibration tests (after Hardin and Black, 1968)

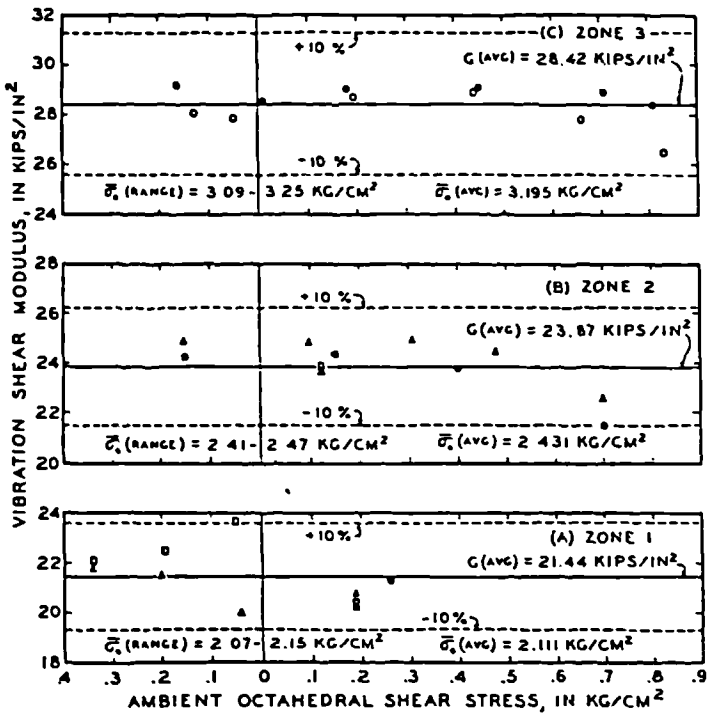

Figure 2.4.13 Effects of stress anisotropy on very small strain stiffness for a kaolinite clay (after Hardin and Black, 1968)

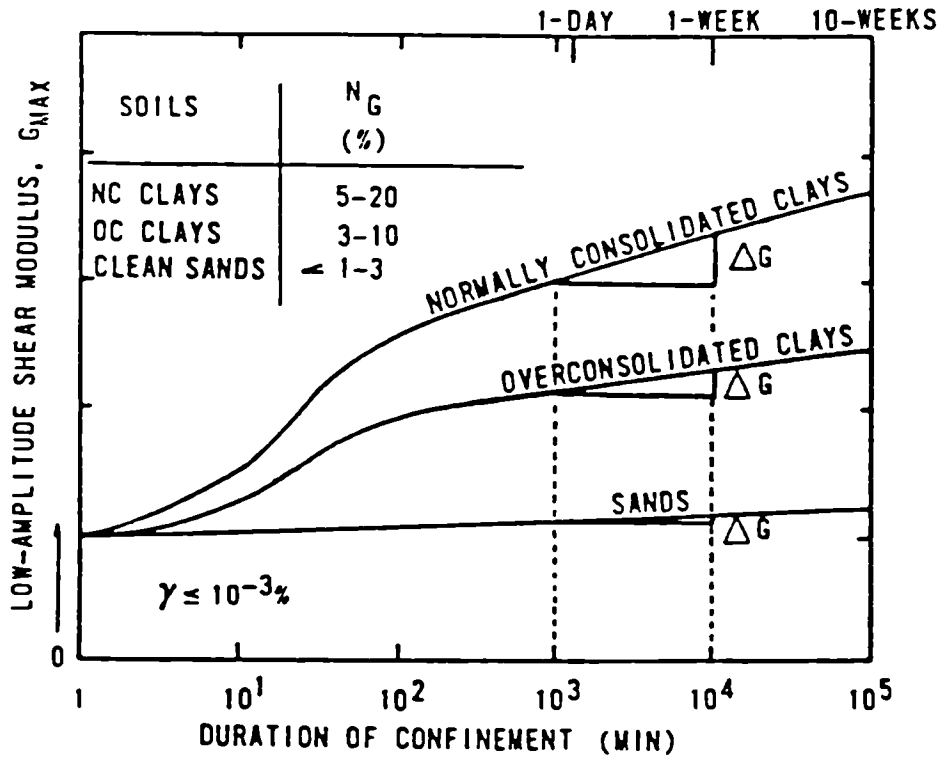

Figure 2.4.14 Effects of time of confinement on very small strain stiffness of soils (after Anderson and Stokoe, 1978)

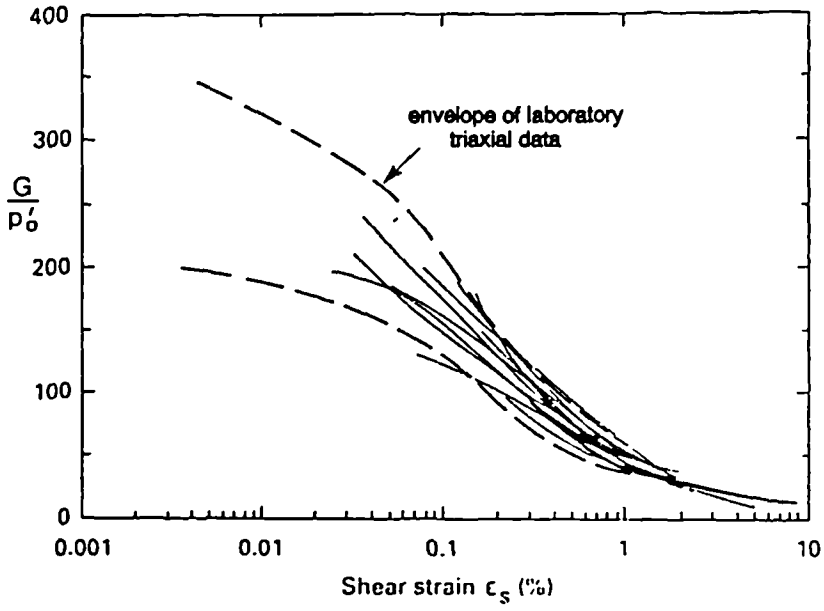

Figure 2.5.1 Secant stiffnesses derived from plate loading tests and triaxial tests for a glacial clay (after Hird et al., 1991)

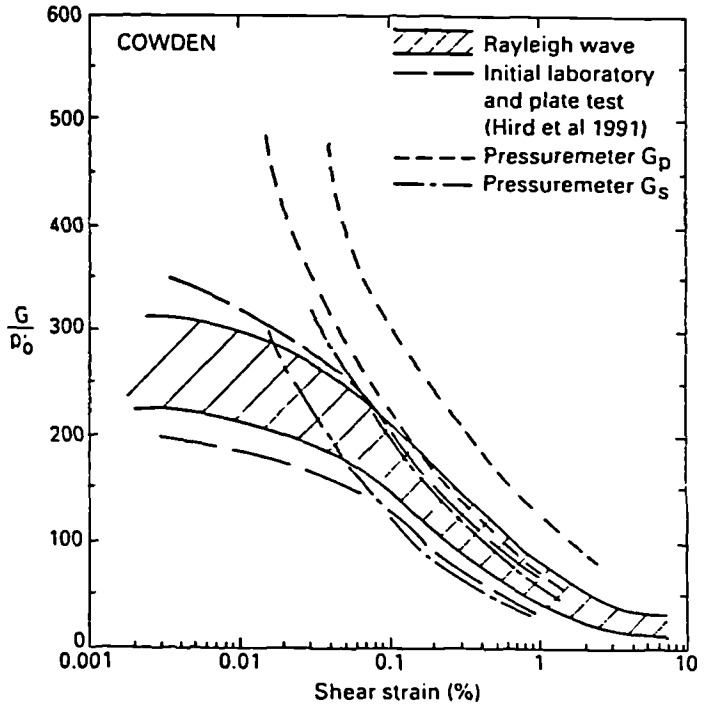

Figure 2.5.2 Normalised stiffness versus shear strain amplitude from different tests at Cowden (after Powell and Butcher, 1991)

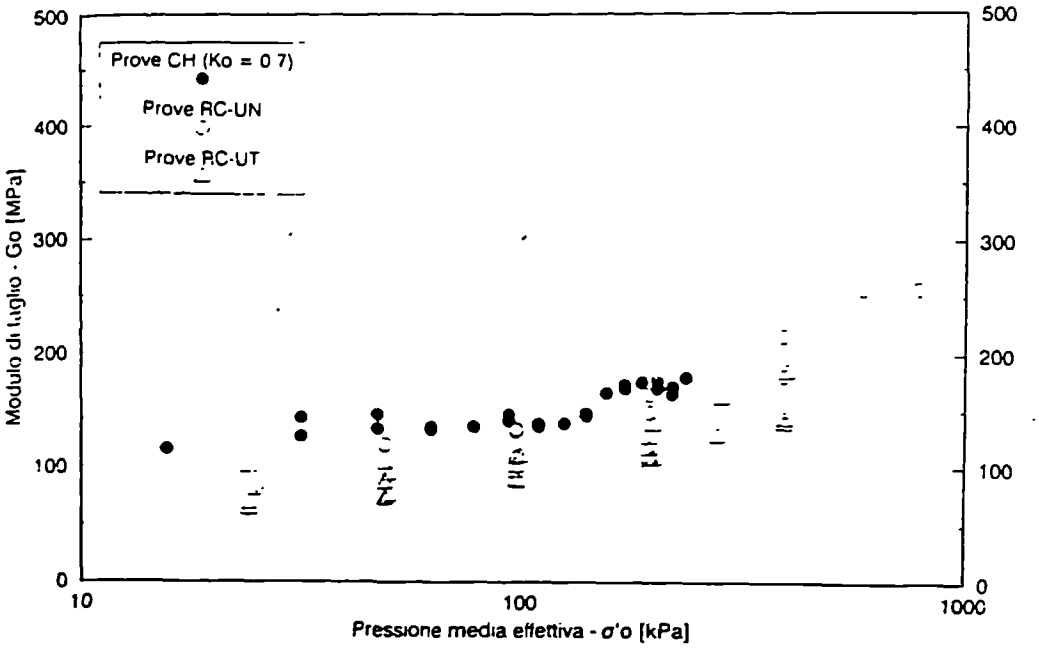

Figure 2.5.3 Very small strain stiffness versus mean effective stress from resonant column and cross-hole tests at Bilancino dam (after Silvestri, 1991)

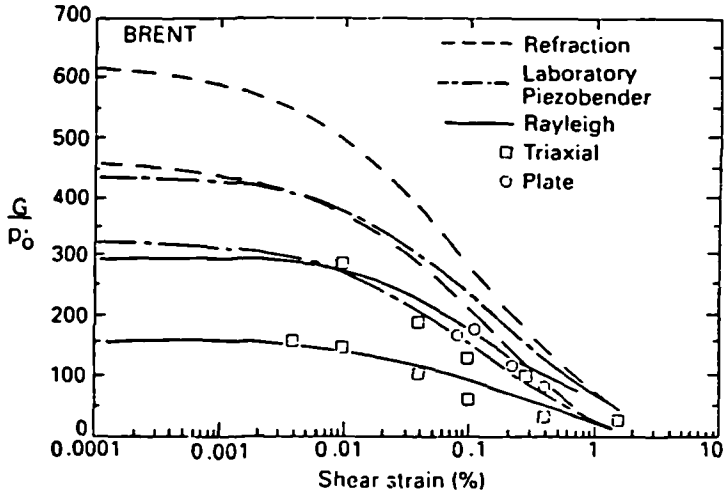

Figure 2.5.4 Normalised stiffness versus shear strain amplitude from different tests at Brent (after Powell and Butcher, 1991)

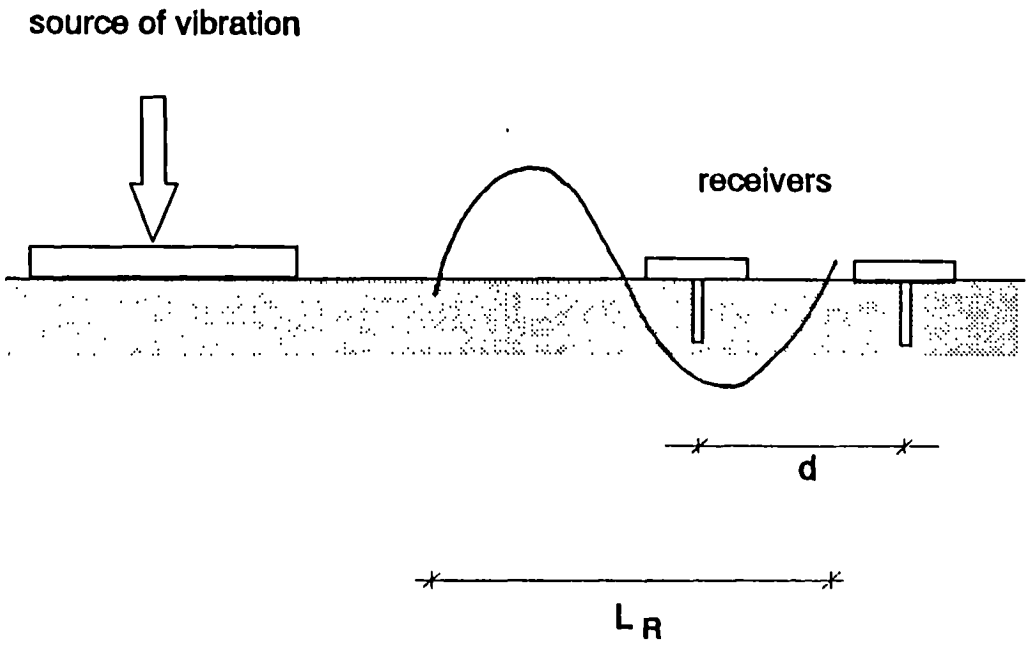

Figure 3.2.1 Layout of surface wave experiment.

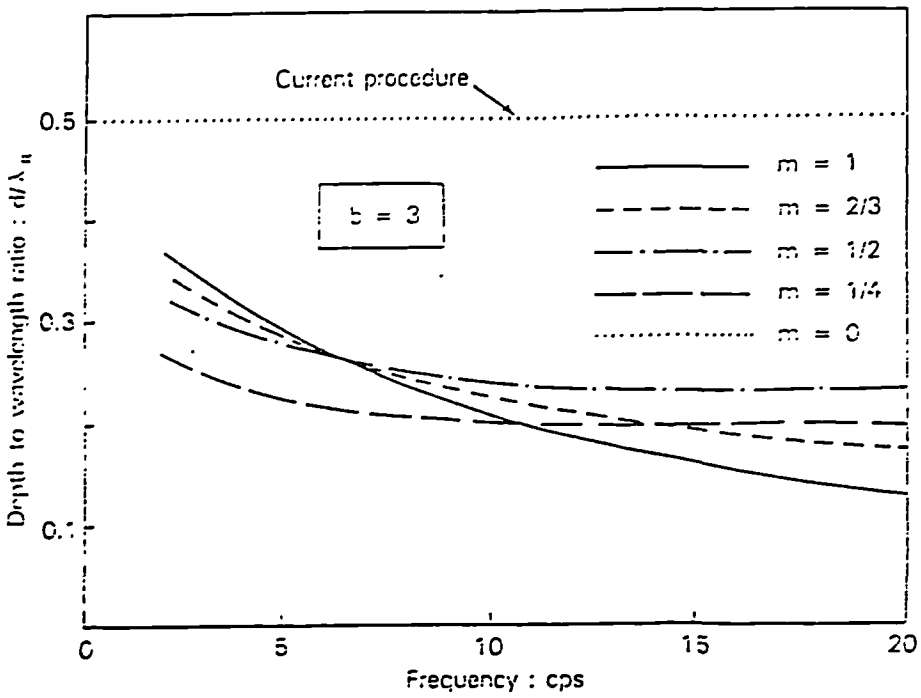

Figure 3.2.2 Depth to wavelength ratio versus frequency. (after Gazetas, 1982).

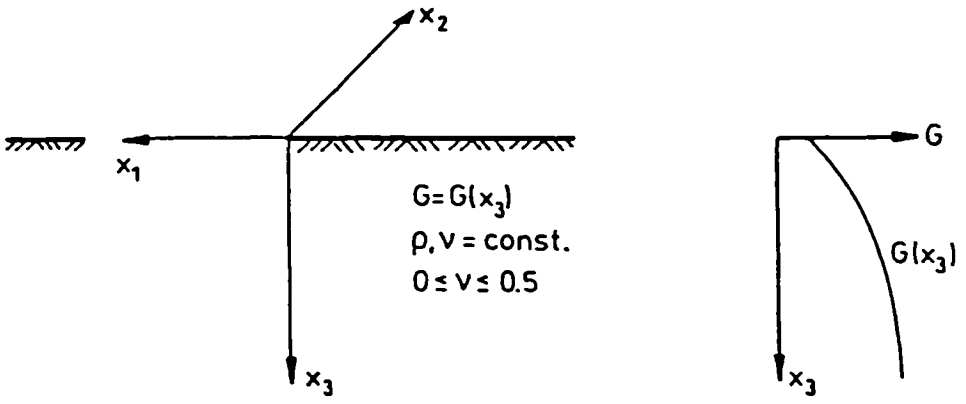

Figure 3.2.3 Variation of shear modulus with depth. (After Vrettos, 1990)

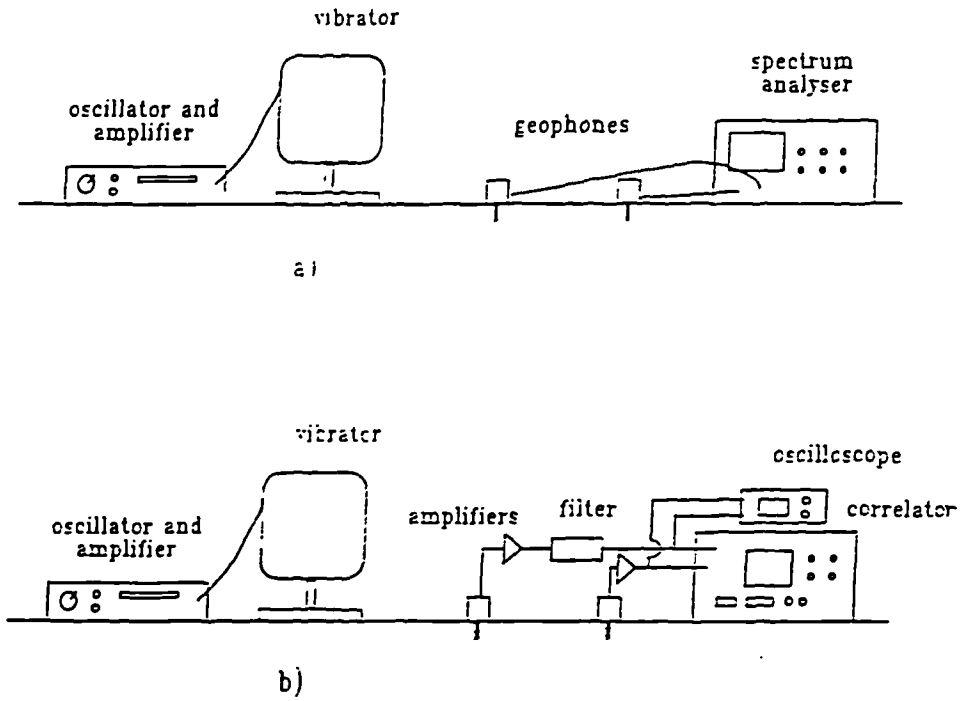

Figure 3.2.4 (a) spectrum analyser technique (b) correlator technique.

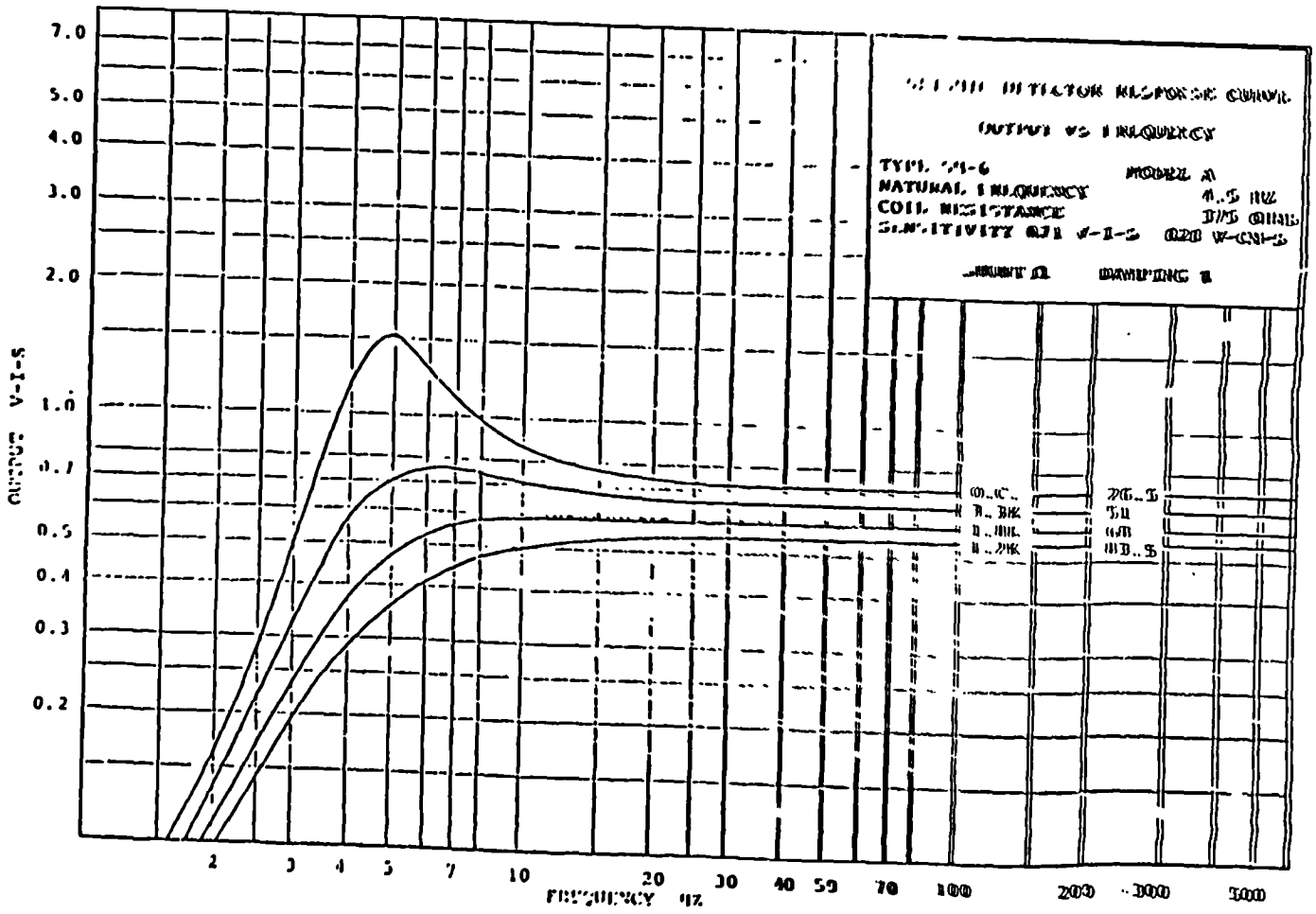

Figure 3.2.5 Response curves for geophone Sensor model SM6.

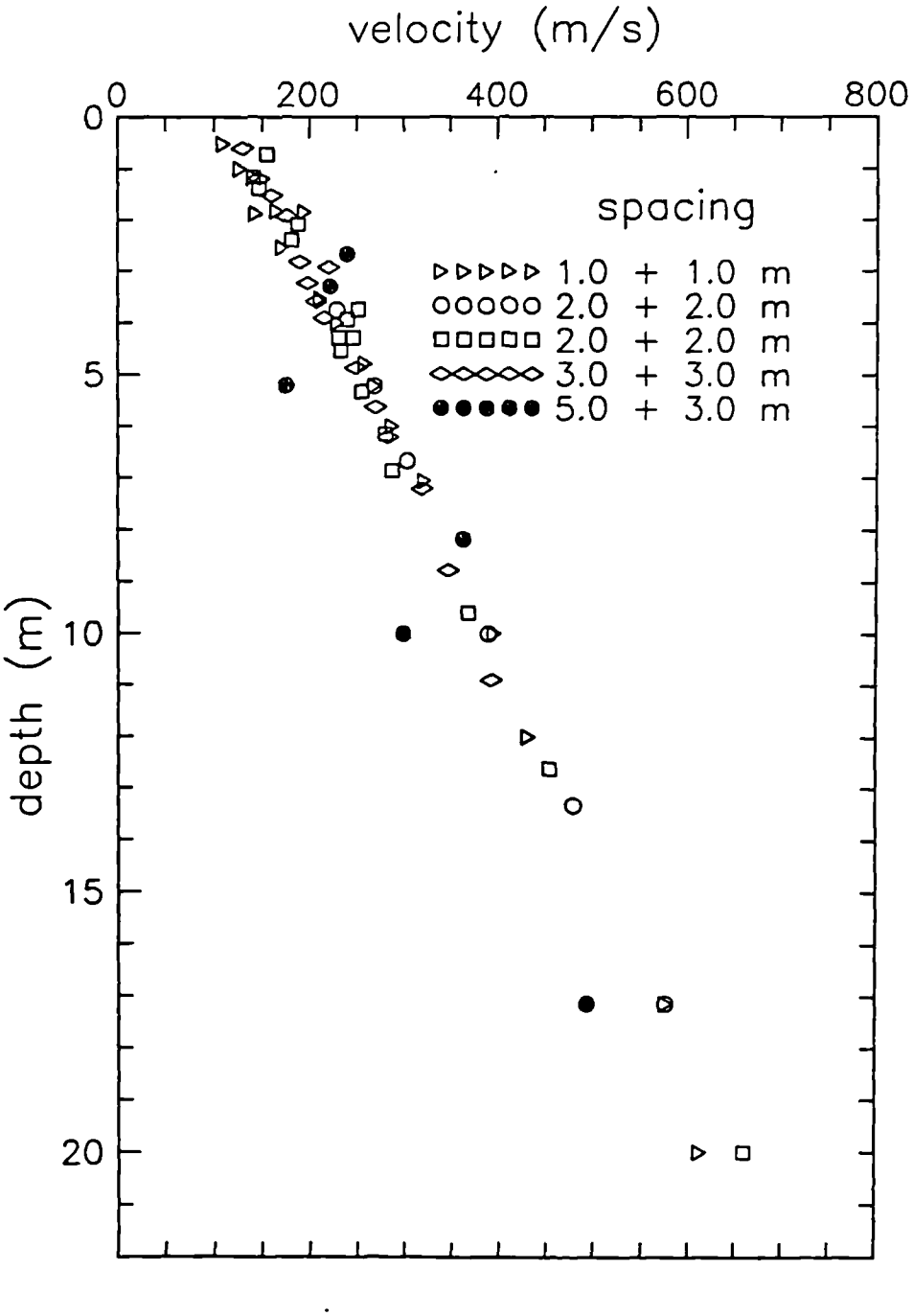

Fig. 3.2.6. North Field, Garston. Analyser technique. Effect of spacing on observed value of Rayleigh wave velocity.

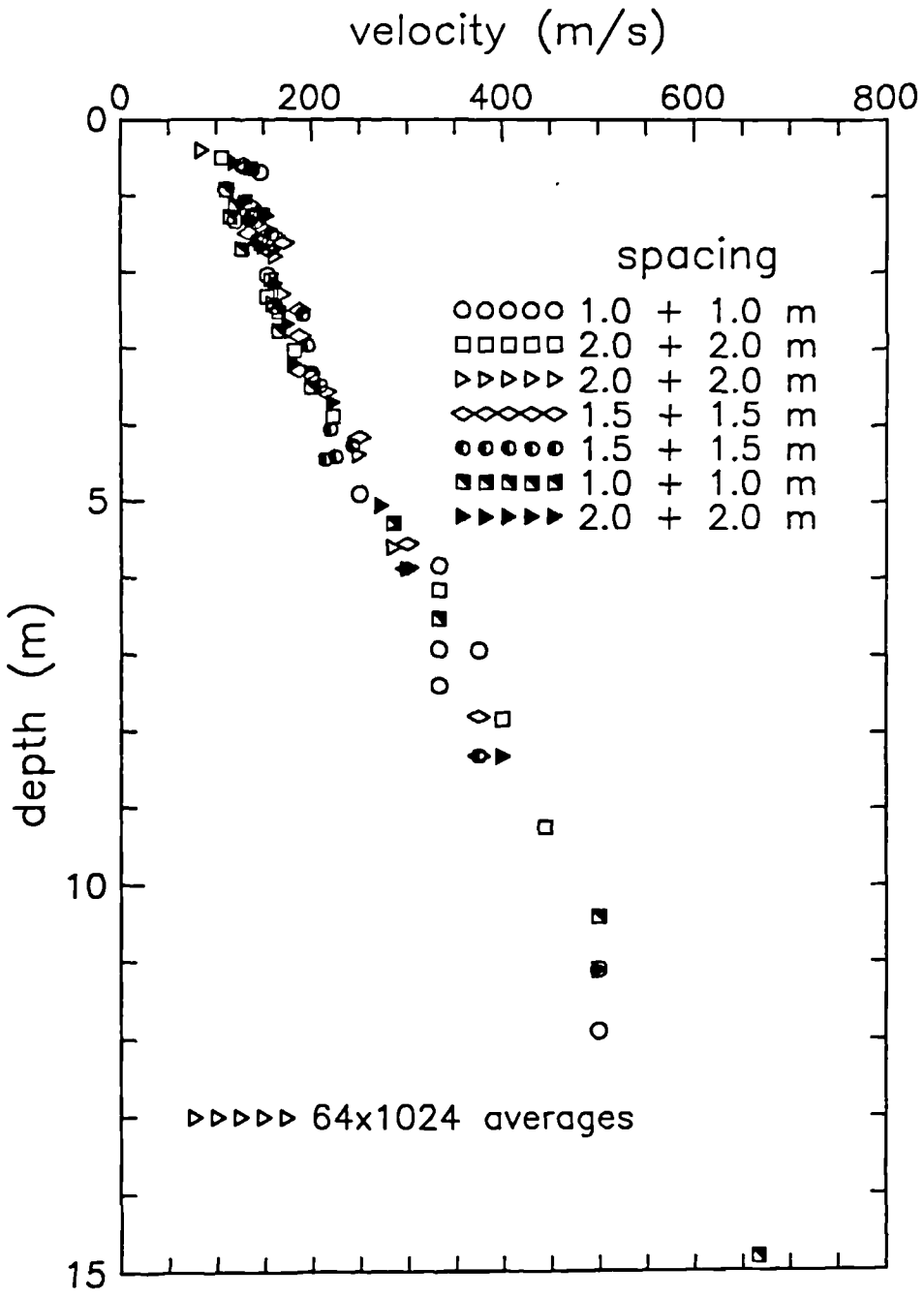

Figure 3.2.7 North Field, Garston. Correlator technique. Effect of spacing on observed value of Rayleigh wave velocity.

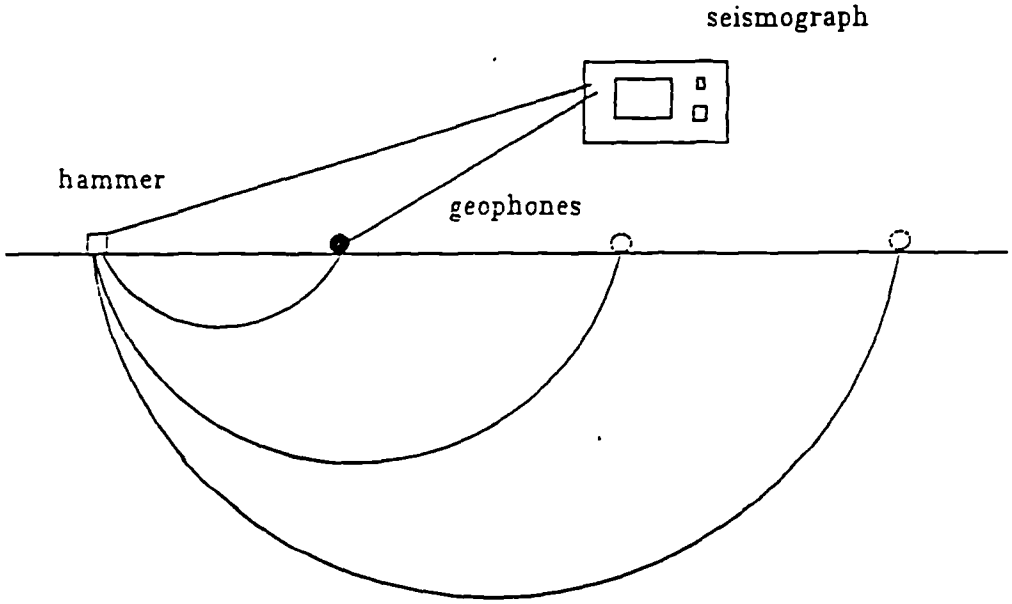

Figure 3.3.1 Layout of pulse refraction survey.

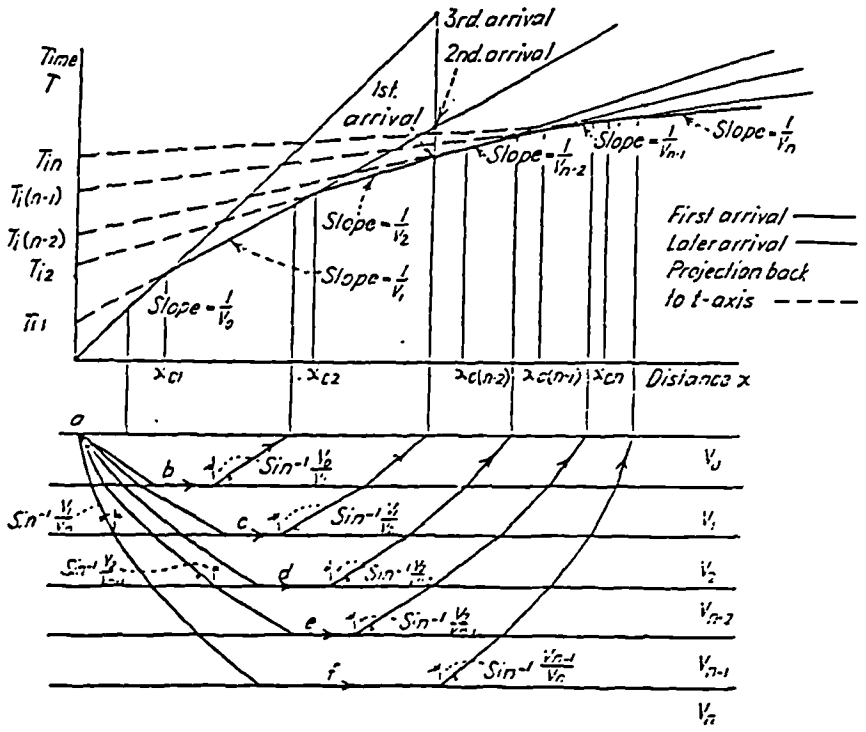

Figure 3.3.2 Ray paths and time distance plot for multilayered earth. (after Dobrin, 1960).

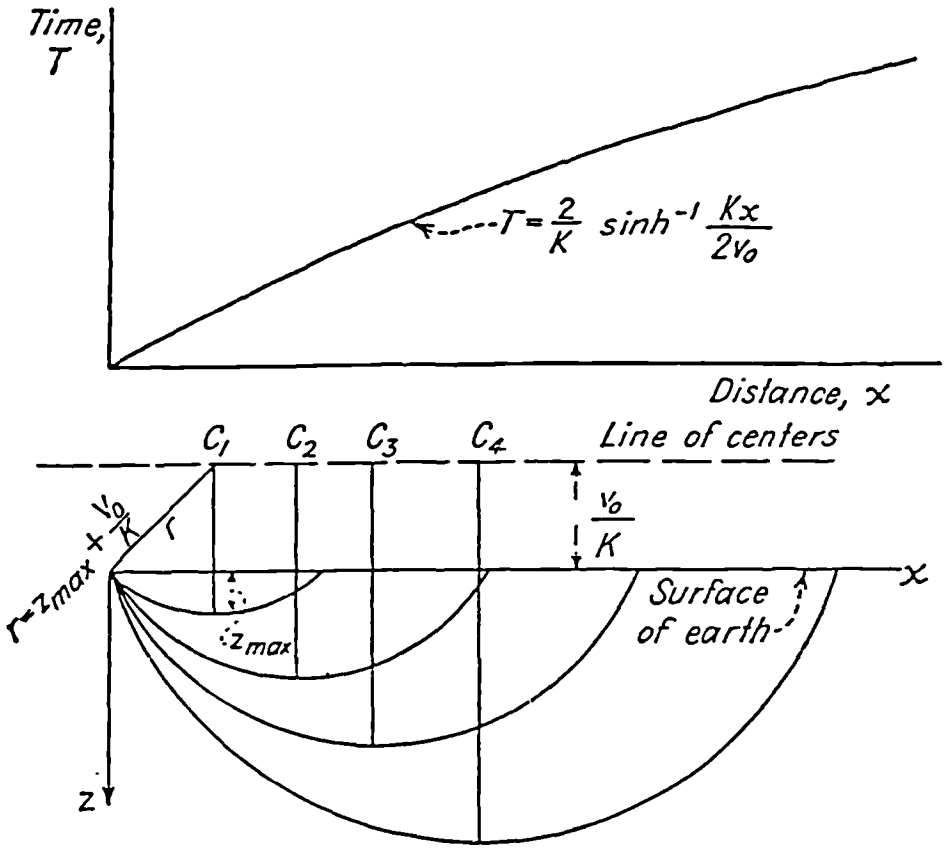

Figure 3.3.3 Ray paths and time distance plot for linear increase of velocity with depth. (after Dobrin 1960).

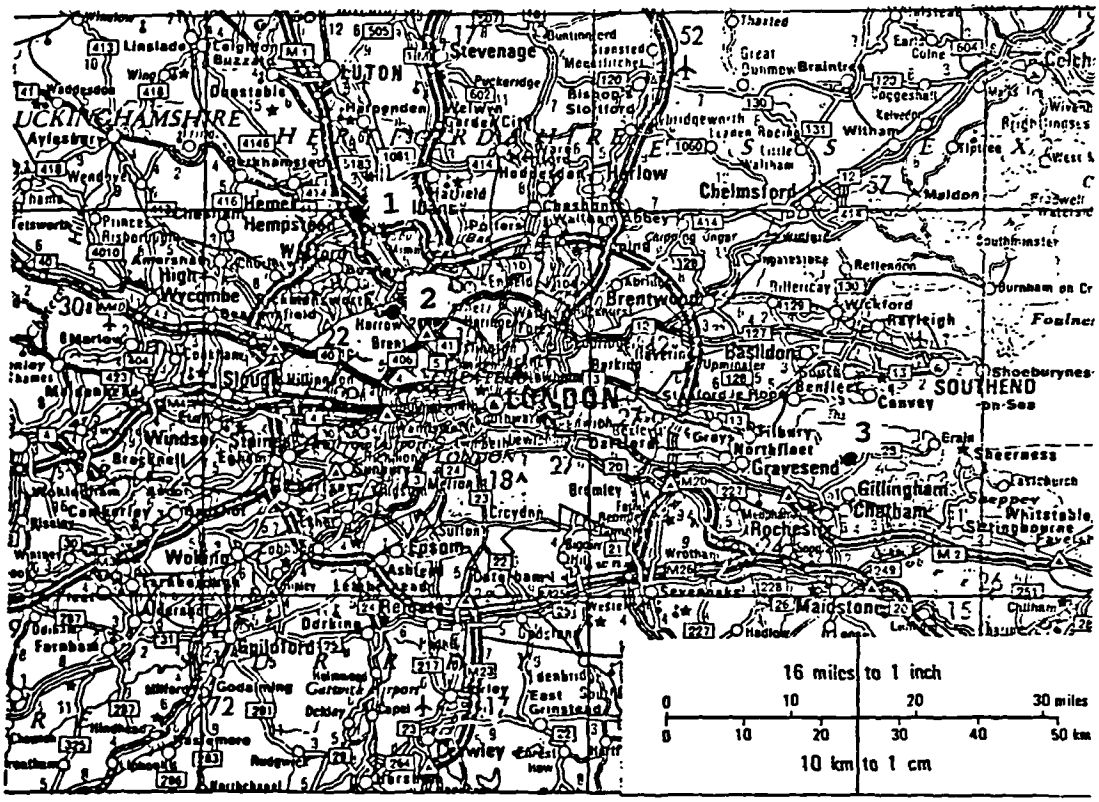

Figure 3.4.1 Location of sites used for the site work.
1. North Field 2. Canons Park 3. Chattenden

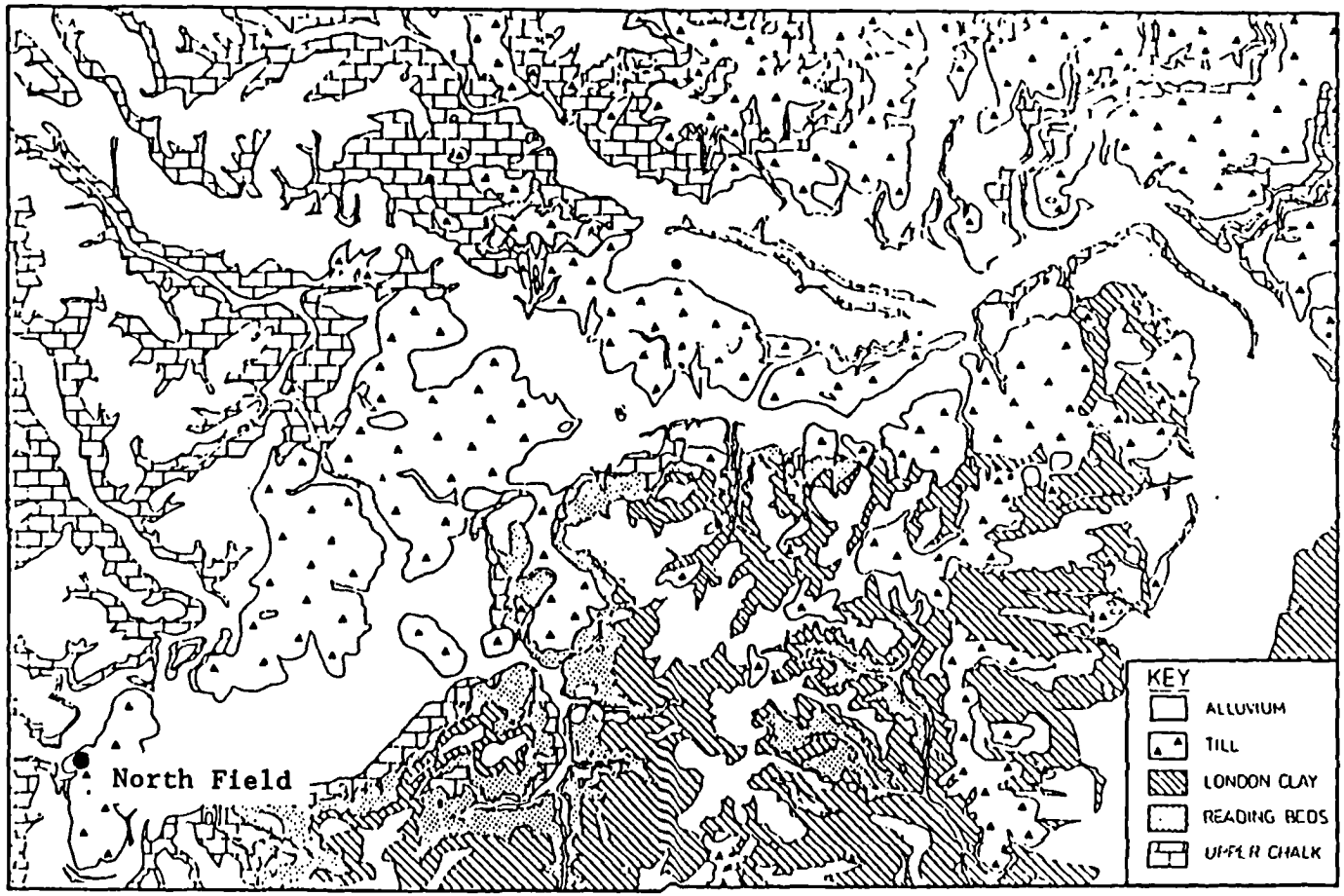

Figure 3.4.2 The Vale of St. Albans: solid and superficial geology.

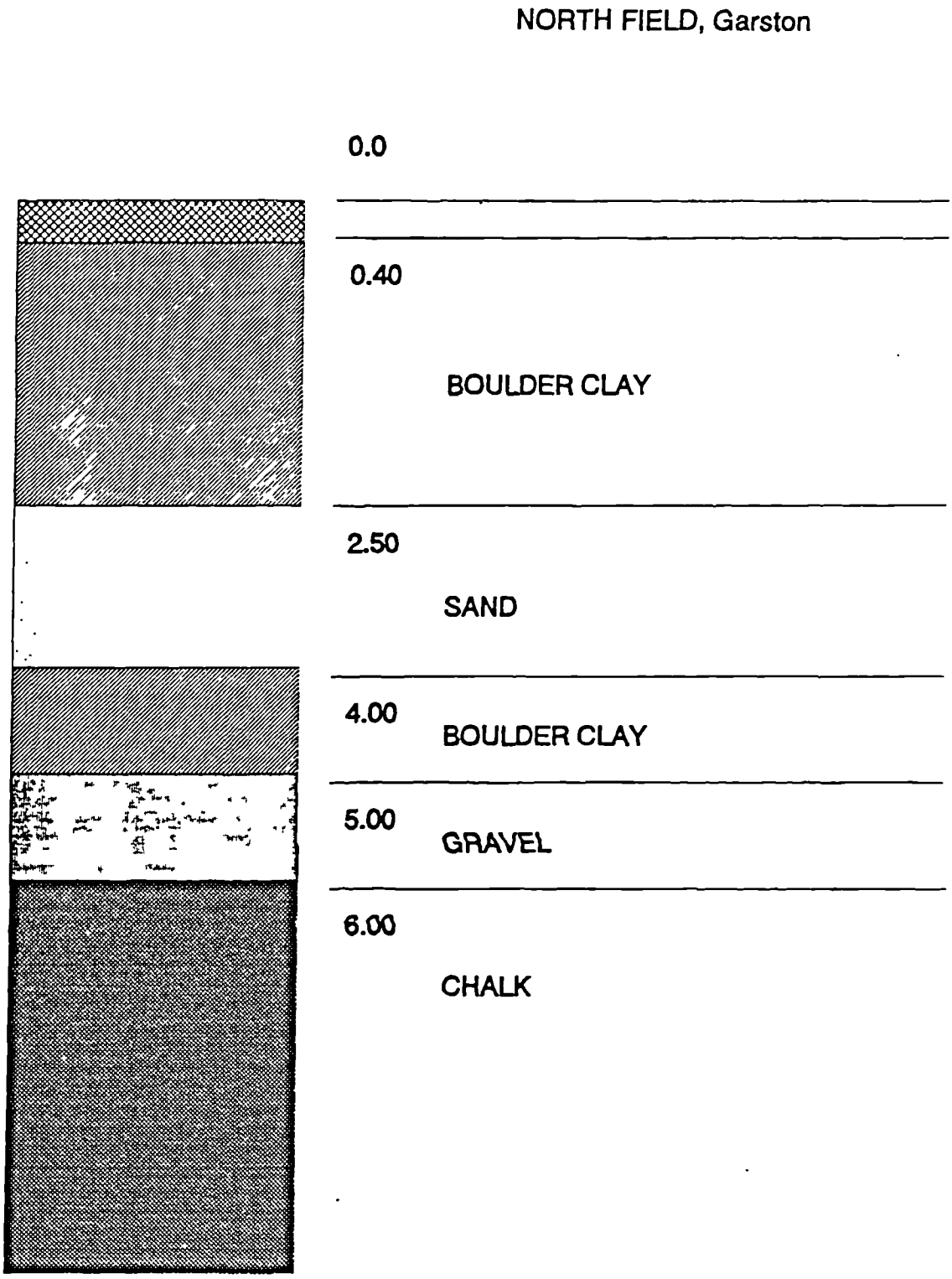

Figure 3.4.3 North Field, Garston. Soil profile.

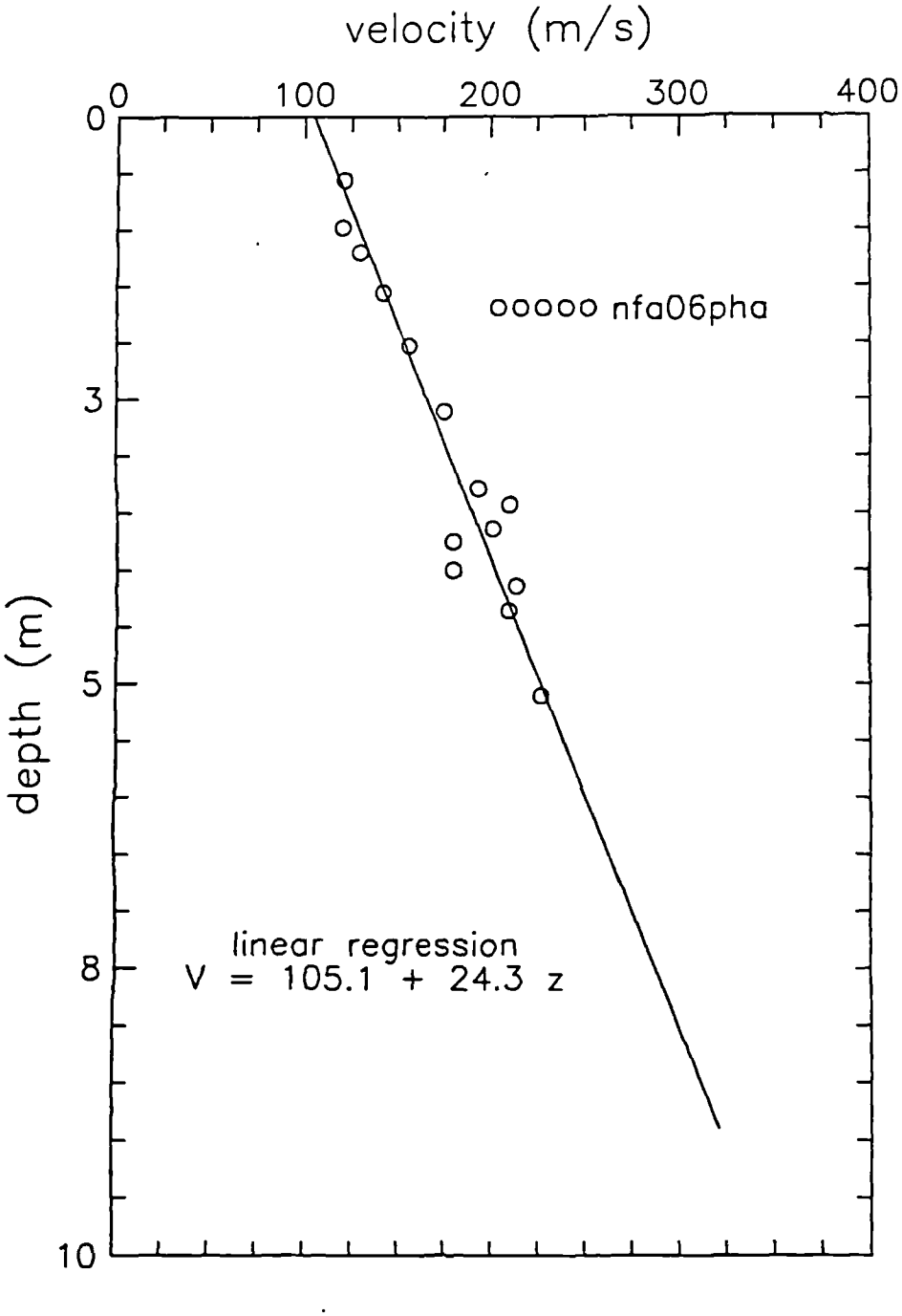

Fig. 3.4.4. North Field, Garston. Phasemeter technique. Rayleigh wave velocity versus depth.

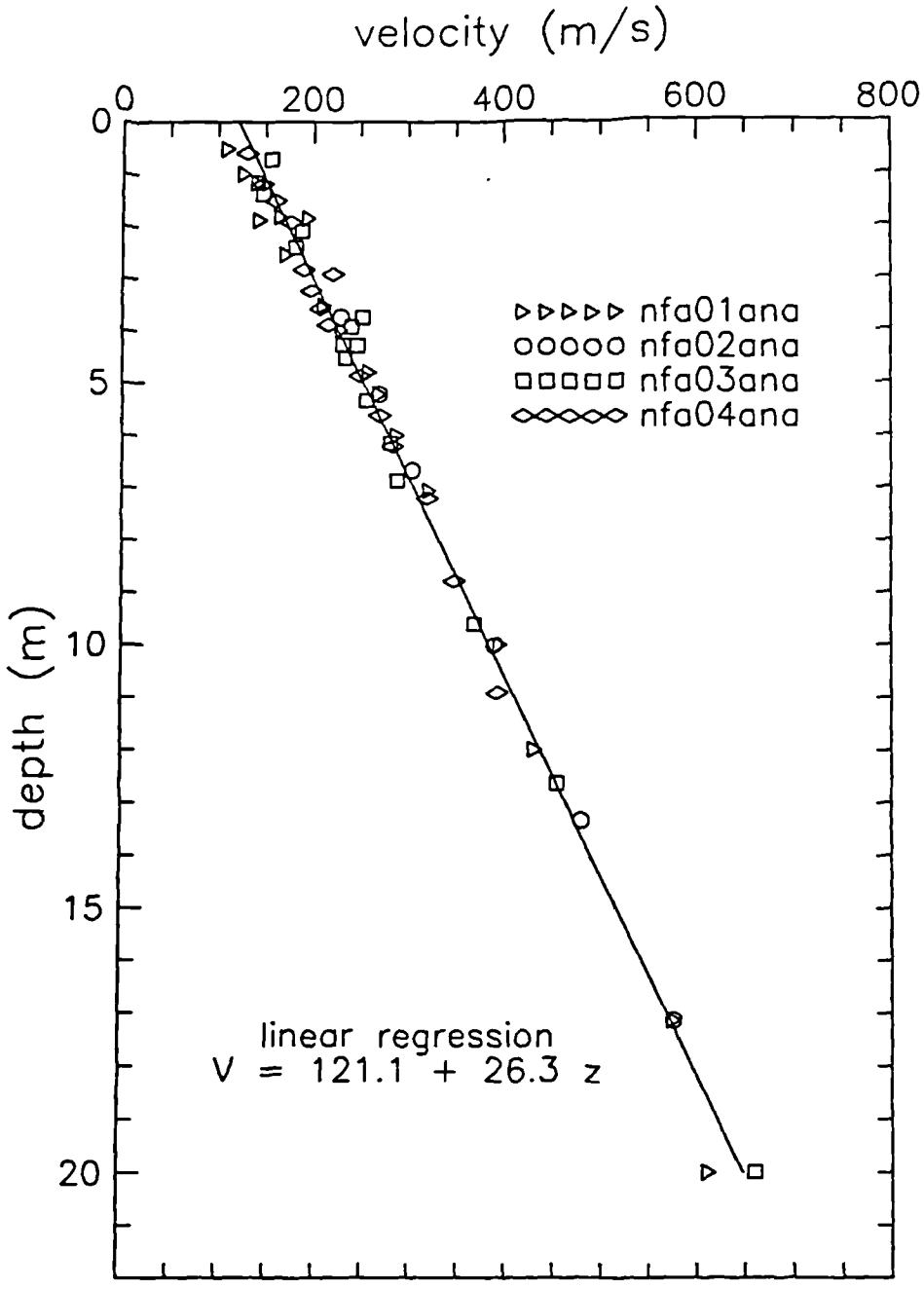

Fig. 3.4.5. North Field, Garston. Analyser technique. Rayleigh wave velocity versus depth.

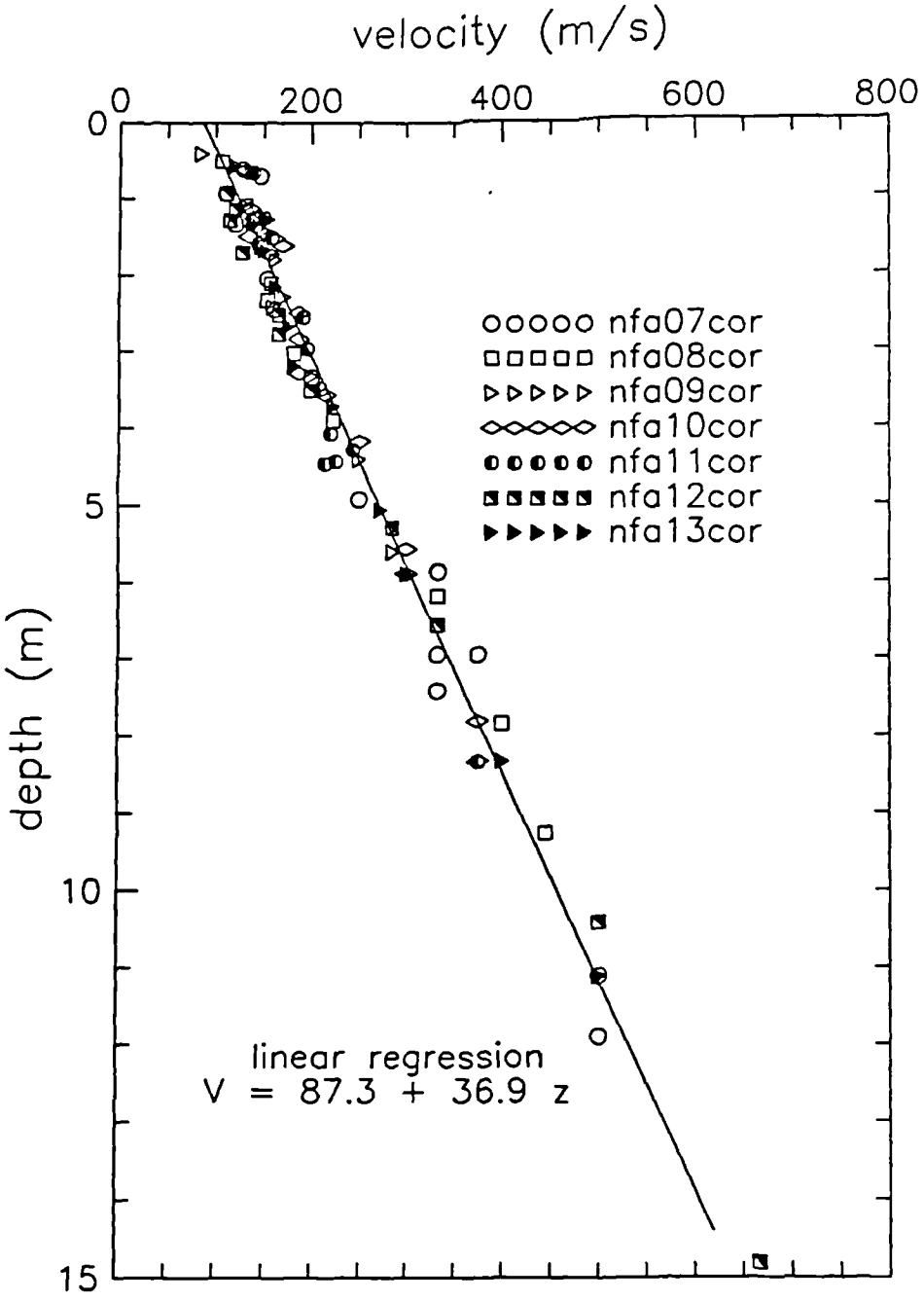

Fig. 3.4.6. North Field, Garston. Correlator technique. Rayleigh wave velocity versus depth.

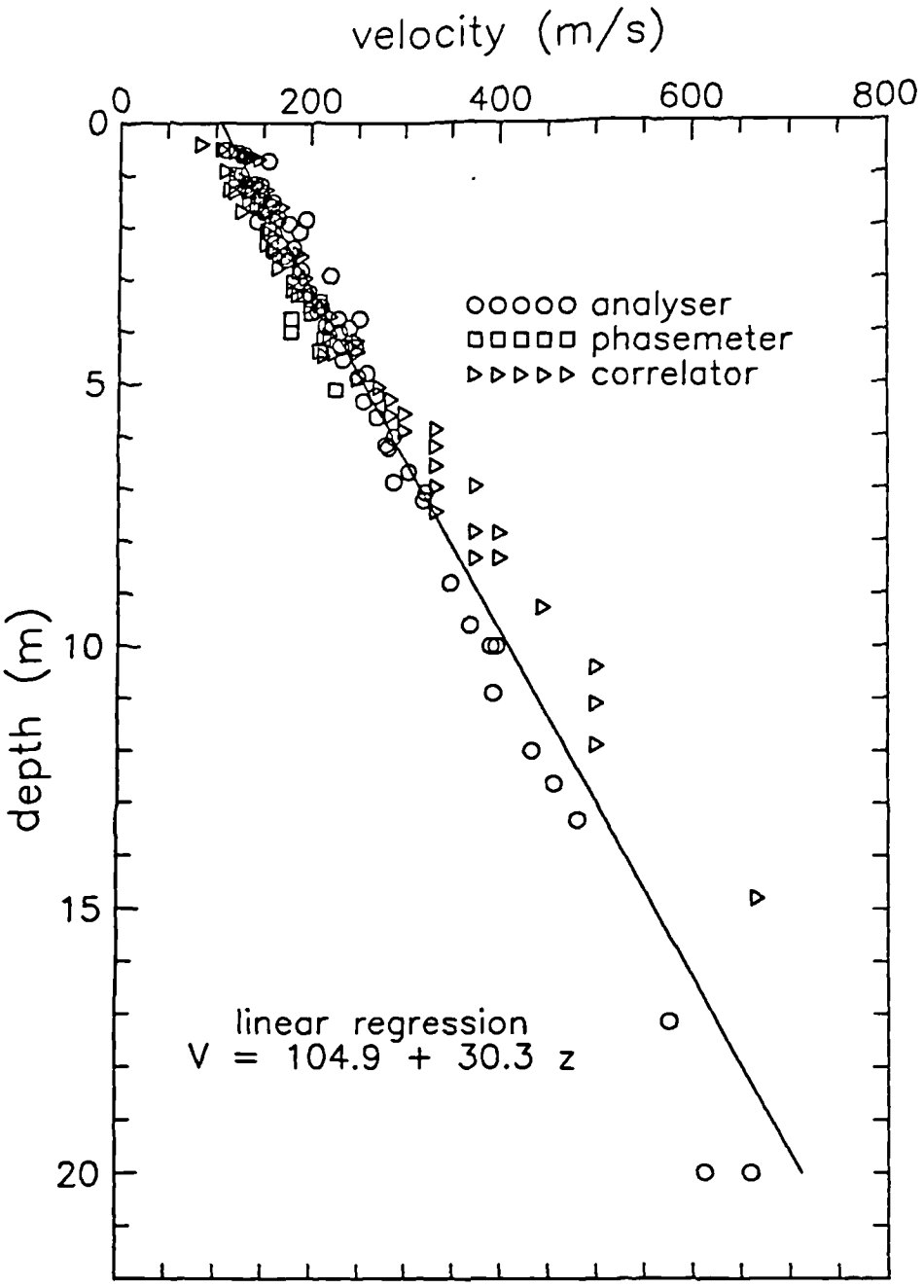

Fig. 3.4.7. North Field, Garston. All data. Rayleigh wave velocity versus depth.

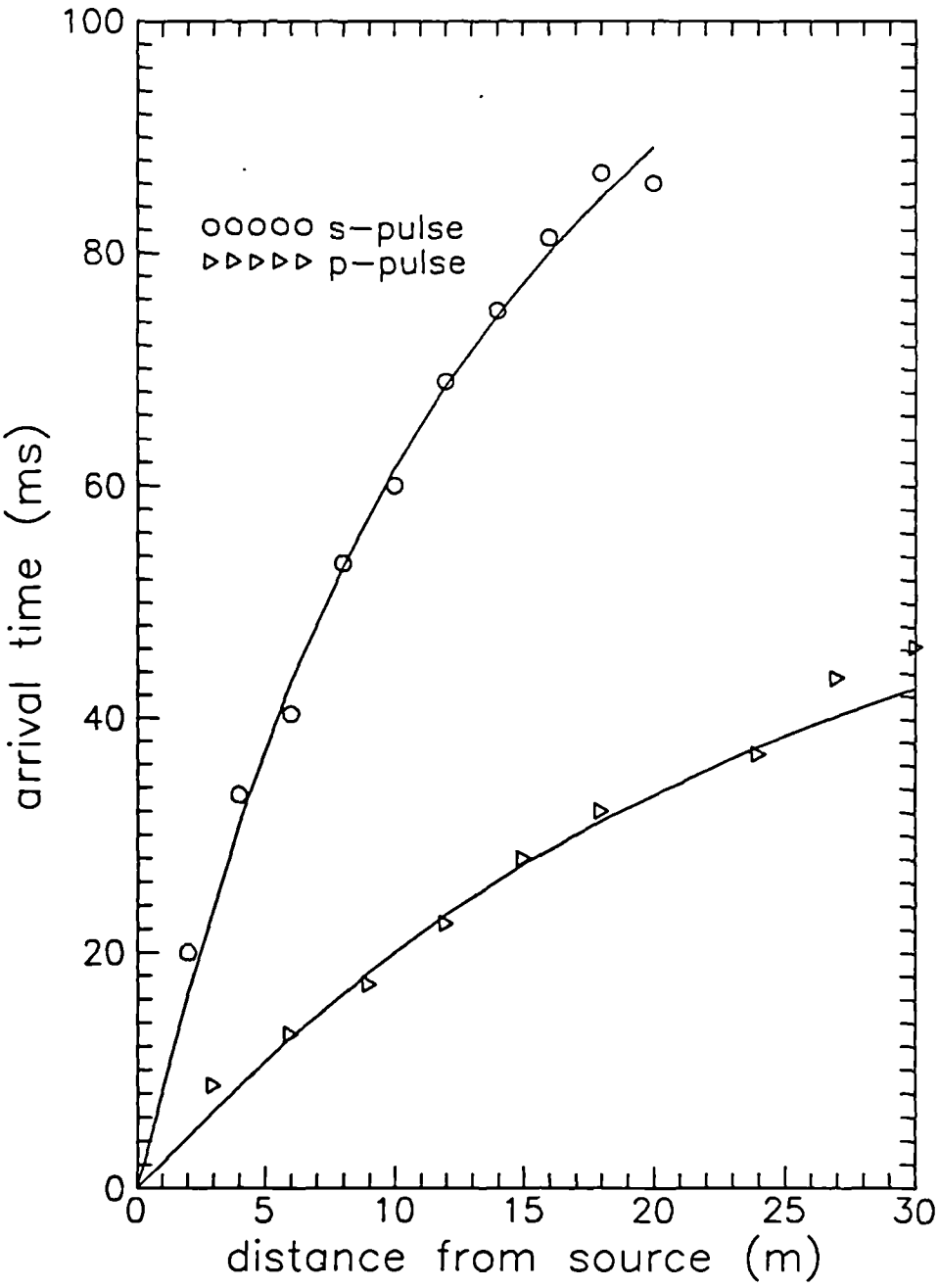

Fig. 3.4.8. North Field, Garston. Pulse refraction surveys. Arrival time versus distance data.

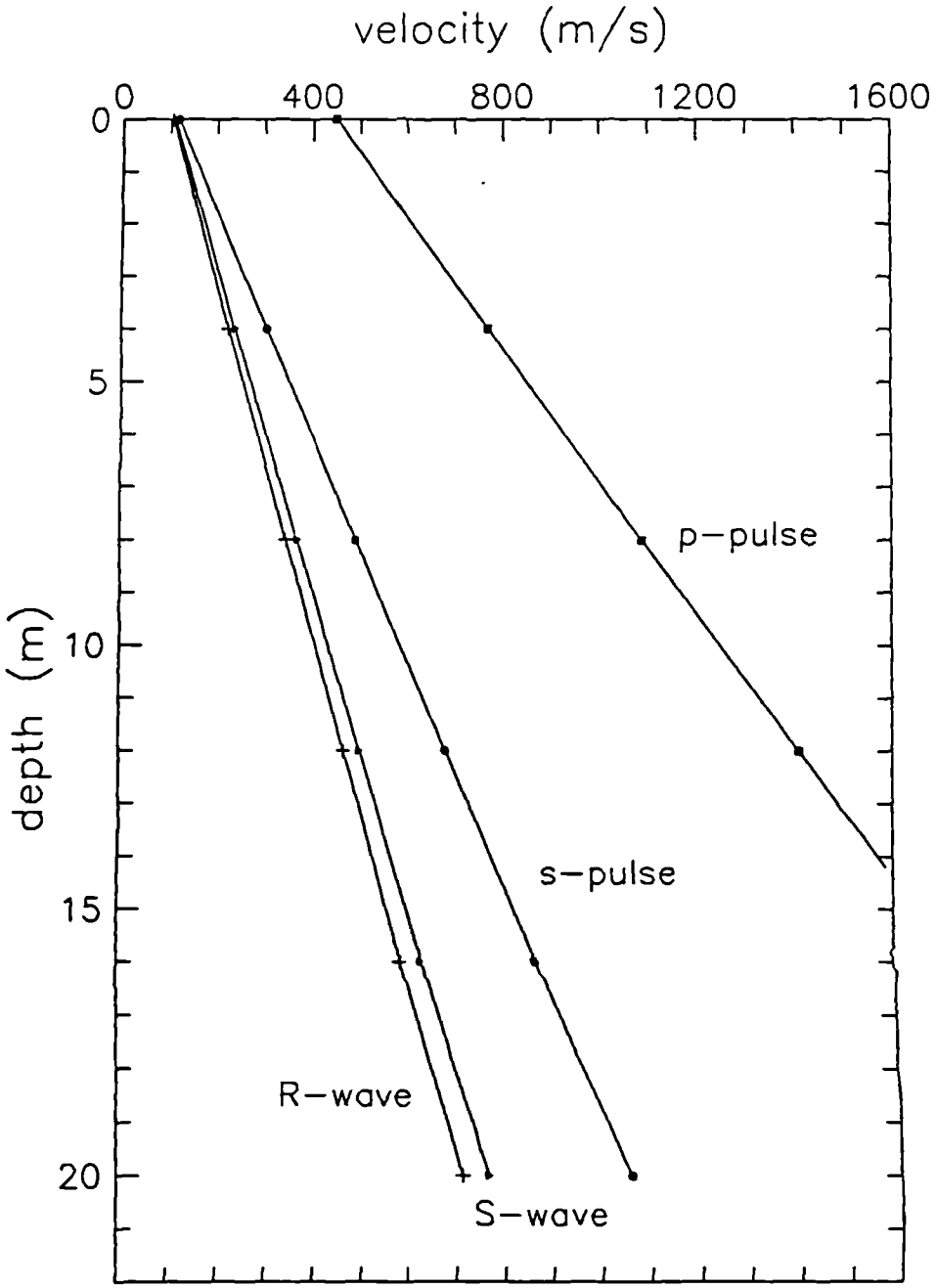

Fig. 3.4.9. North Field, Garston. Seismic wave velocity profiles.

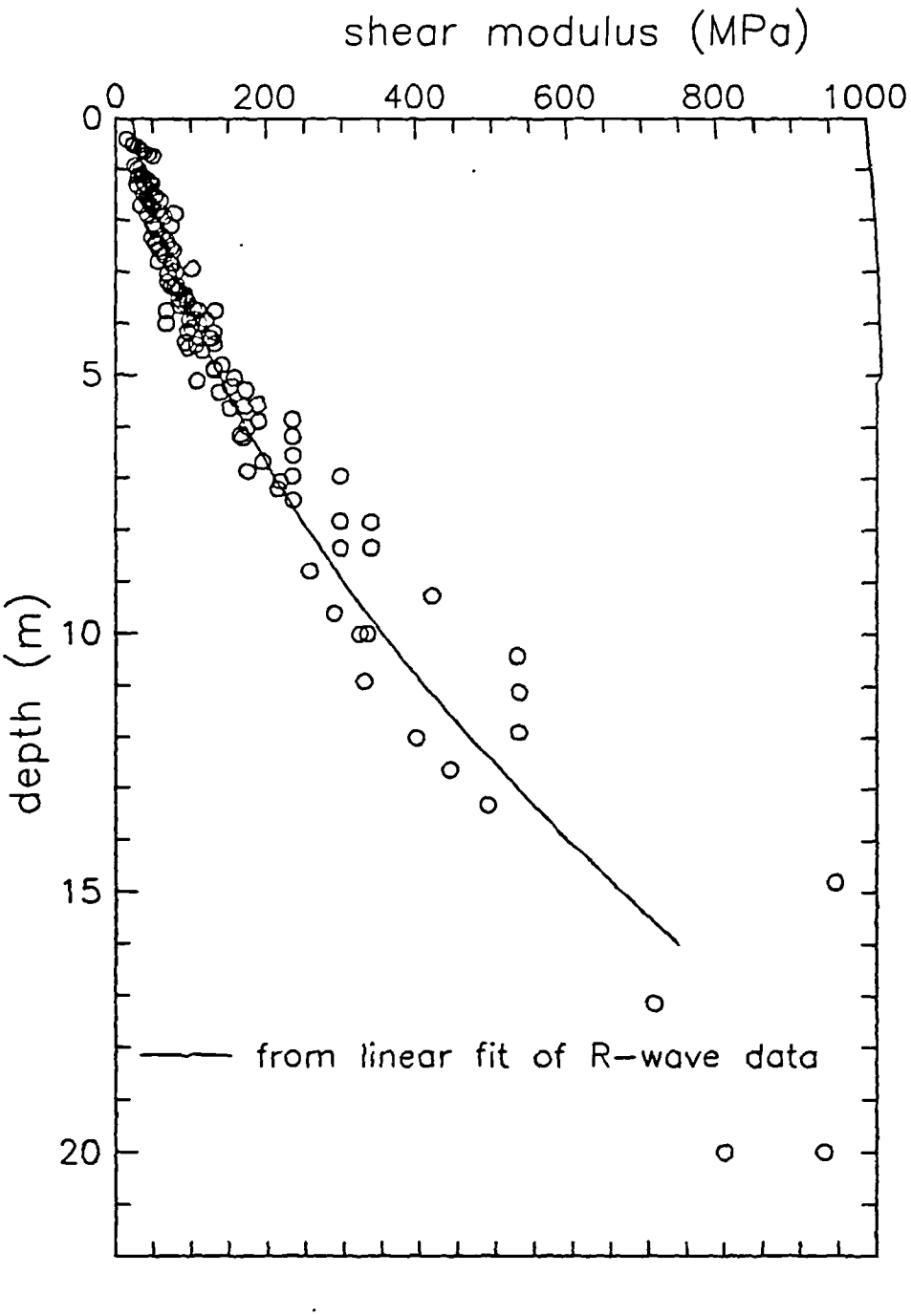

Fig. 3.4.10. North Field, Garston. Shear modulus profile.

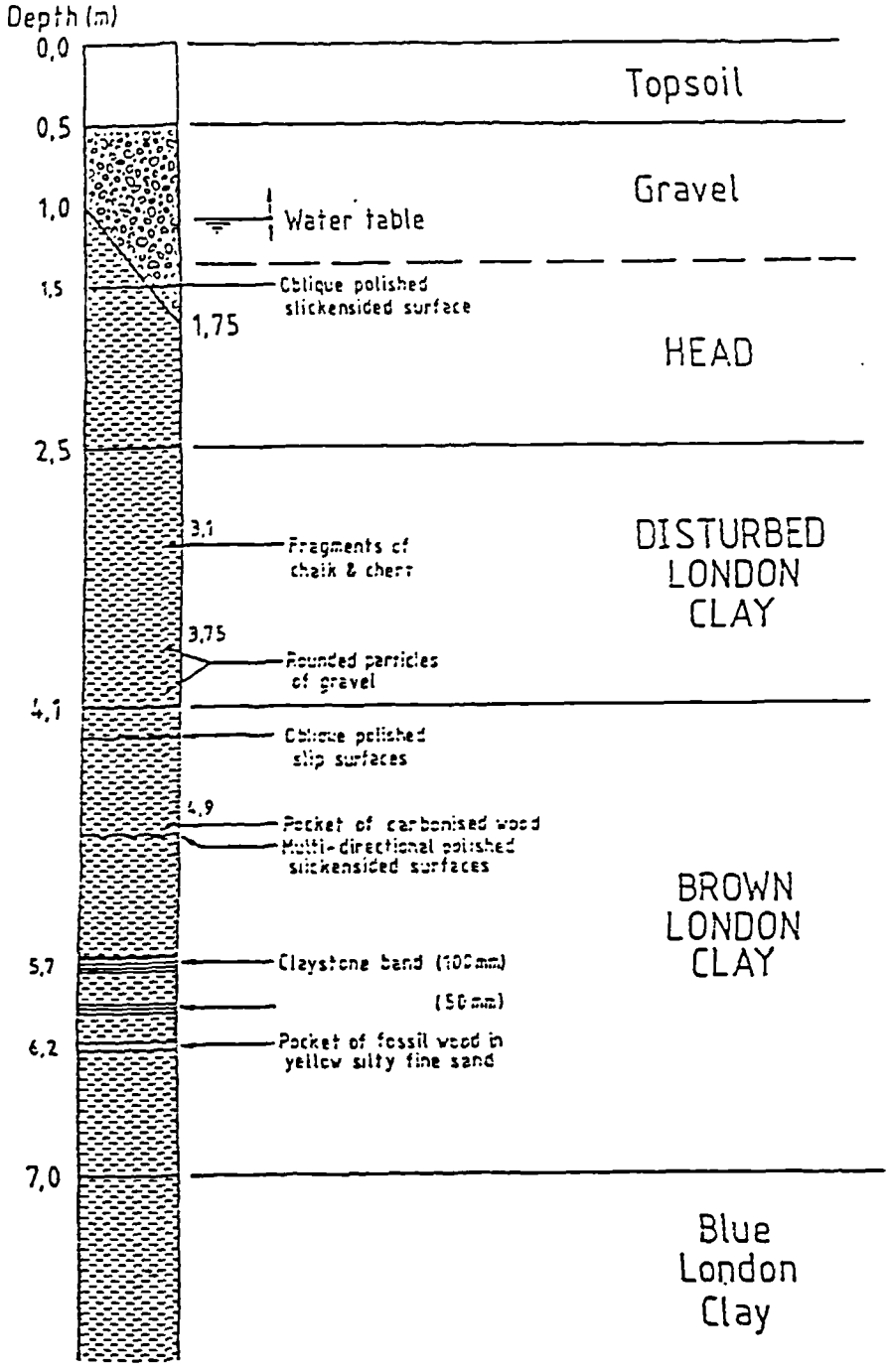

Figure 3.4.11 Canons Park, Middlesex. Soil profile.

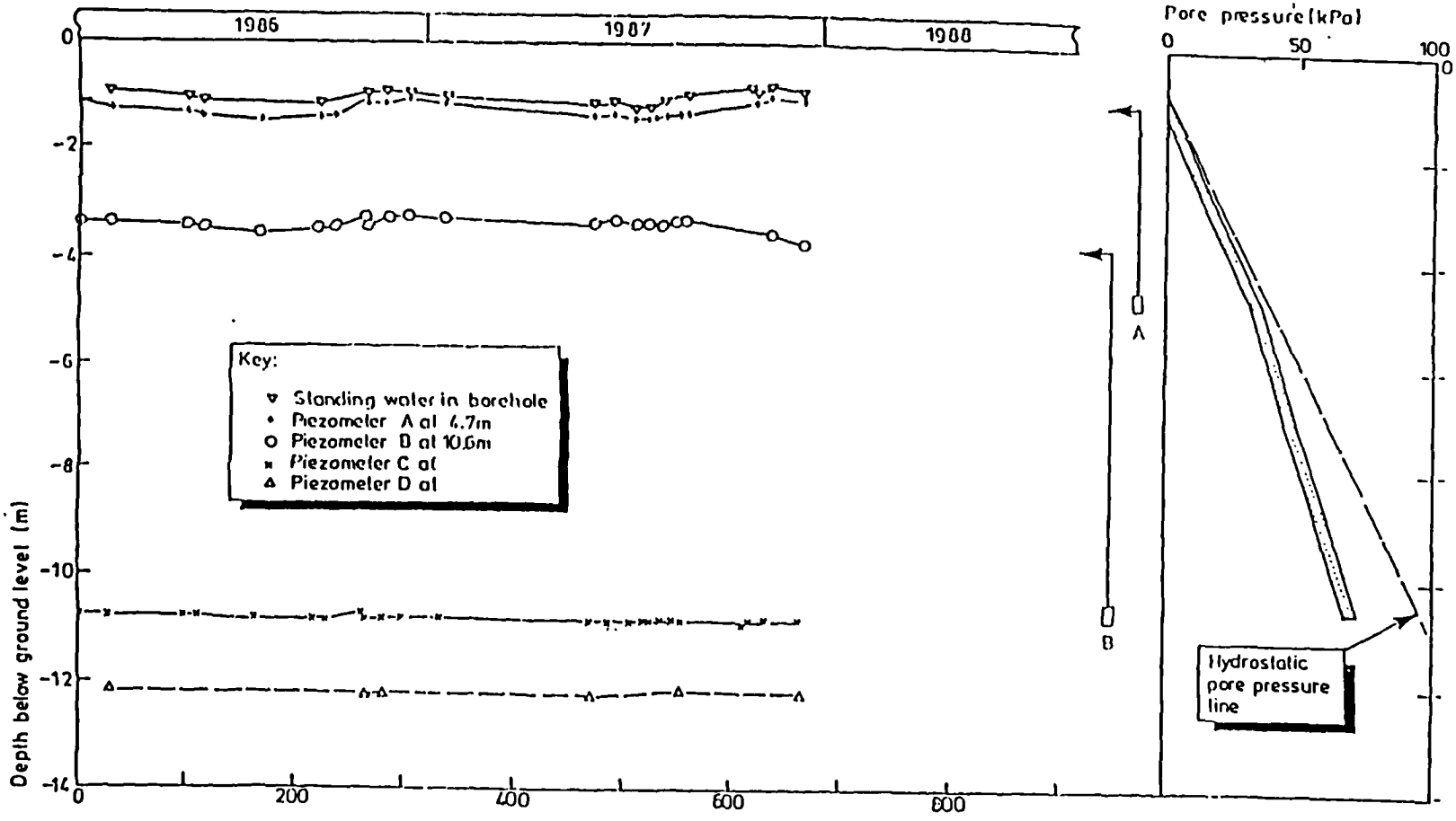

Figure 3.4.12a Canons Park, Middlesex. Ground water conditions (after Powell, 1989)

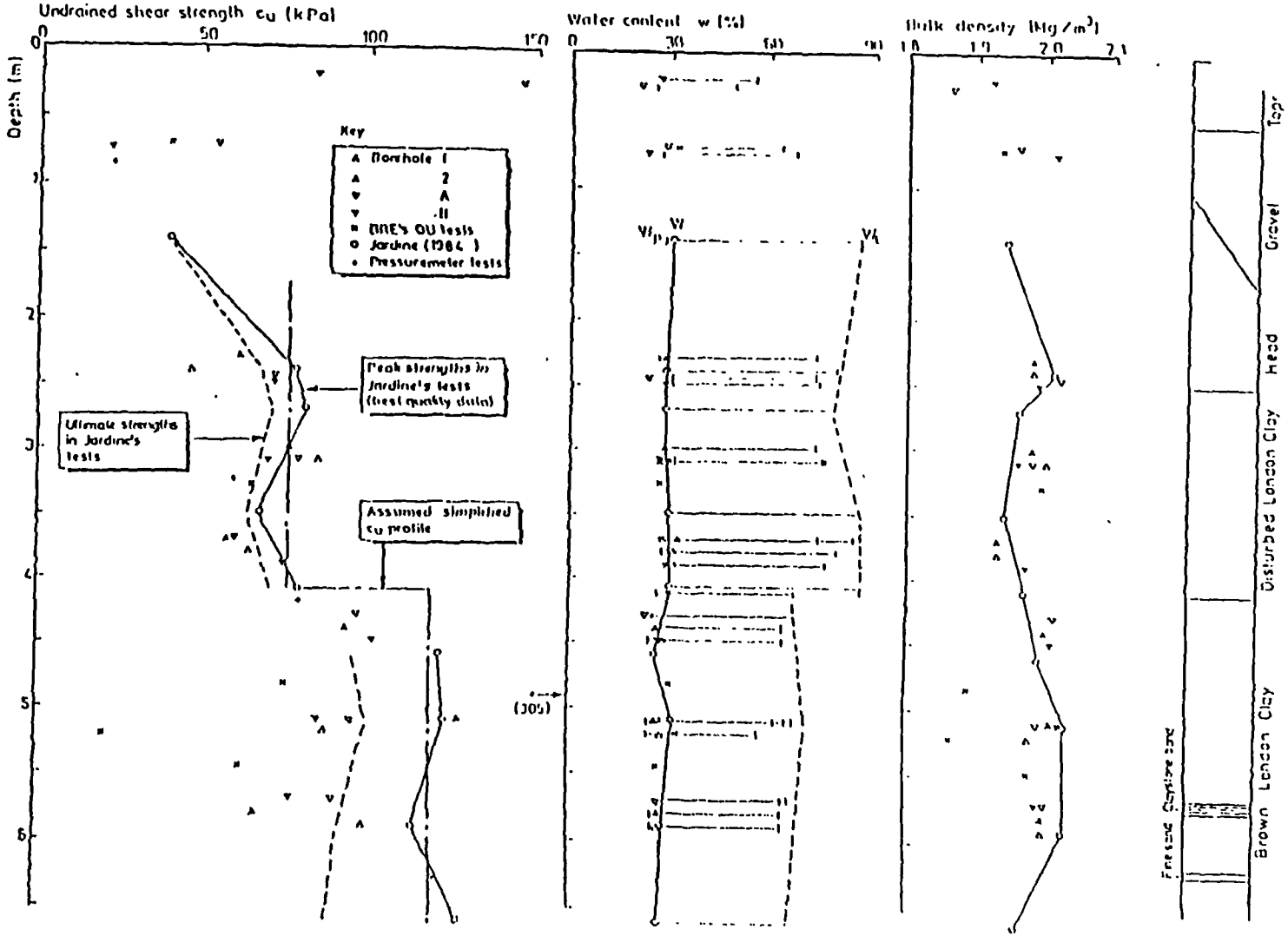

Figure 3.4.12b Canons Park, Middlesex. Profiles of bulk density and undrained shear strength (after Powell, 1989).

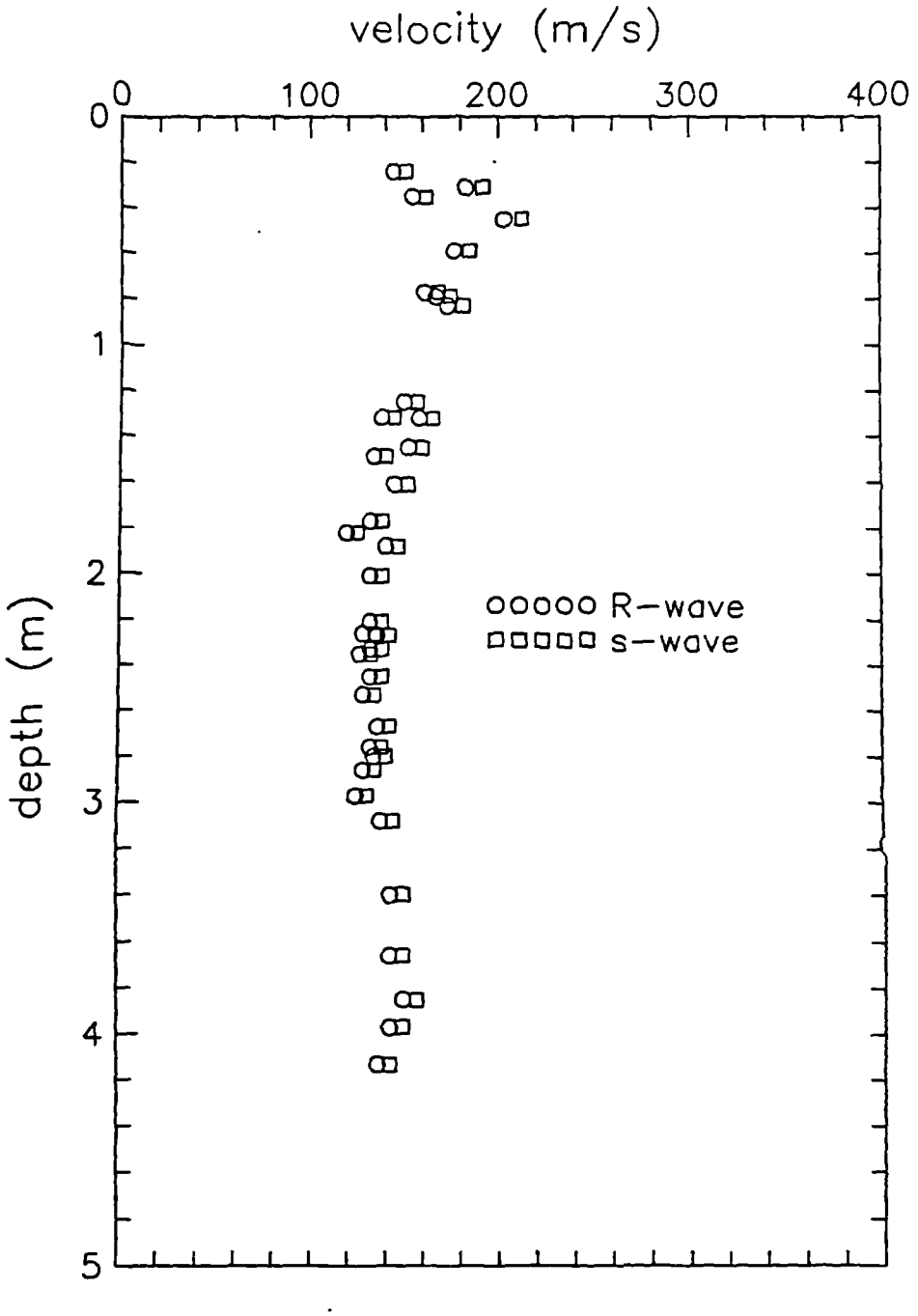

Fig. 3.4.13. Canons Park, Middlesex. Rayleigh wave and shear wave velocity profiles.

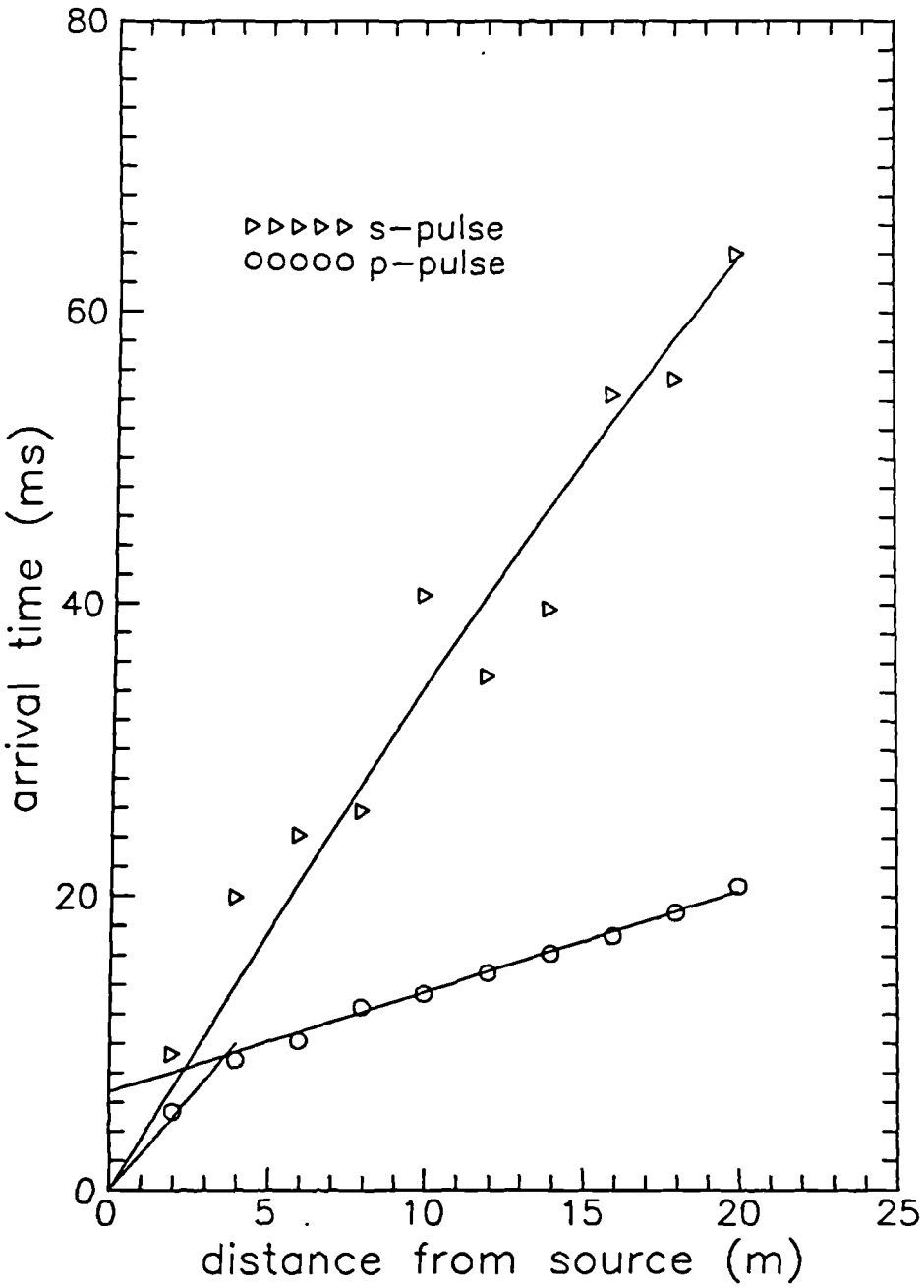

Fig. 3.4.14. Canons Park, Middlesex. Pulse refraction surveys. Arrival time versus distance data.

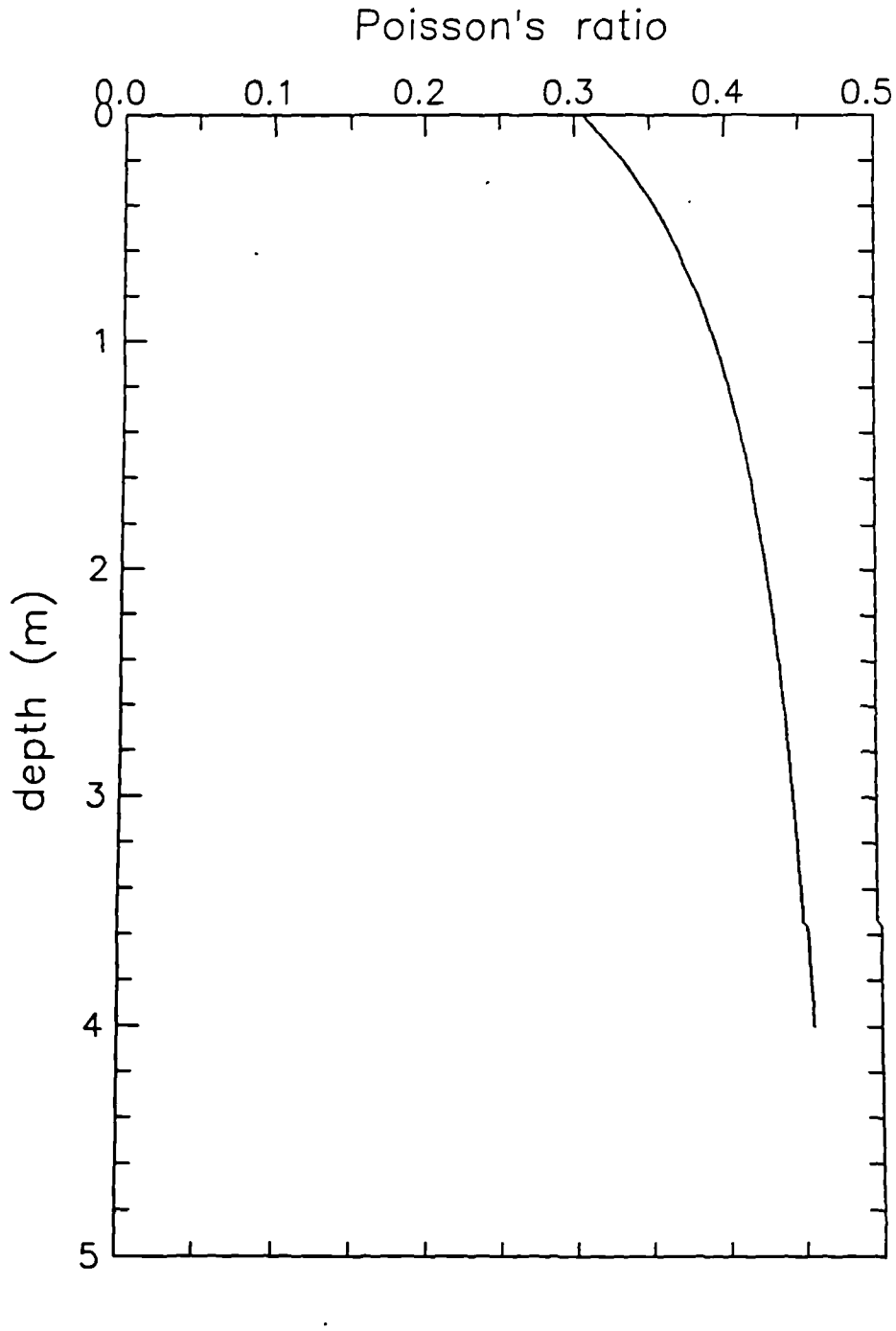

Fig. 3.4.15. Canons Park, Middlesex. Poisson's ratio profile.

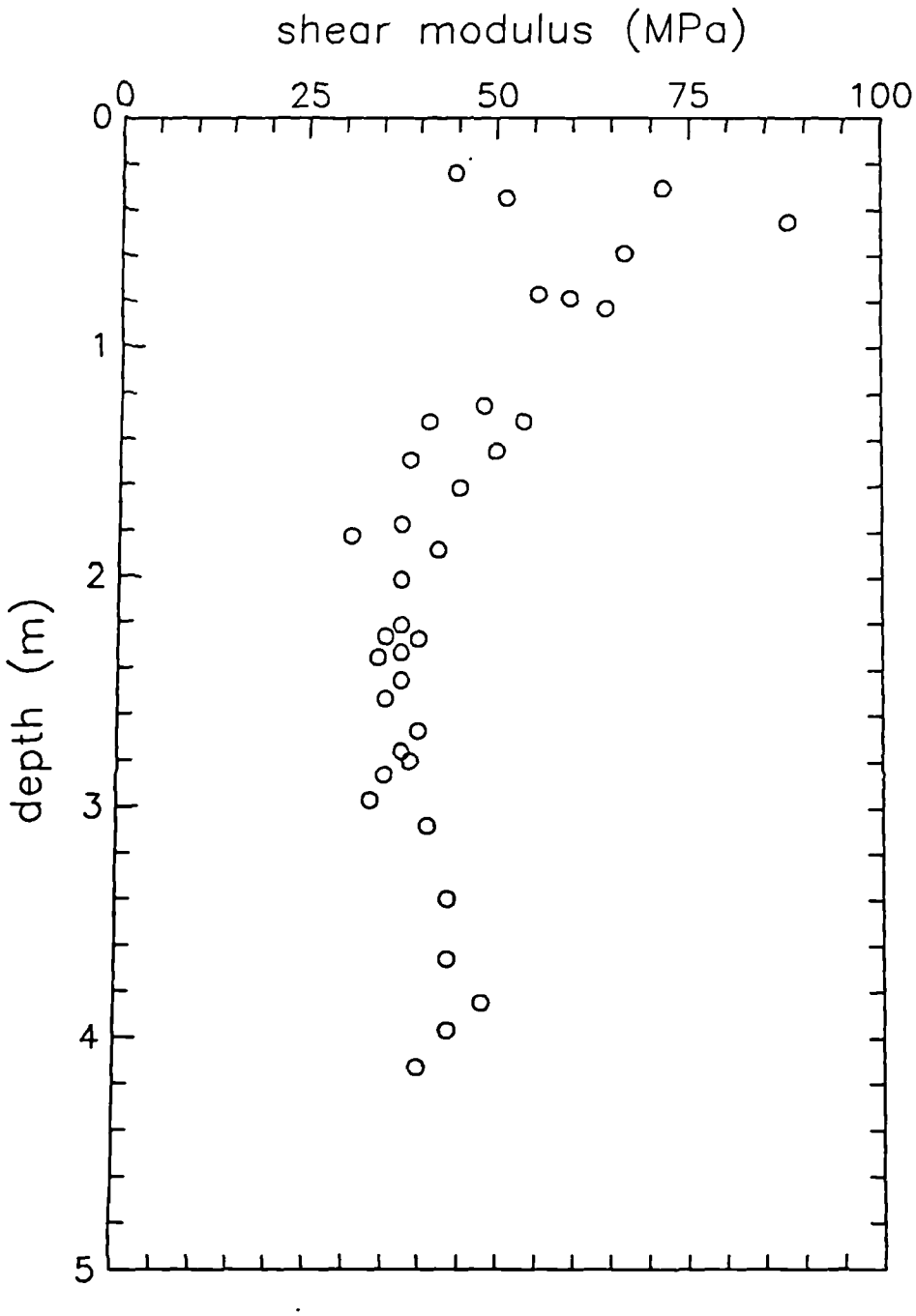

Fig. 3.4.16. Canons Park, Middlesex. Shear modulus profile.

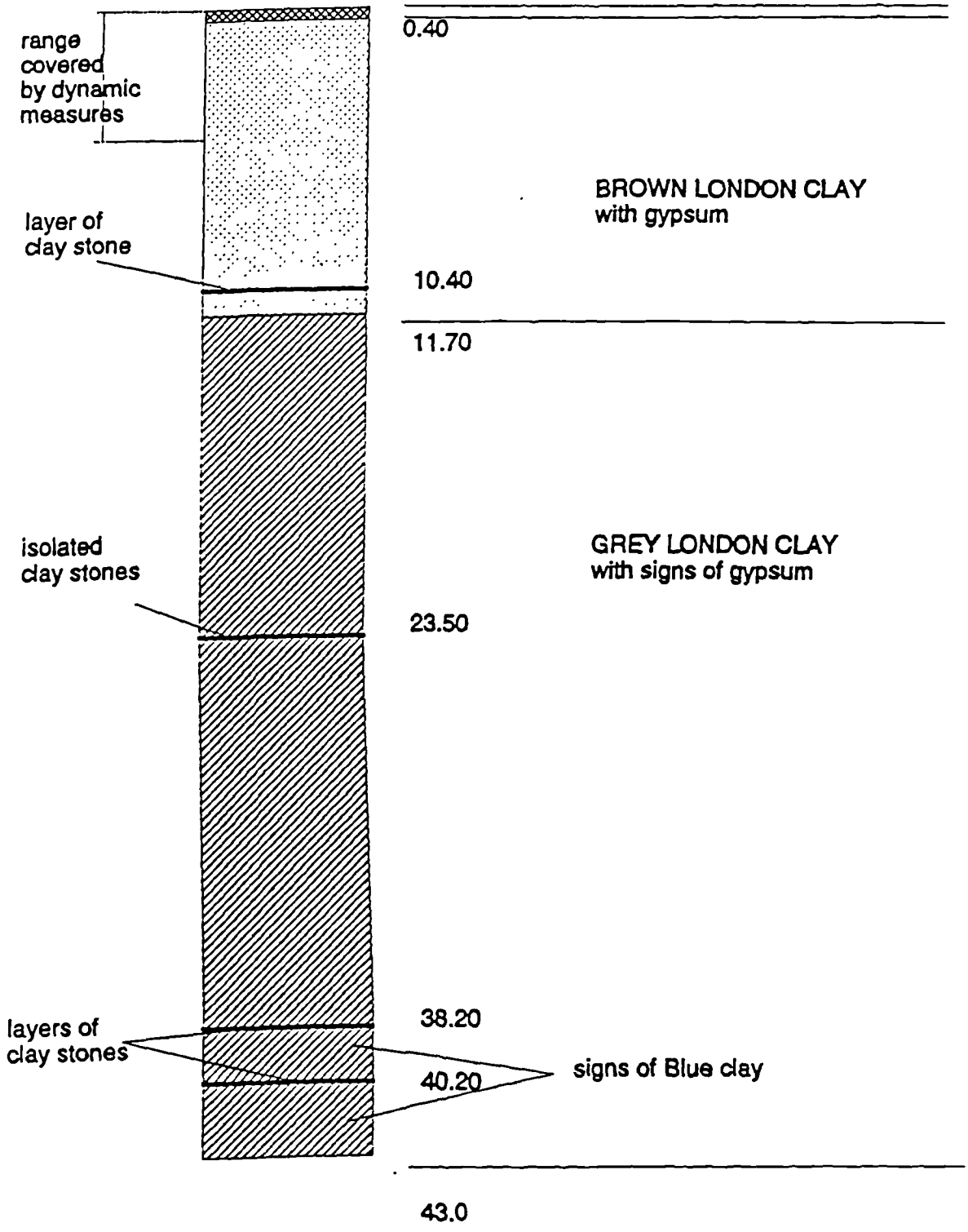

Figure 3.4.17 Chattenden, Kent. Soil Profile.

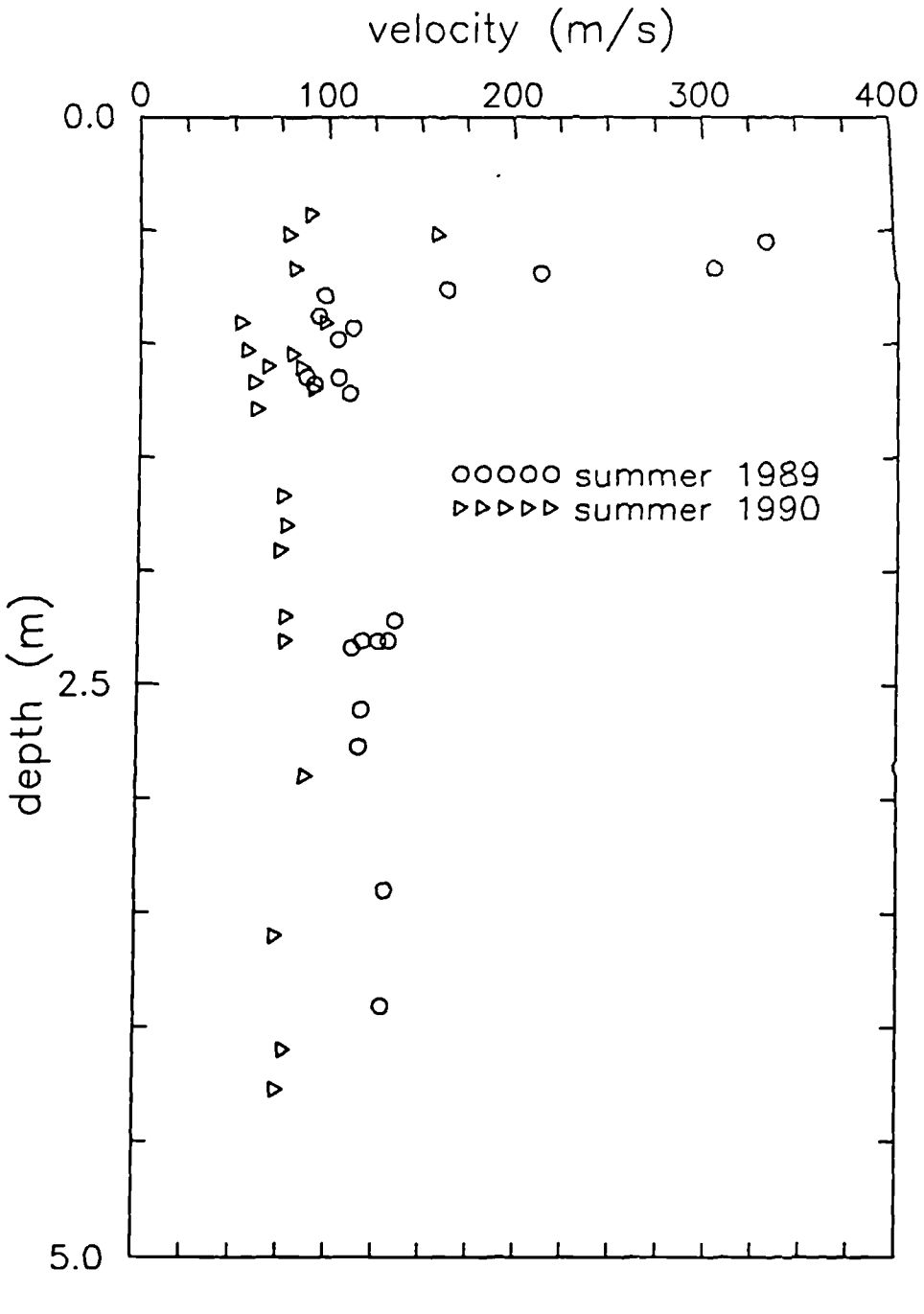

Figure 3.4.18 Chattenden, Kent. Rayleigh wave velocity profile.

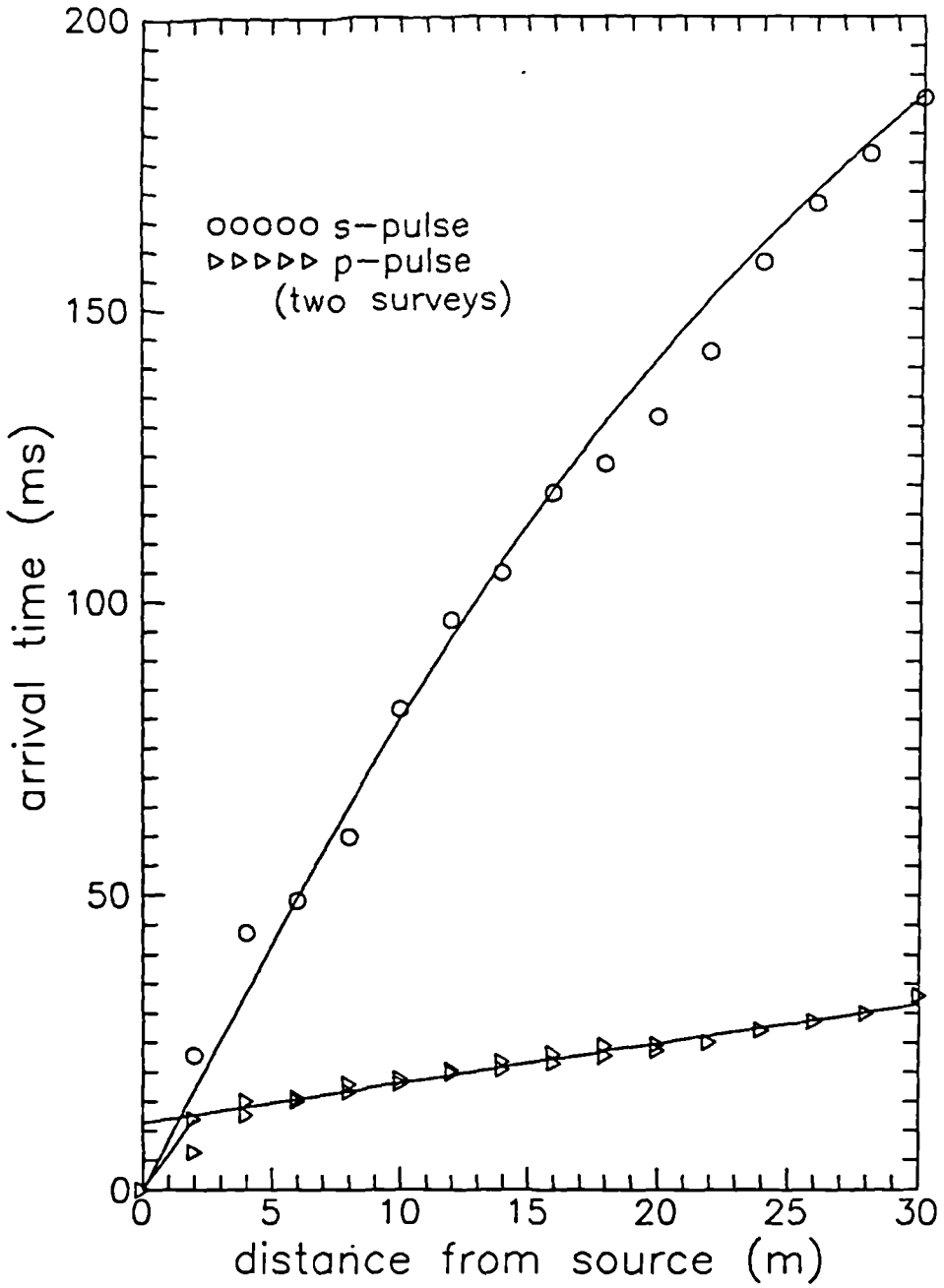

Fig. 3.4.19. Chattenden, Kent. Pulse refraction surveys. Arrival time versus distance data

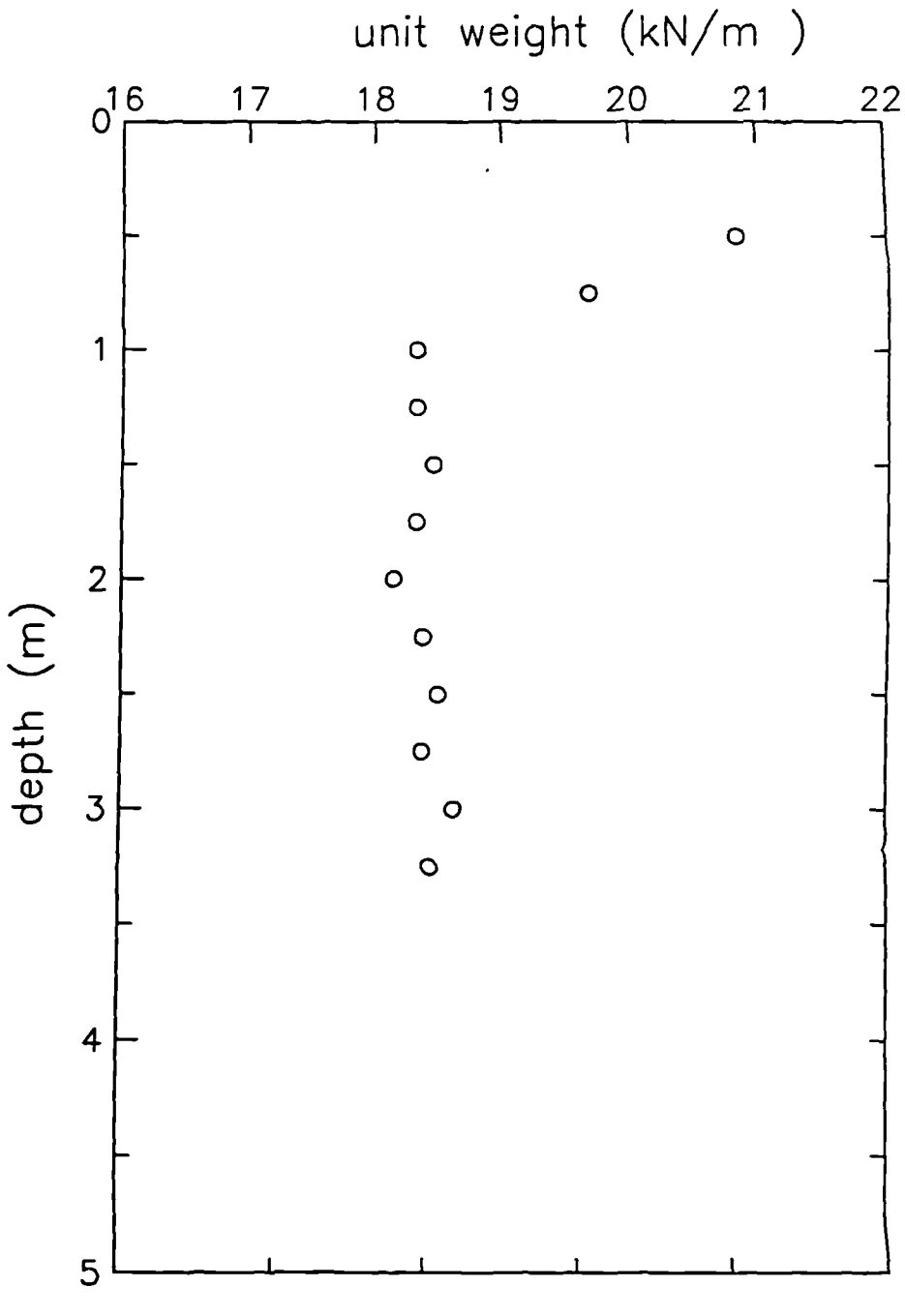

Fig. 3.4.20. Chattenden, Kent. Bulk density profile.

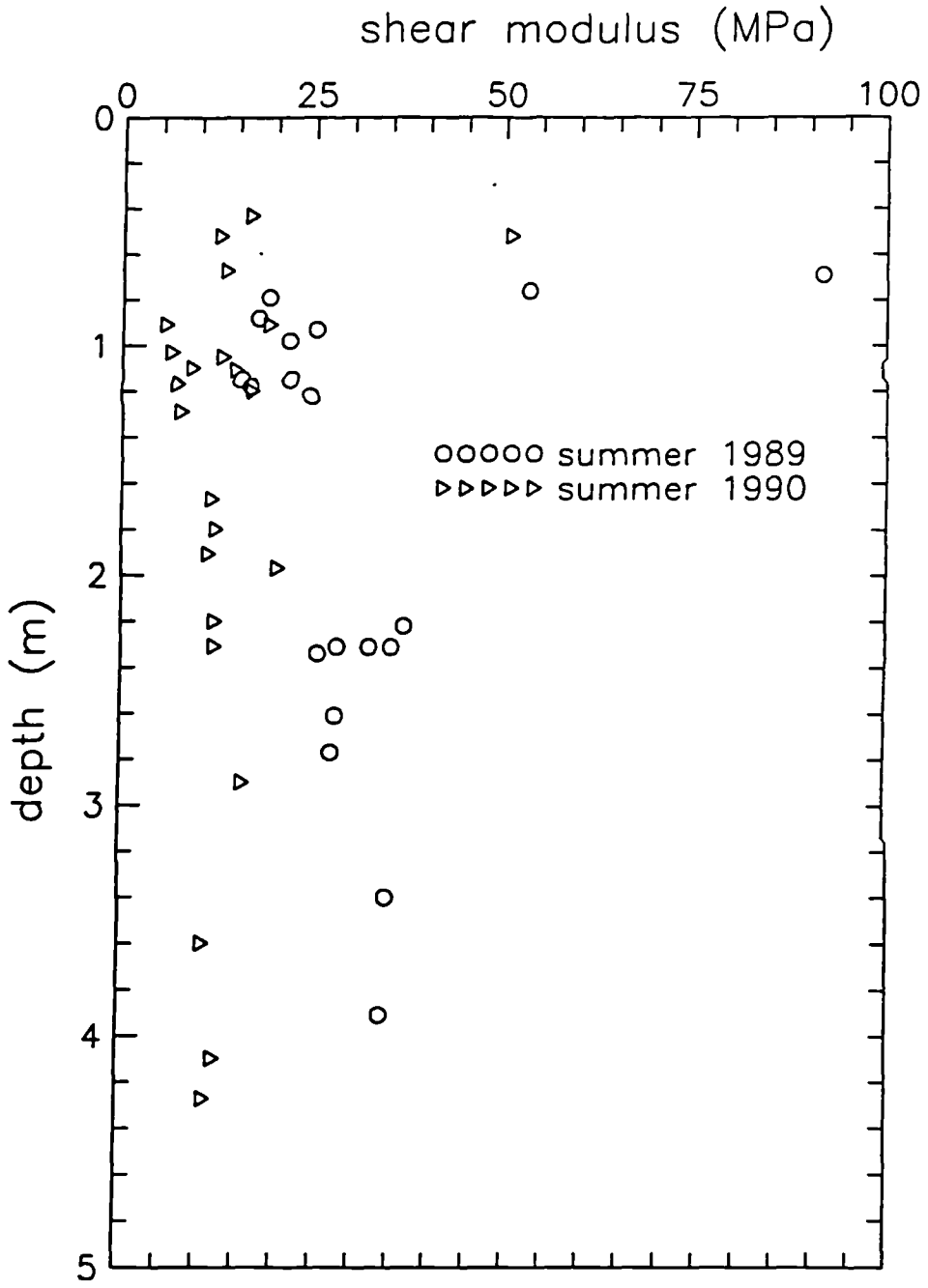

Fig. 3.4.21. Chattenden, Kent. Shear modulus profile.

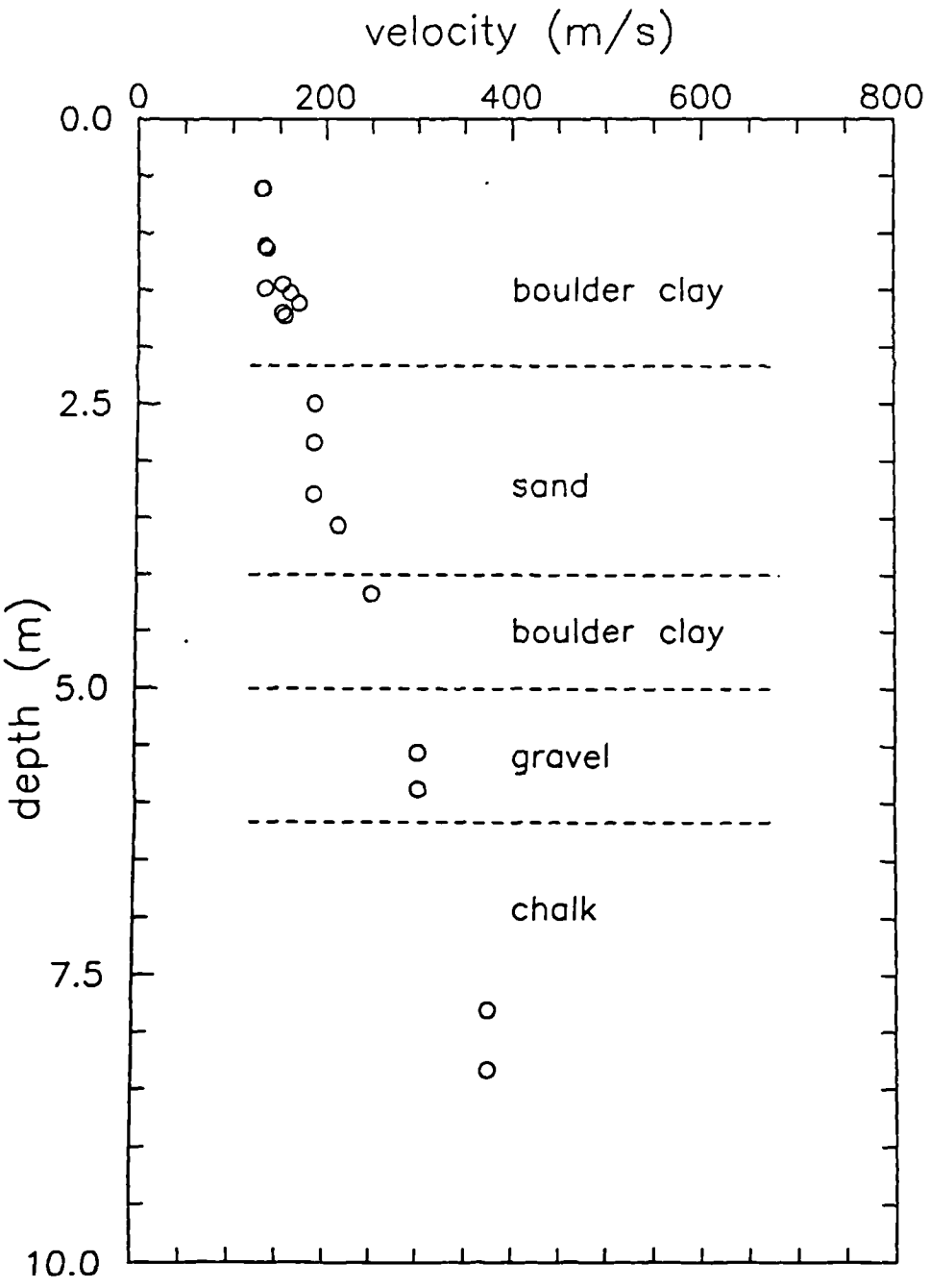

Fig. 3.4.22. North Field, Garston. Test NFA10COR. Rayleigh wave velocity versus depth

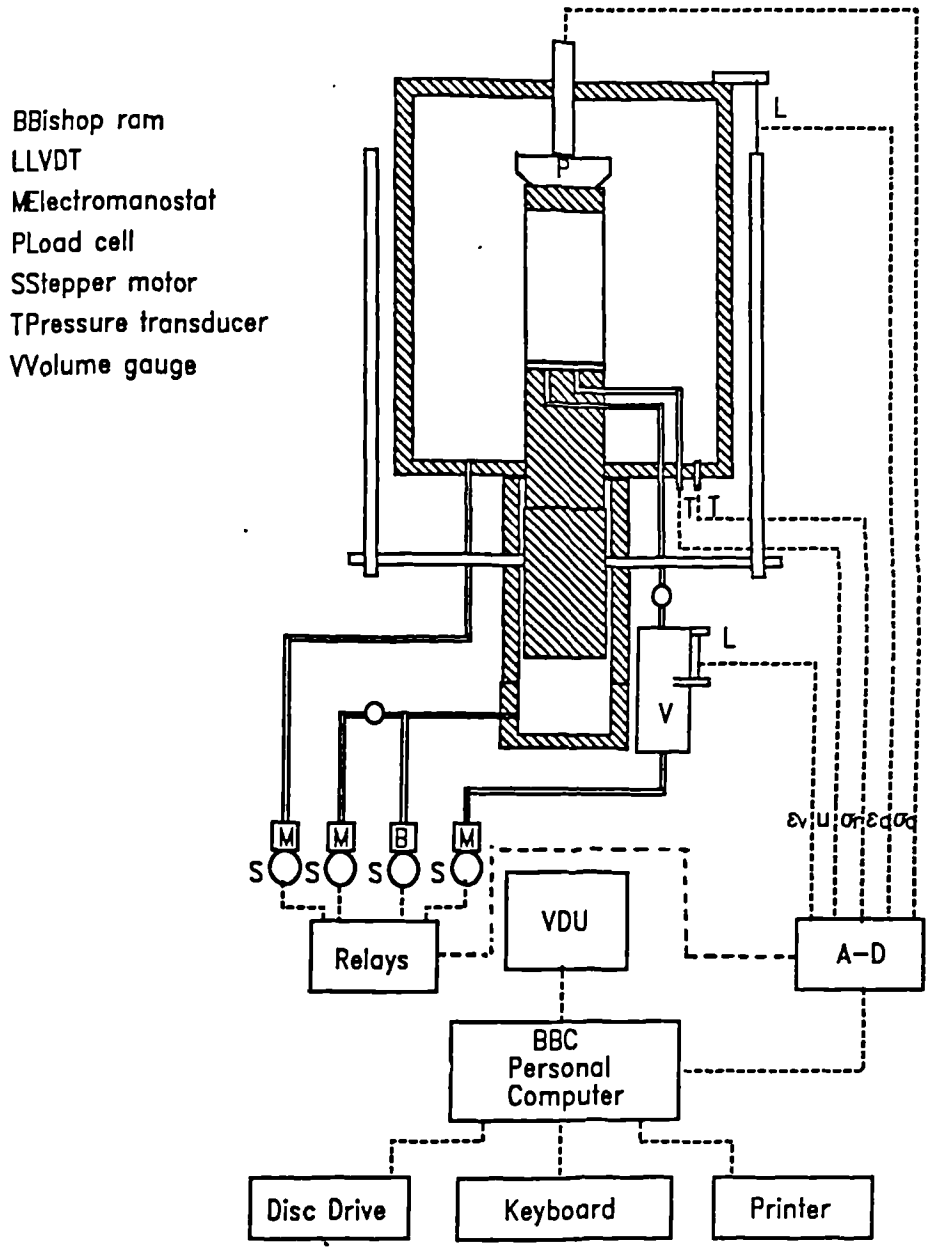

Figure 4.2.1 Schematic diagram of "BBC" control system for stress path cells.

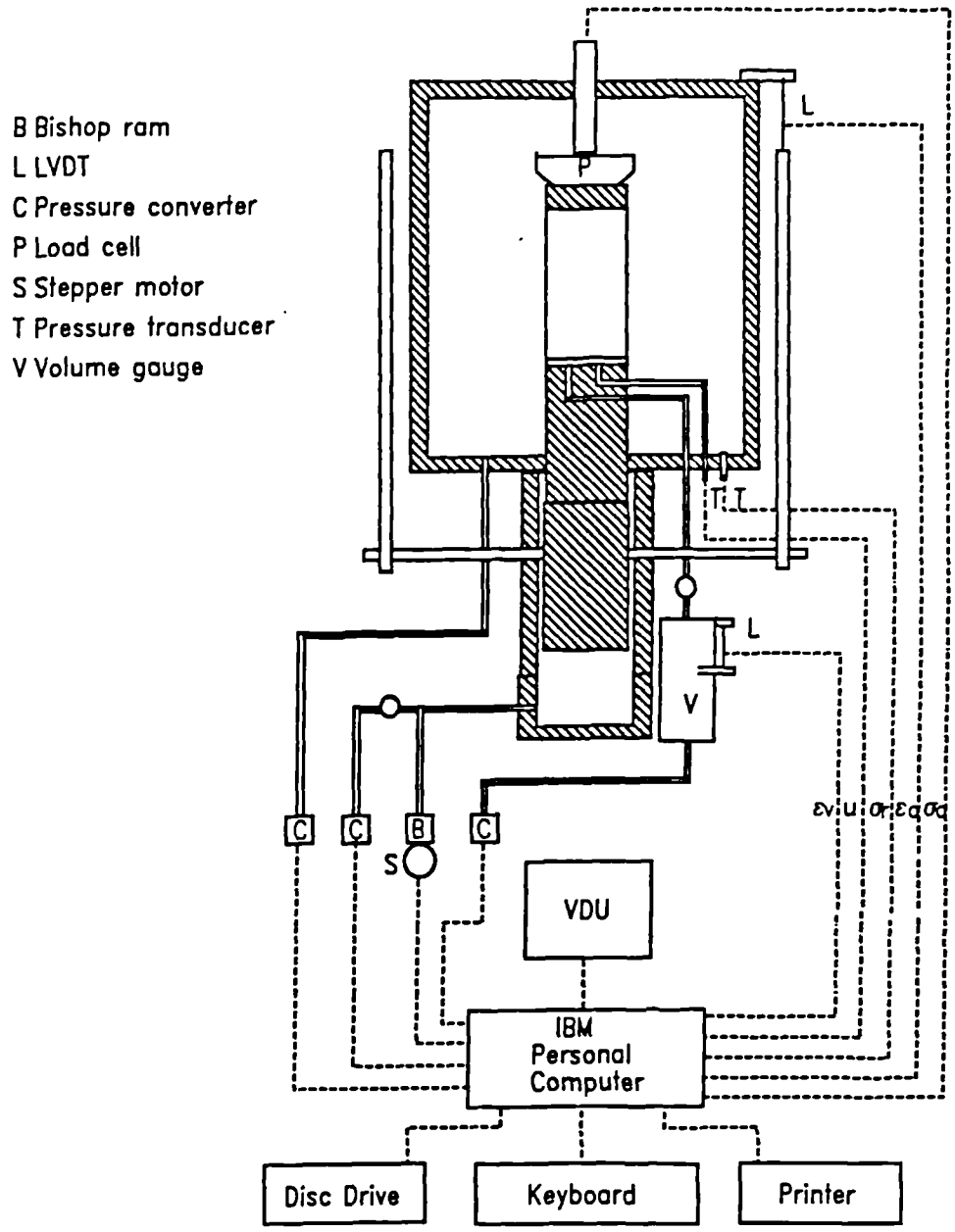

Figure 4.2.2 Schematic diagram of "IBM" control system for stress path cells.

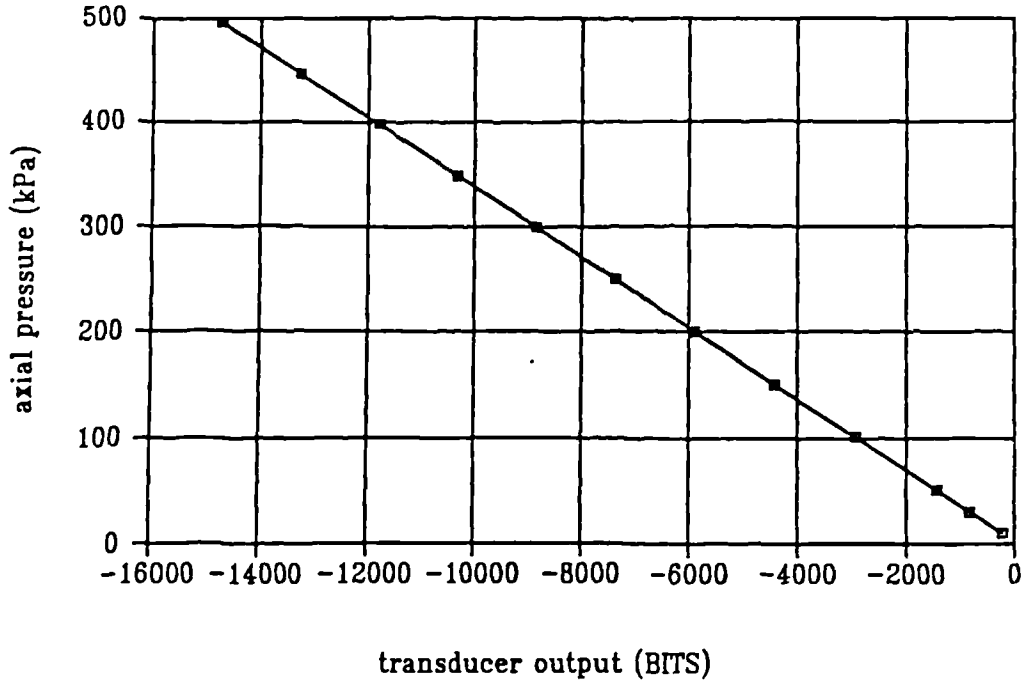

Figure 4.2.3 Typical calibration curve for Surrey University load cell used to measure axial load.

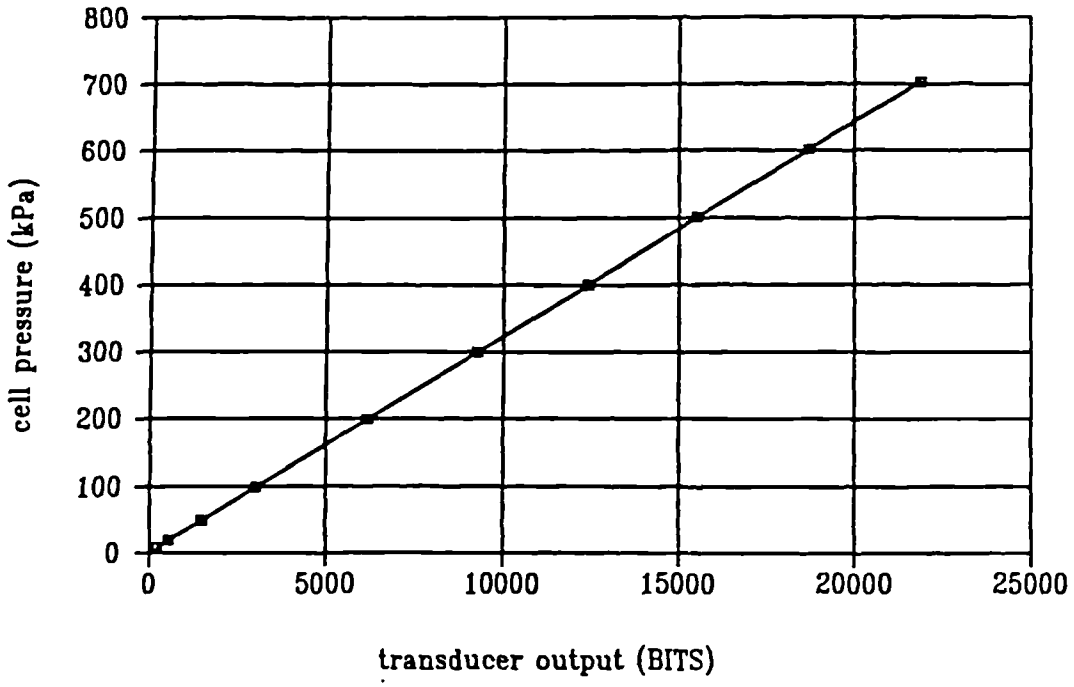

Figure 4.2.4 Typical calibration curve for Druck pressure transducers used to measure cell and pore pressure.

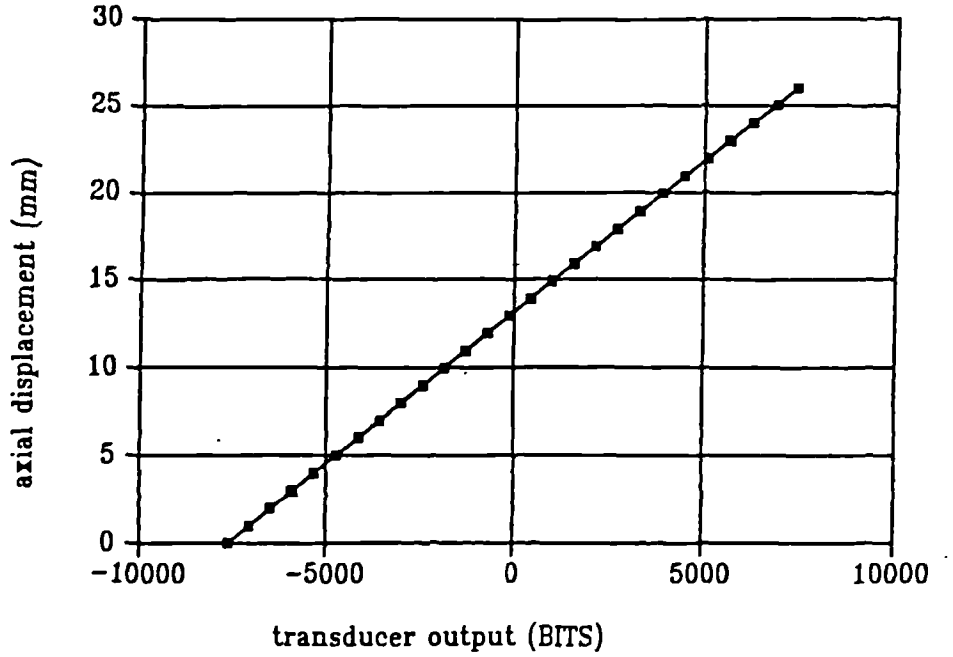

Figure 4.2.5 Typical calibration curve for LVDT used to measure axial strain.

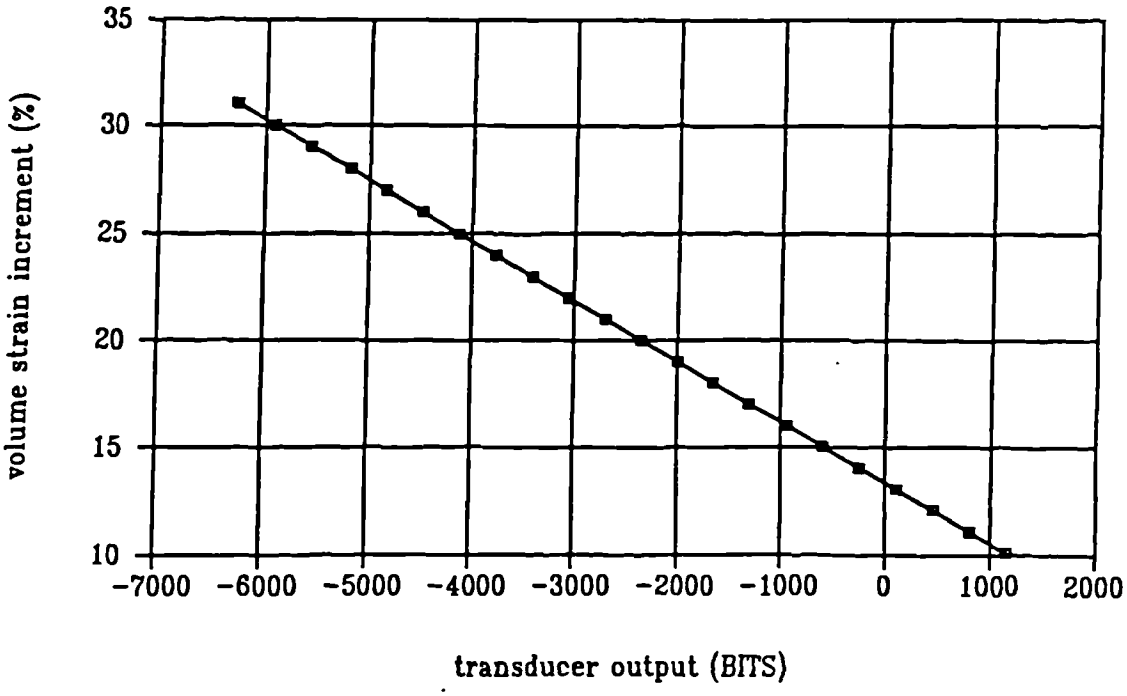

Figure 4.2.6 Typical calibration curve for LVDT used with a volume gauge.

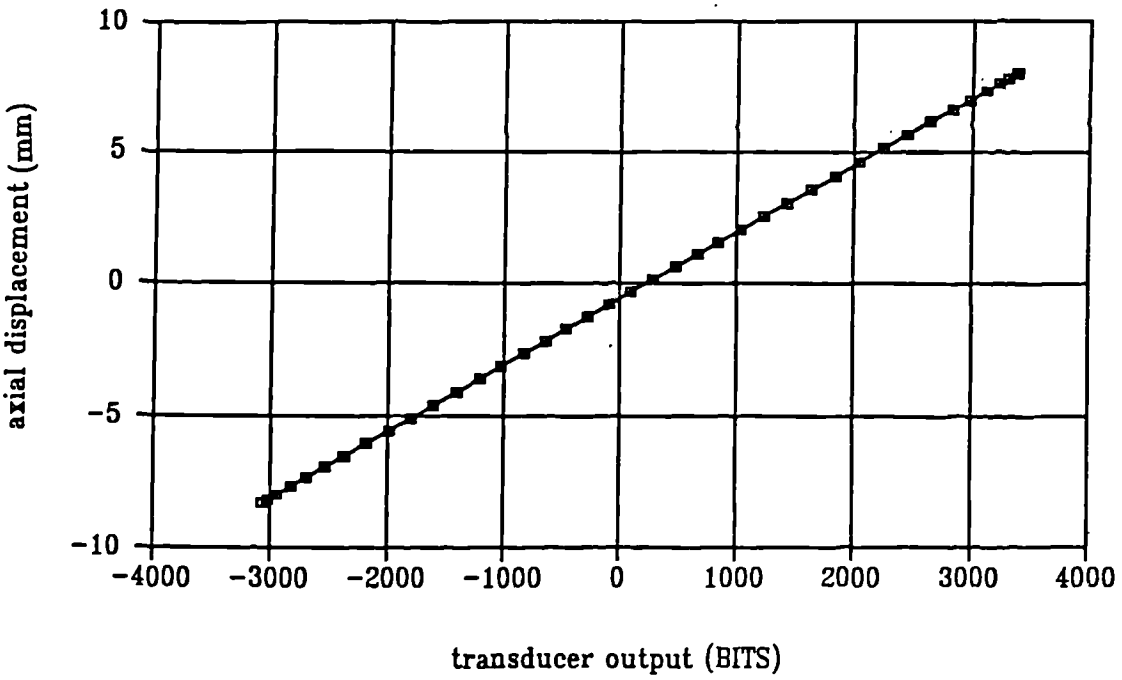

Figure 4.2.7 *Typical calibration* curve for a Hall effect local axial strain gauge.

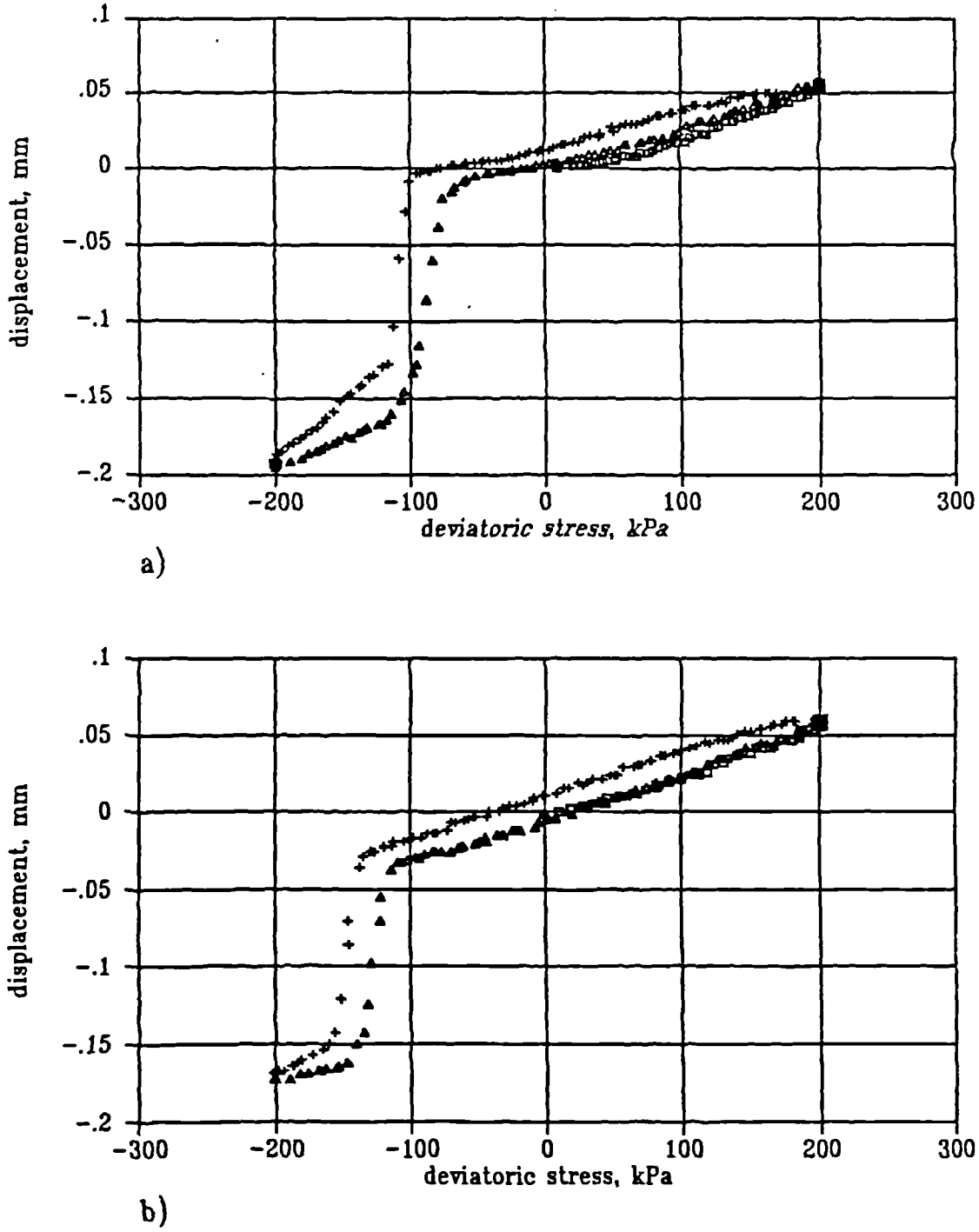

Figure 4.2.8 Typical compliance curves for Surrey University load cell. (a) at constant cell pressure σ_r = 300 kPa (b) at constant cell pressure σ_r = 400 kPa.

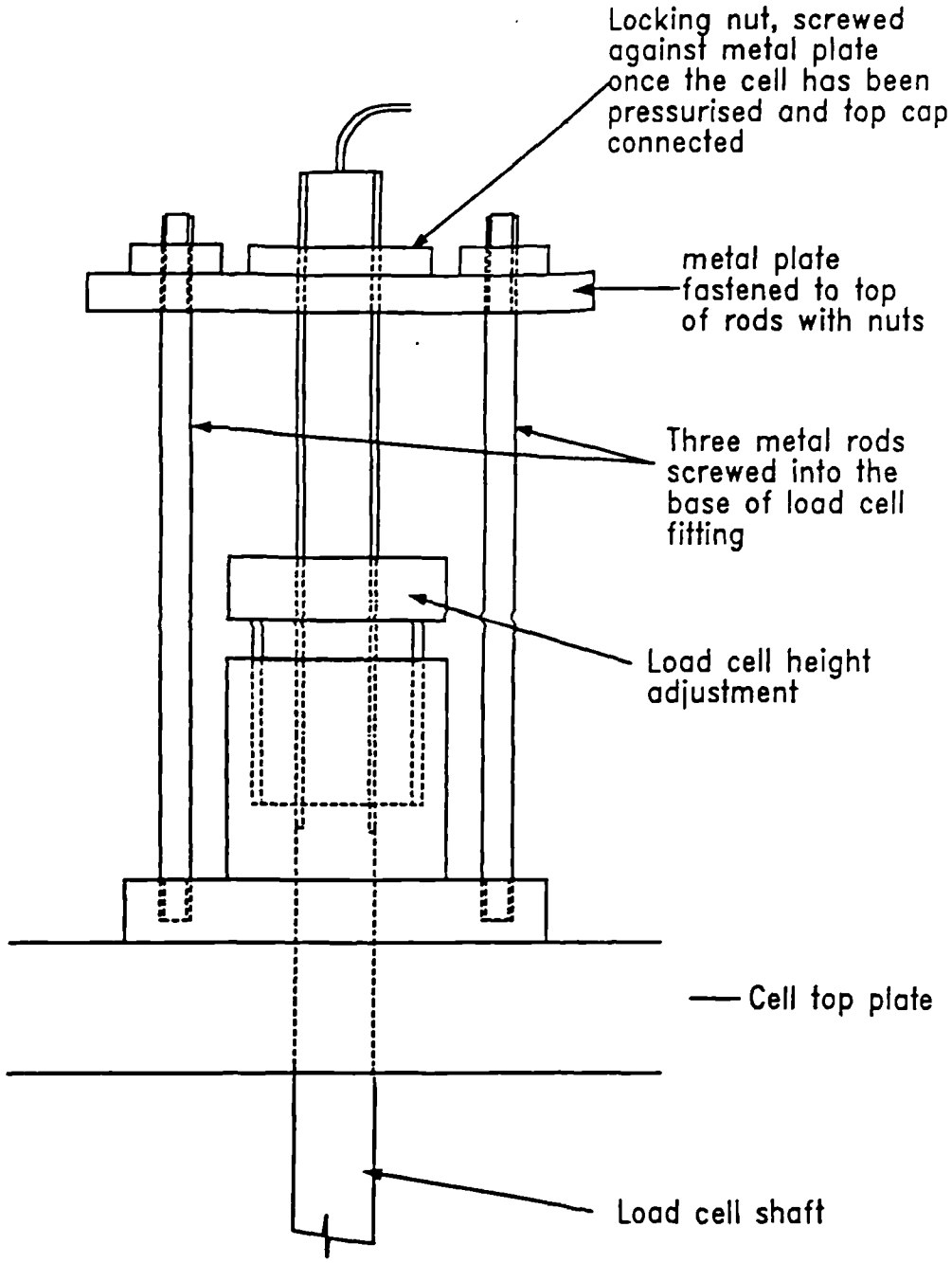

Figure 4.2.9 Diagram showing the locking device used to prevent the movement of the load cell shaft.

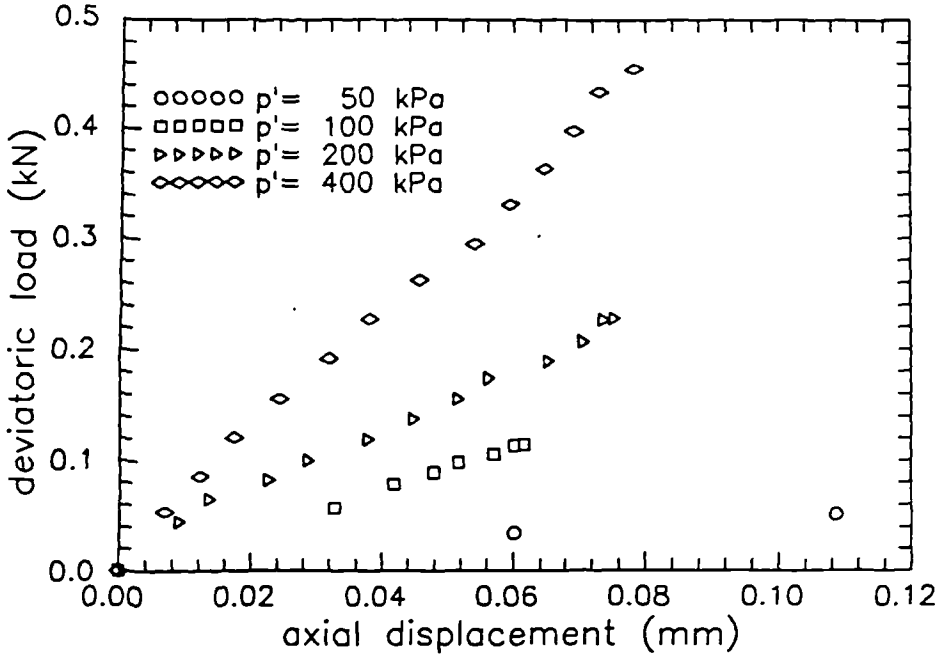

Figure 4.2.10 Typical compliance data for Surrey University load cell at constant mean effective stress.

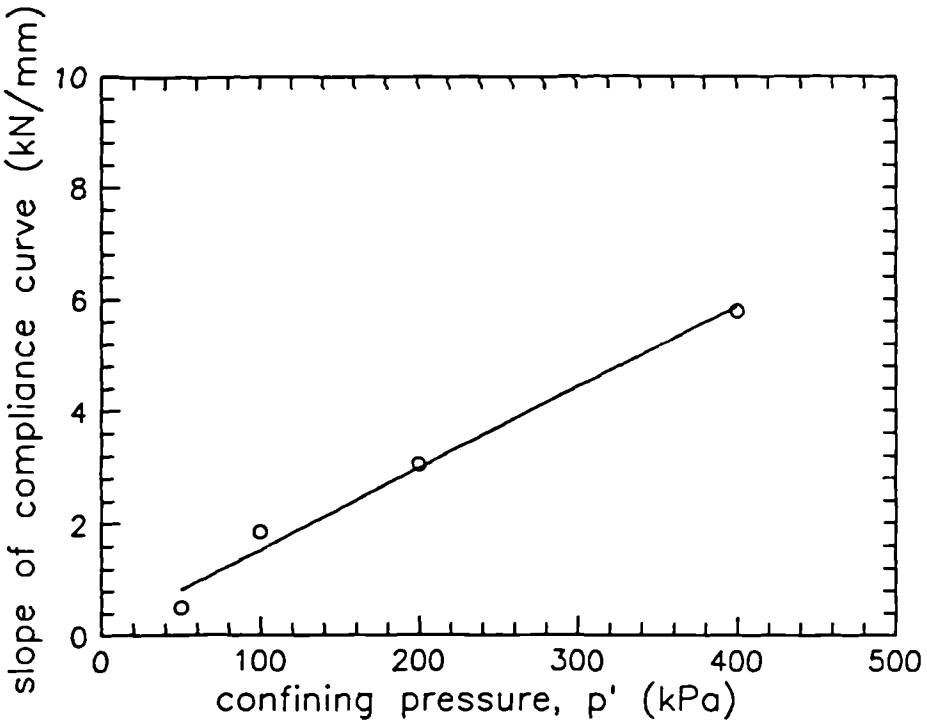

Figure 4.2.11 Typical relation between compliance of the system and mean effective stress.

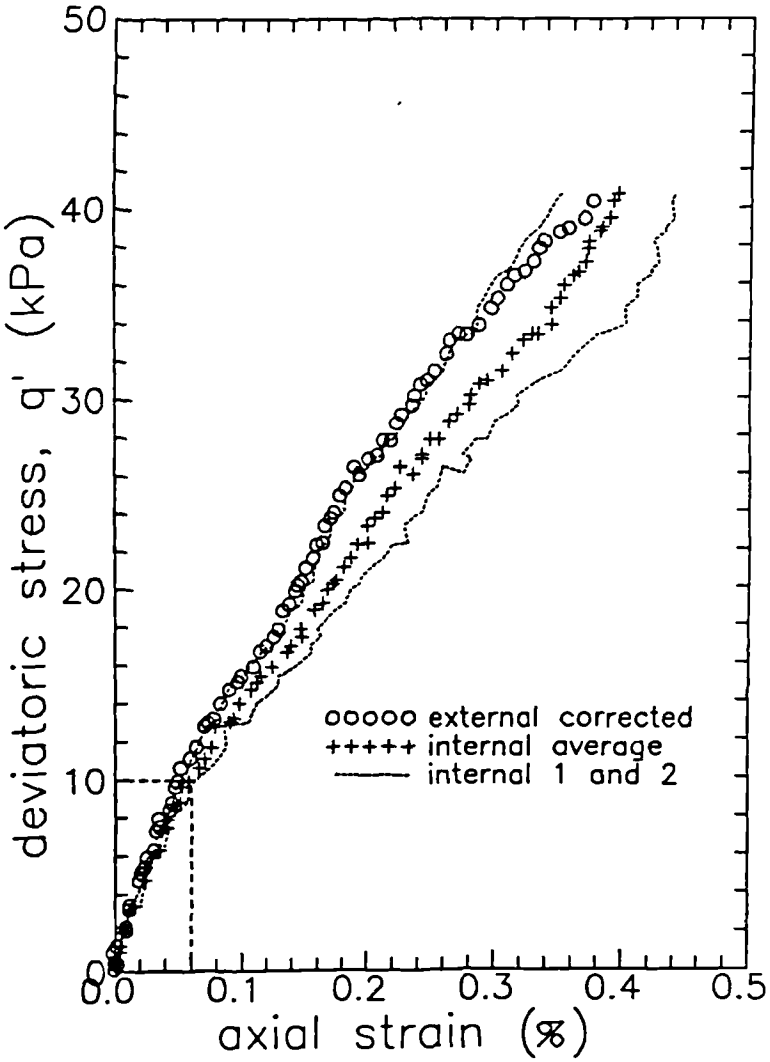

Figure 4.2.12 Set of stress-strain data from the shearing stage of test RLCD2 comparing axial strain measured externally and internally.

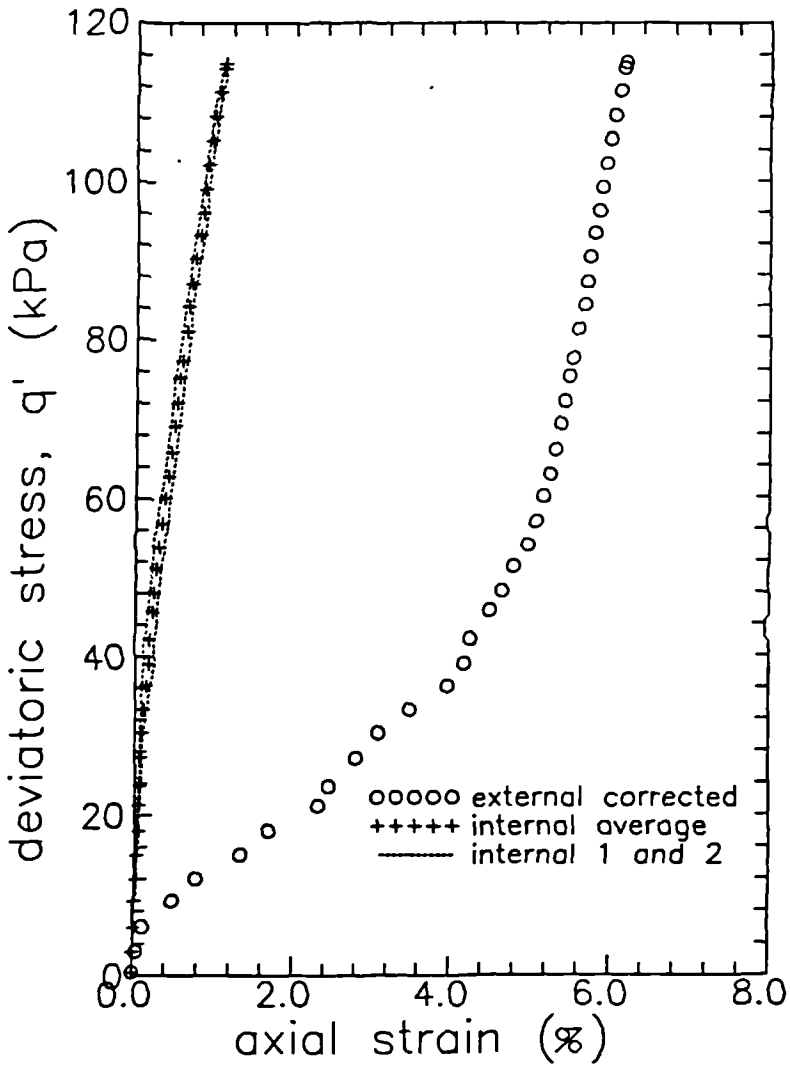

Figure 4.2.13 Set of stress-strain data from the shearing stage of test ULCD comparing axial strain measured externally and internally.

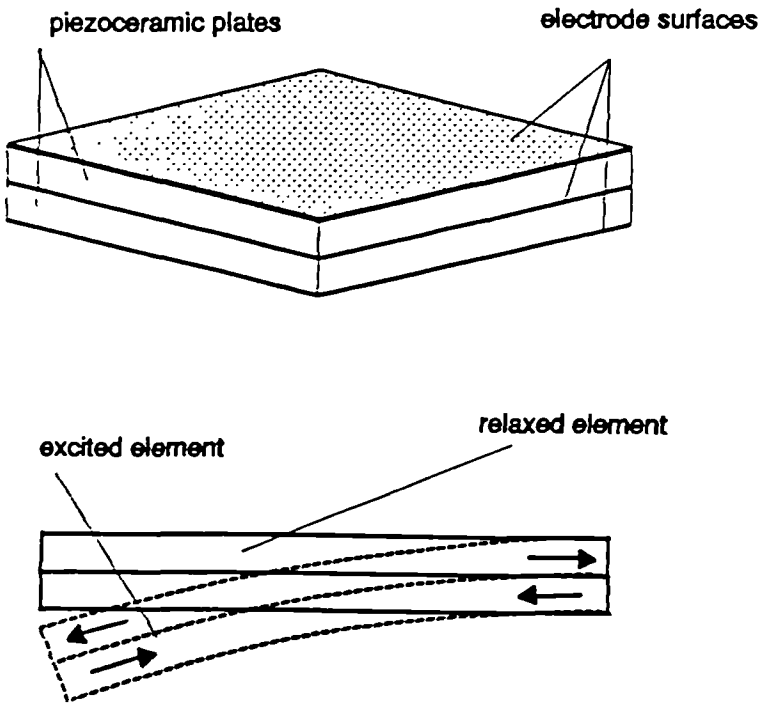

Figure 4.3.1 Diagram showing the mechanism of deformation of a piezoceramic bender element.

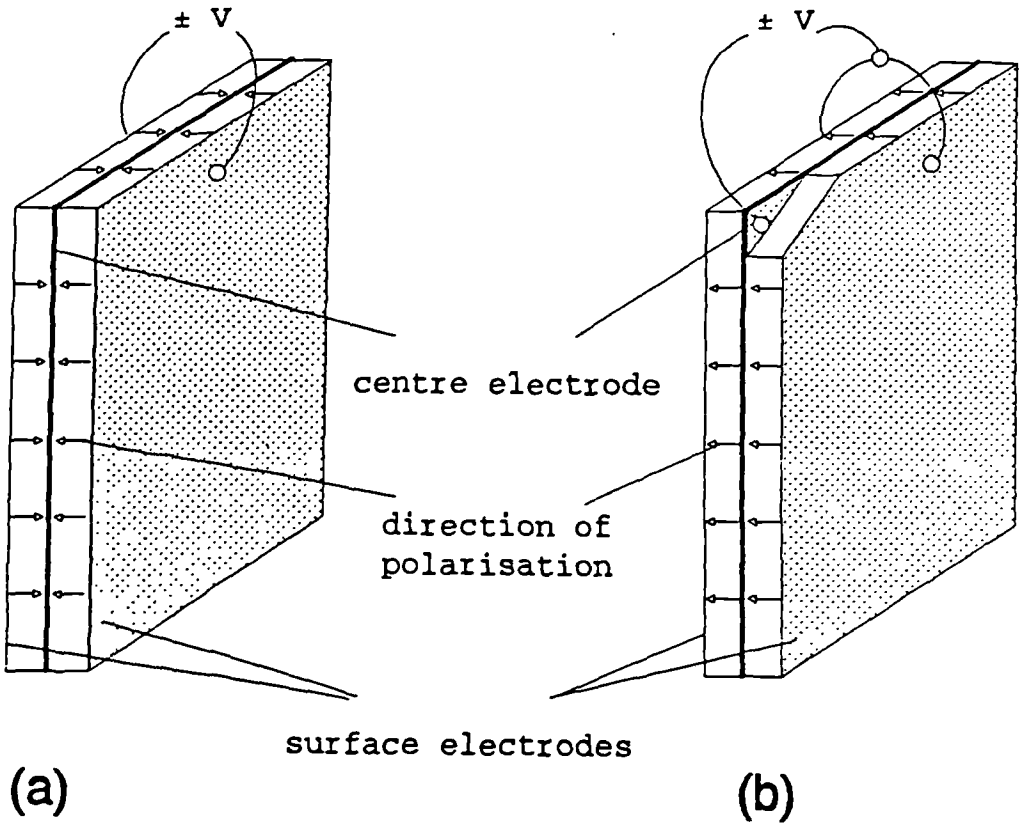

Figure 4.3.2 Electrical connections for bender elements. (a) series connected (b) parallel connected.

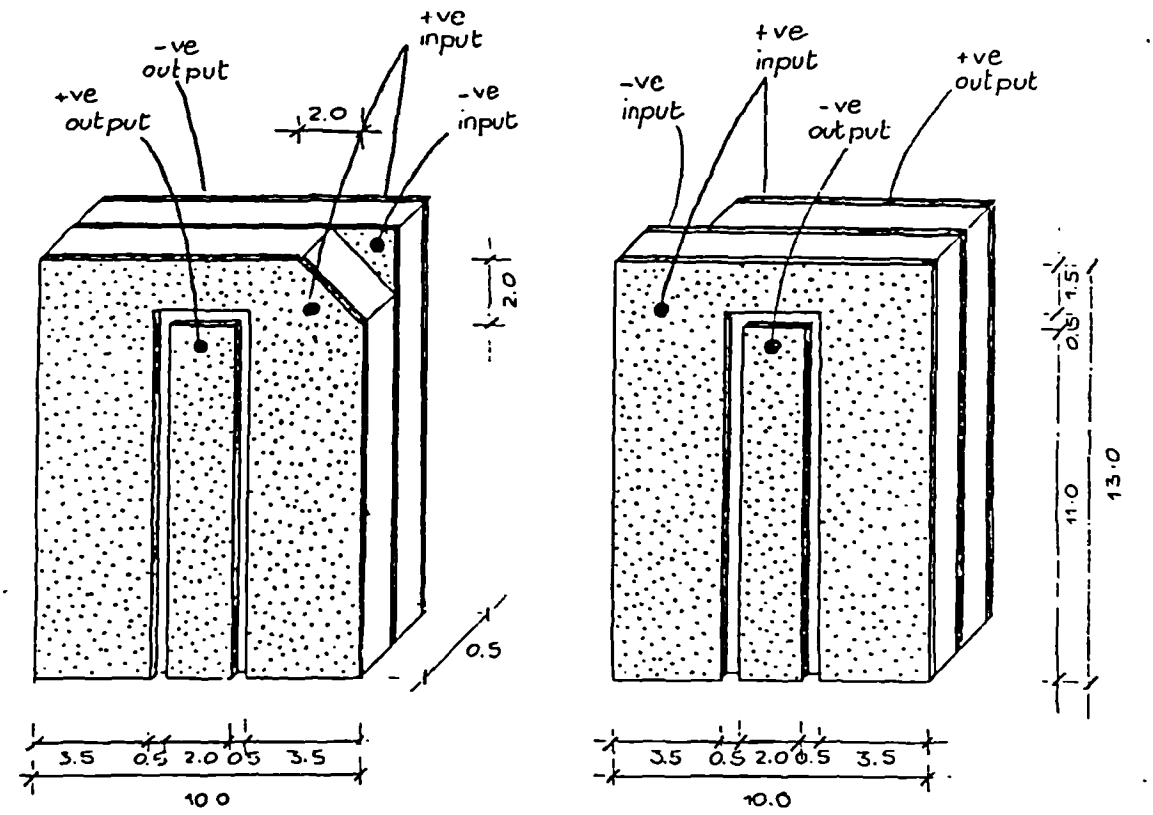

Figure 4.3.3 Electrical connections for self monitoring trasmitter element.

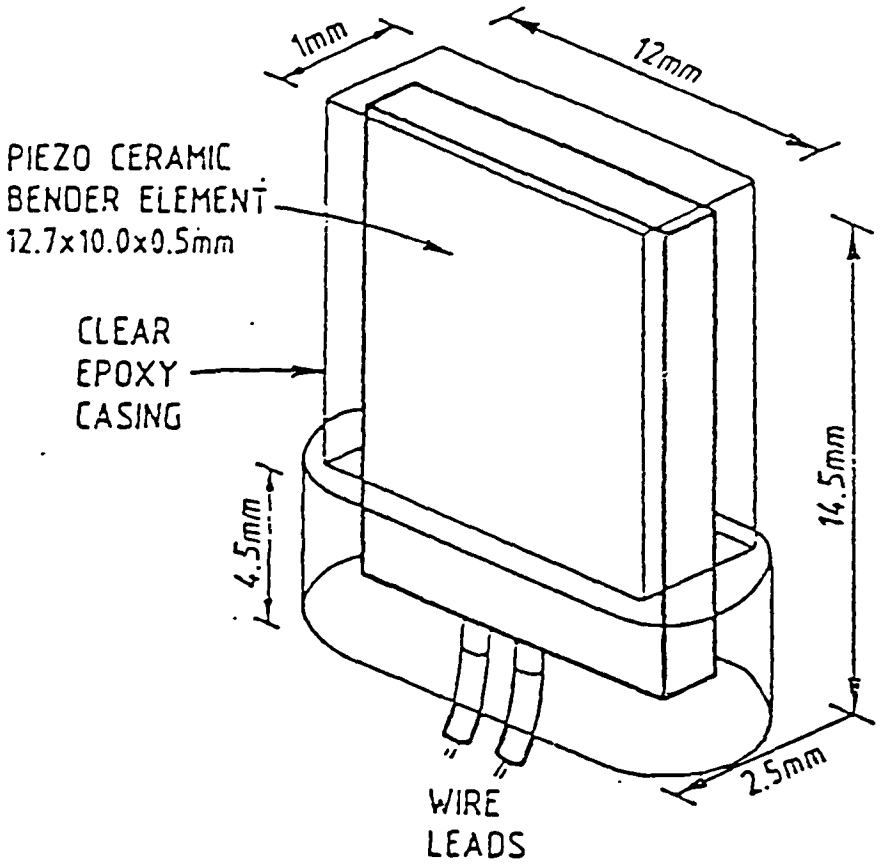

Figure 4.3.4 Geonor bender element in its epoxy casing (after Dyvick and Madshus, 1985)

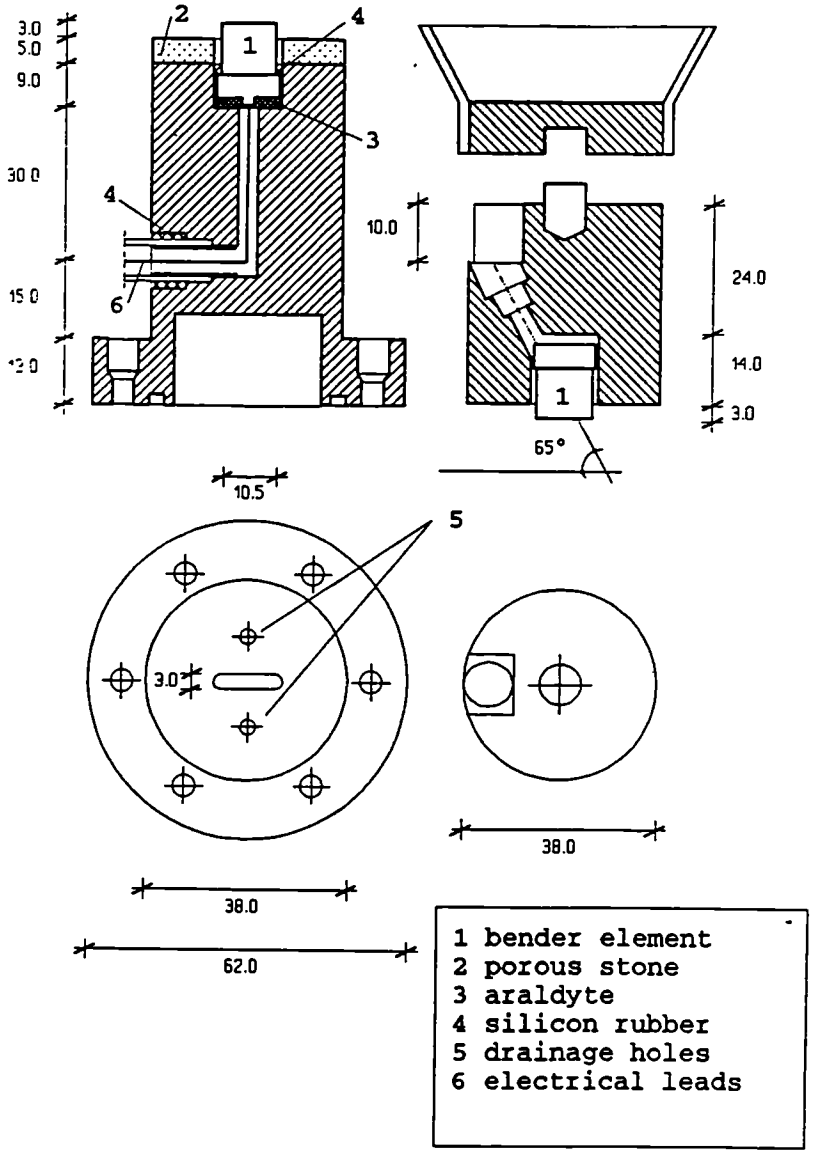

Figure 4.3.5 Modifications to the base pedestal and to the top cap of the triaxial cell required to accomodate the bender elements.

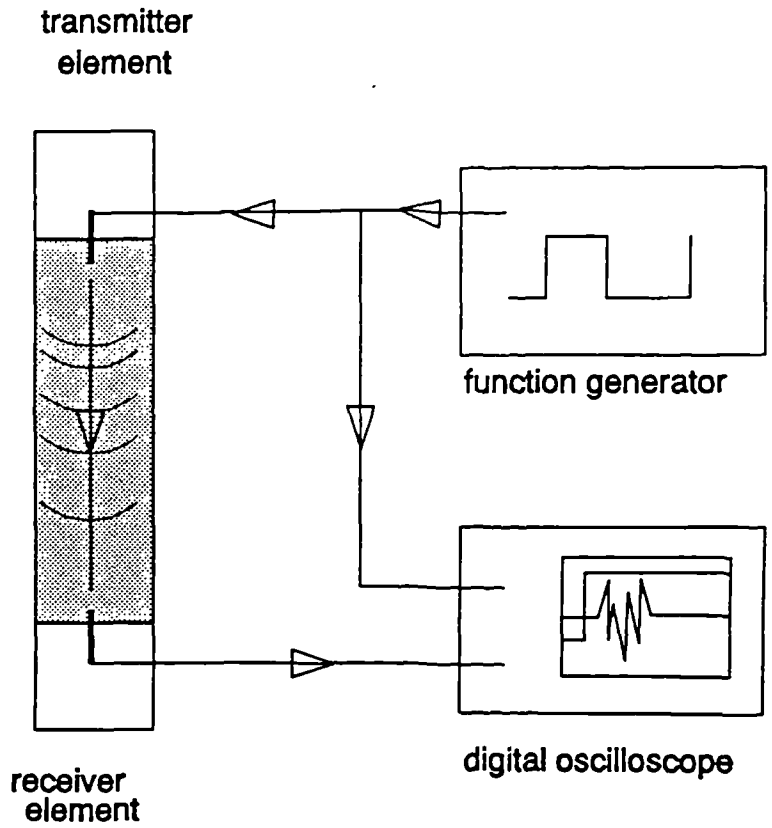

Figure 4.3.6 Diagram of the electronics required to operate the bender elements.

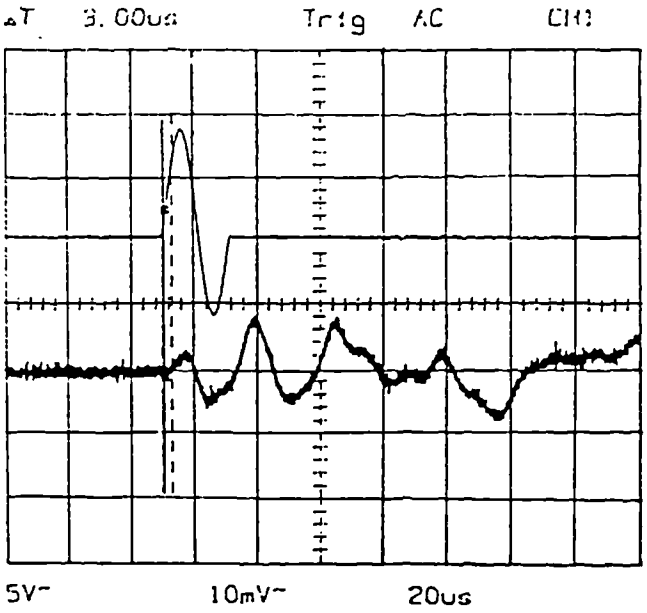

Figure 4.3.7 Calibration of the system. Time delay observed between driving signal and received signal with transmitter element in direct contact with receiver element.

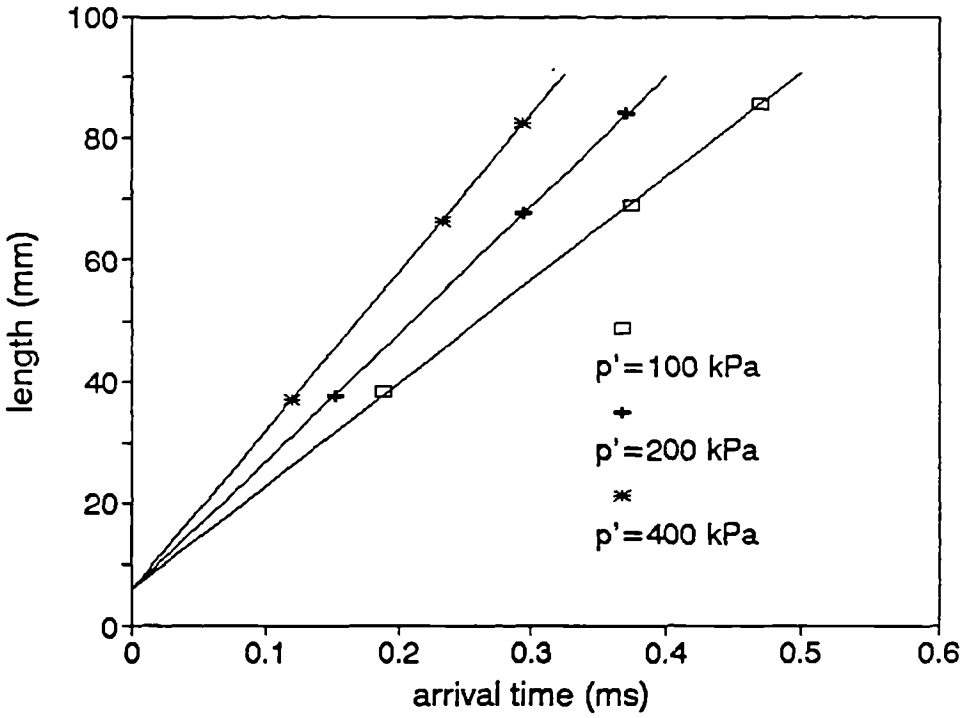

Figure 4.3.8 Calibration of the system. Plot of the length of the sample against the arrival time.

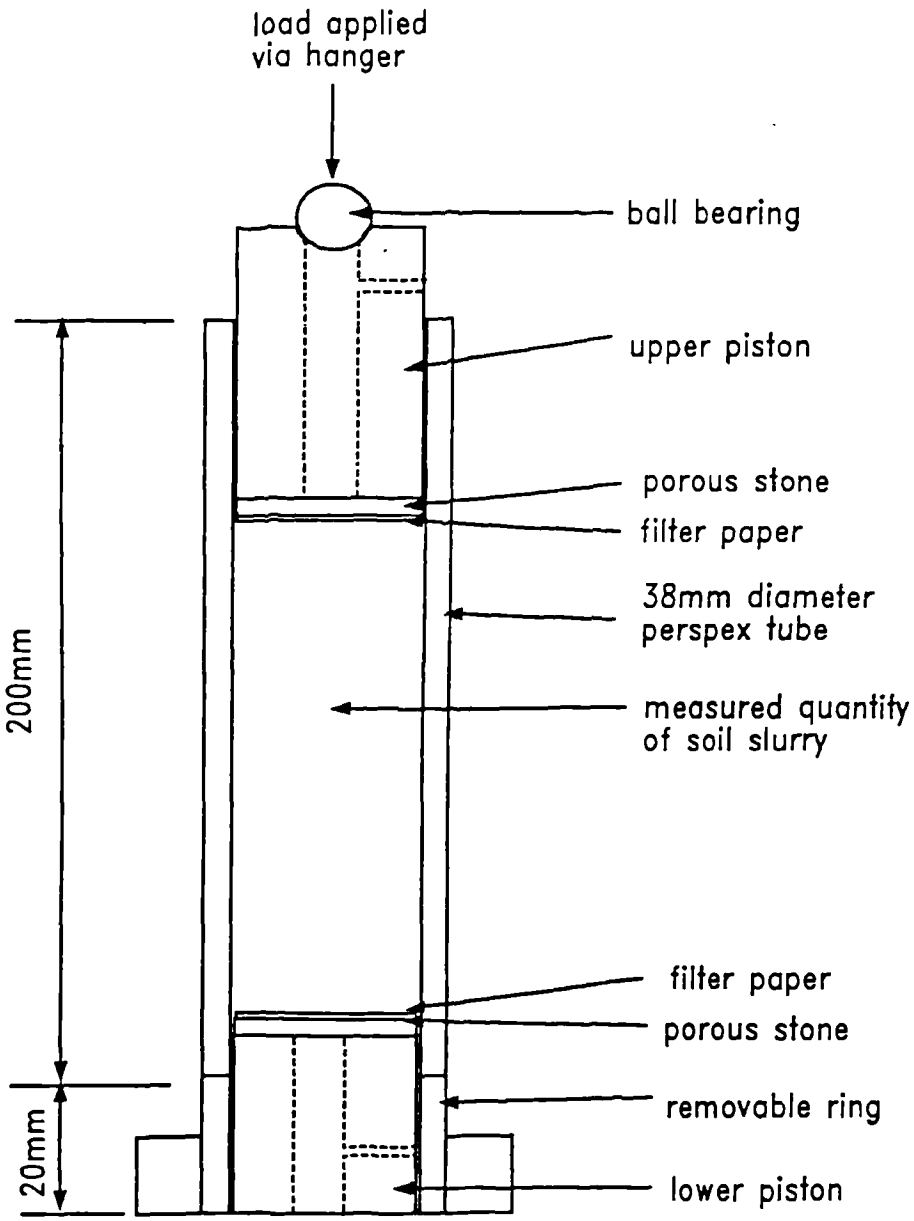

Figure 4.4.1 Diagram of a perspex floating ring consolidation press. (after Stallebrass, 1990).

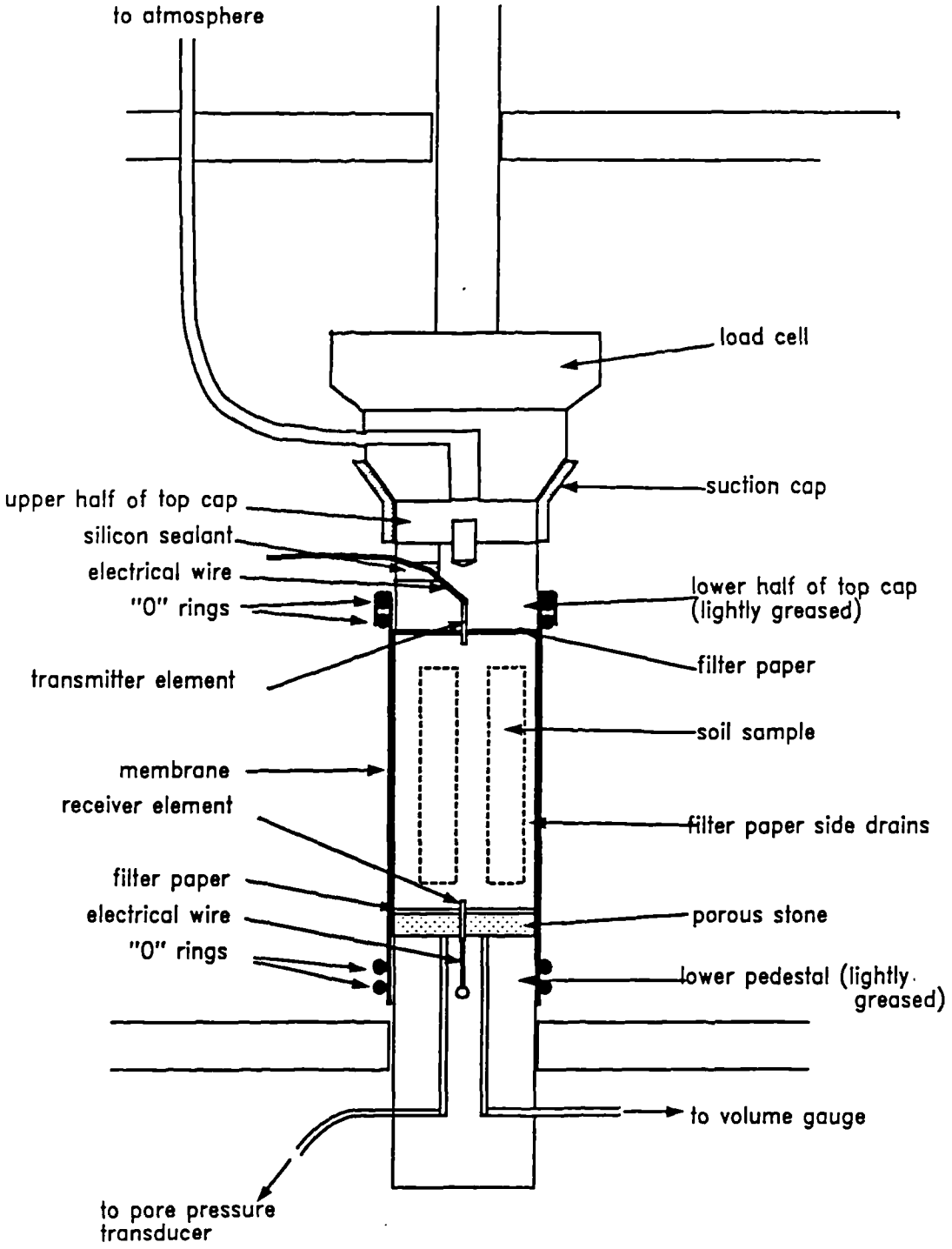

Figure 4.4.2 Diagram showing typical sample set-up in the triaxial cell.

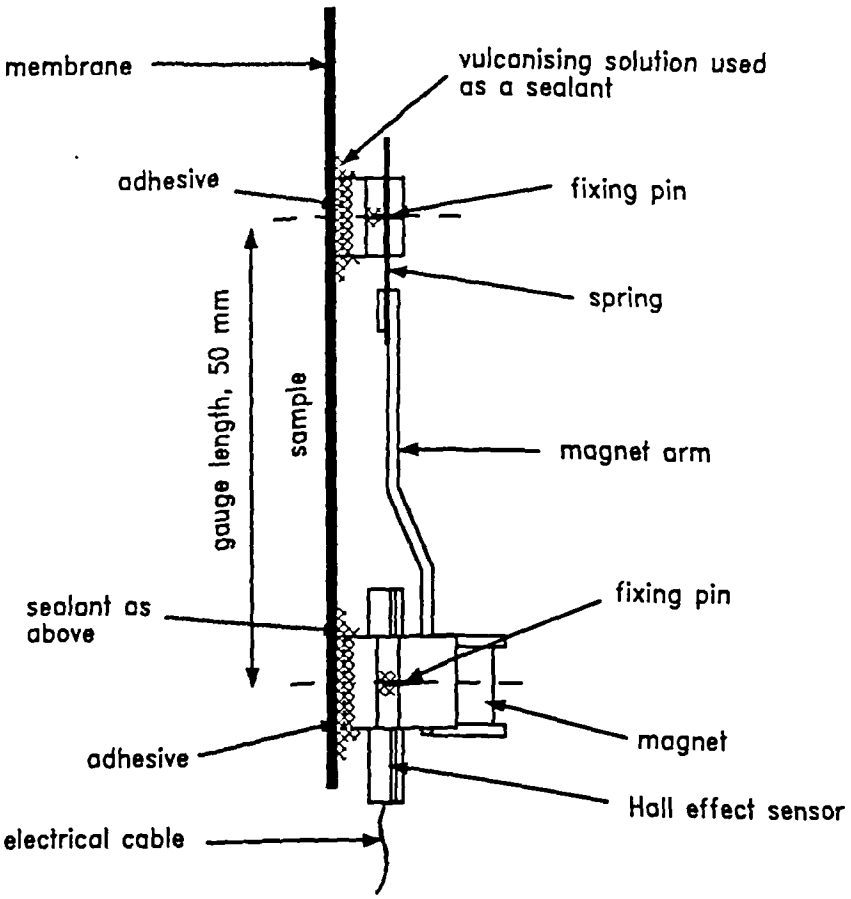

Figure 4.4.3 Diagram showing a local axial strain gauge fitted to the side of the sample.

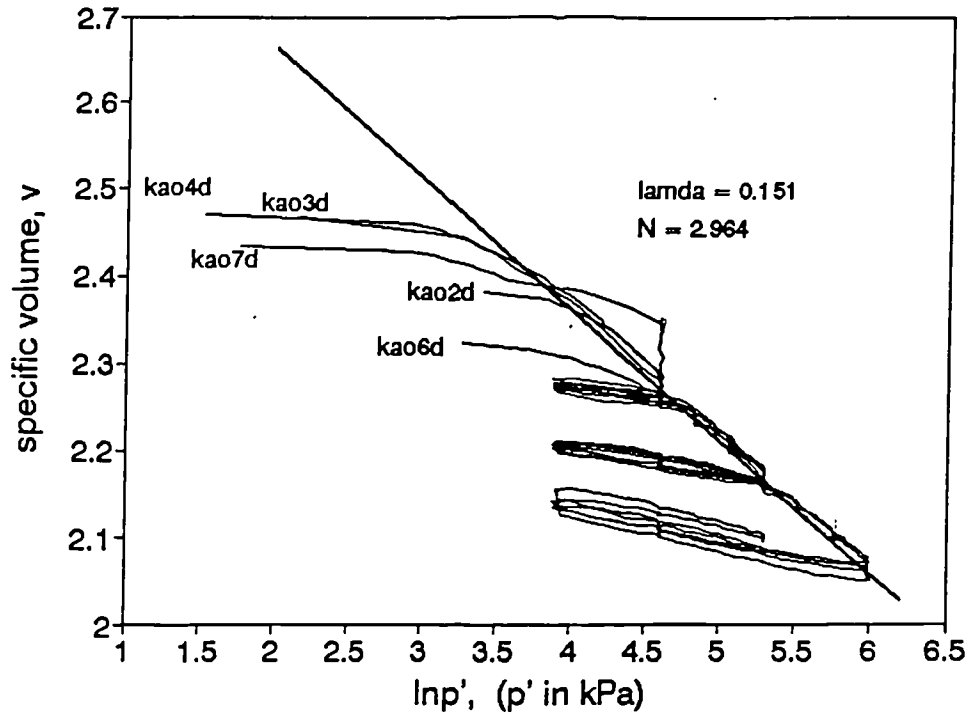

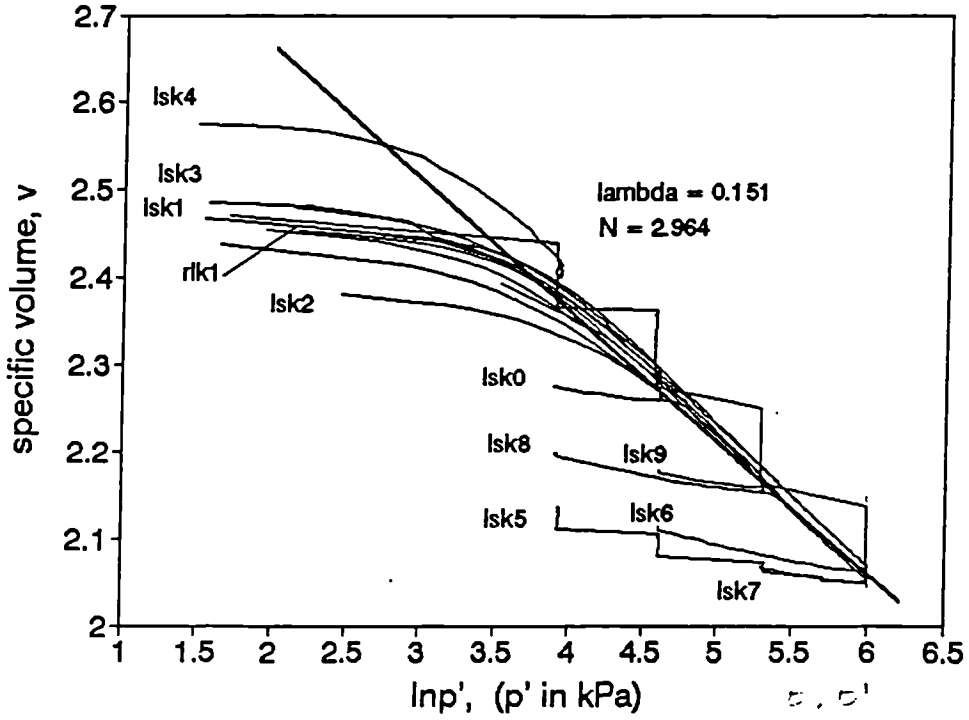

Figure 4.6.1 Speswhite kaolin. All data. isotropic compression and swelling.

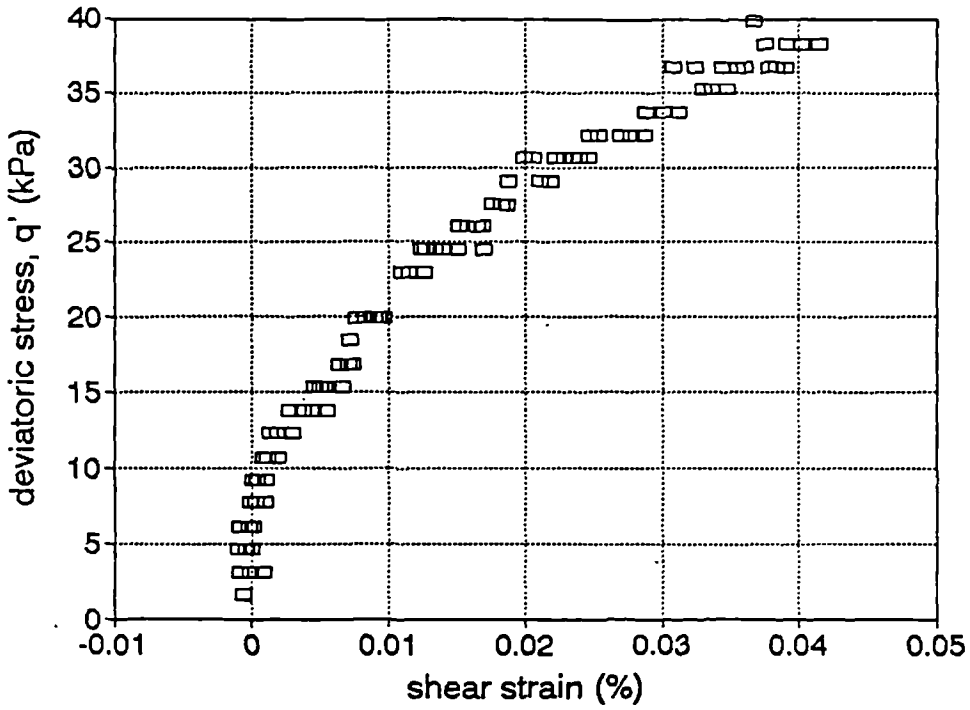

Figure 4.6.2a Initial part of the deviatoric stress versus shear strain curve from the shearing stage of test LSK1 before editing.

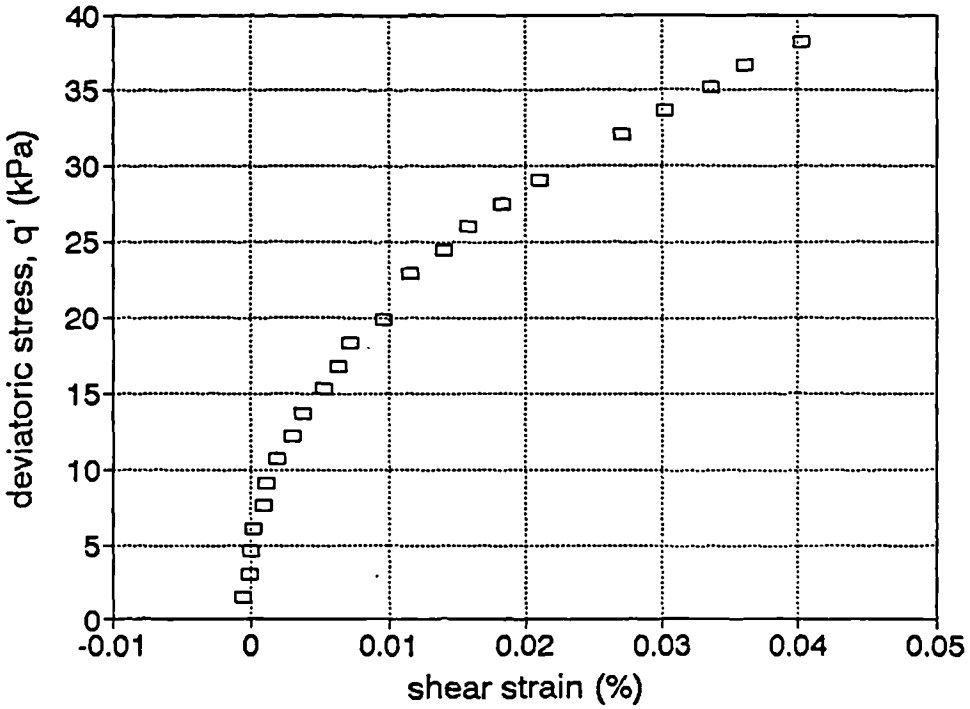

Figure 4.6.2b Initial part of the deviatoric stress versus shear strain curve from the shearing stage of test LSK1 after editing.

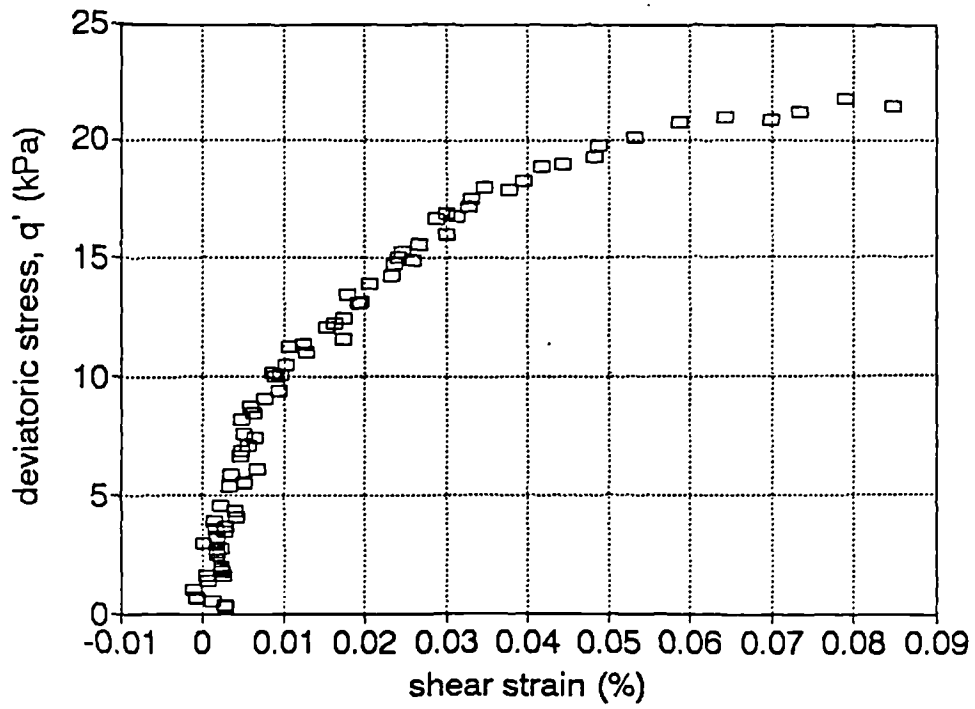

Figure 4.6.3a Initial part of the deviatoric stress versus shear strain curve from the shearing stage of test KAOL, raw data.

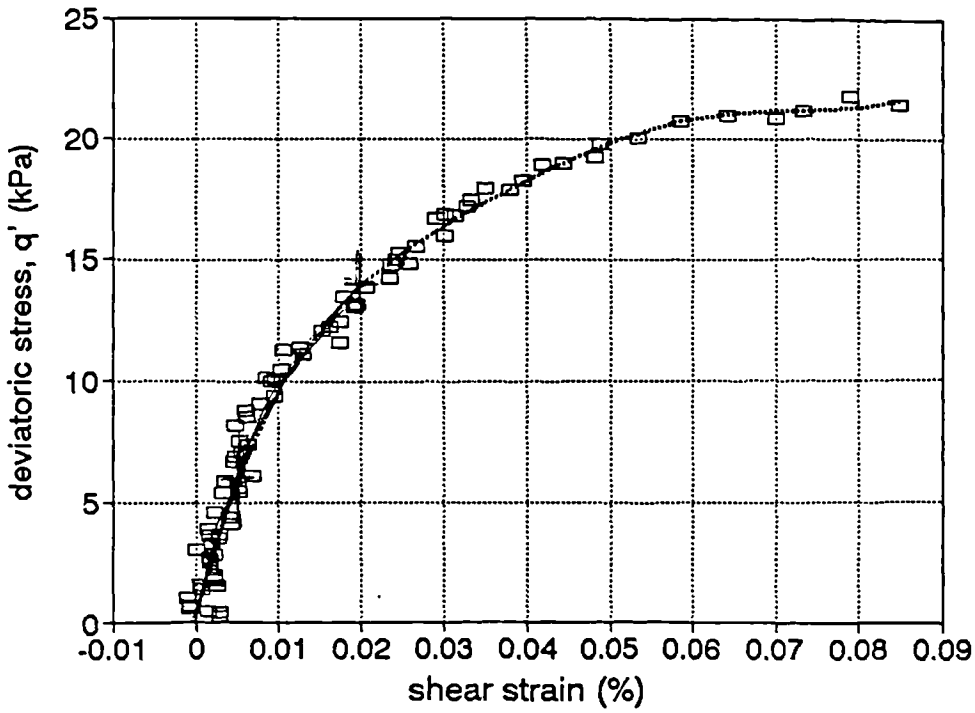

Figure 4.6.3b Initial part of the deviatoric stress versus shear strain curve from the shearing stage of test KAOL with fifth order polynomial fit.

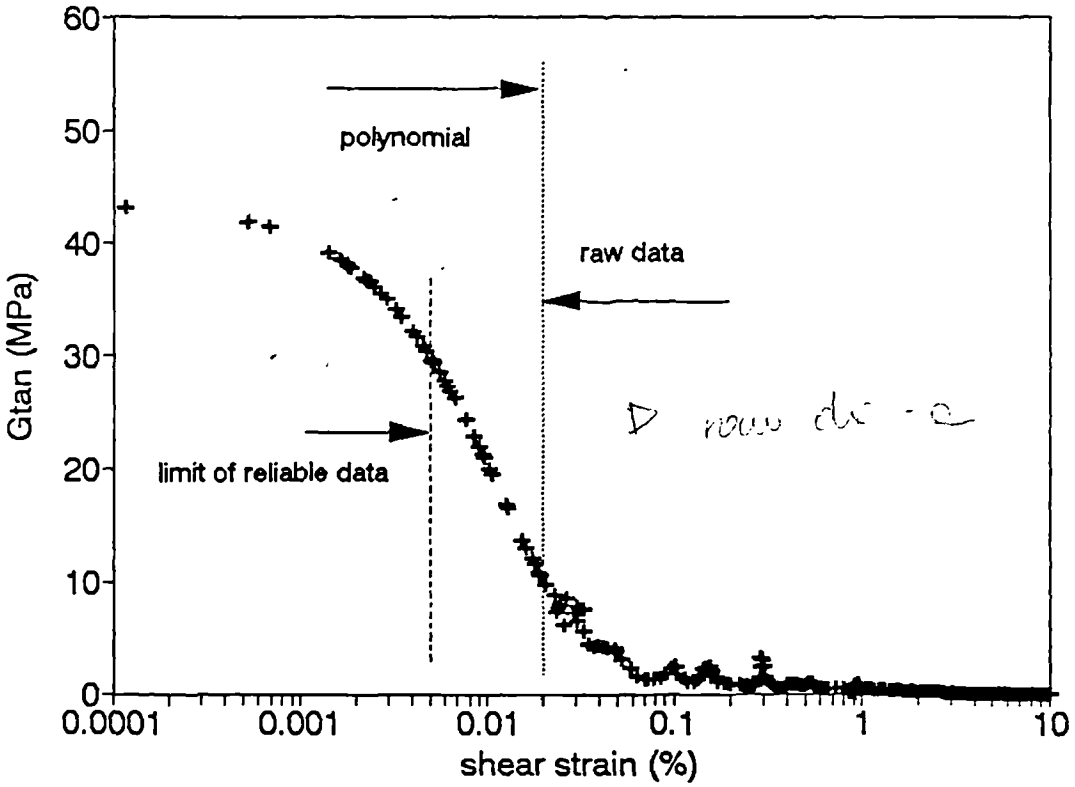

Figure 4.6.4 Shear stiffness versus shear strain amplitude for test KAOL, combined method.

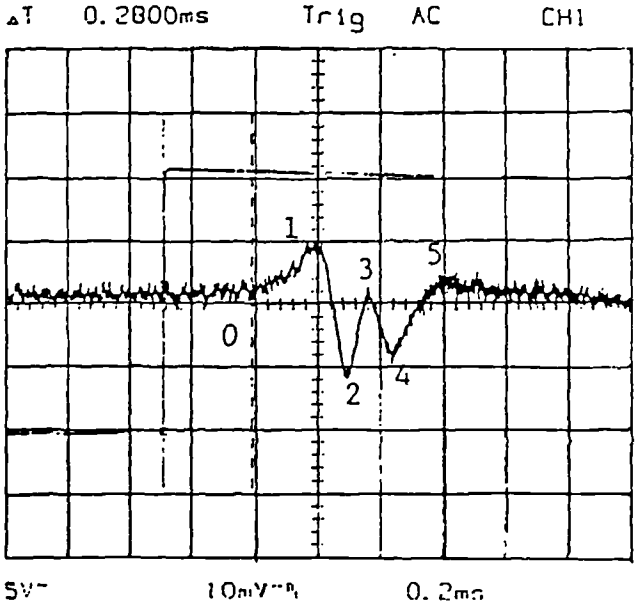

Figure 4.6.5 Example of the time record obtained driving the transmitter element with a square wave of an amplitude of ± 10 V and a frequency of 50 Hz).

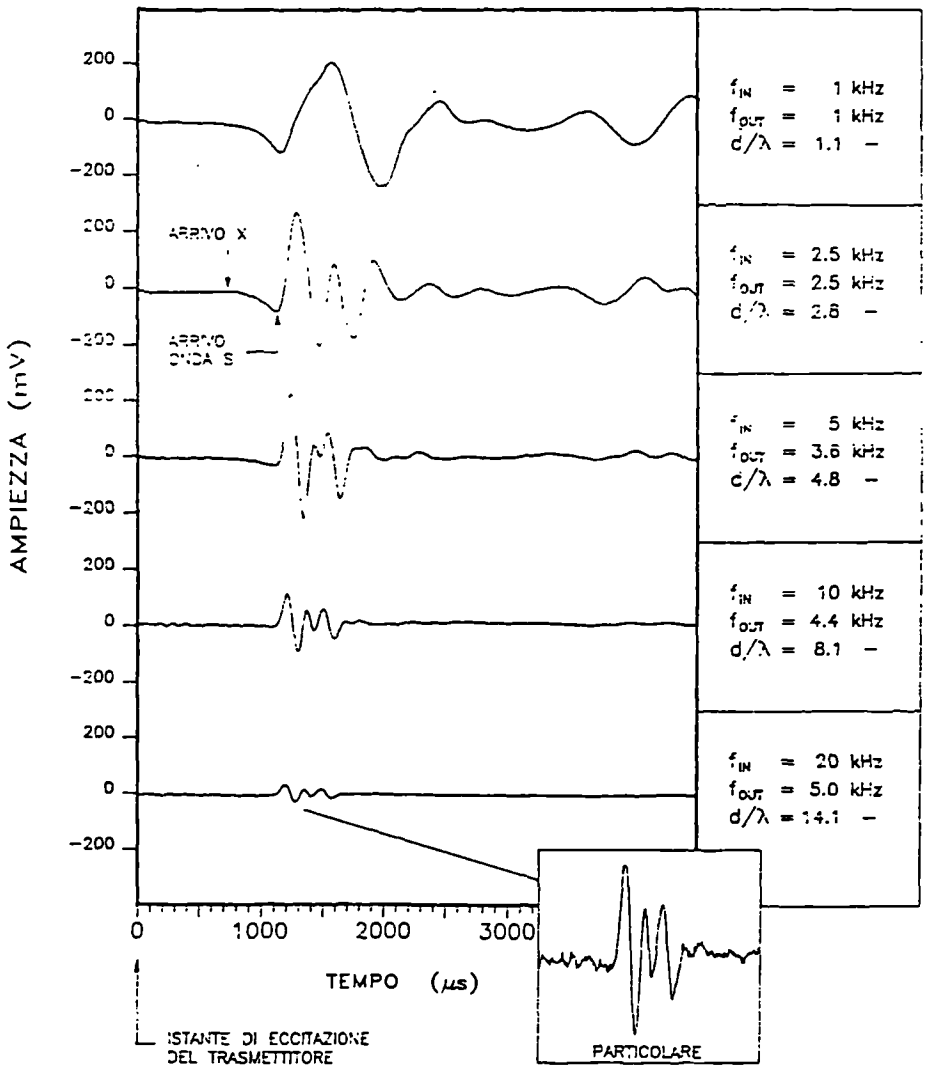

Figure 4.6.6 Example of the time record obtained driving the transmitter element with a single sinusoidal pulse of constant amplitude and increasing frequency (after Brignoli and Gotti, 1992).

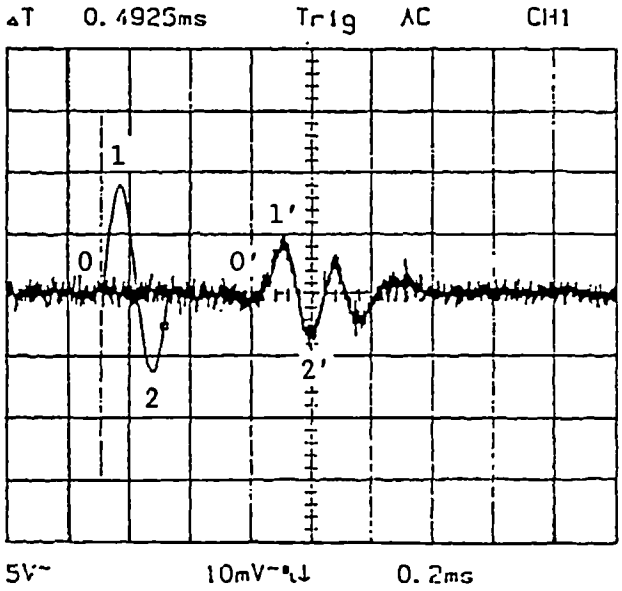

Figure 4.6.7 Example of the time record obtained driving the transmitter element with a single sinusoidal pulse of an amplitude of ± 10 V and a frequency of 5 kHz.

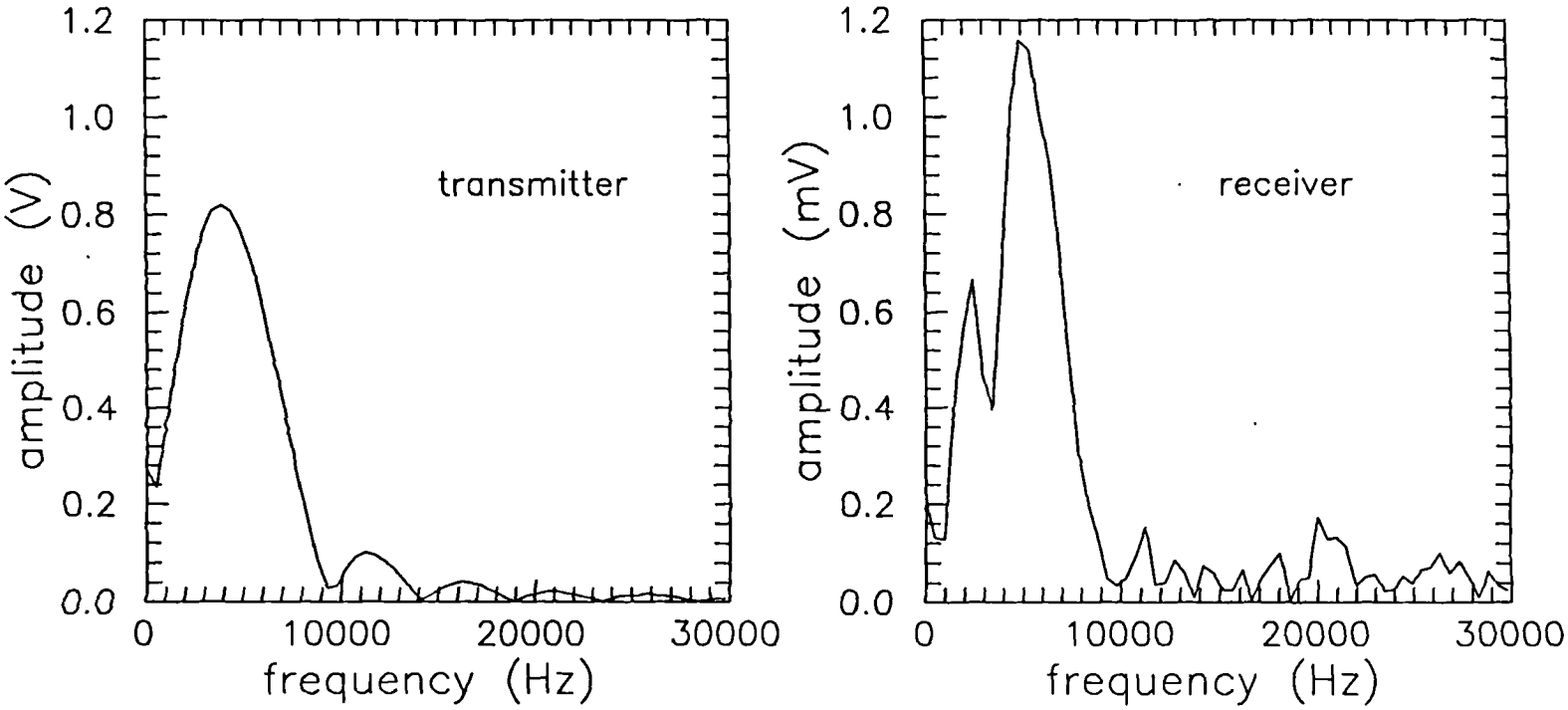

Figure 4.6.8 Linear spectra at receiver and transmitter.

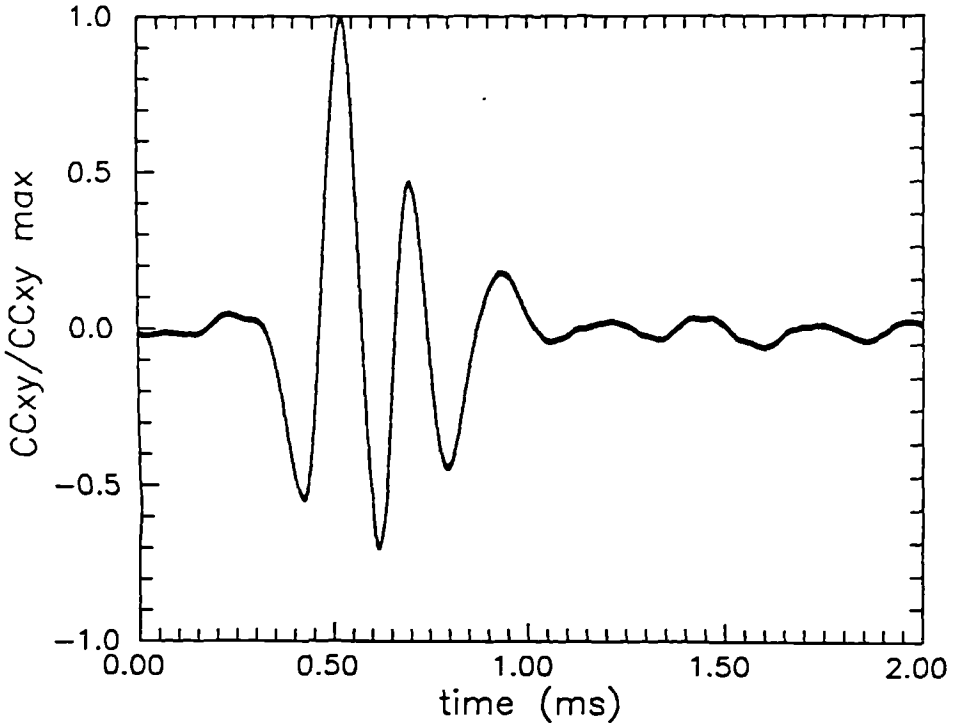

Figure 4.6.9 Cross correlation of the signals at transmitter and receiver, normalised on its maximum value.

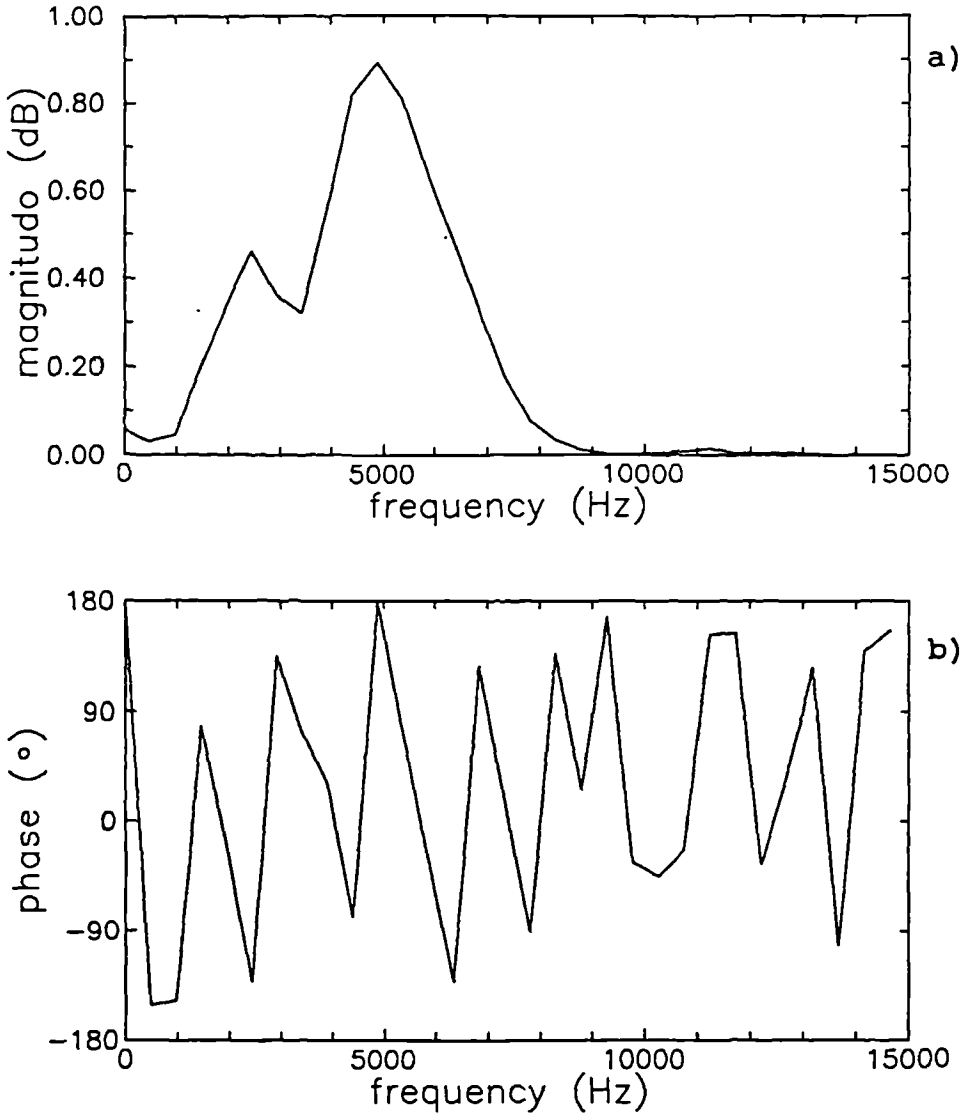

Figure 4.6.10 Cross power spectrum of the signals at transmitter and receiver. (a) magnitude (b) phase.

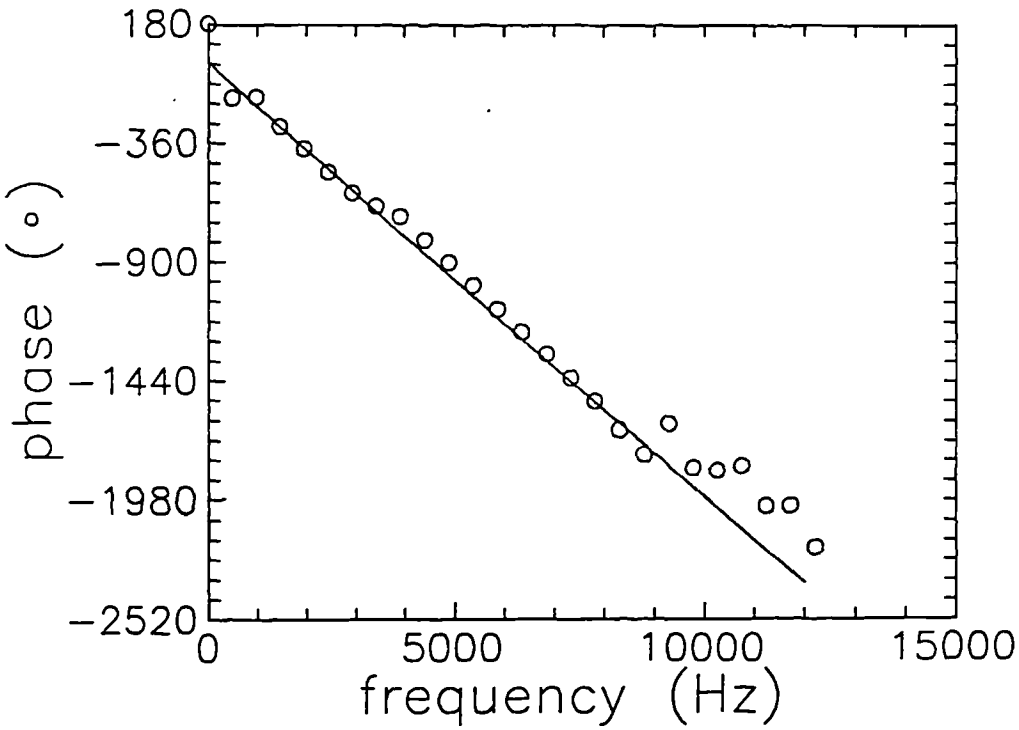

Figure 4.6.11 Linear interpolation of the cross power spectrum absolute phase diagram.

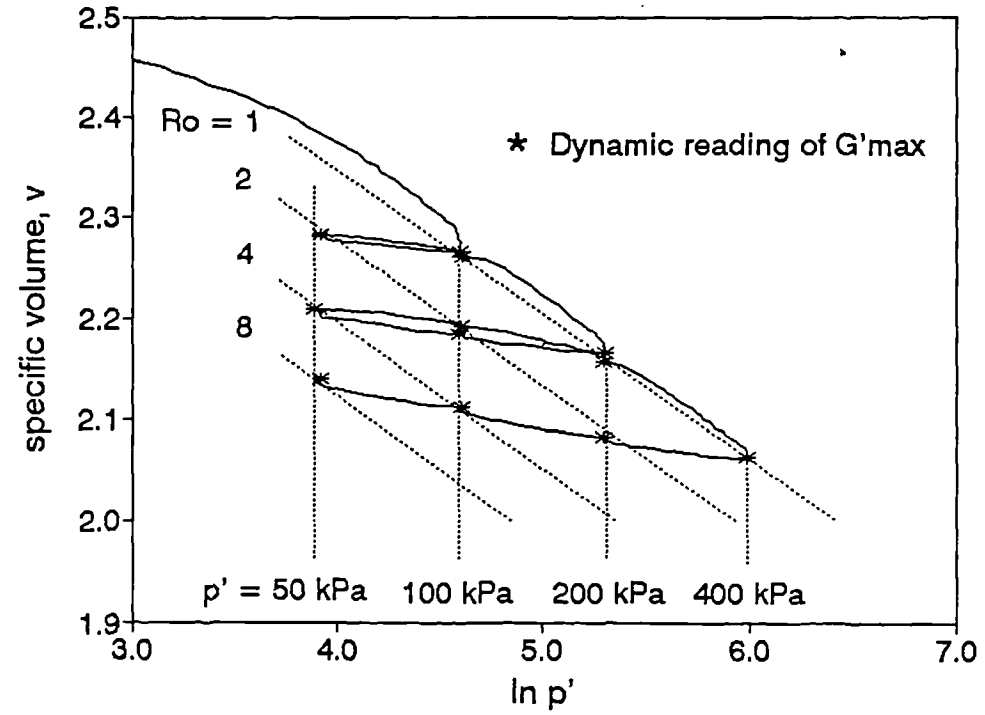

Figure 5.2.1 Diagram showing the basic form of test to determine the effect of state on small strain stiffness in isotropic conditions

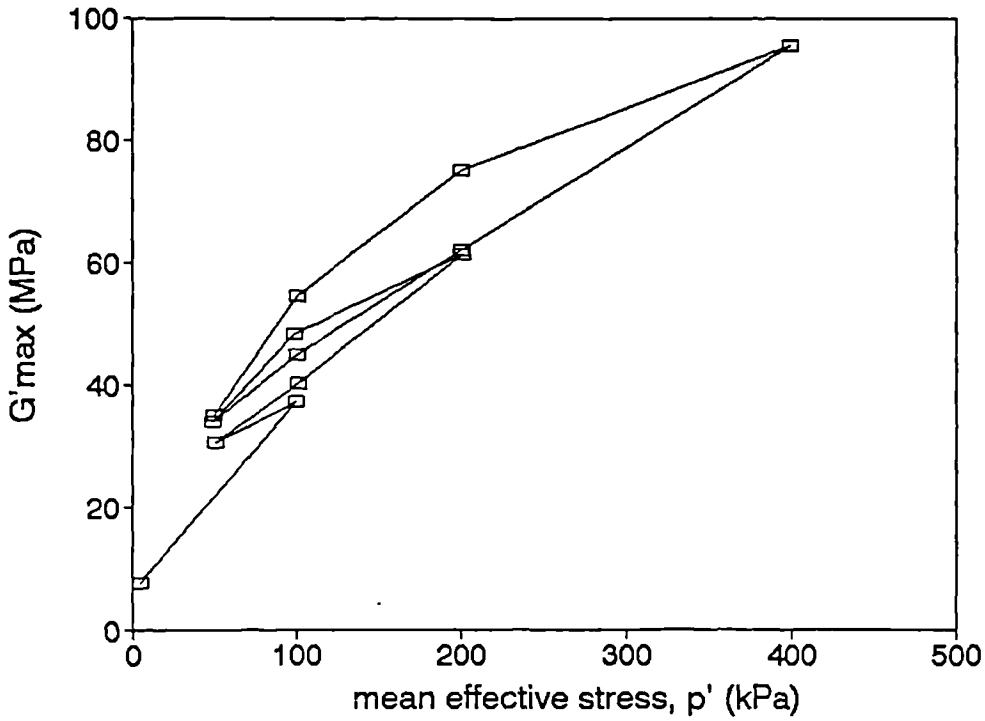

Figure 5.2.2 Typical set of data from test KA0D4 showing the values of G'_{max} obtained at different values of mean effective stress and overconsolidation ratios

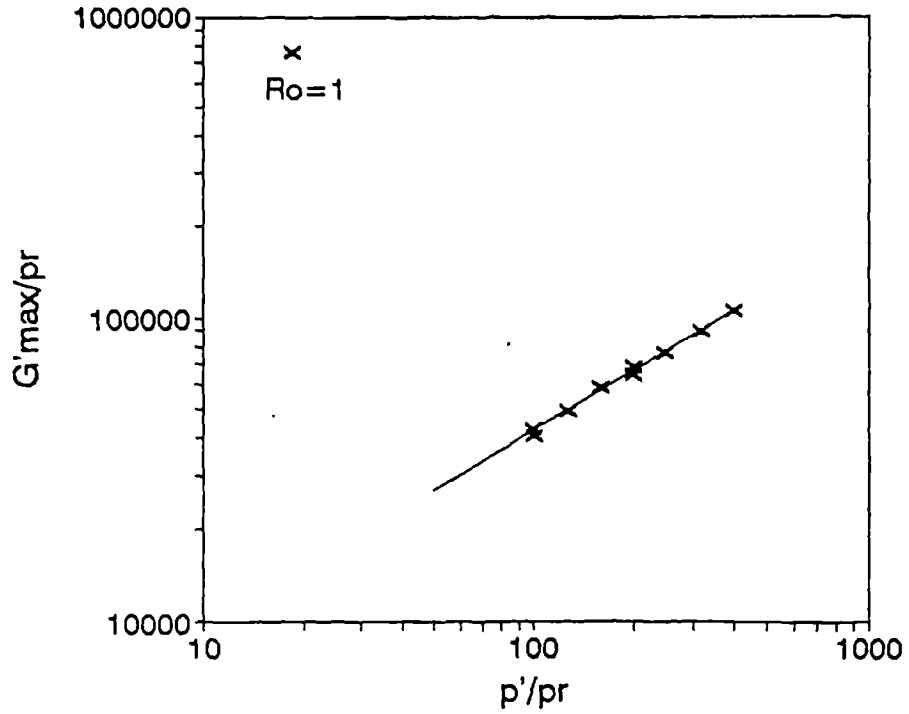

Figure 5.2.3 Speswhite kaolin. Test KAOD7. Dependence of very small strain stiffness on mean effective stress for normally consolidated states (R_o = 1).

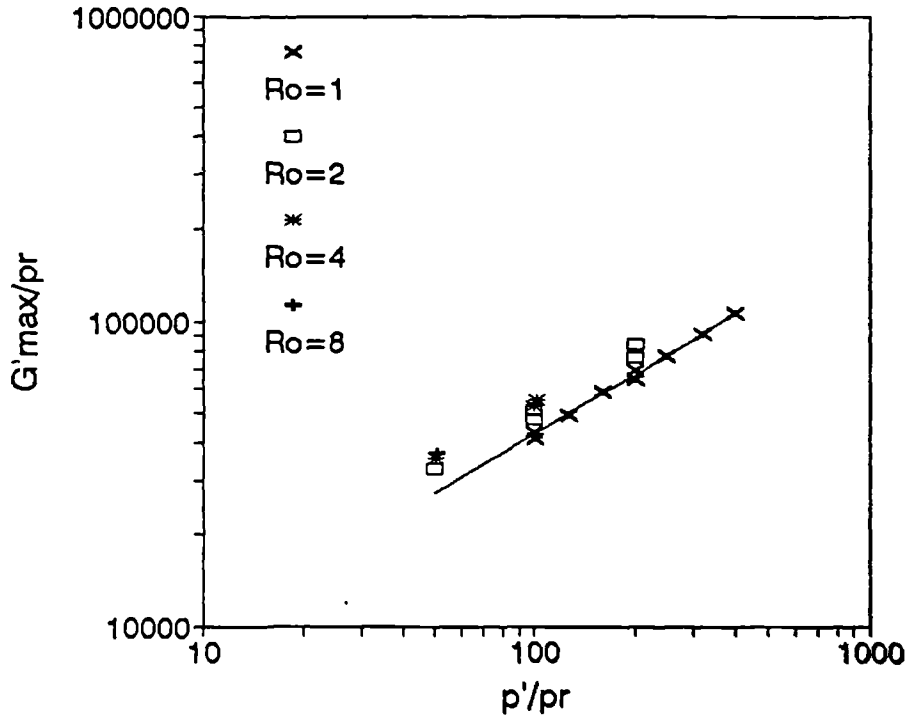

Figure 5.2.4 Speswhite kaolin. Test KAOD7. Dependence of very small strain stiffness on mean effective stress. All readings.

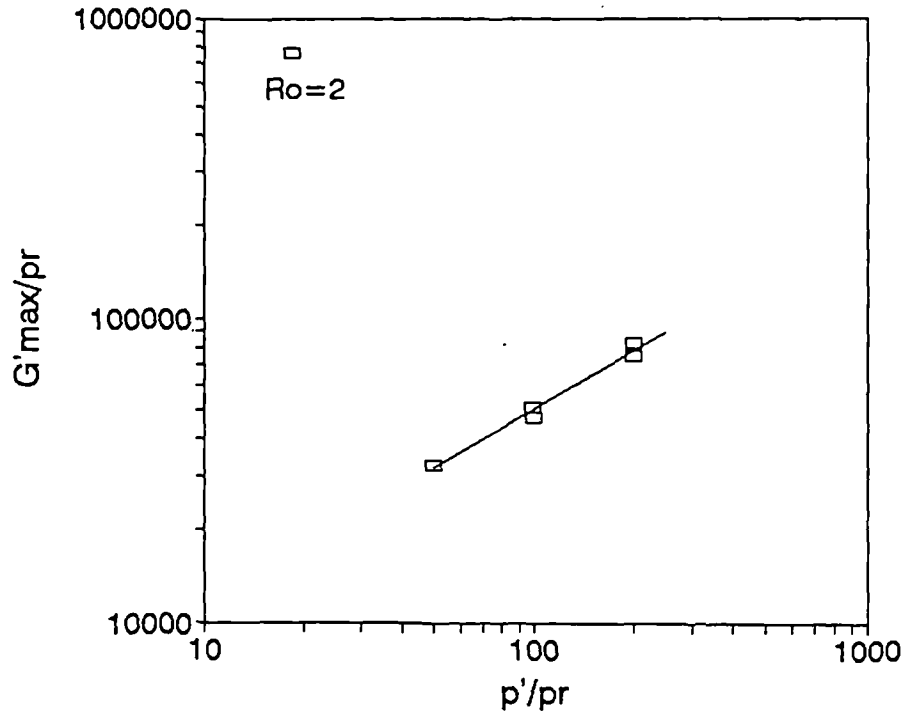

Figure 5.2.5 Speswhite kaolin. Test KAOD7. Dependence of very small strain stiffness on mean effective stress. Nominal R_o = 2.

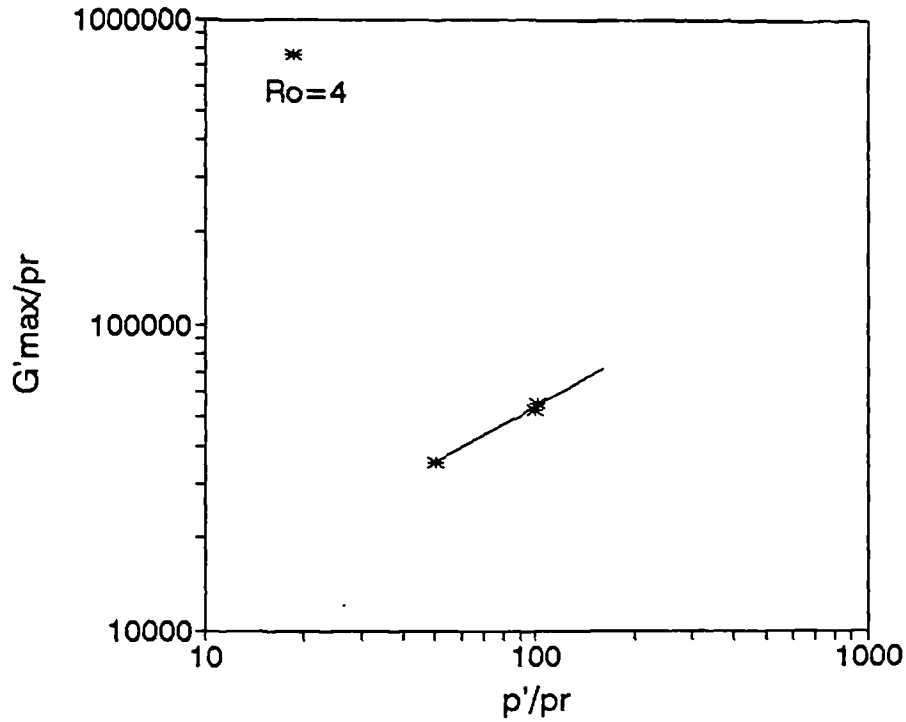

Figure 5.2.6 Speswhite kaolin. Test KAOD7. Dependence of very small strain stiffness on mean effective stress. Nominal R_o = 4.

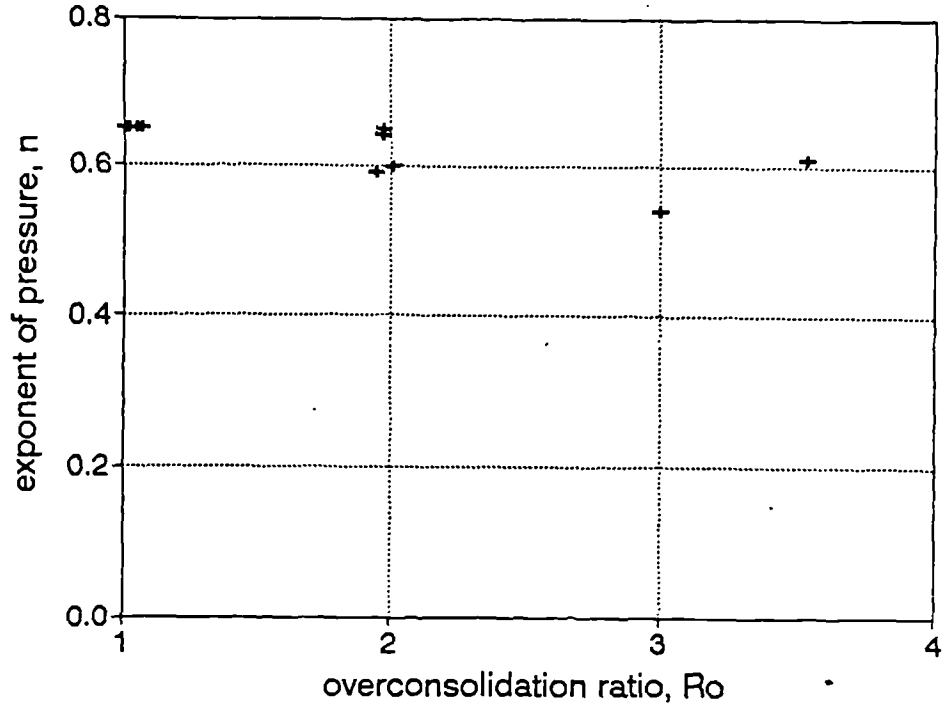

Figure 5.2.7 Speswhite kaolin. Dependence of the exponent of pressure, n, on the overconsolidation ratio, Ro.

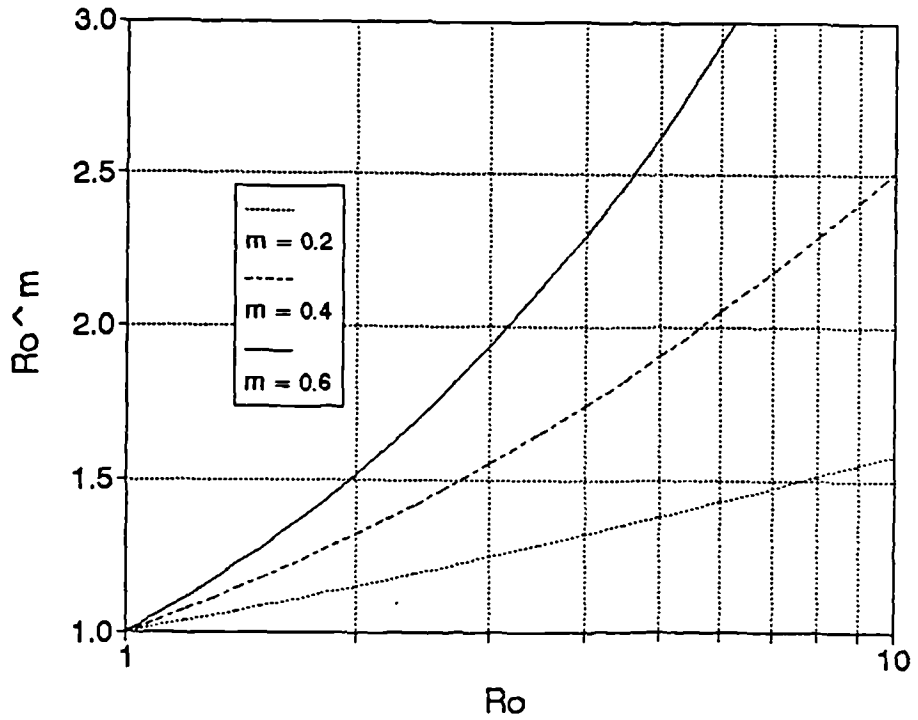

Figure 5.2.8 Relationship between R_o^m and $\log R_o$ for different values of m.

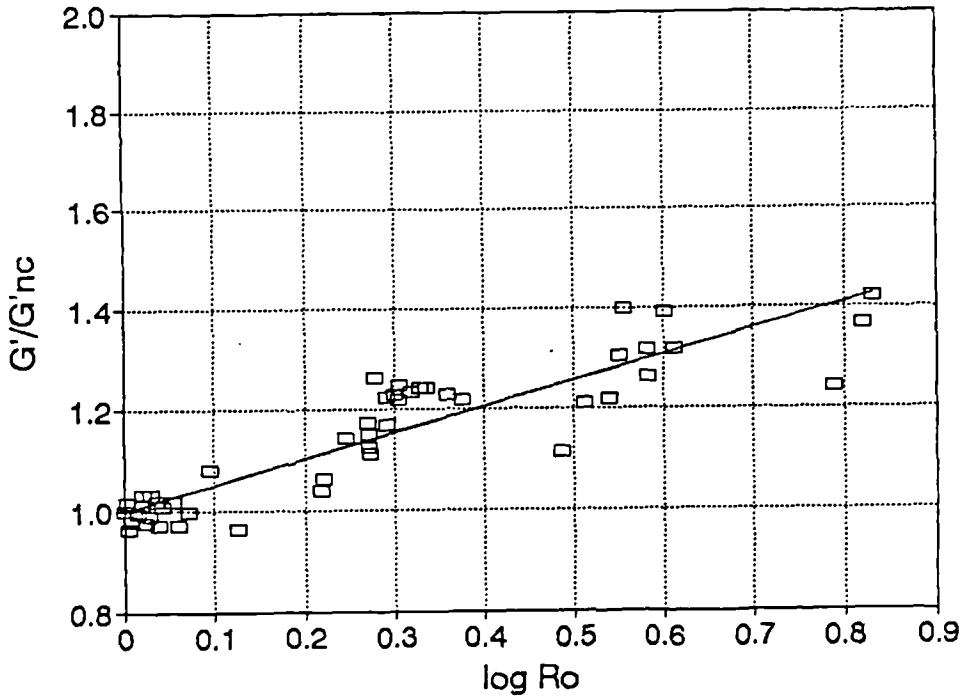

Figure 5.2.9 Speswhite kaolin. All data. Dependence of normalised very small strain stiffness with overconsolidation ratio.

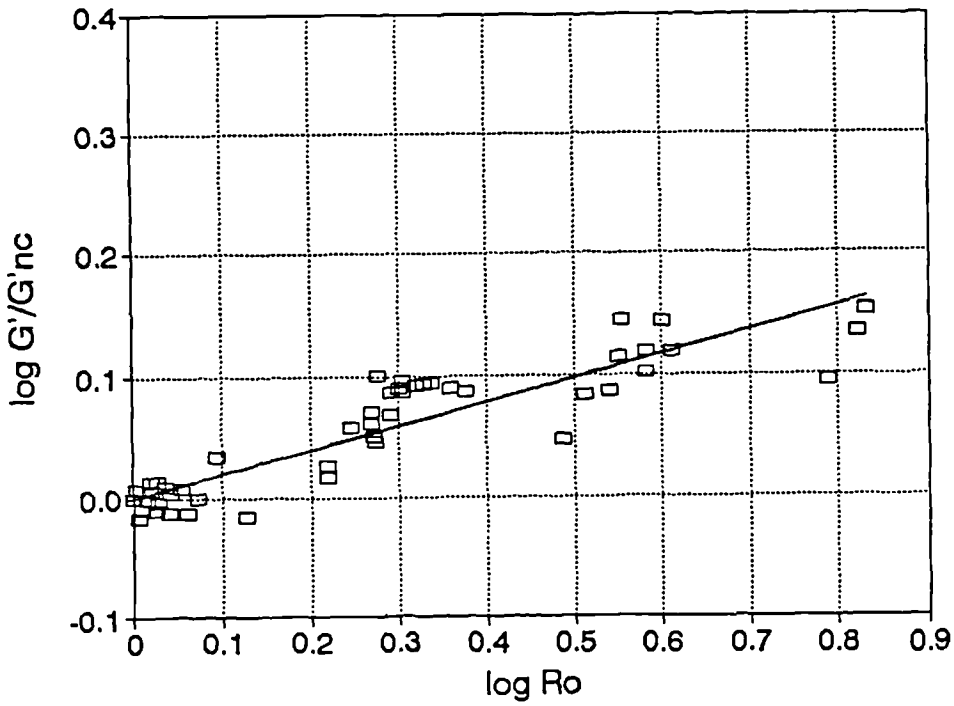

Figure 5.2.10 Speswhite kaolin. All data. Dependence of normalised very small strain stiffness with overconsolidation ratio.

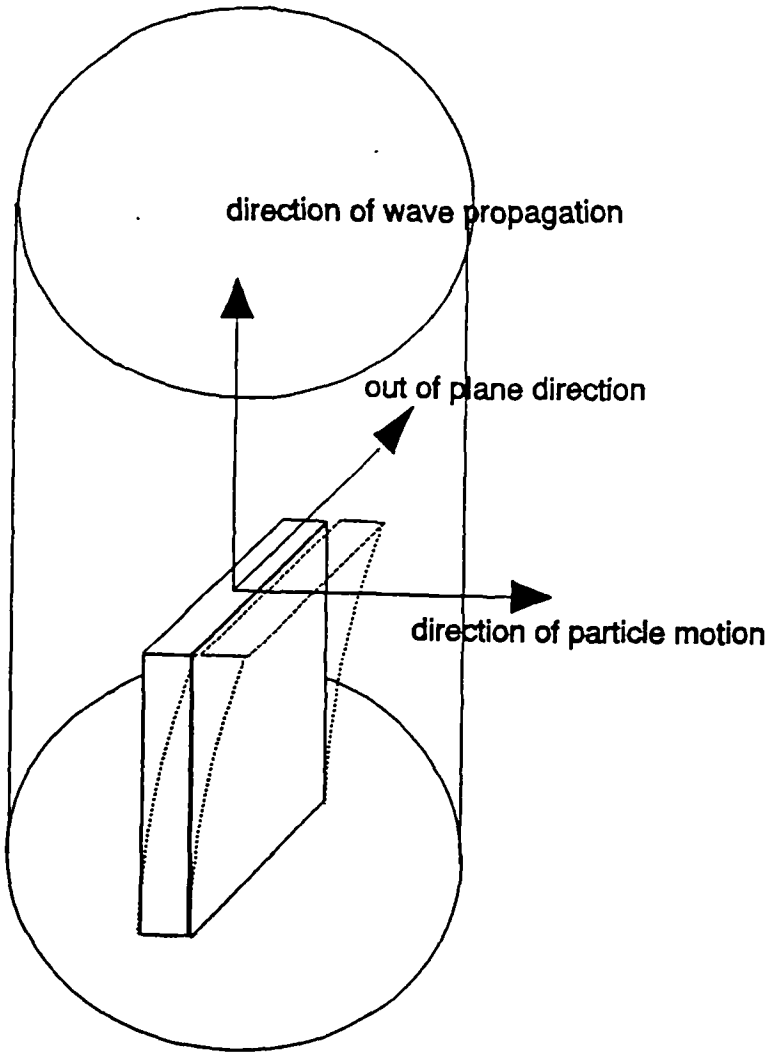

Figure 5.3.1 Diagram illustrating the mode of deformation of a piezoceramic bender element.

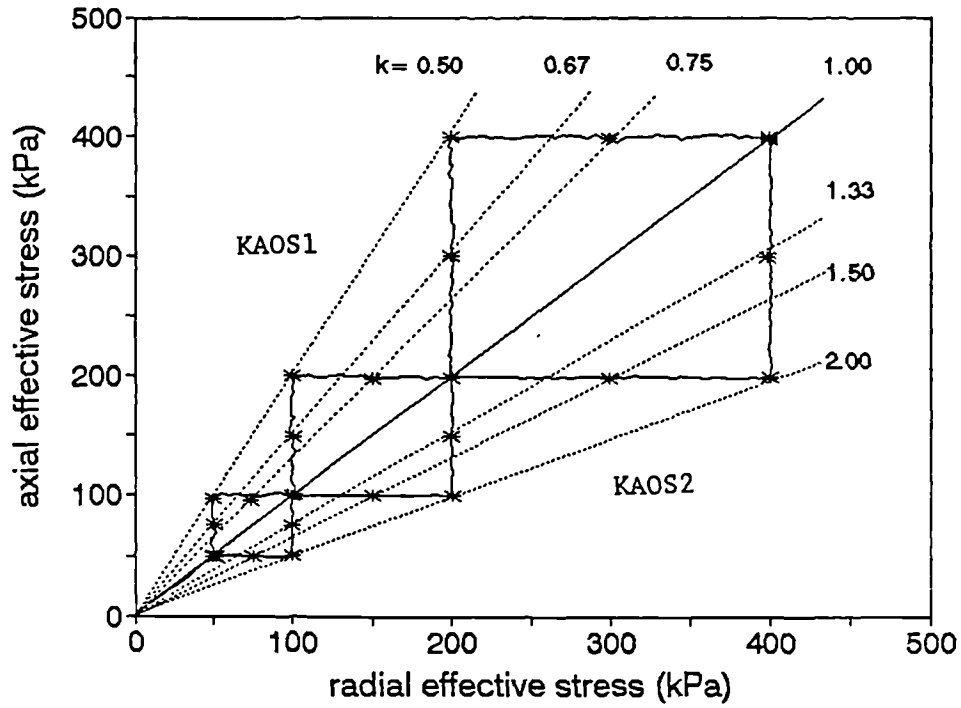

Figure 5.3.2 Stress paths for tests KAOS1 and KAOS2 in the $\sigma_a'-\sigma_r'$ plane.

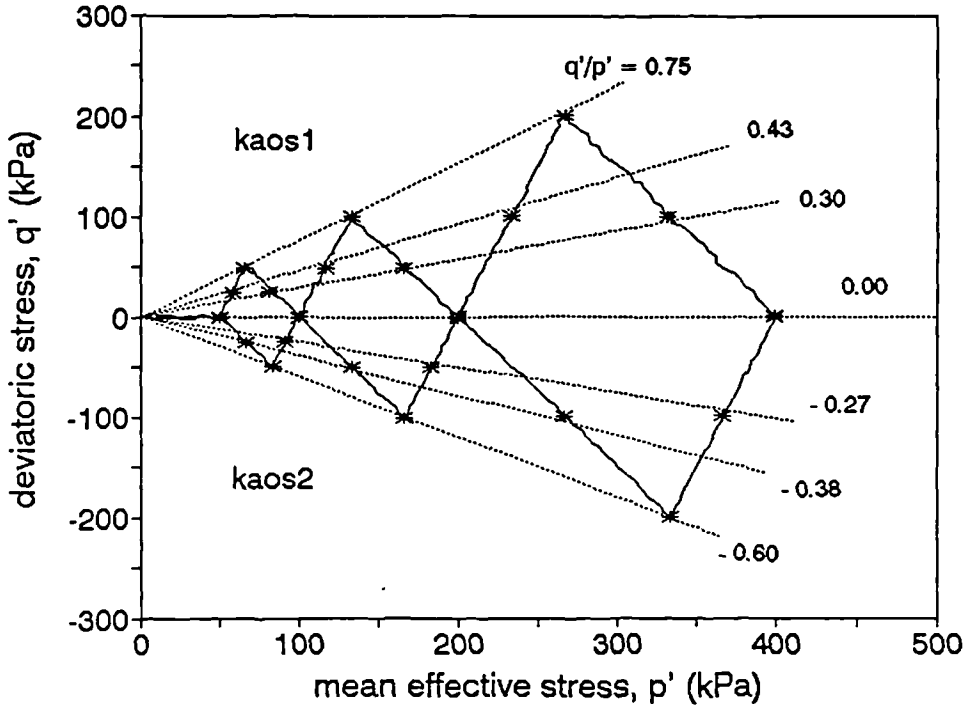

Figure 5.3.3 Stress paths for tests KAOS1 and KAOS2 in the q'–p' plane.

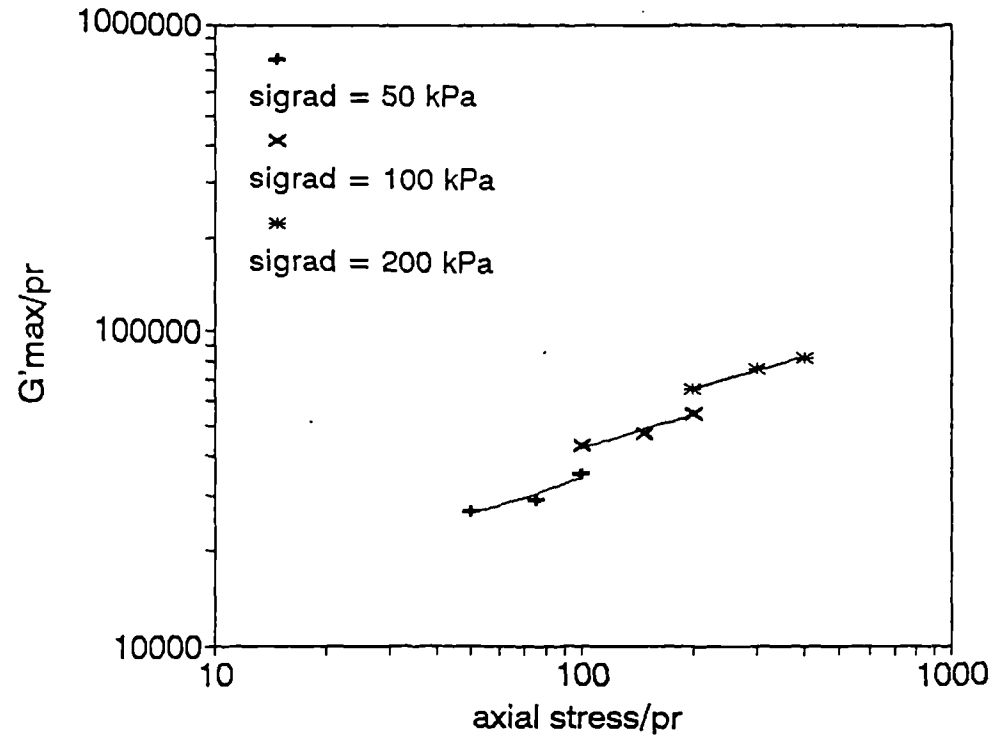

Figure 5.3.4 Speswhite kaolin. Test KAOS1. Dependence of G'_{max} on axial stress.

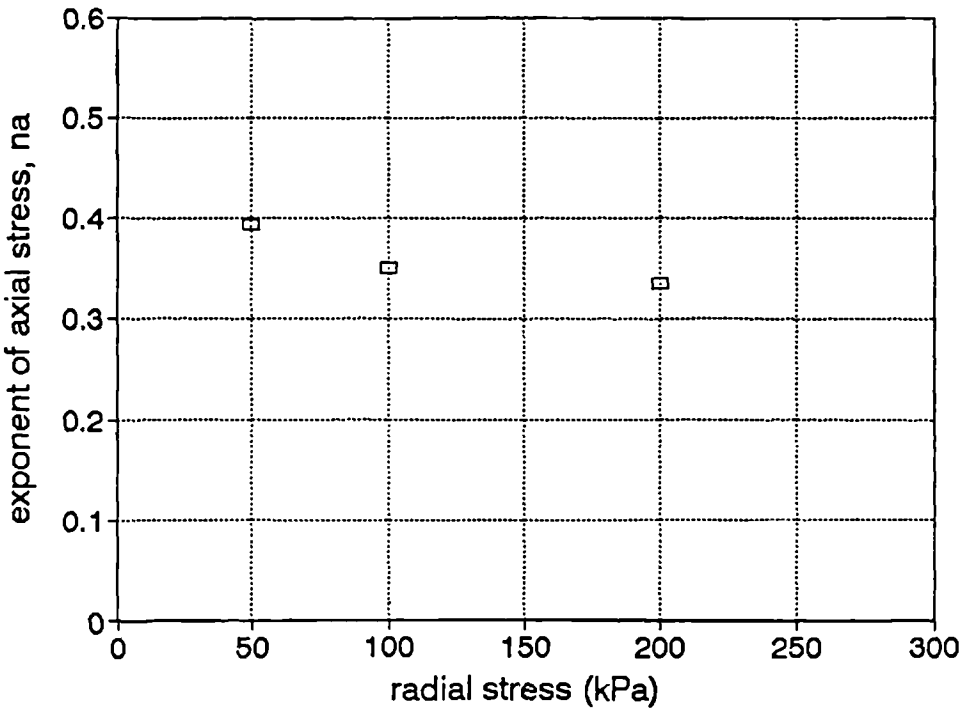

Figure 5.3.5 Speswhite kaolin. Test KAOS1. Dependence of the exponent of axial stress on radial stress.

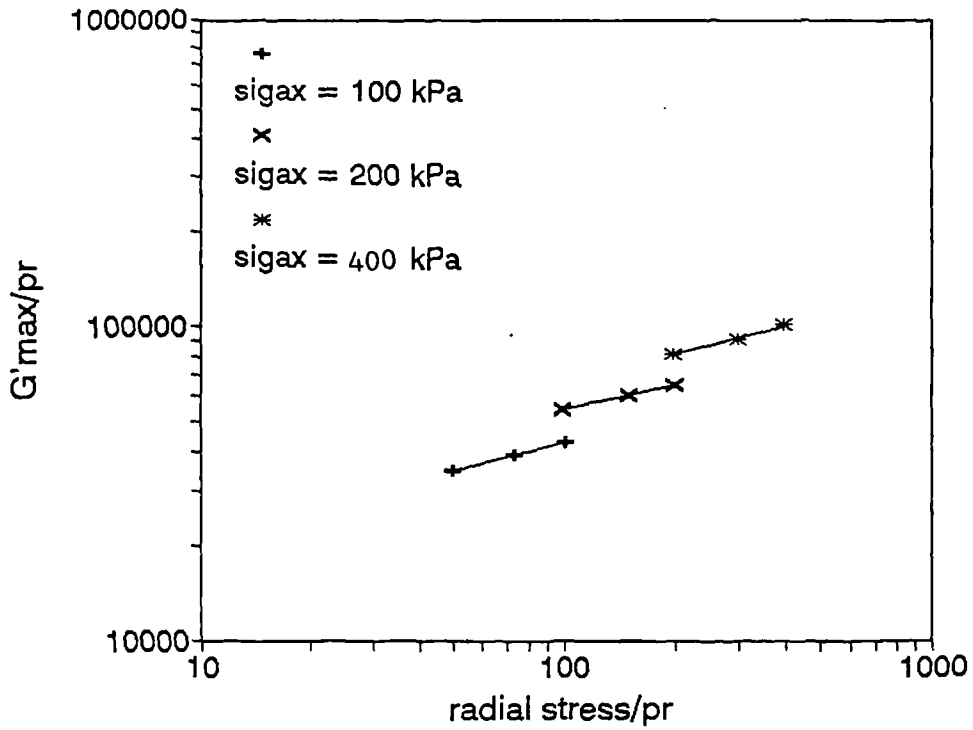

Figure 5.3.6 Speswhite kaolin. Test KAOS1. Dependence of G'_{max} on radial stress.

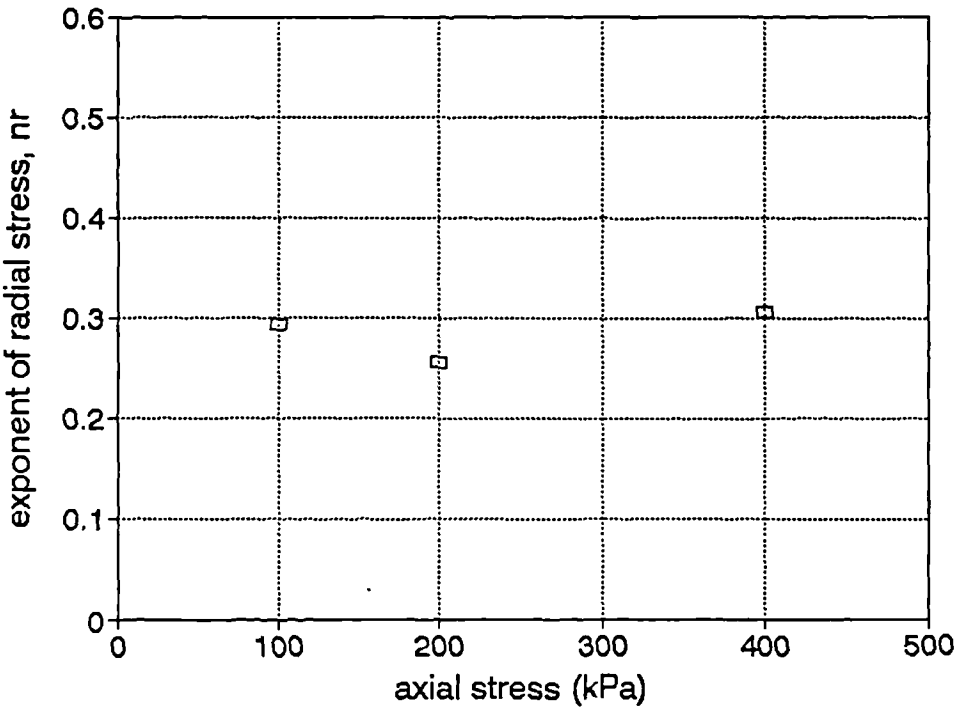

Figure 5.3.7 Speswhite kaolin. Test KAOS1. Dependence of the exponent of radial stress on axial stress.

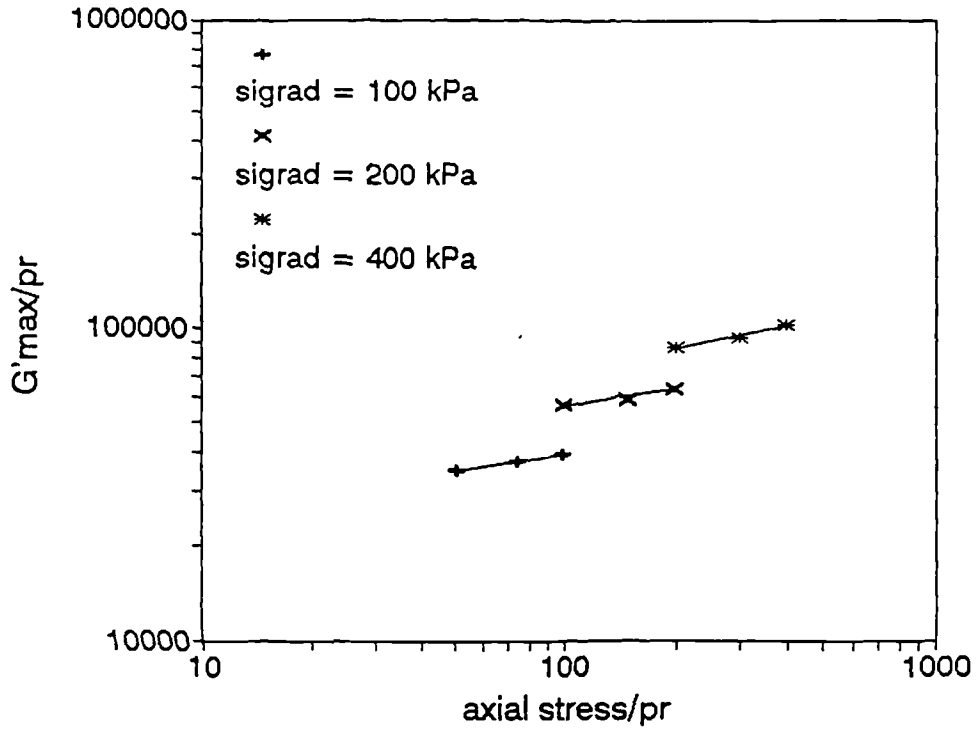

Figure 5.3.8 Speswhite kaolin. Test KAOS2. Dependence of G'_{max} on axial stress.

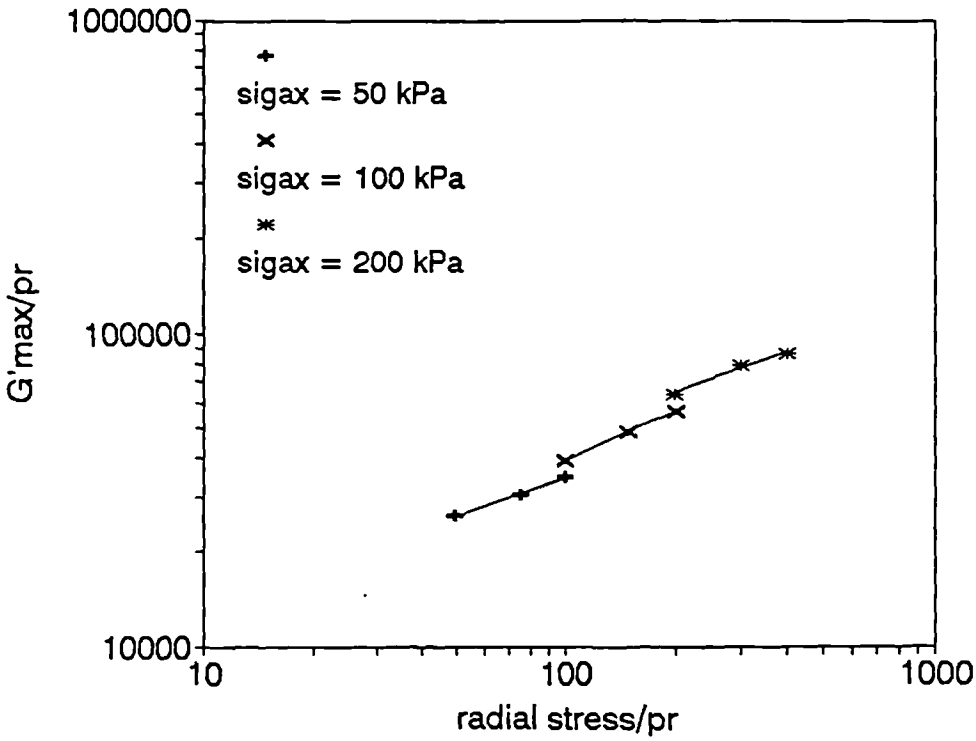

Figure 5.3.9 Speswhite kaolin. Test KAOS2. Dependence of G'_{max} on radial stress.

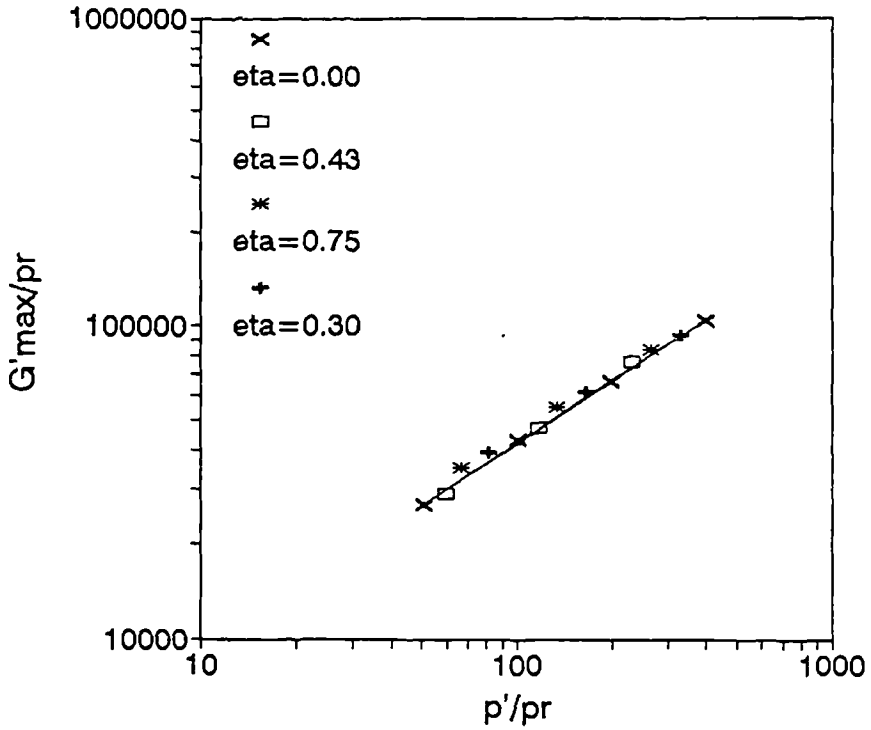

Figure 5.3.10 Speswhite kaolin. Test KAOS1. Dependence of G'_{max} on mean effective stress.

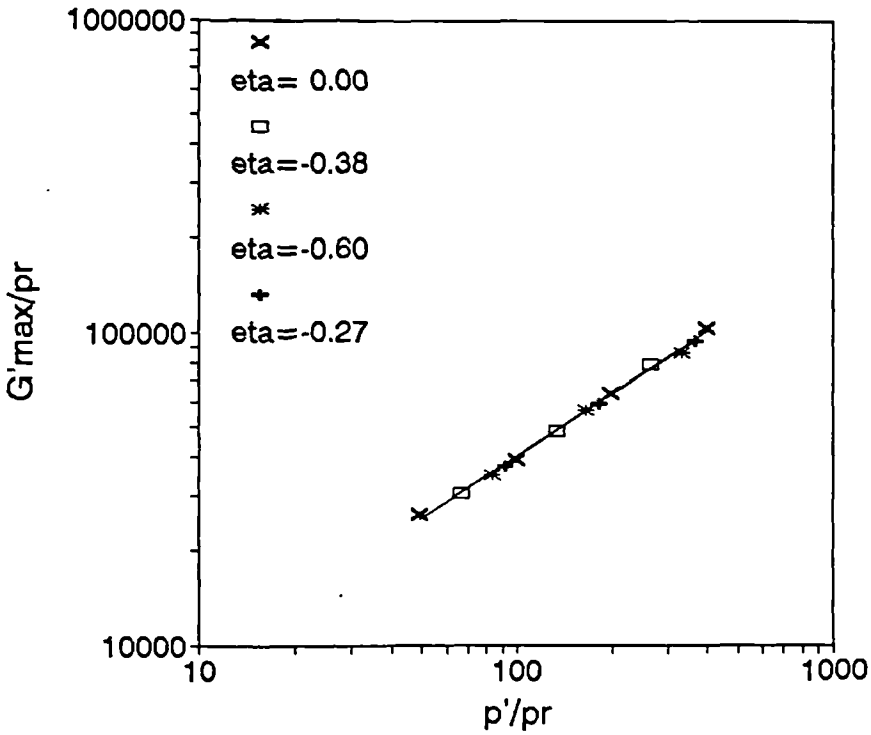

Figure 5.3.11 Speswhite kaolin. Test KAOS2. Dependence of G'_{max} on mean effective stress.

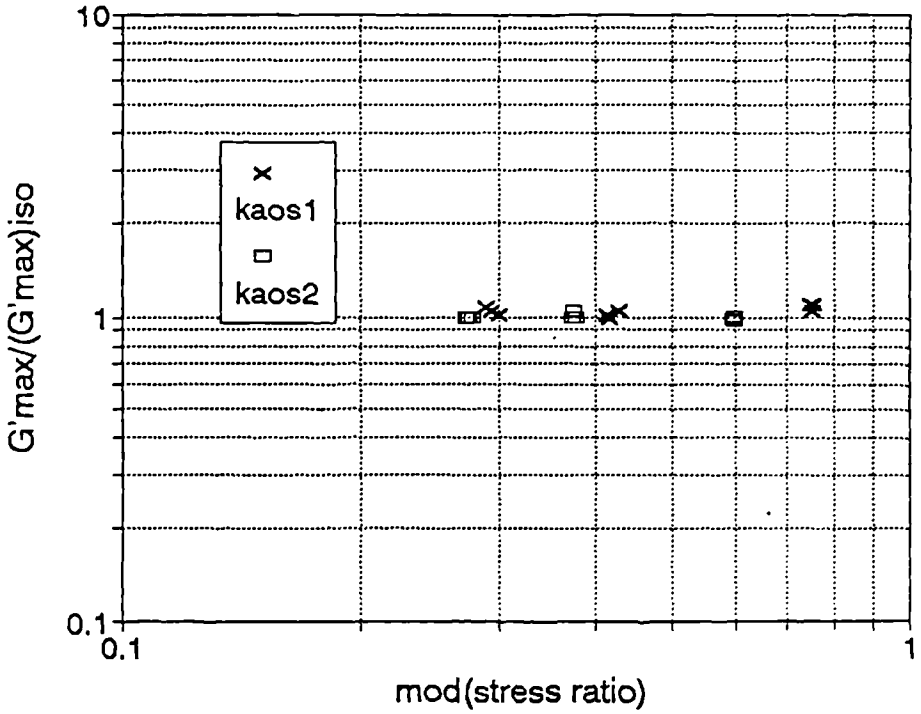

Figure 5.3.12 Speswhite kaolin. Dependence of G'_{max} on stress ratio, η.

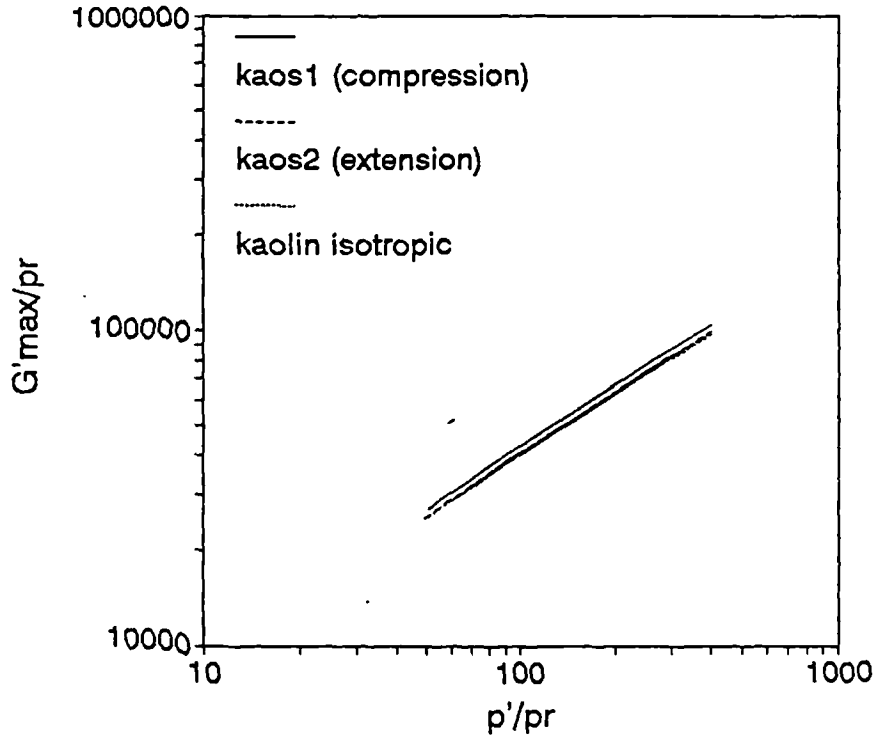

Figure 5.3.13 Spewhite kaolin. Comparison of results from tests KAOS1 and KAOS2 and results from group of tests KAOD.

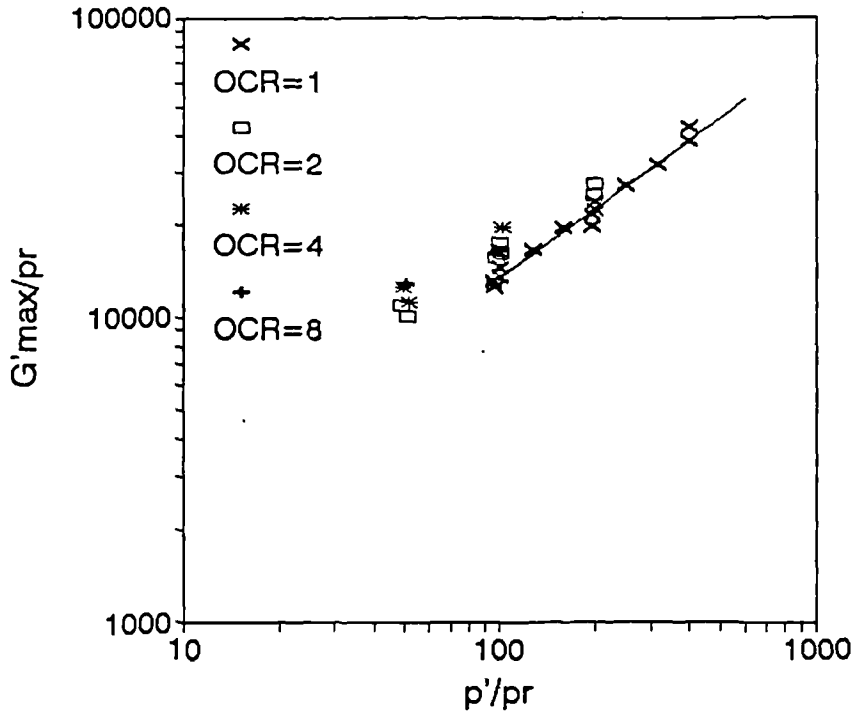

Figure 5.4.1 London clay. All data. Dependence of very small strain stiffness on mean effective stress.

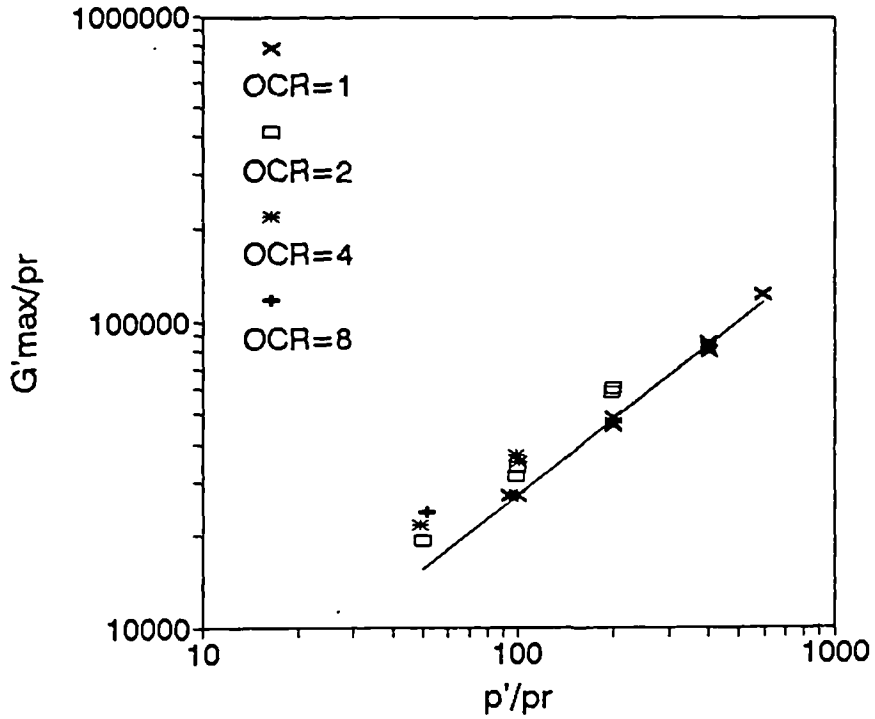

Figure 5.4.2 North Field clay. All data. Dependence of very small strain stiffness on mean effective stress.

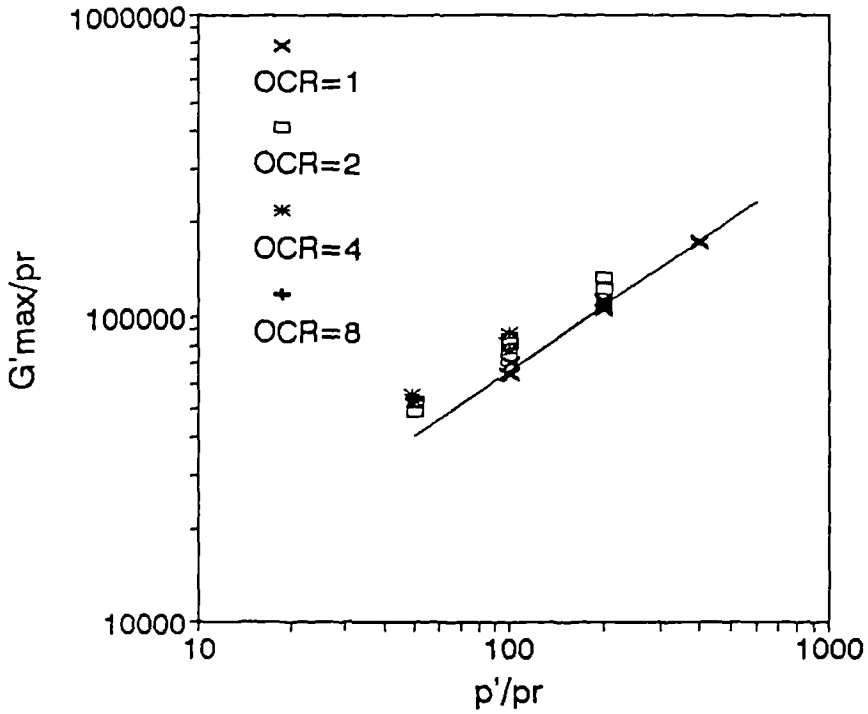

Figure 5.4.3 Slate dust. All data. Dependence of very small strain stiffness on mean effective stress.

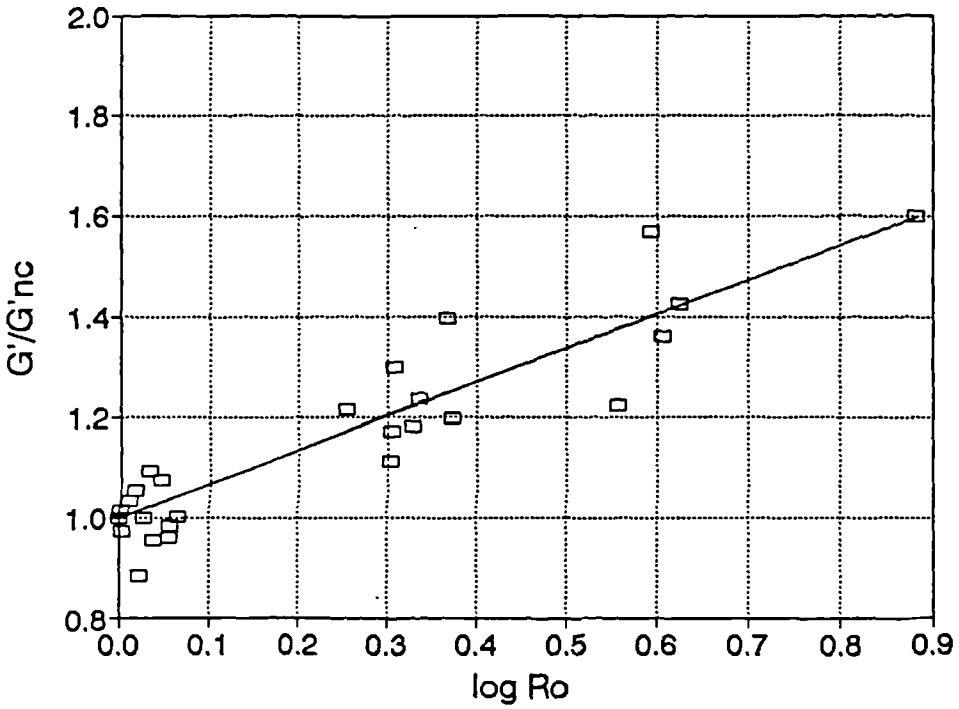

Figure 5.4.4 London clay. All data. Dependence of very small strain stiffness on R_o.

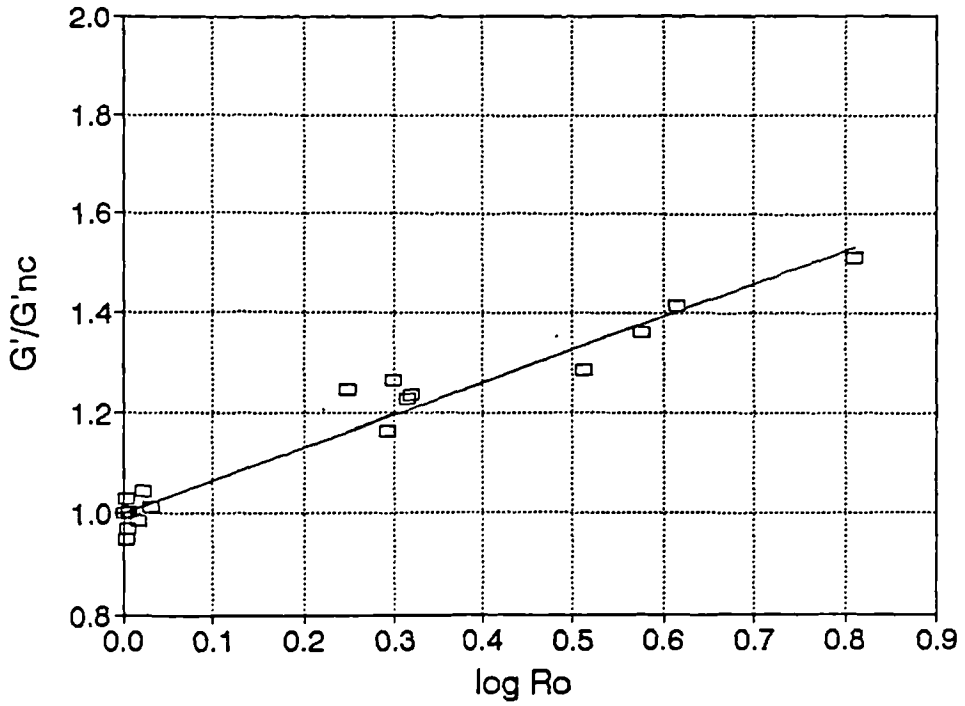

Figure 5.4.5 North Field clay. All data. Dependence of very small strain stiffness on R_o.

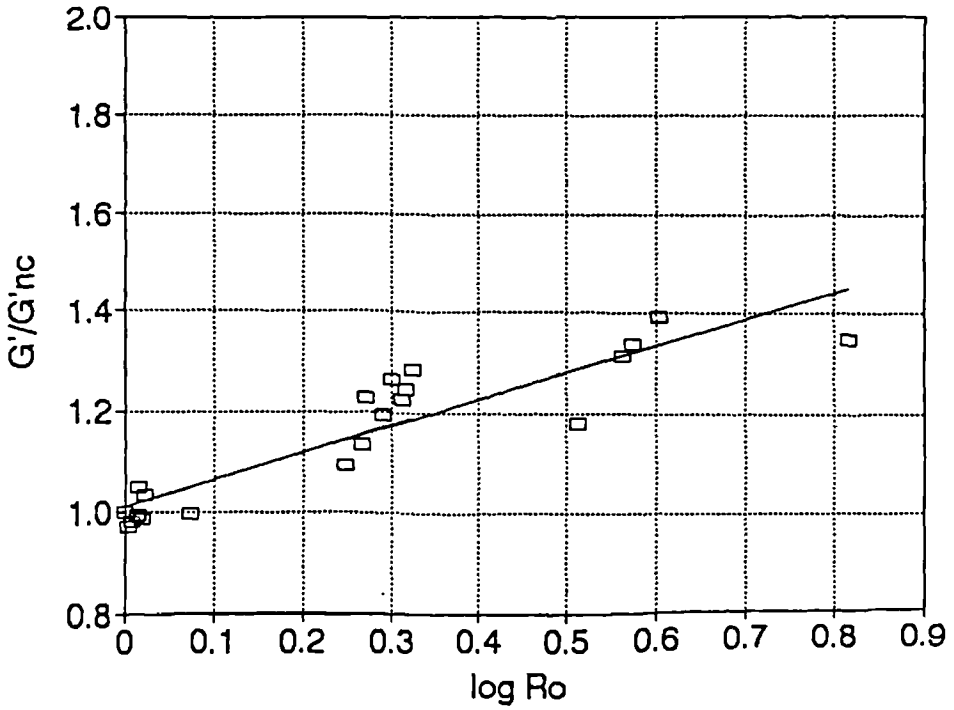

Figure 5.4.6 Slate dust. All data. Dependence of very small strain stiffness on R_o.

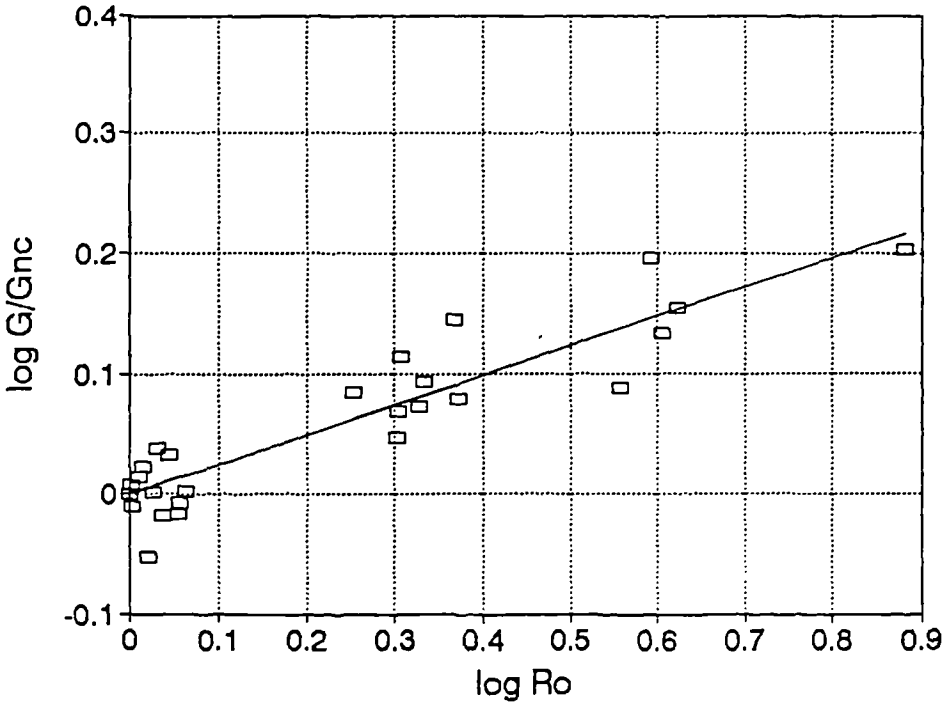

Figure 5.4.7 London clay. All data. Dependence of very small strain stiffness on R_o.

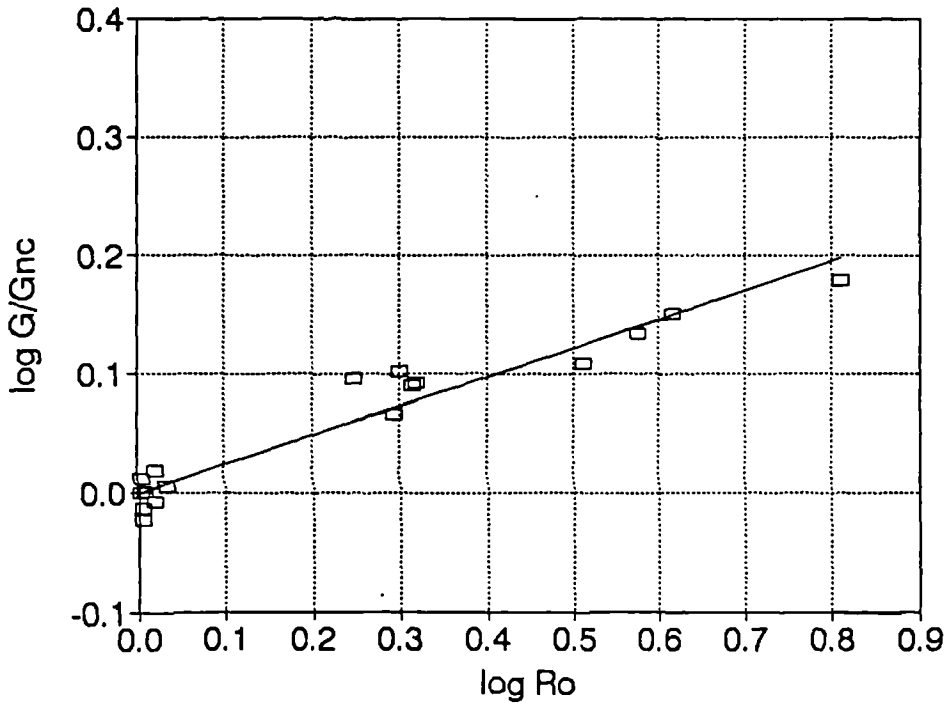

Figure 5.4.8 North Field clay. All data. Dependence of very small strain stiffness on R_o.

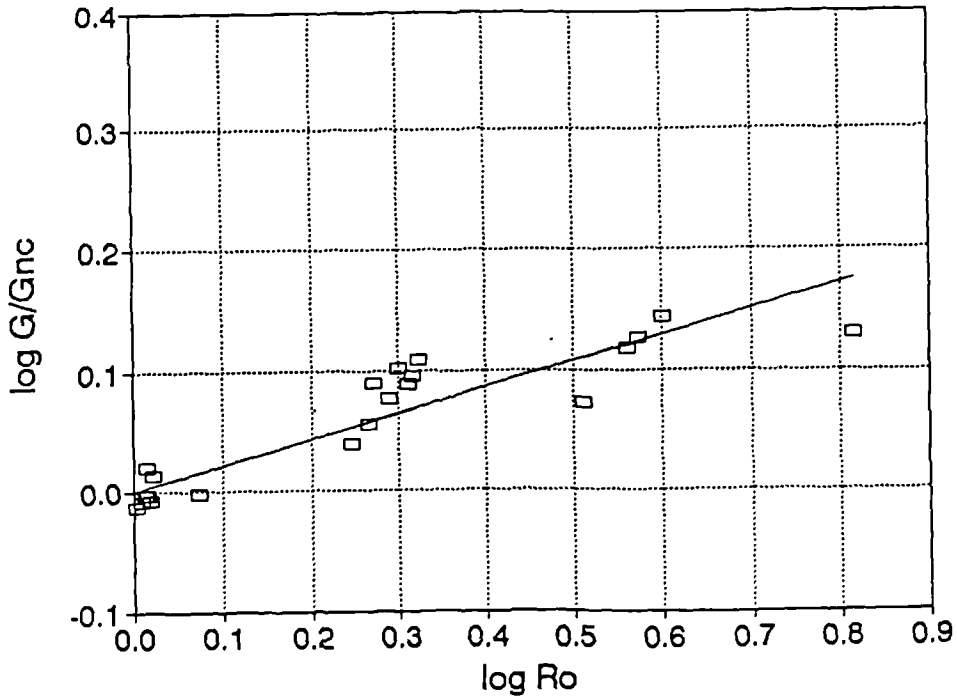

Figure 5.4.9 Slate dust. All data. Dependence of very small strain stiffness on R_o.

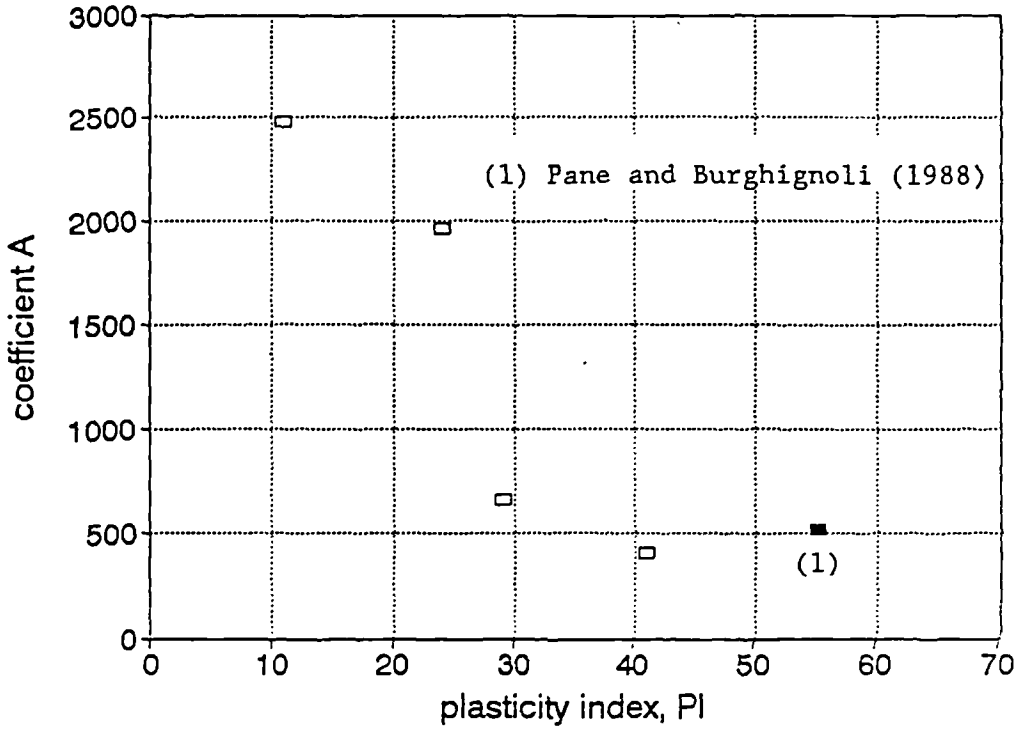

Figure 5.4.10 Dependence of pressure multiplier, A, on plasticity index.

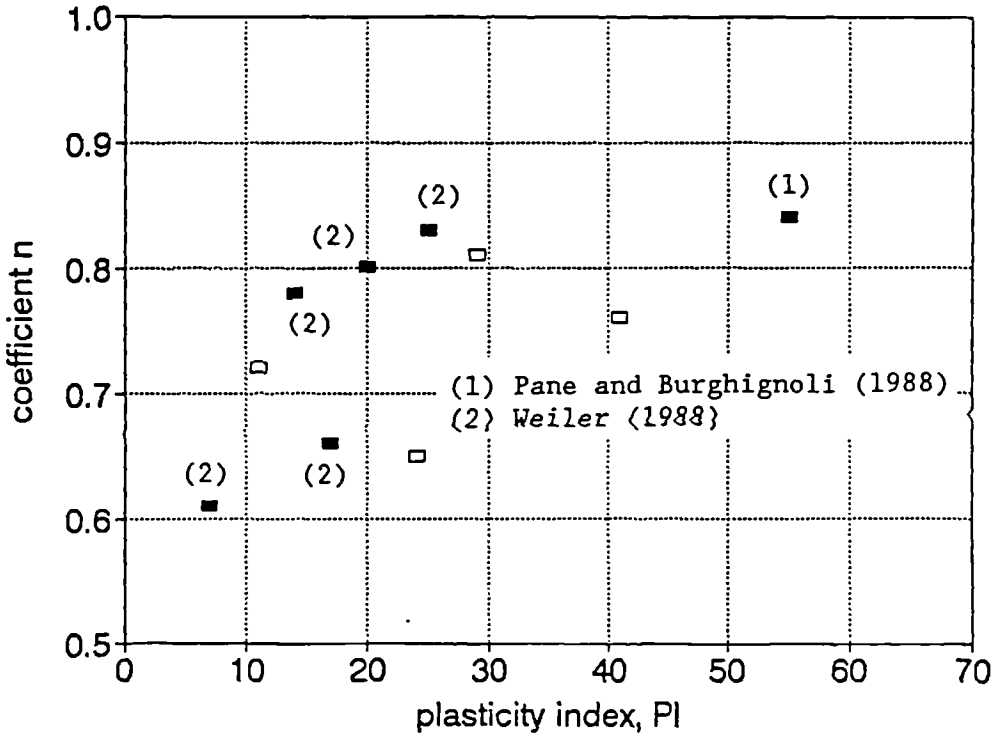

Figure 5.4.11 Dependence of pressure exponent, n, on plasticity index.

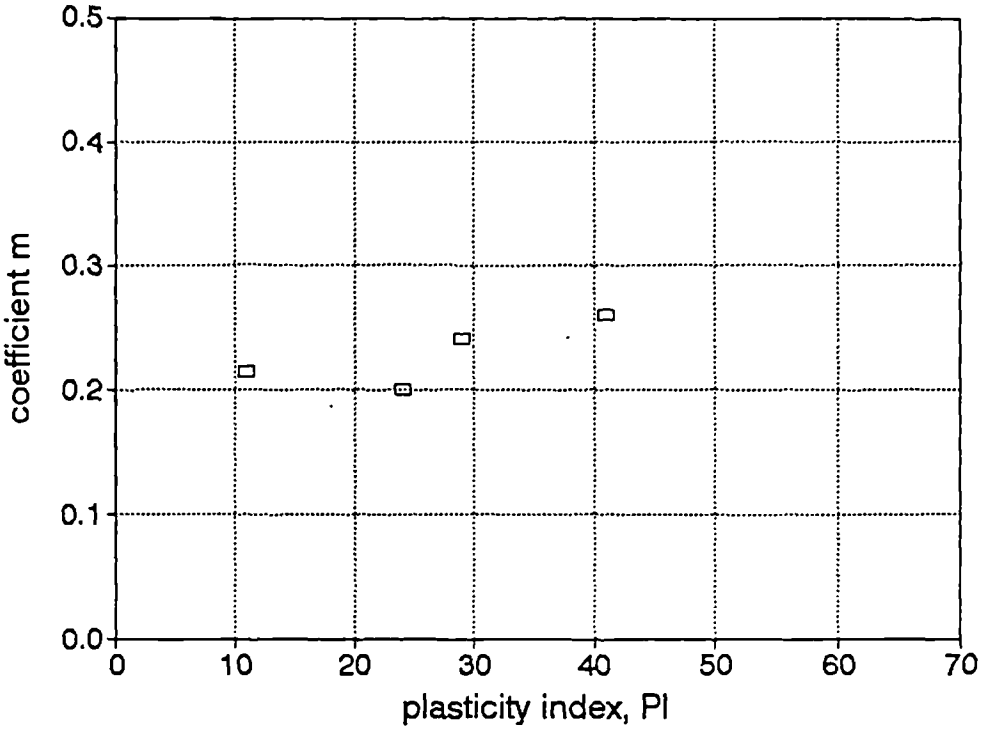

Figure 5.4.12 Dependence of R_o exponent, m, on plasticity index.

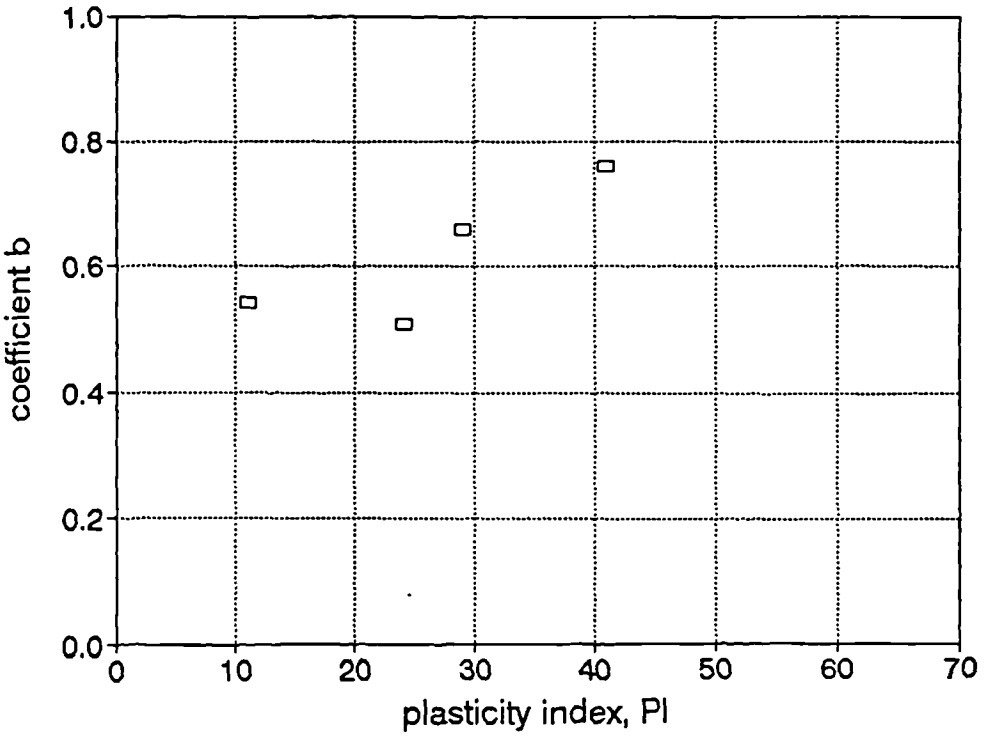

Figure 5.4.13 Dependence of coefficient b on plasticity index.

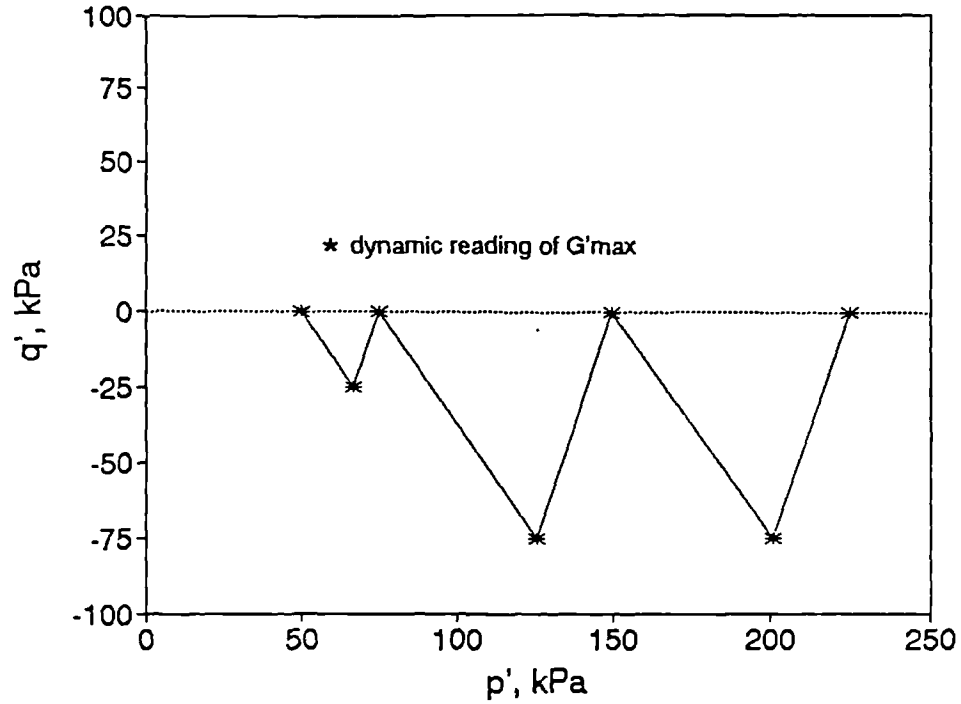

Figure 5.5.1 Test ULCD. Dynamic readings

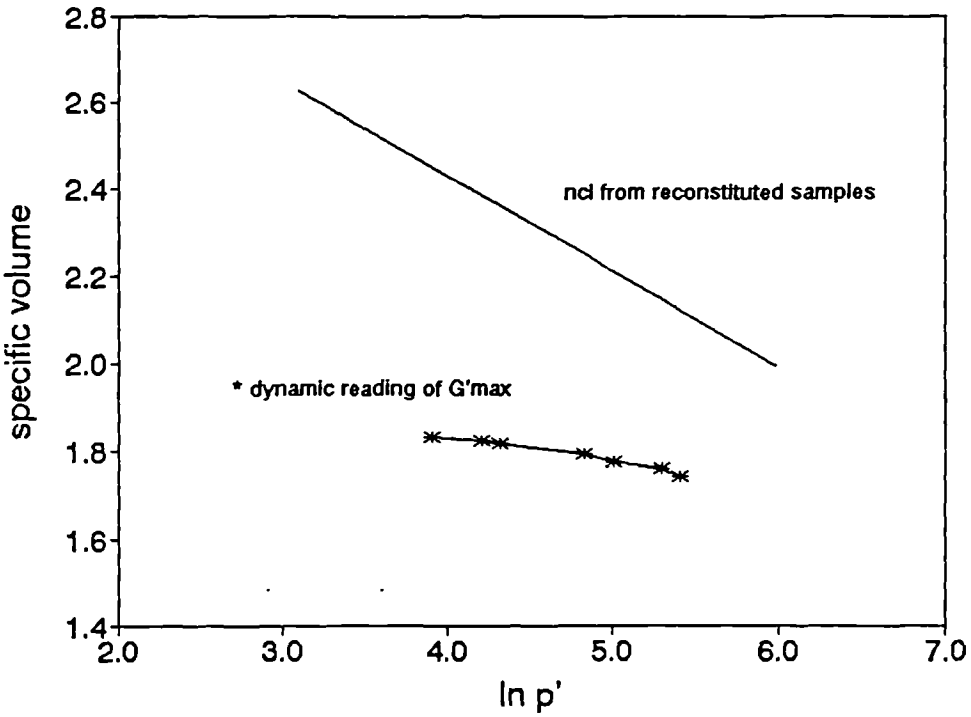

Figure 5.5.2 Test ULCD. State of the soil in the v:lnp' plane

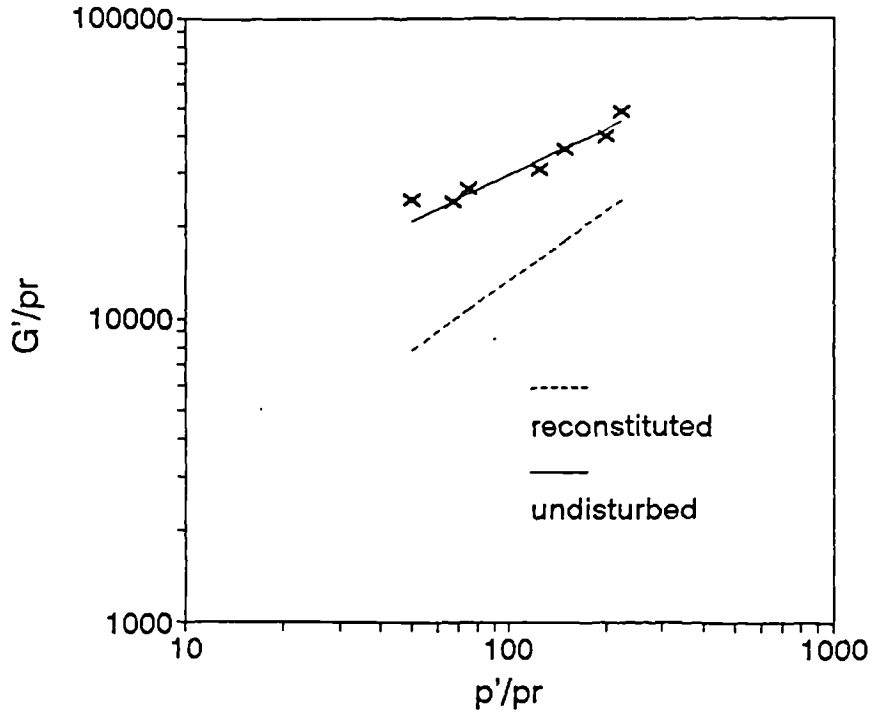

Figure 5.5.3 Test ULCD. Dependence of G'_{max} on mean effective stress

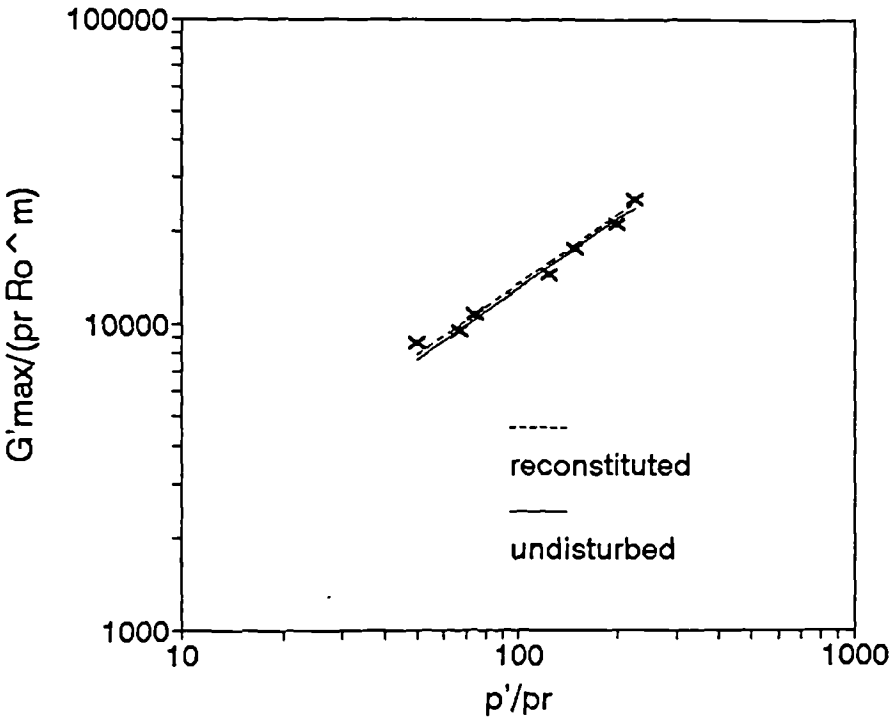

Figure 5.5.4 Test ULCD. Dependence of G'_{max} on mean effective stress

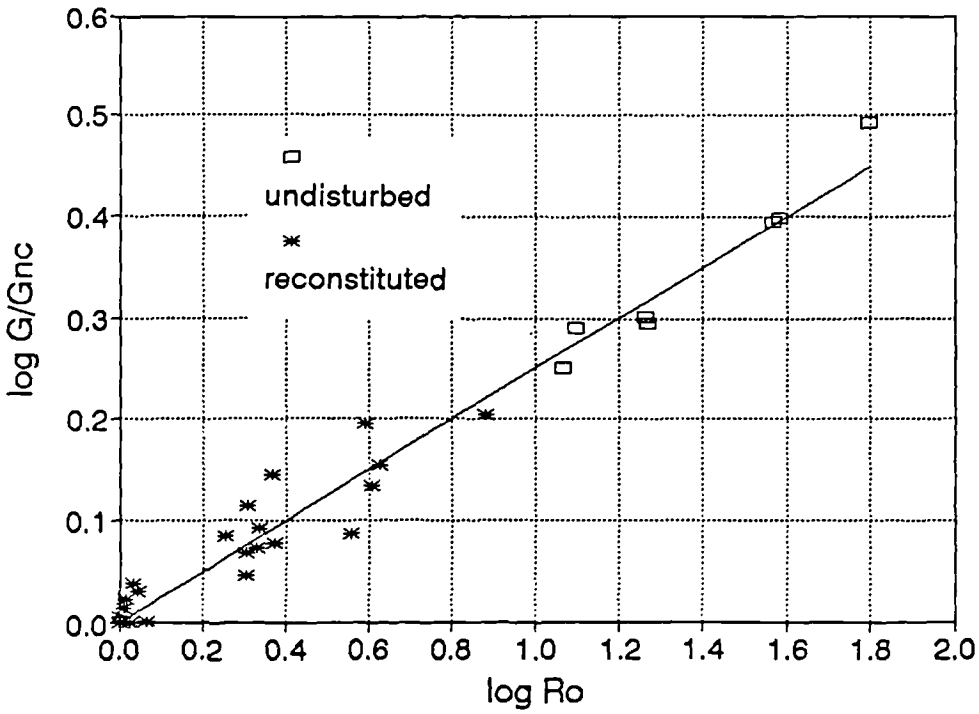

Figure 5.5.5 Test ULCD. Dependence of G'_{max} on overconsolidation ratio

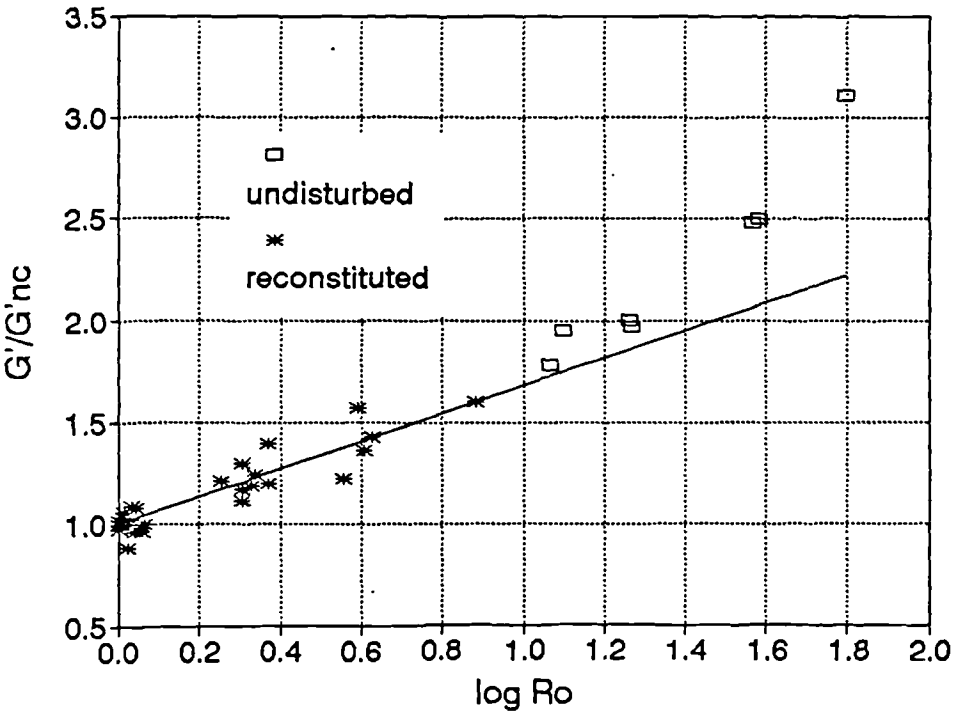

Figure 5.5.6 Test ULCD. Dependence of G'_{max} on overconsolidation ratio

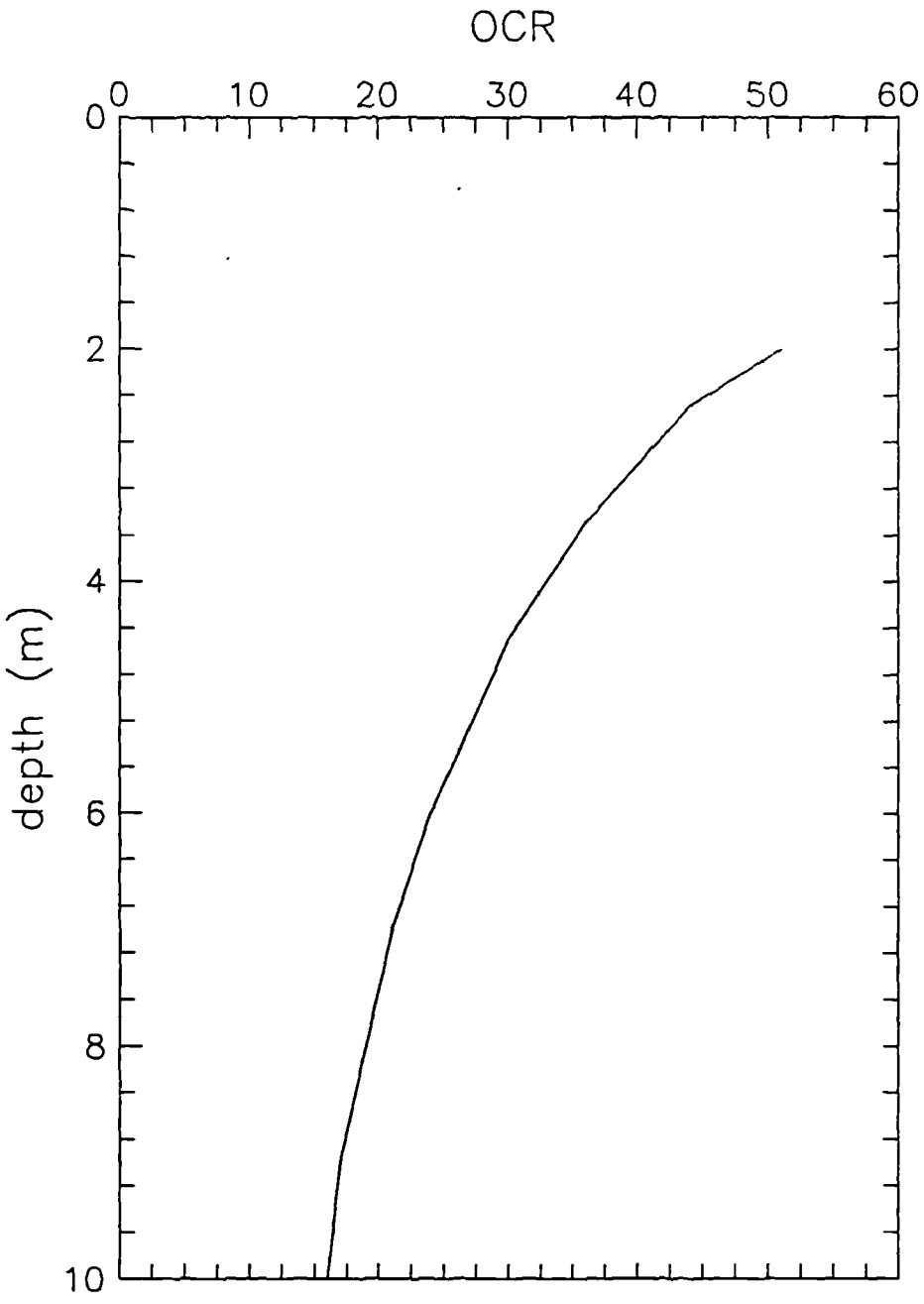

Figure 5.6.1 Chattenden, Kent. Estimated profile of OCR with depth

$\beta = 3*(\sigma_v - \sigma_h)/(\sigma_v + 2*\sigma_h) = 3*(1-K_o)/(1+2*K_o)$

$A = (\sigma_v + 2*\sigma_h)/(\sigma_v^* + 2*\sigma_h^*)$

σ_h^* & σ_h^*: max. values of σ_v & σ_h at point 2

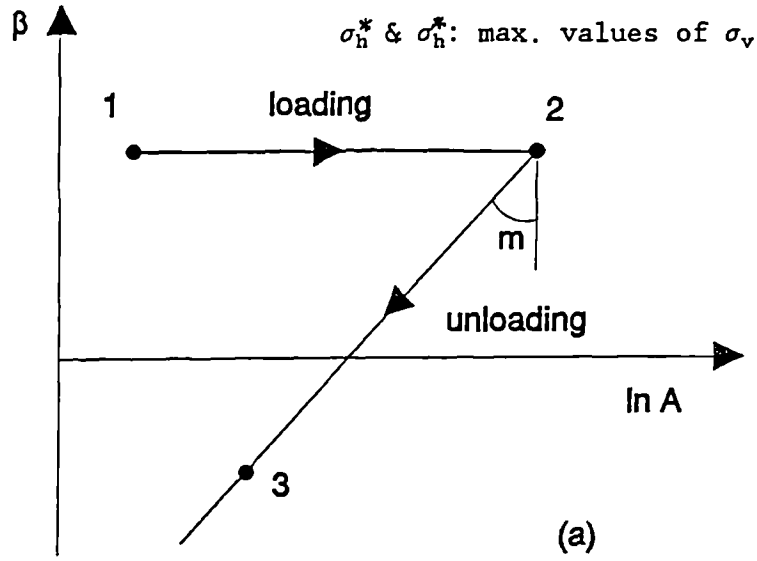

Figure 5.6.2a Diagram illustrating the results of a cycle of one-dimensional compression and swelling in the β:lnA plane

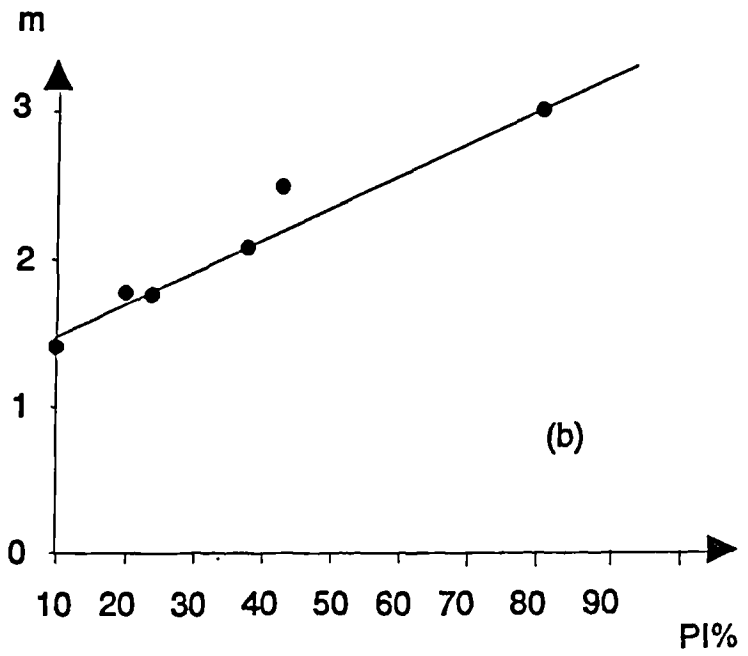

Figure 5.6.2b Variation of coefficient m with plasticity

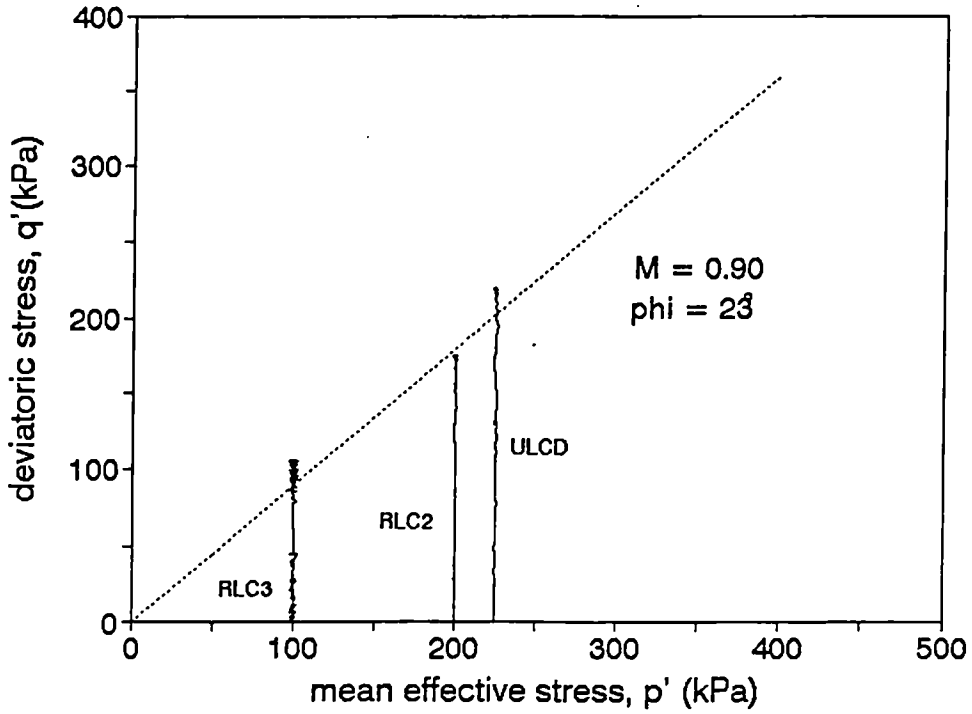

Figure 5.6.3 Shearing stages of tests RLC2, RLC3 and ULCD. Stress paths in the p':q' plane

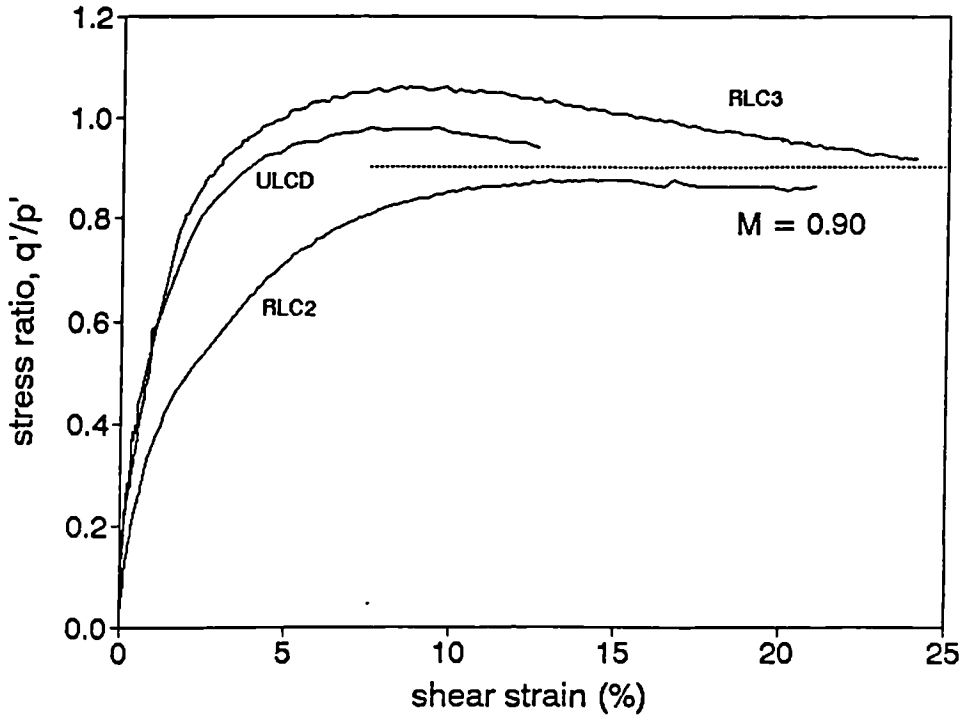

Figure 5.6.4 Shearing stages of tests RLC2, RLC3 and ULCD. Stress ratio versus shear strain

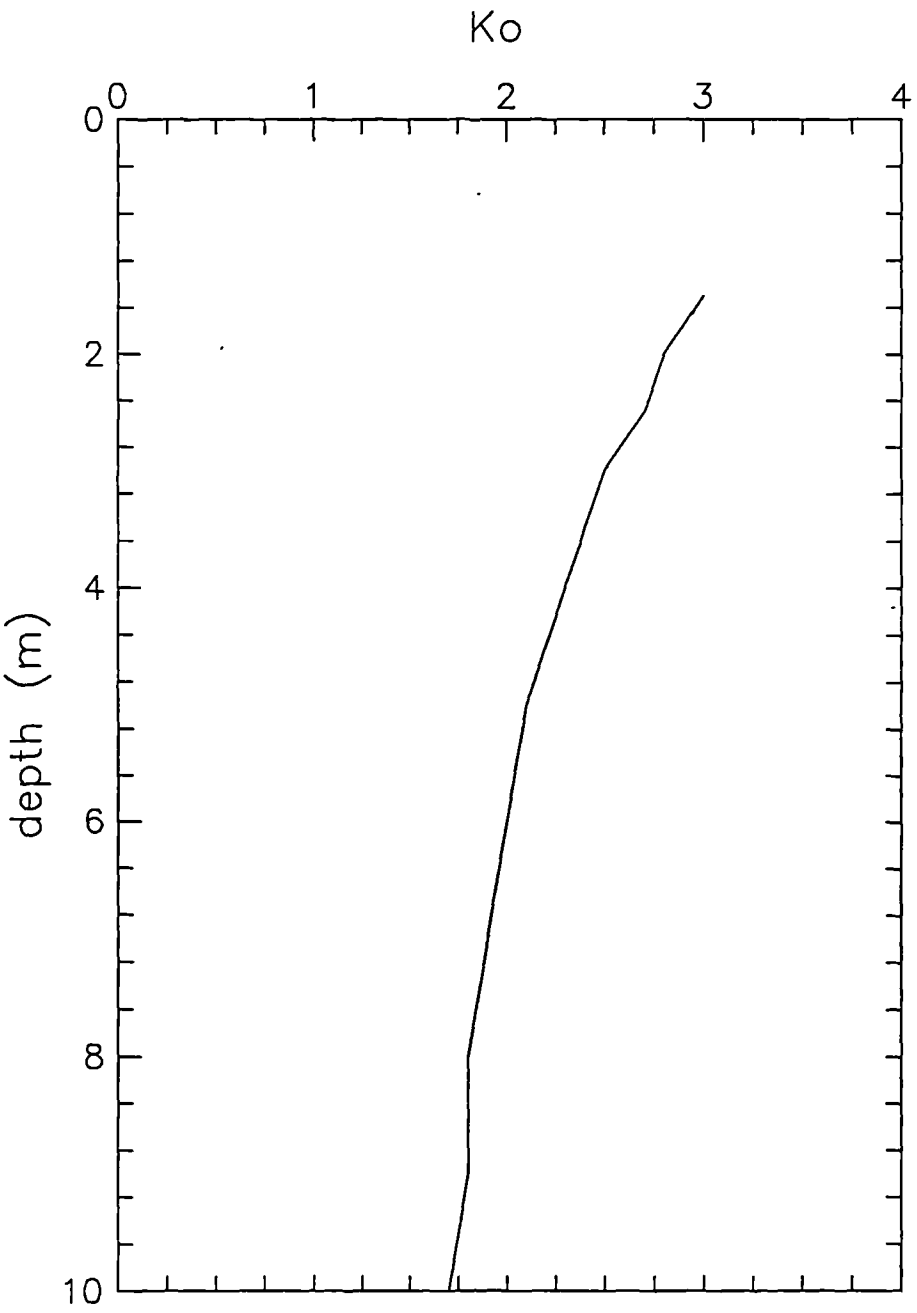

Figure 5.6.5 Chattenden, Kent. Estimated profile of K_o with depth

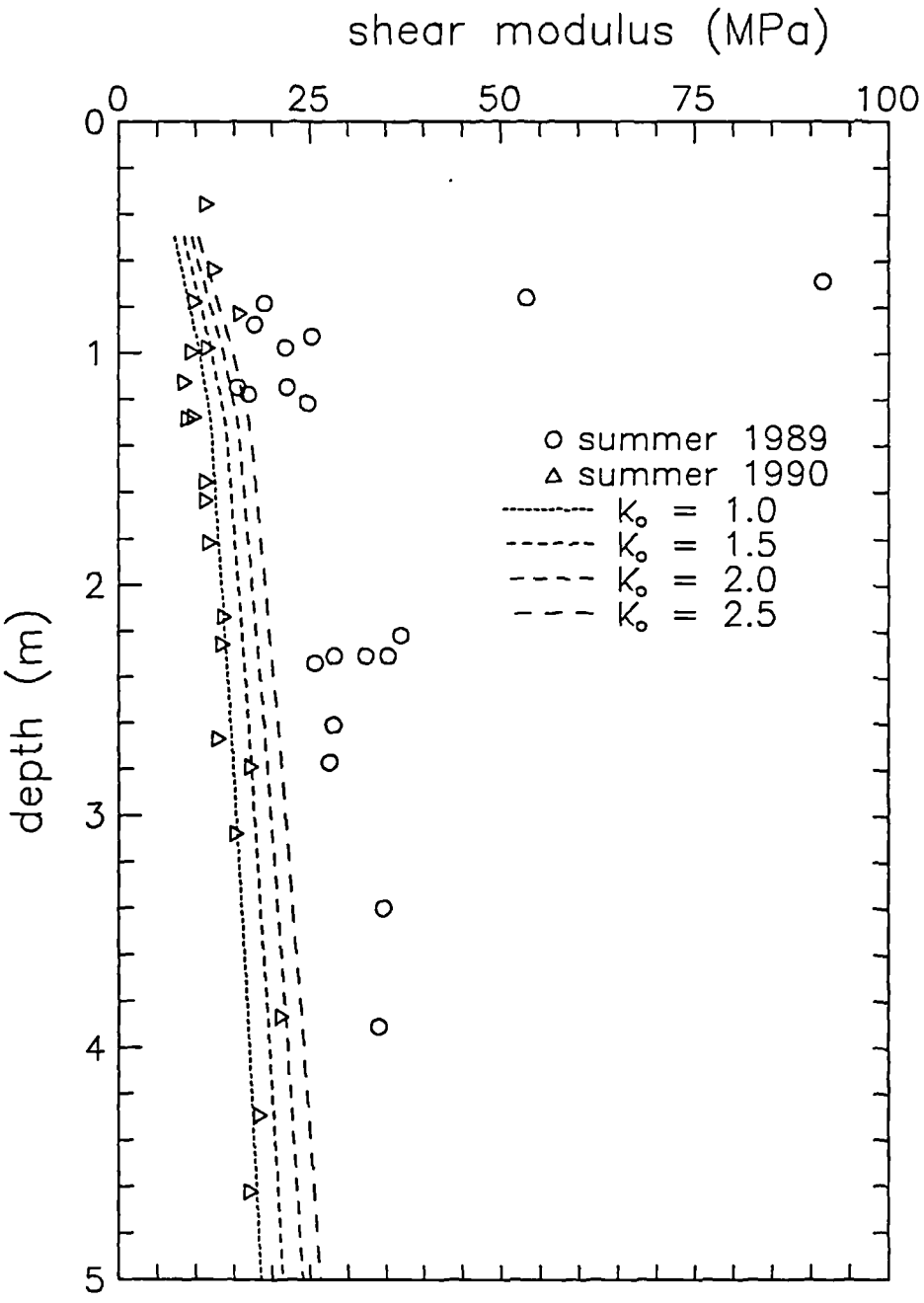

Figure 5.6.6 Chattenden, Kent. Profiles of G'_{max} with depth for different values of constant K_o

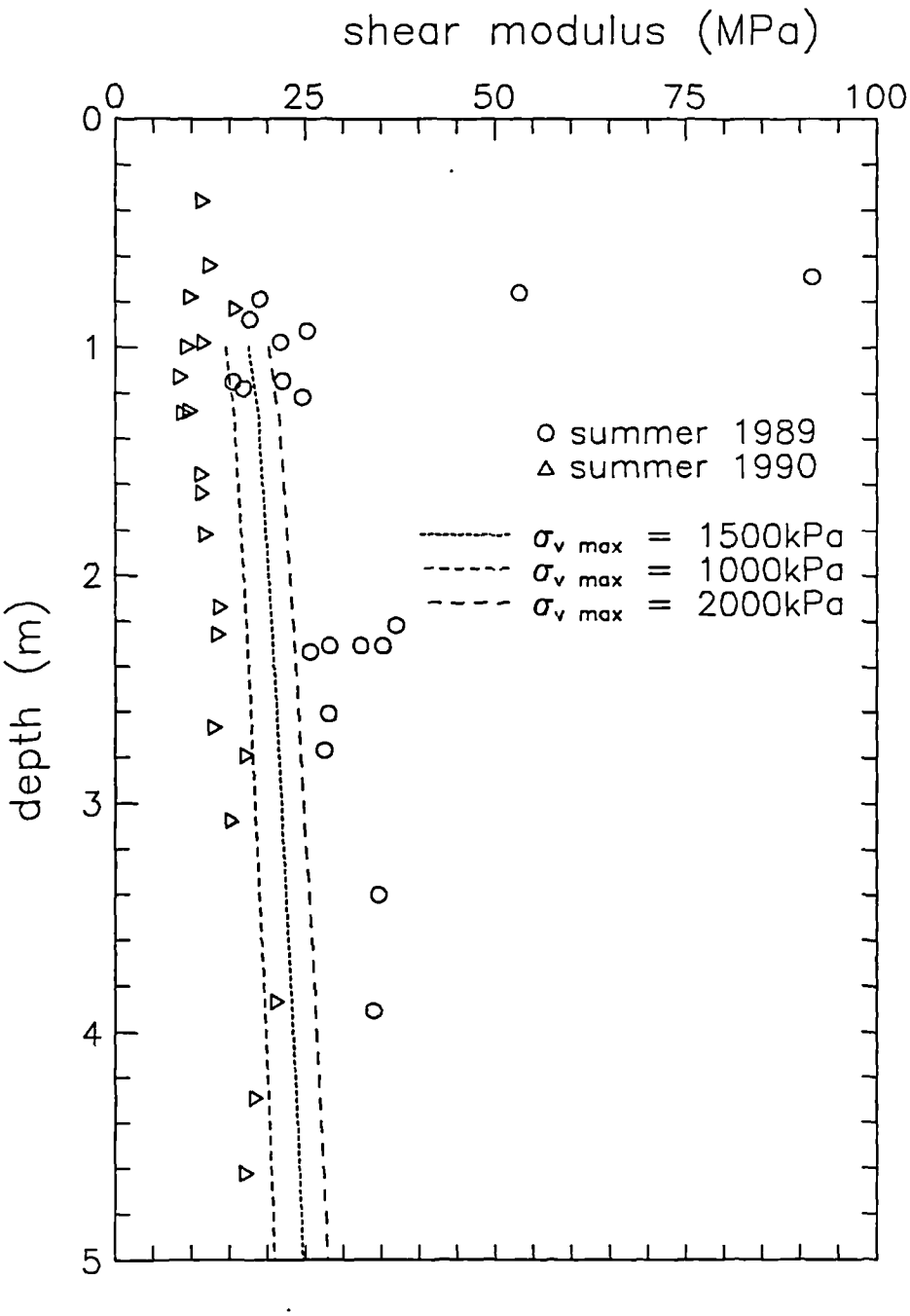

Figure 5.6.7 Chattenden, Kent. Profiles of G'_{max} with depth for K_o varying with depth and different assumptions on the maximum overburden

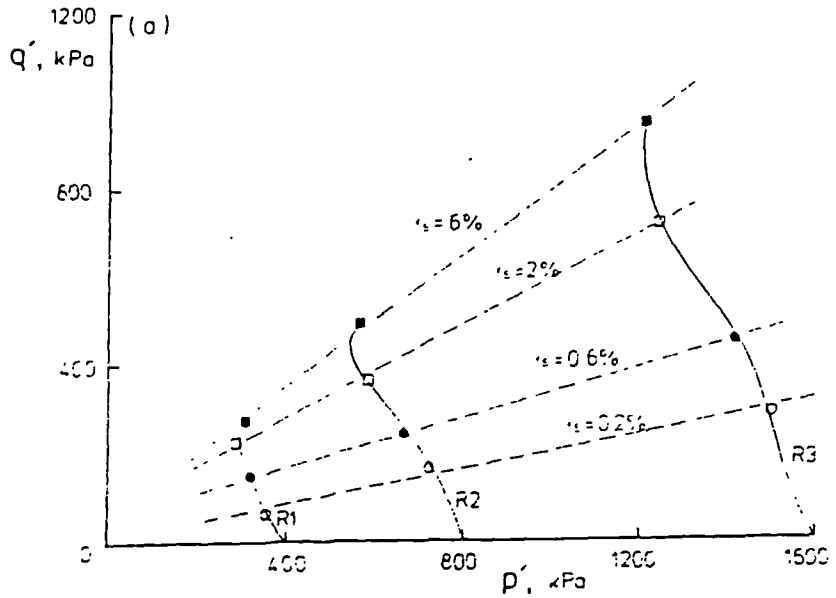

Figure 5.7.1 Stress paths for a set of three undrained triaxial compression tests on reconstituted samples of a glacial till (after Little and Atkinson, 1988)

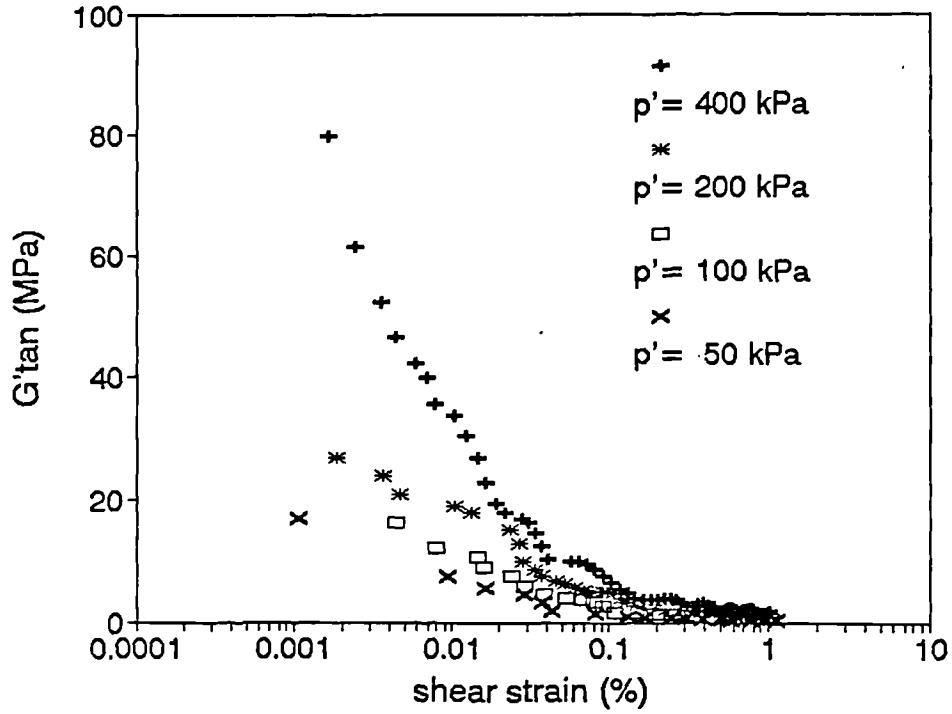

Figure 5.7.2 Speswhite kaolin. Tests LSK1, LSK2, LSK3 and LSK4. Tangent stiffness versus shear strain

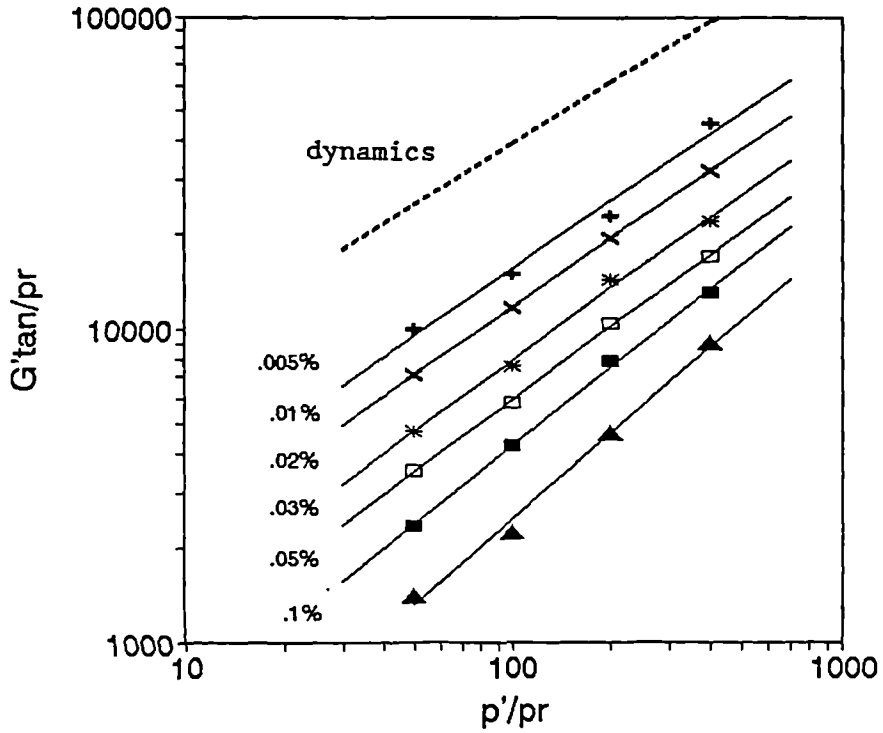

Figure 5.7.3 Speswhite kaolin. Tests LSK1, LSK2, LSK3 and LSK4. Dependence of tangent stiffness on mean effective stress at different shear strain amplitudes

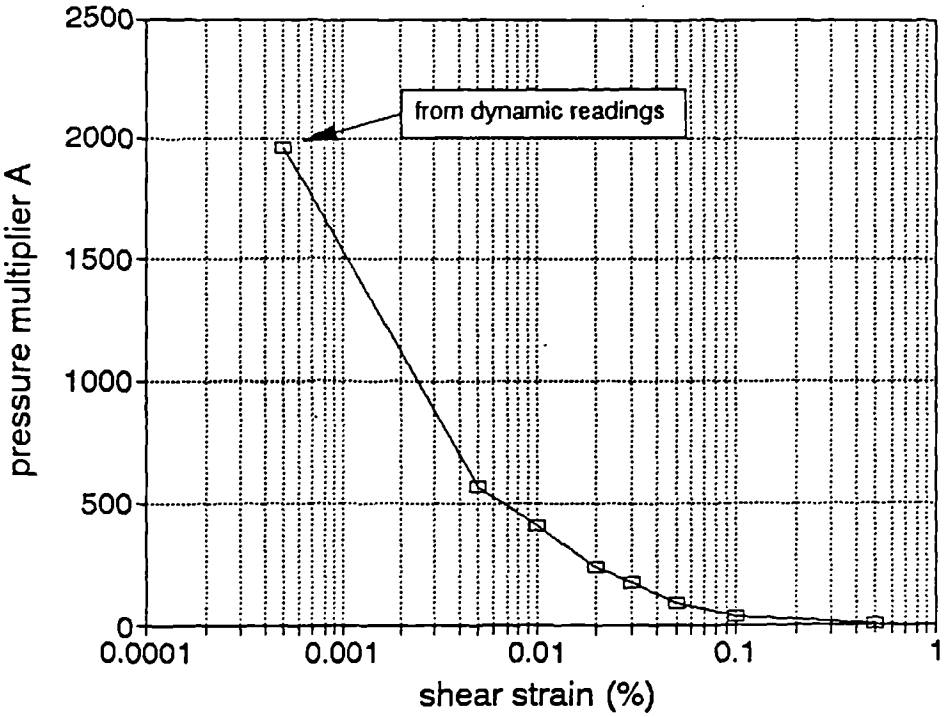

Figure 5.7.4 Speswhite kaolin. Tangent stiffness. Dependence of the pressure multiplier, A, on shear strain amplitude

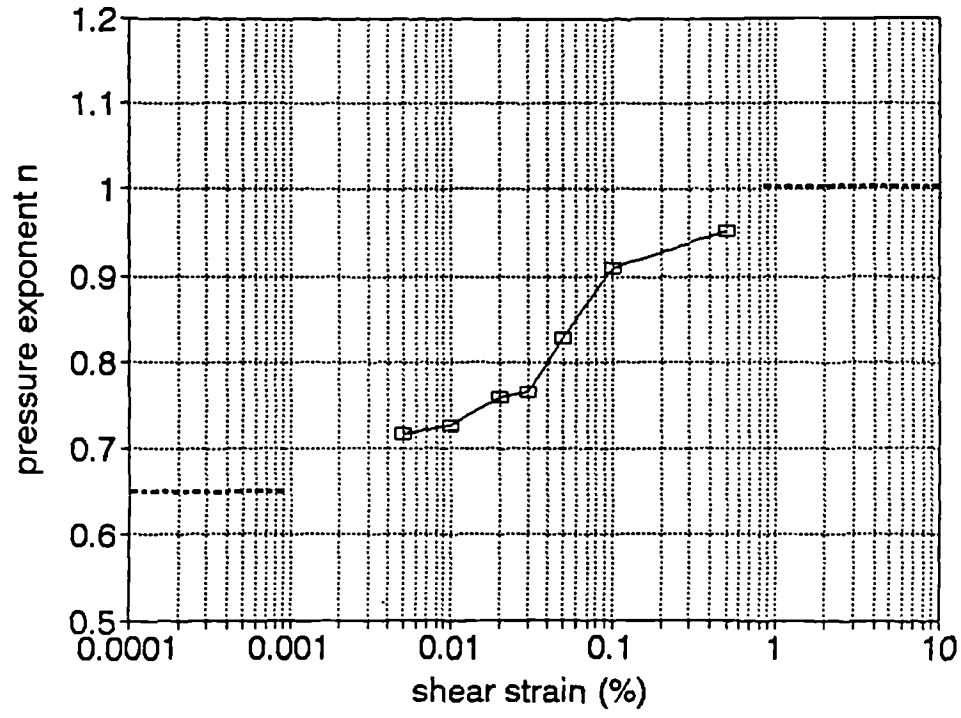

Figure 5.7.5 Speswhite kaolin. Tangent stiffness. Dependence of the exponent of pressure, n, on shear strain amplitude

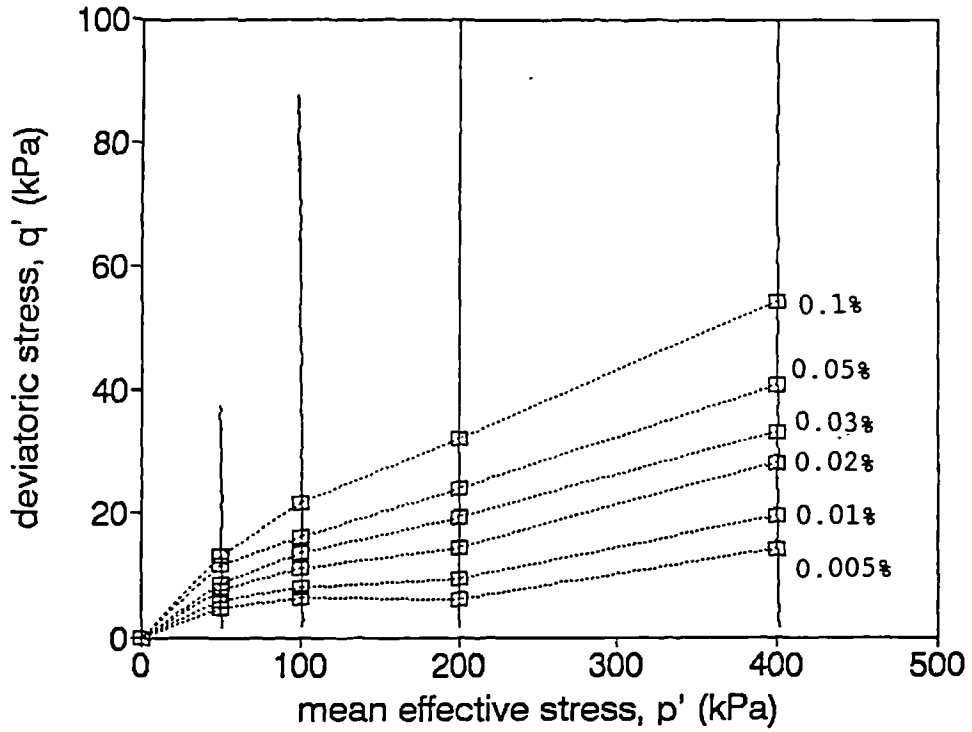

Figure 5.7.6 Stress paths and contours of equal shear strain for tests LSK1, LSK2, LSK3 and LSK4 in the q':p' plane

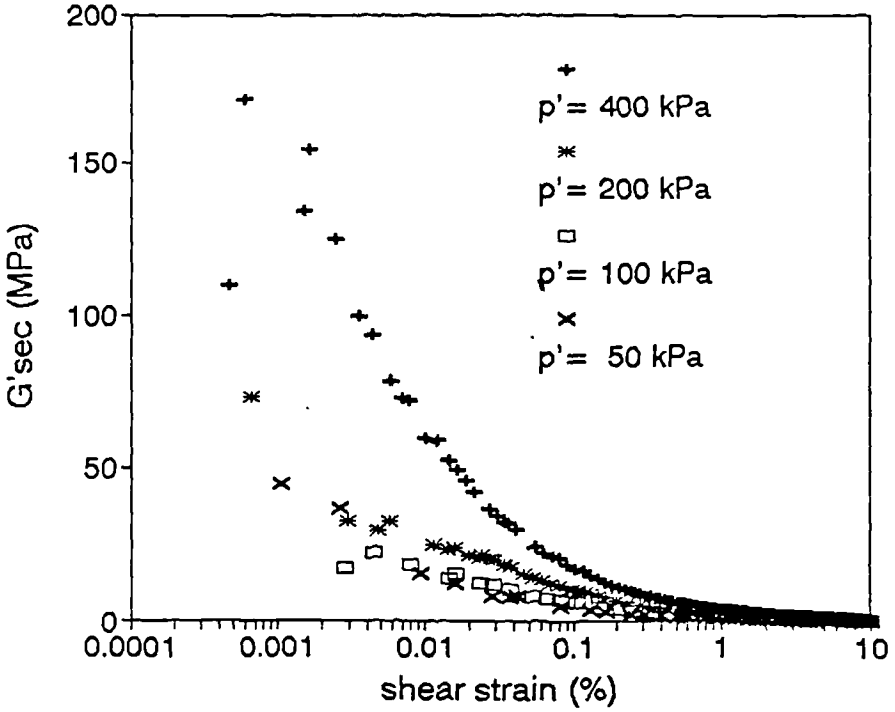

Figure 5.7.7 Speswhite kaolin. Tests LSK1, LSK2, LSK3 and LSK4. Secant stiffness versus shear strain

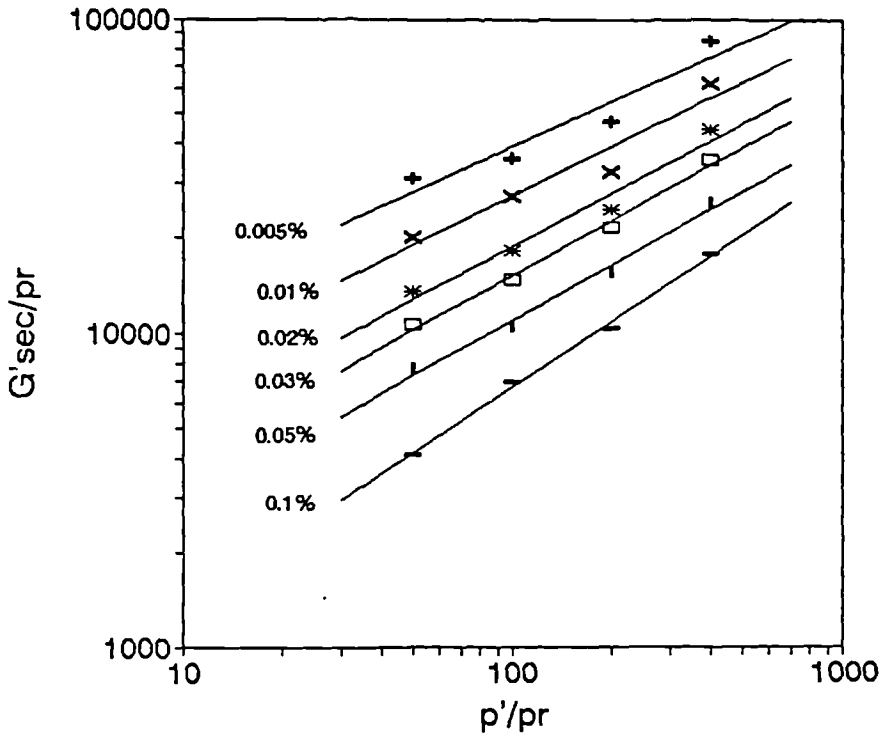

Figure 5.7.8 Speswhite kaolin. Tests LSK1, LSK2, LSK3 and LSK4. Dependence of secant stiffness on mean effective stress at different shear strain amplitudes

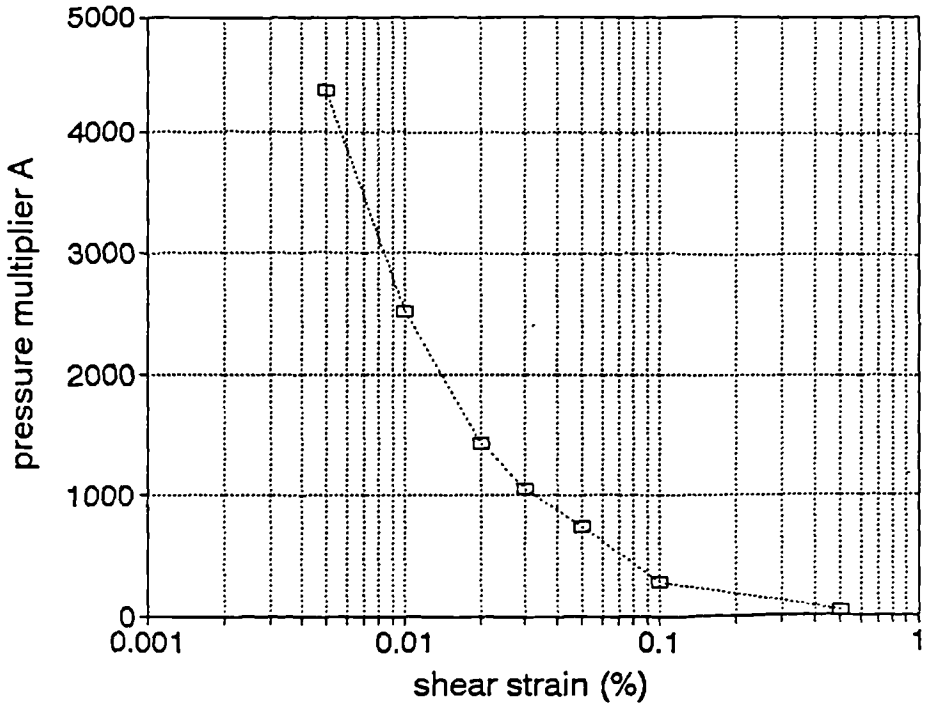

Figure 5.7.9 Speswhite kaolin. Secant stiffness. Dependence of the pressure multiplier, A, on shear strain amplitude

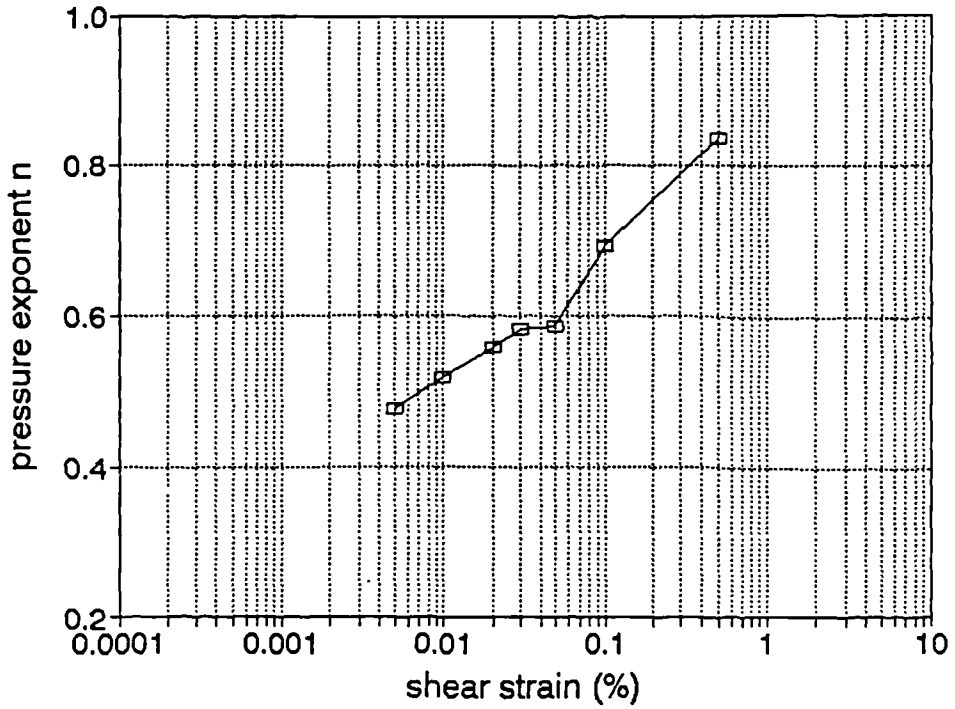

Figure 5.7.10 Speswhite kaolin. Secant stiffness. Dependence of the exponent of pressure, n, on shear strain amplitude

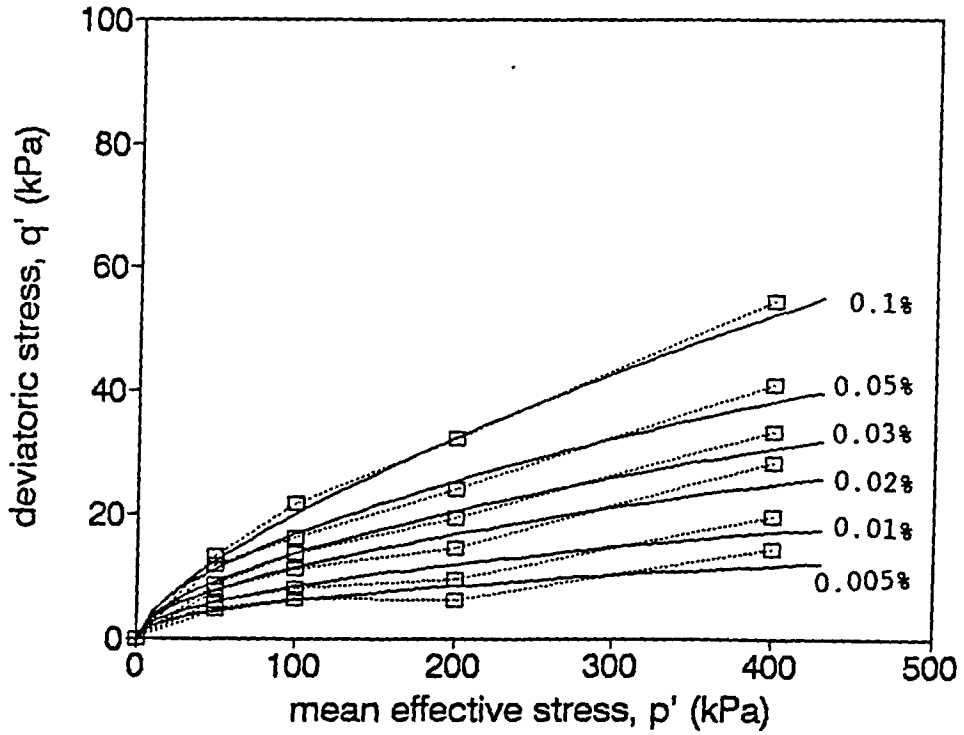

Figure 5.7.11 Contours of equal shear strain

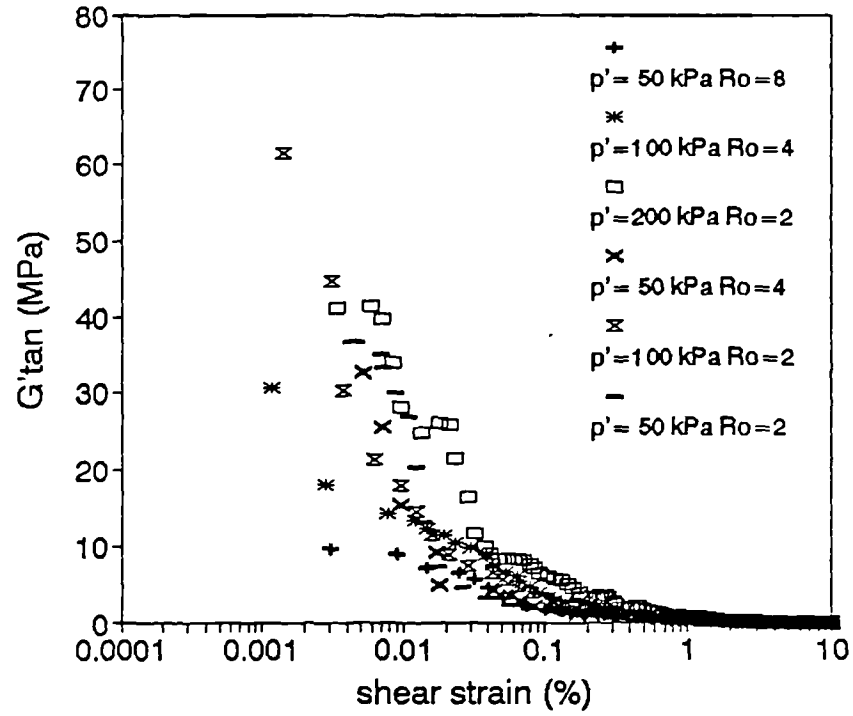

Figure 5.7.12 Speswhite kaolin. Tests LSK5 to LSK10. Tangent stiffness versus shear strain

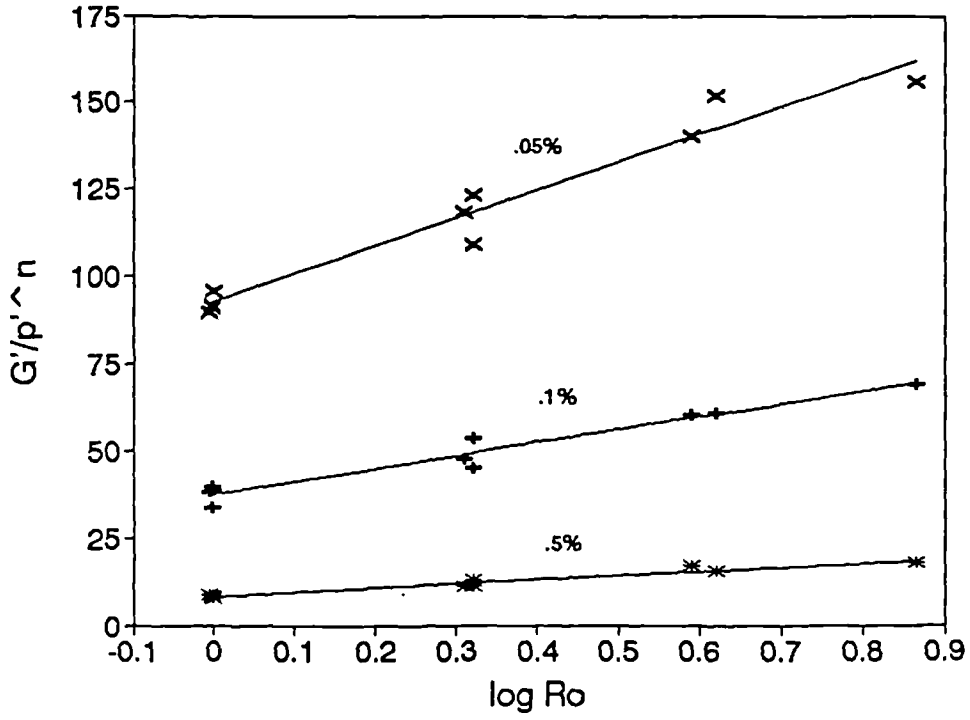

Figure 5.7.13 Speswhite kaolin. Tests LSK1 to LSK10. Dependence of tangent stiffness on overconsolidation ratio at different shear strain amplitudes

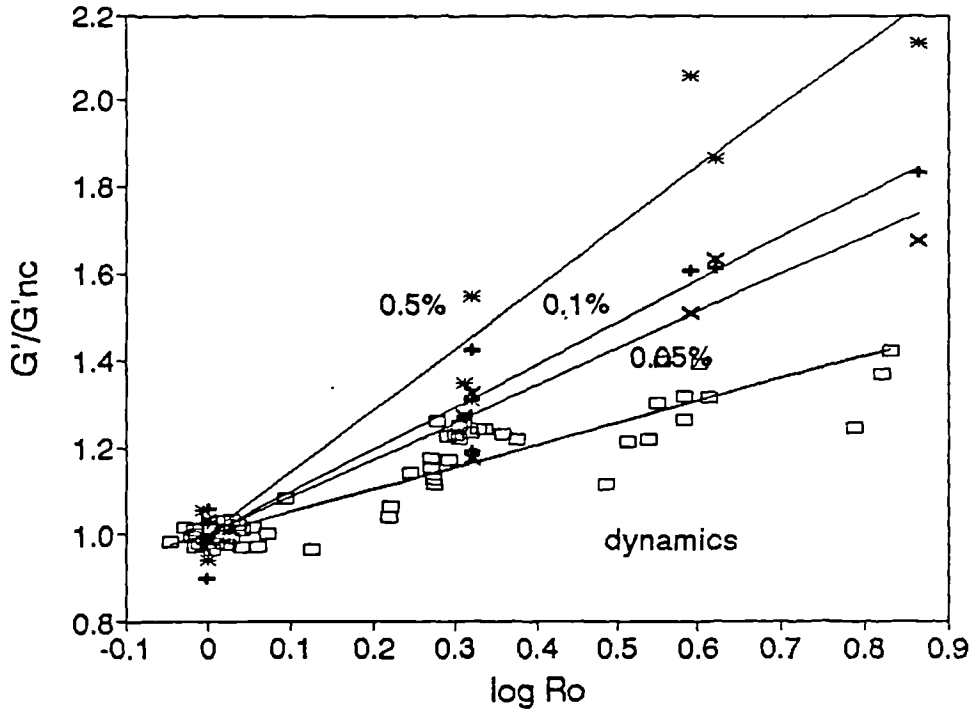

Figure 5.7.14 Speswhite kaolin. Tests LSK1 to LSK10. Dependence of tangent stiffness on overconsolidation ratio at different shear strain amplitudes

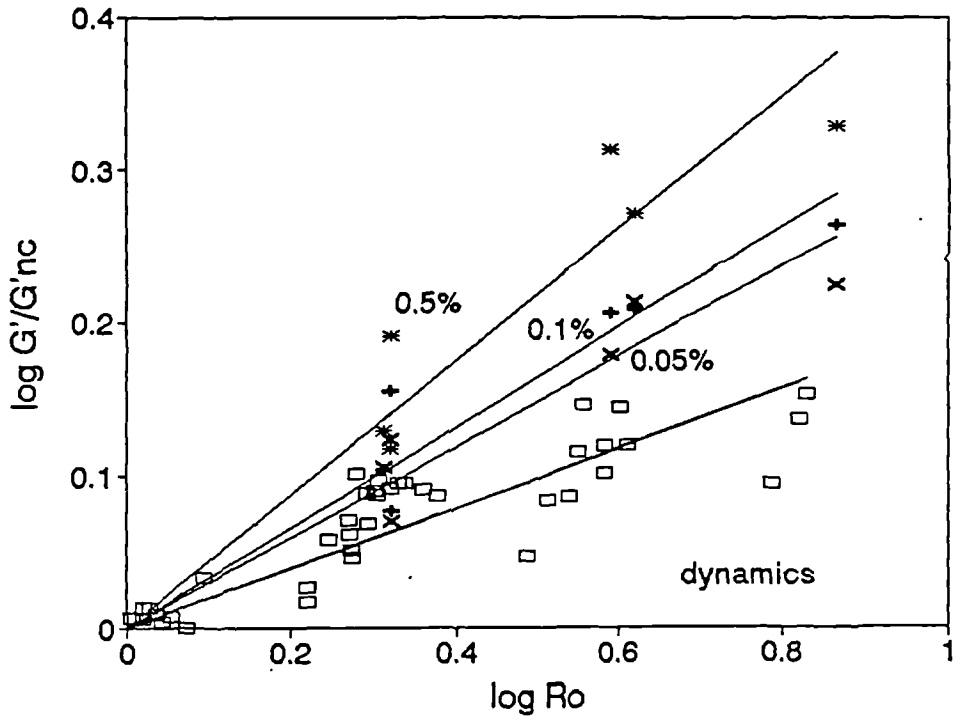

Figure 5.7.15 Speswhite kaolin. Tests LSK1 to LSK10. Dependence of tangent stiffness on overconsolidation ratio at different shear strain amplitudes

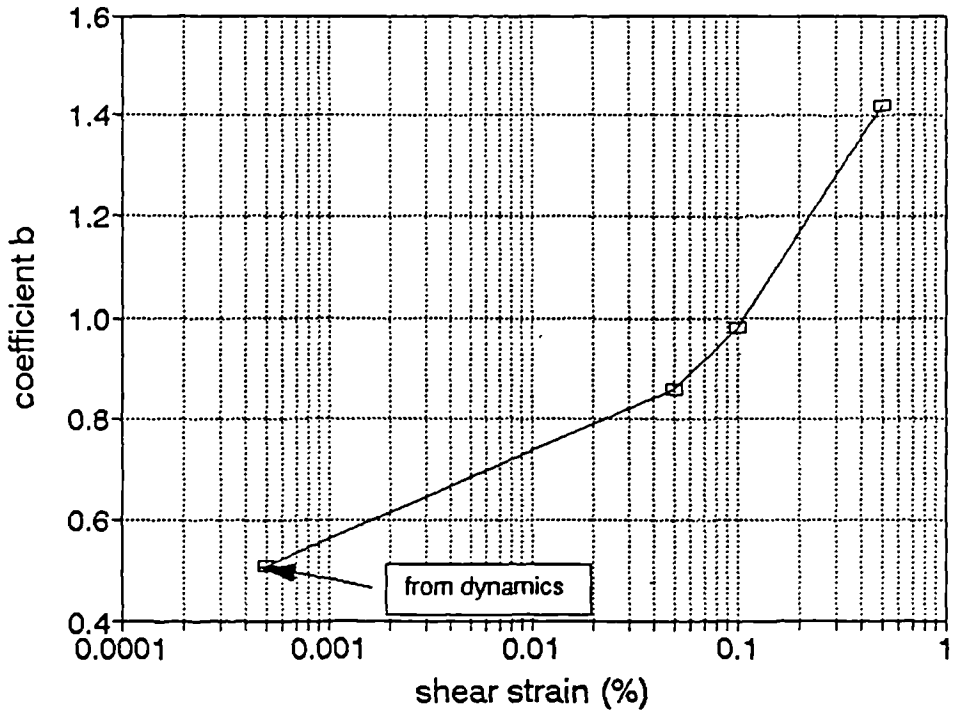

Figure 5.7.16 Speswhite kaolin. Tangent stiffness. Dependence of coefficient b on shear strain amplitude

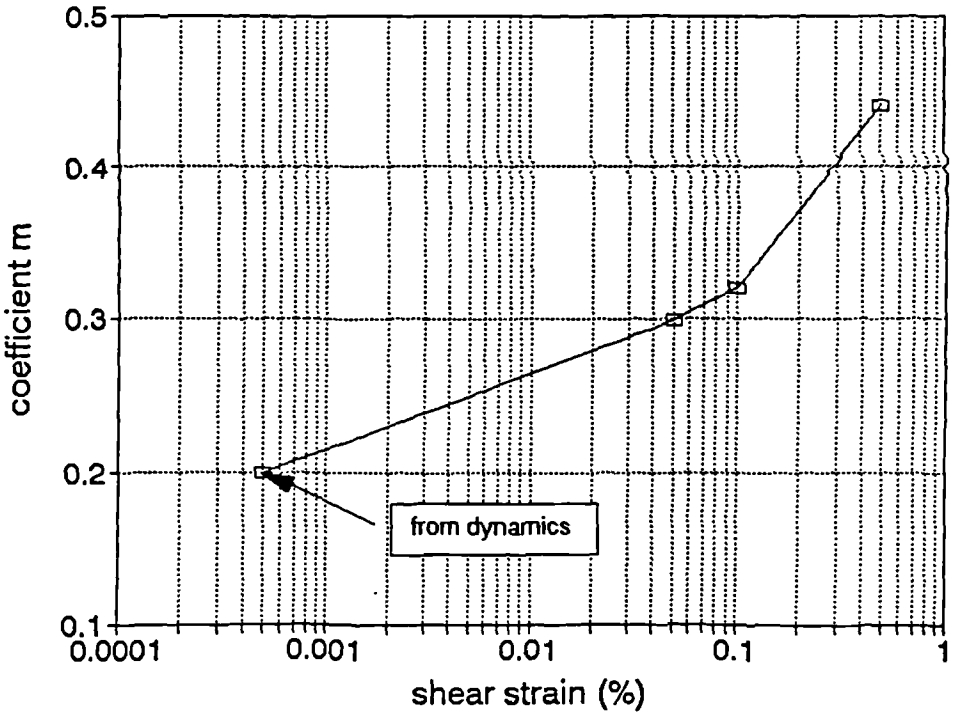

Figure 5.7.17 Speswhite kaolin. Tangent stiffness. Dependence of coefficient m on shear strain amplitude